

Inducing many-body dynamics and detecting unconventional order by light control

Dissertation
zur Erlangung des Doktorgrades
an der Fakultät für Mathematik, Informatik und Naturwissenschaften
Fachbereich Physik
der Universität Hamburg

vorgelegt von
Marlon Nuske
geboren am 07.02.1992 in Eckernförde

Hamburg

August 2020

Gutachter der Dissertation:	Prof. Dr. Ludwig Mathey Prof. Dr. Andreas Hemmerich
Zusammensetzung der Prüfungskommission:	Prof. Dr. Michael Potthoff Prof. Dr. Ludwig Mathey Prof. Dr. Andreas Hemmerich Prof. Dr. Henning Moritz Dr. James Mclver
Datum der Disputation:	26.06.2020
Vorsitzender der Prüfungskommission:	Prof. Dr. Michael Potthoff
Vorsitzender des Fach-Promotionsausschusses Physik:	Prof. Dr. Günter H. W. Sigl
Leiter des Fachbereichs Physik:	Prof. Dr. Wolfgang Hansen
Dekan der Fakultät MIN:	Prof. Dr. Heinrich Graener

Zusammenfassung

In dieser Arbeit untersuchen wir unkonventionelle Ordnung in Festkörpern und in ultrakalten Quantengasen unter Verwendung analytischer sowie numerischer Methoden. Dieser Ansatz ermöglicht uns, die Vorteile beider Systeme zu nutzen, um die zugrundeliegende Physik besser zu verstehen. Wir betrachten dabei vor allem geometrische und topologische Eigenschaften von Graphen und der zugehörigen hexagonalen Gitterstruktur. Zusätzlich beschäftigen wir uns mit der chiralen Ordnung des suprafluiden Zustandes, der im quadratischen Gitter entsteht, wenn Atome ein Bose-Einstein-Kondensat unter Einbindung von p-Orbitalen bilden.

Im ersten Projekt dieser Arbeit betrachten wir den unkonventionellen Quanten-Hall-Effekt, der in Graphen auftritt, wenn es mit zirkular-polarisiertem Licht getrieben wird. In Festkörpern ist der Quanten-Hall-Effekt ein Nachweis für die zugrundeliegenden geometrischen und topologischen Eigenschaften. Wir untersuchen den Quanten-Hall-Effekt unter experimentell-realizierbaren Bedingungen, nämlich unter Berücksichtigung von Dissipation und bei niedrigen Frequenzen des zirkular-polarisierten Lichts. Die Ergebnisse in diesem Regime unterscheiden sich deutlich von den Berechnungen für hohe Frequenzen von T. Oka und H. Aoki (2009). Unser Formalismus liefert daher einen wichtigen Beitrag zum Verständnis von periodisch-getriebenen dissipativen Festkörpersystemen und hilft bei der Interpretation der Ergebnisse der kürzlich durchgeführten Experimente von James McIver et. al. (2019). Unsere Ergebnisse zeigen, dass die topologisch-robuste Quantisierung des Hall-Effekts durch resonante Anregungen beeinträchtigt wird aber die Leitfähigkeit ein geometrischer Effekt ist. Insbesondere erhalten wir einen wesentlichen Beitrag zur Leitfähigkeit indem wir die Berry-Krümmung mit den entsprechenden Besetzungen der Floquet-Bänder gewichten.

Der Quanten-Hall-Effekt ist ein Nachweis topologischer Eigenschaften in

Festkörpern. Diese direkt zu messen, ist in Festkörpern hingegen schwierig. Im zweiten Projekt dieser Arbeit schlagen wir daher — gemeinsam mit dem Team von Christof Weitenberg — vor, topologische Defekte in einem mit Fermionen gefüllten hexagonalen Gitter zu detektieren. Unser Vorschlag basiert darauf, dass wir das Gitter zunächst periodisch modulieren, bevor wir ein Abbild mit der sogenannten Time-of-Flight-Methode erstellen. Aus dem daraus resultierenden Interferenzmuster lässt sich die relative Phase der Atome auf den zwei Untergittern des hexagonalen Gitters bestimmen. Die Mittelpunkte der zugehörigen Phasenwindung geben die Position der topologischen Defekte an. Diese Methode wurde von Matthias Tarnowski et. al. (2017) verwendet, um die Bewegung und Auslöschung von Dirac-Punkten, den topologischen Defekten im hexagonalen Gitter, zu beobachten.

Im dritten Projekt dieser Arbeit verwenden wir ultrakalte Bosonen, um eine andere unkonventionelle Ordnung zu untersuchen: das chirale Bose-Einstein-Kondensat im zweiten Band des quadratischen optischen Gitters mit zweiatomiger Basis. Ultrakalte Quantengase in höheren Bändern von optischen Gittern besetzen üblicherweise Orbitale mit endlichem Drehimpuls. Solche Orbitale spielen beispielsweise für Hochtemperatur-Supraleitung eine wichtige Rolle. Hier zeigen wir, dass das chirale Kondensat ein langlebiger metastabiler Zustand ist, dessen Zerfall zurück ins untere Band unterdrückt ist. Der Vergleich mit Experimenten aus der Gruppe von Prof. Andreas Hemmerich (2020) bestätigt diese Vorhersage. Die chirale Ordnung des Kondensates führt zu destruktiver Interferenz der verschiedenen Zerfallskanäle. Dies stabilisiert das Kondensat gegenüber Zerfall ins erste Band.

Abstract

In this thesis we study unconventional order in both solid-state and ultracold-atom systems using analytic and numerical techniques. This hybrid approach allows to use the advantages of both systems to gain deeper knowledge of the underlying physical mechanisms. Our main focus lies on geometric and topological features of graphene and its hexagonal lattice structure. Additionally, we consider the chiral superfluid order that emerges when p -orbitals are involved in Bose-Einstein condensation.

In the first project we consider an unconventional quantum Hall effect in solid-state graphene driven with circularly polarized light. In solid-state experiments the Hall conductivity represents an evidence of the underlying geometric and topological properties. We study the Hall conductivity in the experimentally feasible regime of dissipative low-frequency driving. In this limit the Hall conductivity behaves fundamentally different from the prediction for the high-frequency limit by T. Oka and H. Aoki (2009). Our formalism therefore makes an important contribution to the application of periodic driving to dissipative solid-state systems and presents an interpretation of the recent experiments by James McIver et. al. (2019). Although the topological quantization of the Hall conductivity is modified by resonant excitations we find that a major contribution to the Hall conductivity is a geometric effect obtained by weighting the Berry curvature of Floquet bands with the respective occupations.

While the consequences of topology are reflected in the Hall conductivity, it is difficult to directly measure topological properties in solids. In the second project of this thesis we therefore propose, in collaboration with the experimental team of Christof Weitenberg, a detection mechanism for topological defects in a hexagonal lattice filled with ultracold fermions. Our proposal is based on a periodic lattice modulation prior to a time-of-flight measurement. This allows to extract the relative phase of the atoms on the two sublattices

of the hexagonal lattice in the resulting interference pattern. The corresponding phase winding reflects the position of topological defects. This detection mechanism has been used by Matthias Tarnowski et. al. (2017) to measure the merging transition of the Dirac points in the hexagonal lattice.

In the third project of this thesis we use ultracold bosons to study a different unconventional order: the chiral condensate in an excited band of the staggered square lattice. Ultracold atoms in excited bands of optical lattices naturally occupy orbitals with finite angular momentum. These are interesting to study since orbital order gives rise to phenomena as important as high-temperature superconductivity. We show that the chiral condensate represents a metastable state, which is long lived as its relaxation to the lowest band is suppressed. We confirm this prediction by comparing our simulations to the experiments performed in the group of Prof. Andreas Hemmerich (2020). By analyzing the relevant relaxation mechanisms, we find that the chiral order of the condensate self stabilizes through destructive interference of the involved relaxation channels.

Acknowledgment

First of all I would like to thank my supervisor Ludwig Mathey for the many inspiring discussions, hints and good ideas which enabled this work to become what it is now. Furthermore I would like to stress that my PhD would not have been the same without the colleagues from Ludwig's group and all the people I know through the graduate schools of the SFB 925 and CUI.

I would also like to thank all experimental collaborators — and especially the teams around James, Christof and Andreas — since all the discussions and continuous comparisons to experiments helped a lot to find the route towards understanding the underlying physical phenomena.

Finally, I would like to thank those people with whom I spend the intense time in isolation, which was both the last weeks of finishing this thesis and the time of Corona: Christopher and Kristina.

Special thanks remains with my parents for their unconditional and sheer unlimited support.

Contents

1. Introduction	11
2. Floquet physics in real solids: light-induced Hall effect in graphene	21
2.1. Master equation for dissipative light-driven graphene	24
2.1.1. Unperturbed graphene Hamiltonian and its diagonalization	24
2.1.2. Electromagnetic waves and gauge choice	27
2.1.3. Coupling graphene to electromagnetic waves	28
2.1.4. Including dissipation and formulating the master equation	29
2.2. Floquet bands and their occupations in driven graphene	33
2.2.1. Dissipationless graphene: band structure and Berry curvature within Floquet theory	36
2.2.2. Dissipative driven graphene: Single-particle correlation function re- veals the band structure	44
2.2.3. Chemical-potential bias in driven graphene	46
2.3. Numerical conductivity simulations and comparison to experiments	48
2.4. Hall conductivity in driven graphene in the low-fluence limit	53
2.4.1. The Rabi problem	53
2.4.2. Mapping driven graphene onto the Rabi problem	54
2.4.3. Interpretation of the Hall conductivity in terms of Rabi Berry cur- vature and Rabi band velocity	56
2.5. Hall conductivity in driven graphene for larger fluence	58
2.6. Resolving the Hall conductivity of individual resonances	60
2.7. Geometric Hall conductivity of the Dirac-point gap	64
2.7.1. High-frequency limit	64
2.7.2. Geometric Hall conductivity for low dissipation	65
2.7.3. Geometric Hall conductivity in the transient response	68
2.8. Characterization of resonant contributions in the low- and high-frequency limit	70
2.9. Comparison of the 2×2 and 4×4 model for zero chemical potential	72
3. Detection of topological Bloch-state defects in ultracold-atom systems	75
3.1. Time of flight images	77
3.2. The hexagonal lattice: transition from graphene to boron-nitride	81
3.2.1. Undriven properties	81
3.2.2. Applying a lattice modulation	84
3.3. Time-of-flight expression for a periodic lattice modulation in perturbation theory	84
3.4. Comparison of experimental, numerical and perturbative results	87
3.4.1. Numerical simulation	87

3.4.2.	Driving regimes	88
3.4.3.	Cross-check of experimental fitting routine	91
4.	Ultracold atoms in higher bands: the s-p_x-p_y-lattice	97
4.1.	Lattice structure and tight-binding Hamiltonian for the s - p_x - p_y -lattice . . .	100
4.1.1.	Tight-binding model	102
4.1.2.	Determining tight-binding parameters	108
4.2.	Dynamics of atoms in excited bands	118
4.2.1.	Theory background: classical field theory	119
4.2.2.	Quench protocol and parameter settings	123
4.2.3.	Condensation in higher bands: the s - p_x - p_y -condensate	123
4.2.4.	Lifetime of atoms in higher bands	130
4.2.5.	Self-stabilization of condensates in higher bands	132
4.2.6.	Oscillation between X -points.	140
4.2.7.	Optimizing the loading procedure	144
4.2.8.	Validity cross check	149
4.3.	Excitation spectra for atoms in higher bands	151
4.3.1.	Multi-mode Gross-Pitaevskii and Bogoliubov theory	151
4.3.2.	Numerical results	160
5.	Summary and Outlook	165
6.	Declaration of contributions	167
A.	Appendix	169
A.1.	Variational Monte-Carlo minimization	169
A.1.1.	Initial state for (S)PGPE simulations	170
A.1.2.	Determining tight-binding parameters	170
A.2.	Equations of motion	171
A.2.1.	PGP-equations	171
A.2.2.	SPGP-equations	173
Bibliography		175

1. Introduction

Topological properties in solids

Bloch's theorem allows the classification of solids in terms of their band structure and its energy gaps, see e.g. [1, 2]. For a given band structure we can distinguish insulators, semiconductors and conductors based on their chemical potential and the temperature. The discovery of anomalous velocities [3–6] and the quantum Hall effect [7] suggested that this classification is not sufficient. There is an additional geometric property influencing transport in solids. Instead of the eigenenergies, i.e. the band structure, geometry is an inherent property of the eigenstates of a system.

We illustrate the idea of the anomalous velocity by considering the motion of a wave packet in a solid. The group velocity of the wave packet has two contributions

$$\mathbf{v}_{\text{group}}(\mathbf{k}) = \nabla_{\mathbf{k}}\epsilon_{\mathbf{k}} + \mathbf{F}_{\text{xy}} \times \frac{\partial \mathbf{k}}{\partial t} \quad .$$

Here $\epsilon_{\mathbf{k}}$ are the eigenenergies of the solid, \mathbf{k} is the lattice momentum and \mathbf{F}_{xy} is the Berry curvature. The first term describes the acceleration of the wave packet due to the gradient of the band structure or more colloquially speaking the wave packet 'rolling downhill', see Fig. 1.1(a). The second term closely resembles the action of the Lorentz force on a particle in a magnetic field. Here, the magnetic field is replaced by the Berry curvature, an intrinsic geometric property of the eigenstates, see Fig. 1.1(b). The Berry-curvature contribution to the group velocity is closely related to the geometric phase factor (Berry's phase [8]) that a particle picks up when transported around a closed circuit in momentum space.

The anomalous contribution to the group velocity that is due to the Berry curvature has direct implications for the transport properties of solids. The paradigmatic example is the quantum Hall effect [7]: in certain materials the Hall conductivity σ_{xy} shows robust plateaus as a function of applied chemical potential or magnetic field. These plateaus are quantized in units of e^2/h . This quantization is directly related to the Chern number c , which is the integral of the Berry curvature over the Brillouin zone. While the Berry curvature is a geometric, i.e. local, property of the eigenstates, the Chern number represents a topological, i.e. global, quantity and is therefore always an integer, see e.g. [9, 10]. The quantization of the Hall conductivity is then implied by the relation $\sigma_{\text{xy}} = c e^2/h$ [11].

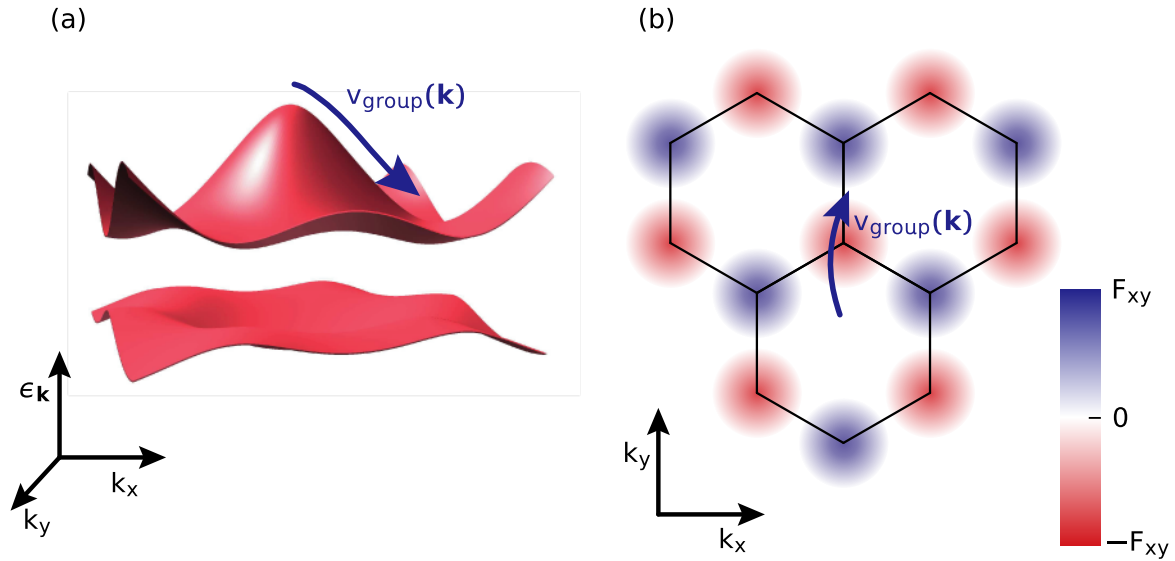


Figure 1.1 – Sketch of the motion of a wave packet in a solid. There are two contributions to the group velocity: an accelerating force due to the gradient of the band structure (a) and the contribution of the Berry curvature (b). For the latter contribution, the out-of-plane Berry curvature F_{xy} acts as a magnetic field, giving rise to an accelerating force perpendicular to the motion of the wave packet.

The discovery of the quantum Hall effect and its topological explanation has inspired a new field of physics. Among the extraordinary phenomena explored within the field of topology are the quantum spin Hall effect [12–16], the fractional quantum Hall effect [17–19] and topological insulators [20–22].

Ultracold atoms

There are only few examples where the underlying geometric and topological quantities, such as Berry phase and Berry curvature, are observable in solids [23]. In contrast such properties are readily accessible in ultracold-atom systems [24, 25]. By loading ultracold atoms into artificial lattices [26, 27] build from several intersecting laser beams, they can be used as a quantum simulator for phenomena relevant in solid-state systems [28]. Since the first realization of a Bose-Einstein condensate [29–31], an extensive toolbox has been developed for preparing and detecting ultracold atoms. There is a series of examples where the ultracold-atom toolbox has lead to deeper understanding of mechanisms underlying solid-state phenomena: the high amount of control in ultracold-atom systems often allows to continuously tune between different limiting cases, as in the superfluid to Mott-insulator transition [32] or for the comparison of Klein tunneling to regular tunneling [33]. The access to microscopic quantities has lead to the observation of real-space Bloch oscillations [34] and the visualization of topological properties such as the direct observation of edge

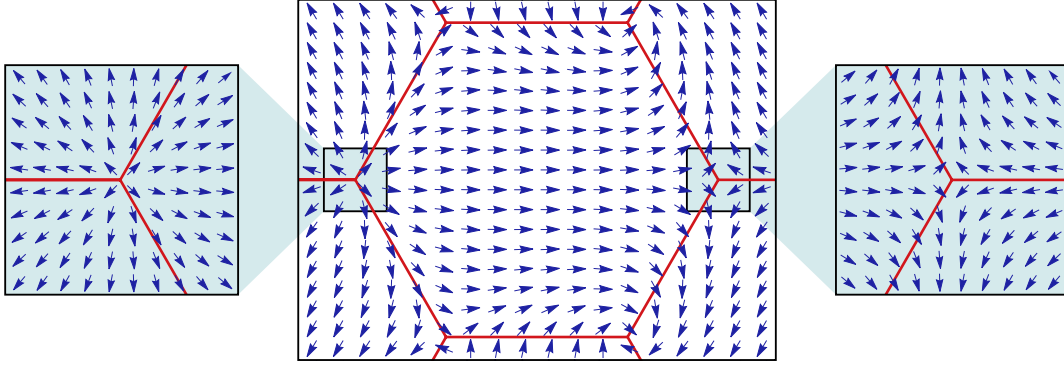


Figure 1.2 – Pseudo-spin winding of the hexagonal lattice. At each point in momentum space we visualize the eigenstate on the Bloch sphere. We show the case of graphene, where the eigenstates are always on the equator of the Bloch sphere and hence there is no out-of-plane component. The Dirac points are positioned at the six edges of the Brillouin zone, which is marked by a red hexagon. The insets show a zoom to the two nonequivalent Dirac points. By following the arrows around a closed loop around the Dirac points we see that the pseudo-spin winds clockwise and anti-clockwise at the two Dirac points, respectively.

states [35–37]. Ultracold atoms do not only allow an alternative view on solid-state phenomena but also give access to topological phases that have not yet been discovered in solids, by using artificial gauge fields and synthetic dimensions [38, 39]. In fact, many archetypal topological models can be implemented and studied with ultracold atoms [40].

Graphene

We are particularly interested in the topological properties of the hexagonal lattice. The prime example of a solid featuring the hexagonal lattice structure is graphene, a single sheet of carbon [41]. Since its experimental extraction [42], graphene has attracted widespread attention due to its exceptional properties [43]. These range from remarkable thermal and electric conductivity via Klein tunneling to unconventional quantum Hall effects [44–48]. Further versatile properties emerge, when using graphene as the building block of graphene stacks, nanoribbons and composite materials [41]. Since carbon is ubiquitous in nature, graphene is not only multifaceted in its applications but also abundantly available. In fact, the technology is ready for mass-scale production and consumer-based applications [49].

On the microscopic level the hexagonal lattice structure has two lattice sites per unit cell such that the lowest two bands are well separated from the remaining bands. In graphene, i.e. without a potential imbalance between the lattice sites, these two bands have crossings with linear dispersion relation at the Dirac points. The eigenstates of the hexagonal lattice can be visualized on the Bloch sphere at each point in momentum space,

see Fig. 1.2. In graphene the resulting pseudo-spin texture has opposite winding at the two Dirac points giving rise to a Berry phase of $-\pi$ and π , respectively. This pseudo-spin winding of the eigenstates is responsible for the exceptional transport properties of graphene [50].

Floquet theory

The interaction of light and matter is widely used not only to probe but also to induce materials properties. Probing the steady state subject to periodic driving acts as a powerful tool for the design of new materials. This complements the established approach to solid-state physics, where only the equilibrium properties of a given material are probed. An outstanding example for light-induced unconventional properties is the enhancement of superconductivity in cuprate materials by applying terahertz pulses [51–55].

The steady state of periodically driven systems can often be described by an effective static system. This idea is the foundation of Floquet theory [56–58] and yields a powerful instrument to design specific properties in solids, for reviews see e.g. Refs. [59, 60], for further examples see also Refs. [61–63]. In the same way as a periodic lattice potential leads to the repetition of the band structure in momentum space, periodic driving leads to the repetition of the band structure in energy space. For the latter case the replica of the bands are also referred to as Floquet quasi-energies or bands. This has intriguing consequences for the topological properties of driven systems. For an undriven system there is usually a correspondence between the edge states, which appear in the band gaps of the spectrum, and the Chern number of the neighboring bands [64]. For driven systems edge states may wind around the periodic boundary of the energy spectrum, hence giving rise to nontrivial edge states even in the absence of a finite Chern number [65–67].

Floquet theory has been applied successfully to ultracold-atom systems [68], extending the ultracold-atom toolbox by an additional tuning knob. This has led to the observation of the driven superfluid to Mott-insulator transition [69, 70], artificial magnetic fields [71, 72] and topological charge pumps [73–75].

Light-driven graphene

While the static properties of graphene are truly remarkable, it unfolds even more extraordinary features when driven periodically. It has been proposed in Refs. [76–80] that illuminating graphene with circularly polarized light opens a topologically nontrivial band gap at the Dirac point. When the driving frequency is assumed to be large compared to the bandwidth of graphene, it resembles the famous Haldane model [81] with a Chern

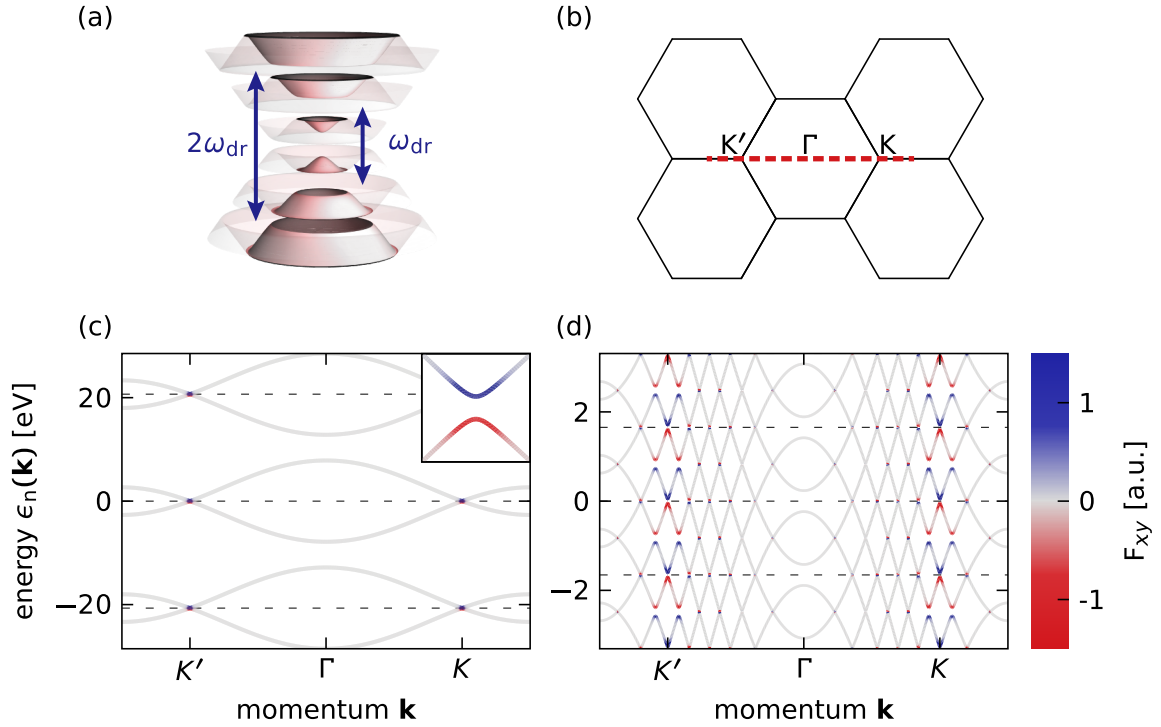


Figure 1.3 – (a) Dirac cone of the resonantly driven graphene band structure. Band gaps open at the Dirac point and at rings in momentum space where multiples of the driving frequency ω_{dr} equal the band gap. (b) Reciprocal hexagonal lattice indicating the symmetry point Γ and the Dirac points K and K' . (c) and (d) Floquet spectrum of driven graphene colored by Berry curvature F_{xy} for a cut through the Brillouin zone shown by the dashed red line in (b). For panel (c) we use an off-resonant driving frequency $\omega_{\text{dr}} = 2\pi \cdot 5 \text{PHz} = 20.7 \text{eV}$ and for panel (d) a resonant $\omega_{\text{dr}} = 2\pi \cdot 400 \text{THz} = 1.7 \text{eV}$. The inset in panel (c) shows a zoom to the Dirac point. For off-resonant driving it is a good assumption that only the undressed Floquet bands centered around $\epsilon_n(\mathbf{k}) = 0$ are occupied and hence there is a well defined lowest energy state. Such a notion can not be extended to the resonant case. For panels (c) and (d) we use an electric field strength $E_{\text{dr}} = 26 \text{MV m}^{-1}$.

number of the lowest band equal to¹ $c = -2$. Under the additional assumption that only the lowest band is filled, graphene is driven into a topologically insulating state with quantized Hall conductivity $\sigma_{xy} = -2e^2/h$. This idealized limit is indeed achievable in ultracold-atom systems by making use of artificial gauge fields [82–85]. In solids, this regime is significantly more challenging. The band gap at the Dirac point scales as $\propto E_{\text{dr}}^2/\omega_{\text{dr}}^3$. Hence for a driving frequency ω_{dr} that is larger than the bandwidth the field strength E_{dr} needs to be increased to experimentally unrealistic values in order to obtain a sizable band gap. A sizable band gap is therefore only possible for low-frequency driving in the regime of terahertz. This regime was realized in recent experiments by James

¹We already account for spin and valley degeneracy.

McIver et. al. [86], which are the motivation for the first project of this thesis.

When illuminating graphene with terahertz radiation, additional resonant band gaps open at rings in momentum space where multiples of the driving frequency equal the energy difference of the two graphene bands [87–90], see Fig. 1.3(a). Each of these resonant band gaps contributes to the Berry curvature [91–93]. Summing all contributions gives the Chern number of a given band, which can crucially depend on driving field strength and frequency [80]. For a driving frequency of 50 THz we estimate that there are about 80 resonant band gaps and the Chern number can take values on the order of 10^2 – 10^3 . These Chern numbers have, however, only minor significance for the Hall conductivity in solids. The Hall conductivity would only be given by the Chern number if a single Floquet band were occupied. We can easily see that this is usually not the case when a system is driven in the resonant regime. At each resonance, avoided crossings occur [94], and hence the undriven band structure is nontrivially connected to the driven band structure. This, together with the periodicity in energy makes it impossible to define an ordering of Floquet quasi-energies, see Fig. 1.3(b,c,d). Hence there is no notion of a lowest Floquet band, which at low temperature might be the one that is occupied. Instead the relative occupations of different Floquet bands are determined by a competition between driving and dissipation [95].

Periodic driving and dissipation

Although there are first attempts to reformulate Floquet theory when including dissipation [96], the interplay of periodic driving and dissipation is far from being well understood. The fundamental question of periodically driven dissipative systems is whether the steady state can be rewritten in Gibbs form as a Boltzmann distribution of appropriately defined quasi-energies. This would allow a similar mapping as Floquet theory achieved for non-dissipative systems and allow the application of statistical mechanics to the driven state. So far the question, whether a Gibbs state exists, could only be answered for rather simple analytically solvable systems [97–104] and in certain limiting cases such as high-frequency driving [105–107]. The fundamental problem for low-frequency driving is the above-mentioned periodicity of the eigenenergy spectrum, which makes it impossible to define an ordering of Floquet quasi-energies [108] and hence obtain an intuition for the action of dissipation. At the same time, dissipation may actually be important for periodic driving in solids since it can counteract heating due to resonant excitations [109]. It has even been proposed that certain engineered dissipation mechanisms may enhance [110] or induce [111] topological properties.

The importance and complexity of dissipation is likely the reason why the Floquet topo-

logical insulator, although proposed almost ten years ago [91], has not yet been observed in solids. While Floquet bands have been observed in solids [112] their relative occupations are determined by a complicated interplay of driving and dissipation. The only experimental observation of a Floquet topological insulator has instead been in non-dissipative helical waveguides [113, 114], hence founding the field of topological photonics [115].

Dissipative light-driven graphene

The aim of the first project of this thesis, presented in chapter 2, is to give further insight on the interplay between dissipation and periodic driving by considering the example of dissipative light-driven graphene. We develop a master equation formalism that includes a periodic driving force, a longitudinal bias field and dissipation. Our formalism shows good agreement with experimental results from Ref. [86]. We find that the electron distribution in driven graphene perfectly resembles the Floquet band structure. We compute the Hall conductivity and find that a major contribution is a geometric effect. In fact, we find that the Hall conductivity is approximately given by the sum of Berry curvature and band velocity of Floquet bands weighted with their respective occupations. Although the electron distribution in graphene is a highly nontrivial steady state that depends on the details of driving and dissipation, the resulting derived quantities such as the Hall conductivity can still be evaluated in analogy to an effective undriven system. Our formalism allows to investigate the crossover from strong to weak dissipation. In the latter case we recover the effective high-frequency limit and the Dirac-point contribution to the Hall conductivity is $-2e^2/h$. Notably we do not recover this result for finite dissipation when increasing the driving frequency by orders of magnitude. This stresses the importance of dissipation for modeling solid-state systems.

The transition to the weakly dissipative regime allows the application of our formalism to ultracold-atom systems. Hence the theoretical framework presented in this thesis is bridging the gap between quantum simulators and solid-state physics. We are aiming to learn from both fields of physics in order to understand the underlying physical phenomena.

Detecting topological properties

As we have noted above, ultracold atoms have the advantage that topological properties are more accessible than in solids. In fact, it is usually easier to get access to the eigenstates in ultracold atoms. Therefore it is not only possible to measure the band gap at topological defects [82, 116], but also the eigenstates and topological properties themselves. A number of different methods have been proposed for the detection of topological properties in

ultracold atoms, each of them having its own advantages and difficulties: accelerating wave packets through the lattice is at the heart of Berry’s gedanken experiment but makes it cumbersome to cover the full Brillouin zone [84, 85, 117–119]. Projecting onto a flat band structure [120–122] is a more efficient technique, but only works for periodically driven systems. The detection of edge and bulk currents using time-of-flight images is still awaiting an experimental implementation [123]. Within the second project of this thesis, presented in chapter 3, we therefore propose an efficient method that allows to determine the properties of the eigenstates in the full Brillouin zone within a single experimental sequence [N1]. Our method is based on the interference of the atoms from different sublattices in a hexagonal lattice. An additional periodic lattice modulation allows to extract the information on the relative phase of the eigenstates.

Ultracold atoms, excited states and metastability

Ultracold atoms give access to a wide range of parameter regimes with rich tunability between different ground states. They are, however, usually limited to the lowest band of a lattice and hence bosons — as a result of the no-node theorem — can only occupy s -orbitals [124]. Higher orbital order, such as p - or d -orbital order, has been identified as one of the main ingredients for metal-insulator transitions, high-temperature superconductivity and colossal magnetoresistance [125–130]. Additionally the band crossings of excited bands may lead to nontrivial topological order [133, 138–140]. These potential applications have triggered the idea of loading ultracold atoms into excited bands of an optical lattice [124, 141–145]. The first experimental realization of ultracold atoms in excited bands has been achieved by stimulated Raman transitions [146]. Slightly later a different approach was successful that makes use of a tunable staggered square lattice [131–137]. The atoms are loaded at large imbalance between the two sublattices and then transferred to excited bands by suddenly interchanging the depth of the sublattices. This preparation scheme enables a well controlled transfer of atoms and hence allows addressing bands up to the 11th band. Condensation in excited bands reflects the nontrivial orbital order. In the second band of the staggered square lattice this leads to condensation with chiral order parameter [131, 134].

In the third project of this thesis, presented in chapter 4, we study the excitation of ultracold bosons into excited bands and the subsequent decay dynamics within classical field theory. Most notably we find that the chiral condensate self-stabilizes against decay to the first band and hence represents a metastable state. Metastability is a phenomenon ubiquitous in nature. Commonly metastability arises in a classical context when a system is trapped in a local minimum and a free-energy barrier inhibits relaxation to the true

ground state [147–149]. While a similar mechanism can also occur in quantum-mechanical systems, for example in quantum-tunneling scenarios [150–152], the quantum-mechanical origin for metastability can be more diverse. In a classical system the only relevant energy scales are the height of the free-energy barrier and the temperature of the system. For a quantum mechanical system Bose-Einstein condensation can lead to metastability for temperatures that are significantly larger than the free-energy barrier [153], since for such a case only the small thermal fraction of atoms can decay. Quantum mechanically metastability can even occur as an inherent property of the state in question [154–156] or due to a mechanism of constructive interference [157].

Here we propose a mechanism for metastability where destructive interference of the dissipation channels leads to inhibition of relaxation [N3]. We confirm this mechanism both theoretically as well as experimentally, in collaboration with the group of Prof. Andreas Hemmerich. We identify the two main decay mechanisms and find that the chiral order of the condensate leads to destructive interference for both of them individually. The condensate is a dark state with respect to decay and hence a perfect condensate at $T = 0$ has infinite lifetime. At any finite temperature there is a fraction of thermal atoms. These are not protected from decay and eventually lead to heating and the destruction of the condensate. We therefore identify three different relaxation stages: coherence buildup, inhibited relaxation and loss of coherence, fast relaxation to the thermal ground state.

2. Floquet physics in real solids: light-induced Hall effect in graphene¹

Periodic driving has been applied widely as a tool to induce unconventional properties in ultracold-atom and solid-state systems [59, 68]. The response of a system subject to periodic driving can be split into one part that is periodic with the driving force and an additional effective slow or stroboscopic motion. Floquet theory is based on the idea that it is often sufficient to consider this effective slow motion in order to describe the main properties of the system. Within Floquet theory the slow motion can be captured by an effective static system. The properties of this effective static system can be profoundly different from those of the original undriven system.

One such example where periodic driving leads to unconventional new properties is graphene. Without driving graphene features a linear dispersion relation at the Dirac point, see Fig. 2.1(a). Driving graphene with high-frequency circularly polarized light induces a phase transition to a topologically nontrivial state. The effective static system corresponding to this driven state resembles the famous Haldane model [81] and hence is characterized by integer Chern number and a quantized Hall conductivity. This has been proposed in Refs. [76–80] under the assumption that a driving frequency ω_{dr} is used, which is large compared to the electronic state energies. This limit is only realized for frequencies above the bandwidth of graphene. In order to observe the quantized Hall conductivity one has to additionally assume that the driven system is approximately in a band insulating state of the effective Hamiltonian. Such a regime of low dissipation and a driving frequency larger than the bandwidth is indeed accessible in ultracold-atom experiments [82–85].

In contrast, the proposed nonequilibrium topological state is in a much more challenging regime in solid-state systems. The effective energy gap in the high-frequency limit is $\Delta_{\text{hf}} \propto E_{\text{dr}}^2/\omega_{\text{dr}}^3$ [76]. The technological development of on-chip femtosecond-resolved transport measurements reported in Ref. [86] allows for a measurable gap when driven in

¹Parts of this chapter have been published in Ref. [N2].

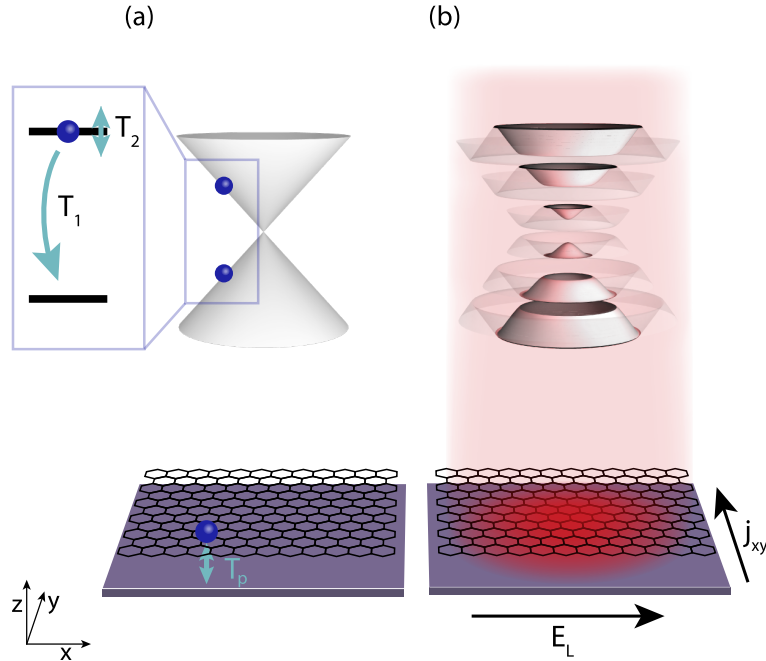


Figure 2.1 – Dirac cone of the undriven (a) and driven (b) graphene band structure (top) and the corresponding real-space lattice (bottom). For graphene driven with circularly polarized light gaps open at each resonance and at the Dirac point. Applying a longitudinal field E_L induces a transverse Hall current j_{xy} . In our numerical simulation we include dissipative processes through phenomenological parameters. These correspond to decay from the upper to the lower band with time scale T_1 , dephasing on a time scale T_2 and the exchange of particles with the back gate on a time scale T_p . This figure has been published in Ref. [N2].

the regime of tens of terahertz. The required frequency regime is, however, several orders of magnitude higher, ideally above the graphene bandwidth, which is on the order of tens of petahertz. In order to obtain a sizable gap the driving field strength E_{dr} needs to be simultaneously increased by orders of magnitude, leading to unrealistic experimental requirements.

In this chapter we therefore develop a protocol for the application of Floquet theory to the realistic solid-state regime. As an example we consider graphene driven in the low-frequency dissipative regime. In this regime a series of resonant band gaps opens, see Fig. 2.1(b). Each resonance contributes Berry curvature hence leading to an extensive set of different possible Chern numbers of the effective bands [80]. While in the experimentally realistic regime several hundred resonant band gaps open, we find that only few of them are actually relevant for the dynamics of driven graphene. Band gaps that are higher order in the driving field have only small magnitude and are therefore suppressed by dissipation and finite temperature. Dissipation also has a crucial influence on the driven steady state in graphene. We find that Floquet theory nevertheless provides a very good prediction for

the effective steady-state band structure and only the occupations of the respective bands crucially depend on damping and dephasing. Predominantly those bands are occupied that are adiabatically connected to the undriven band structure. In contrast, the reaction of the system to a chemical-potential bias is profoundly different from that of a static system. When increasing the chemical potential the first momentum modes that obtain double occupancy are not the ones at the Dirac point, but instead those on a ring around the Dirac point. The size of the ring is given by the zero-detuning Rabi frequency and hence is determined by the field strength and the frequency of the driving field.

When applying a longitudinal electric field E_L to driven graphene, a transverse Hall current is induced. Floquet theory provides an interpretation of this Hall current as a geometric effect. In fact, the total Hall conductivity σ_{xy} is to good approximation given by the sum of the Floquet Berry curvature F_{xy}^σ and the Floquet band velocity v_y^σ weighted with the occupations $n_\sigma(\mathbf{k})$ of the corresponding Floquet bands, labeled by $\sigma = \pm 1$

$$\sigma_{xy} \approx \frac{1}{A} \sum_{\substack{\mathbf{k} \in \text{1.BZ} \\ \sigma = \pm 1}} (F_{xy}^\sigma(\mathbf{k}) + v_y^\sigma(\mathbf{k})/E_L) n_\sigma(\mathbf{k}) \quad . \quad (2.1)$$

Here A is the lattice size and the sum runs over all momenta \mathbf{k} in the first Brillouin zone. Like the occupations $n_\sigma(\mathbf{k})$, the resulting Hall conductivity depends on dissipation.

For the investigation of the Hall conductivity in driven graphene we develop a numerical simulation platform that is based on a full quantum-mechanical description combined with phenomenological damping and dephasing mechanisms, see Fig. 2.1(a). We find good quantitative agreement with experimental data from Ref. [86]. Within our model we can isolate the contributions of individual resonances and the Dirac point. For the first resonance mapping graphene onto the Rabi problem gives intuitive insights into the origin of the Hall conductivity as a geometric effect. We also investigate how the system approaches the effective high-frequency limit when increasing the driving frequency. In this limit the resulting conductivity is expected to approach the value of $-2e^2/h$. We find that this is indeed the case when reducing the dissipation strength and when considering the transient response before the steady state is reached. When increasing the driving frequency at fixed dissipation strength we find that the system approaches a high-temperature state with vanishing Hall conductivity instead.

2.1. Master equation for dissipative light-driven graphene

In this section we develop the formalism for computing the time evolution of electrons in light-driven graphene. We first consider the noninteracting system and couple the electromagnetic field via minimal coupling. Within a semi-classical picture a Hamiltonian with dispersion relation $\epsilon(\mathbf{k})$ is coupled to the scalar potential ϕ and vector potential \mathbf{A} as

$$H(\mathbf{r}, \mathbf{k}) = \epsilon(\mathbf{k} \rightarrow \mathbf{k} - q\mathbf{A}(\mathbf{r}, t)/\hbar) + q\phi(\mathbf{r}, t) \quad , \quad (2.2)$$

where \mathbf{r} is the position, $\hbar\mathbf{k}$ the momentum and $q = -|e|$ the charge of the electrons. For our case the Weyl gauge $\phi = 0$, among other assumptions, will ensure that the Hamiltonian remains block diagonal in momentum space. A product ansatz for the density matrix is therefore appropriate

$$\rho = \otimes_{\mathbf{k}} \rho_{\mathbf{k}} \quad .$$

We discretize momentum space and solve the full quantum-mechanical time evolution at each momentum point \mathbf{k} by solving the master equation for the density matrix. In this process we explicitly allow for empty and doubly-occupied states of the density matrix. Hence, each density matrix $\rho_{\mathbf{k}}$ has four states given by the four ways of occupying the two single-particle states at the corresponding momentum. The master equation contains the unitary contributions from the equilibrium Hamiltonian and the light-matter interaction. The latter contains both the circularly polarized driving term, as well as a longitudinal DC probing field. In addition to these unitary contributions, interaction effects are treated by including a dissipative environment. This environment is modeled within a Lindblad formalism by introducing a decay rate $\gamma_1 = 1/T_1$ from the upper to the lower state, a dephasing rate $\gamma_2 = 1/T_2$, and a single-particle exchange rate $\gamma_p = 1/T_p$ with a fermionic bath of temperature T and chemical potential μ .

We compute observables such as the longitudinal and transverse current by summing their expectation values over all individual momentum modes.

2.1.1. Unperturbed graphene Hamiltonian and its diagonalization

We consider a tight-binding model² including only nearest-neighbor tunneling for graphene. The graphene lattice has two nonequivalent lattice sites per unit cell, see Fig. 2.2(a). The

²More information on tight-binding models will be given in chapter 4.

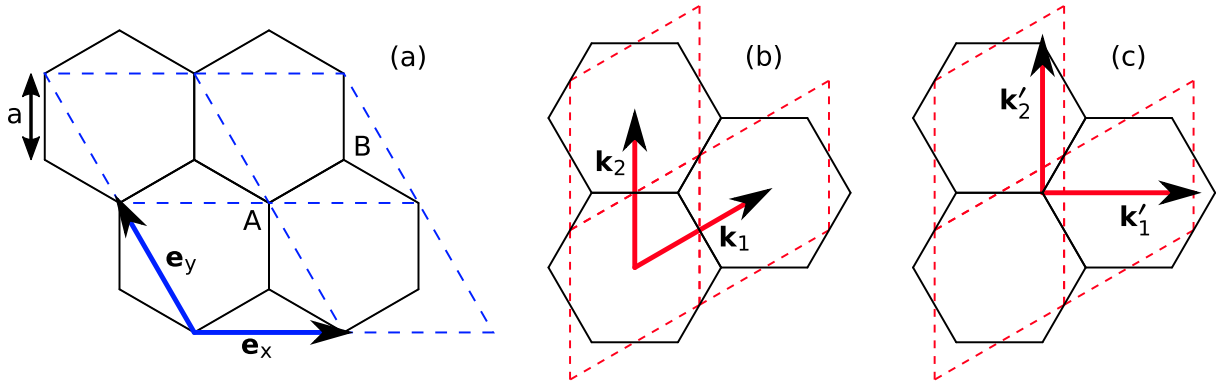


Figure 2.2 – (a) Sketch of the hexagonal lattice with unit vectors \mathbf{e}_x and \mathbf{e}_y . Solid black lines show the hexagonal lattice of Wigner-Seitz unit cells. The dashed blue parallelograms show an equivalent lattice spanned by \mathbf{e}_x and \mathbf{e}_y . Both lattices contain two sites, A and B , per unit cell. (b) Reciprocal lattice of the hexagonal lattice. Solid black hexagons show the first Brillouin zones at each lattice point and dashed red lines show the lattice spanned by the two reciprocal lattice vectors \mathbf{k}_1 and \mathbf{k}_2 . (c) Same as (b) but with the unit vectors for the linearized dispersion relation. Panels (a) and (b) have been published in [N8].

lattice constant in graphene is $a \approx 1.42 \text{ \AA}$ and gives the distance between two sublattice sites. The lattice vectors $\mathbf{e}_{x,y}$ shown in Fig. 2.2(a) connect next-nearest neighbor sites and therefore have length $d = \sqrt{3}a \approx 2.46 \text{ \AA}$. As a result of the two sublattice sites the momentum-space Hamiltonian is a 2×2 matrix for each momentum \mathbf{k} , for details see e.g. [N8]. It is given by

$$H_{0,\mathbf{k}} = \psi_{\mathbf{k}}^\dagger \begin{pmatrix} 0 & \epsilon_{\mathbf{k}}^* \\ \epsilon_{\mathbf{k}} & 0 \end{pmatrix} \psi_{\mathbf{k}}$$

where $\epsilon_{\mathbf{k}} = -J(1 + e^{ik_x d} + e^{i(k_x+k_y)d})$

$$\epsilon_{\mathbf{k}} = |\epsilon_{\mathbf{k}}| e^{i\phi_{\mathbf{k}}} \quad ,$$

$\mathbf{k} = k_x \mathbf{k}_1 + k_y \mathbf{k}_2$, the basis vectors \mathbf{k}_1 and \mathbf{k}_2 are shown in Fig. 2.2(b) and

$$\psi_{\mathbf{k}} = \begin{pmatrix} c_{\mathbf{k},A} \\ c_{\mathbf{k},B} \end{pmatrix} \quad .$$

The operators $c_{\mathbf{k},C}^\dagger$ ($c_{\mathbf{k},C}$) create (annihilate) an electron on sublattice site $C \in \{A, B\}$. This Hamiltonian is diagonalized by the unitary transformation

$$U_{\mathbf{k}} = 1/\sqrt{2} \begin{pmatrix} 1 & 1 \\ e^{i\phi_{\mathbf{k}}} & -e^{i\phi_{\mathbf{k}}} \end{pmatrix} \quad (2.3)$$

and the resulting diagonal Hamiltonian is

$$U_{\mathbf{k}}^\dagger H_{0,\mathbf{k}} U_{\mathbf{k}} = \begin{pmatrix} |\epsilon_{\mathbf{k}}| & 0 \\ 0 & -|\epsilon_{\mathbf{k}}| \end{pmatrix} .$$

Linearized graphene Hamiltonian

For the electronic properties of graphene it is usually sufficient to consider the electronic states close to the Fermi level. For undoped graphene the Fermi level is directly at the Dirac point. It is therefore a good approximation to linearize the dispersion relation around each of the two nonequivalent Dirac points $\mathbf{K}, \mathbf{K}' = (-\tau_z \frac{2\pi}{3d}, -\tau_z \frac{2\pi}{3d})$, $\tau_z = \pm 1$. We obtain

$$\epsilon_{\mathbf{k}} \approx \hbar v_F (\tau_z k'_x + i k'_y) \quad ,$$

where

$$\begin{aligned} k'_x &= \frac{\sqrt{3}}{2} \left(-\tau_z \frac{2\pi}{3d} + k_y \right) \\ k'_y &= \tau_z \frac{\pi}{d} - k_x - \frac{k_y}{2} \end{aligned}$$

and $\hbar v_F = -Jd$. The Fermi velocity in graphene is $v_F \approx 10^6 \text{ m s}^{-1}$ [41] resulting in the effective hopping strength $J \approx -2.78 \text{ eV}$. We can define a new set of unit vectors such that $\mathbf{k} = \mathbf{K}^{(\prime)} + k'_x \mathbf{k}'_1 + k'_y \mathbf{k}'_2$. This set of vectors is shown in Fig. 2.2(c) and turns out to be orthonormal in contrast to the original unit vectors.

The linearized Hamiltonian is now

$$\begin{aligned} H_{0,\mathbf{k}} &= \psi_{\mathbf{k}}^\dagger h_{\mathbf{k}} \psi_{\mathbf{k}} \quad , \tag{2.4} \\ \text{where } h_{\mathbf{k}} &= \hbar v_F (\tau_z \sigma_x k'_x + \sigma_y k'_y) \\ \tau_z k'_x + i k'_y &= \sqrt{k'^2_x + k'^2_y} e^{i\phi'_{\mathbf{k}}} = k e^{i\phi'_{\mathbf{k}}} \end{aligned}$$

and $\sigma_{x,y,z}$ denote the Pauli matrices. When replacing $\phi_{\mathbf{k}}$ with $\phi'_{\mathbf{k}}$ in Eq. 2.3, the above Hamiltonian is diagonalized by the unitary transformation given in Eq. 2.3 and the resulting diagonal Hamiltonian is

$$U_{\mathbf{k}}^\dagger H_{0,\mathbf{k}} U_{\mathbf{k}} = \pm \hbar v_F k \quad .$$

Since we work with the linearized Hamiltonian throughout this section we drop the primes on the momenta from now on. For later convenience we note that the bandwidth of the

full tight-binding bands in graphene is $6|J| \approx 16 \text{ eV} \approx 24.4 \hbar \cdot \text{PHz}$.

2.1.2. Electromagnetic waves and gauge choice

Before we couple the graphene Hamiltonian to the electromagnetic light fields we give a brief introduction on electromagnetic waves. We present the wave forms that we will need for driving graphene with circularly polarized light and discuss different gauge choices. It turns out that it is crucial for our calculations to use the Weyl gauge.

In order to illustrate the importance of the Weyl gauge we first consider the simplest case of a uniform electric field $\mathbf{E}_{\text{uniform}}(\mathbf{r}, t) = E\hat{\mathbf{e}}_x$ and vanishing magnetic field $\mathbf{B} = 0$. Within the Weyl gauge we obtain the vector potential³

$$\mathbf{A}_{\text{uniform}}(\mathbf{r}, t) = Et\hat{\mathbf{e}}_x \quad .$$

An intuitive picture for this gauge choice inspired by Eq. 2.2 is a time-dependent shift of the band structure. An alternative gauge choice would be a special case of the Coulomb gauge, choosing $\mathbf{A} = 0$. In this case we obtain $\phi = Ex$ and an intuitive picture is given by a tilt of the lattice potential. This tilt leads to a nonperiodic lattice potential and hence the resulting Hamiltonian is not diagonal in momentum space. We see that even for this simplest case of a uniform electric field it is crucial to apply the Weyl gauge in order to obtain a Hamiltonian diagonal in momentum space.

We turn to a slightly more complicated case of a linearly polarized electromagnetic wave

$$\mathbf{E}_{\text{linear}}(\mathbf{r}, t) = E\hat{\mathbf{e}}_x \cos(\mathbf{k}\mathbf{r} - \omega t) \quad ,$$

where the wave vector \mathbf{k} and the frequency ω are related by the speed of light $ck = \omega$ and for definiteness we have chosen the electric field along the x -direction. We are particularly interested in illuminating a 2-d graphene sheet under perpendicular incidence. Without loss of generality we can assume the graphene sheet to lie in the x - y -plane at $z = 0$ and the light to be propagating in the z -direction $\mathbf{k} = k\hat{\mathbf{e}}_z$. For this case we can simplify

$$\mathbf{E}_{\text{linear}}(z, t) = E\hat{\mathbf{e}}_x \cos(kz - \omega t) \quad .$$

Again we use the Weyl gauge to obtain

$$\mathbf{A}_{\text{linear}}(z, t) = \frac{E}{\omega}\hat{\mathbf{e}}_x \sin(kz - \omega t)$$

³Remember that $\mathbf{E} = \nabla\phi - \frac{d\mathbf{A}}{dt}$ and $\mathbf{B} = \nabla \times \mathbf{A}$.

$$\mathbf{B}_{\text{linear}}(z, t) = \frac{1}{\omega} \mathbf{k} \times \mathbf{E}_{\text{linear}} = \frac{Ek}{\omega} \hat{\mathbf{e}}_y \cos(kz - \omega t) \quad .$$

For later convenience we also give the corresponding equations for a circularly polarized electromagnetic wave

$$\begin{aligned} \mathbf{E}_{\text{circular}}(z, t) &= E [\hat{\mathbf{e}}_y \sin(kz - \omega t) - \hat{\mathbf{e}}_x \sigma_{\text{pol}} \cos(kz - \omega t)] \\ \mathbf{A}_{\text{circular}}(z, t) &= -\frac{E}{\omega} [\hat{\mathbf{e}}_x \sigma_{\text{pol}} \sin(kz - \omega t) + \hat{\mathbf{e}}_y \cos(kz - \omega t)] \quad , \end{aligned} \quad (2.5)$$

where σ_{pol} defines the polarization of the light. For a pulsed electromagnetic wave with Gaussian envelope

$$\mathbf{E}_{\text{circ,gaus}}(z, t) = \mathbf{E}_{\text{circular}}(z, t) \exp\left(-\frac{(kz - \omega t)^2}{(2\sigma)^2}\right)$$

the vector potential can only be evaluated in terms of the error function $\text{Erf}(x)$

$$\mathbf{A}_{\text{circ,gaus}}(z, t) = -\frac{E\sqrt{\pi}\sigma}{\omega} e^{-\sigma^2} \begin{pmatrix} \text{Re} [\text{Erf}(\frac{kz - \omega t}{2\sigma} + i\sigma)] \\ \sigma_{\text{pol}} \text{Im} [\text{Erf}(\frac{kz - \omega t}{2\sigma} + i\sigma)] \end{pmatrix} \quad .$$

For our numerical simulations we evaluate the error function using numerical libraries for the Dawson function. Finally, for a tanh-type envelope we assume that the envelope varies slower than the driving frequency and hence

$$\begin{aligned} \mathbf{E}_{\text{cir,tanh}}(z, t) &= \mathbf{E}_{\text{circular}}(z, t) \frac{\tanh\left(\frac{\omega(t-t_0)}{\sigma}\right) + 1}{2} \\ \mathbf{A}_{\text{cir,tanh}}(z, t) &\approx \mathbf{A}_{\text{circular}}(z, t) \frac{\tanh\left(\frac{\omega(t-t_0)}{\sigma}\right) + 1}{2} \quad . \end{aligned}$$

2.1.3. Coupling graphene to electromagnetic waves

We couple the light field to the linearized graphene Hamiltonian from Eq. 2.4

$$H_0 = \psi_{\mathbf{k}}^\dagger H_{0,\mathbf{k}} \psi_{\mathbf{k}} \quad .$$

Within minimal coupling and using the Weyl gauge the interaction Hamiltonian is

$$\begin{aligned} H_{\text{int}} &= \sum_{\mathbf{q}} j_{\mathbf{q}} \cdot A_{\mathbf{q}} \\ j_{\mathbf{q}} &= \frac{e}{\hbar} \sum_{\mathbf{k}} \psi_{\mathbf{k}+\mathbf{q}/2}^\dagger \frac{d\hbar_{\mathbf{k}}}{d\mathbf{k}} \psi_{\mathbf{k}-\mathbf{q}/2} \quad , \end{aligned}$$

where we made the assumption of \mathbf{q} being small. At this point we see the importance of a vector potential $\mathbf{A}(r)$ that is spatially uniform within the x - y -plane. For this case the Fourier transform is peaked around small momenta and we can assume $\mathbf{A}_k = \mathbf{A}\delta_{\mathbf{k},0}$. Only for this case the interaction Hamiltonian becomes diagonal in momentum space

$$H_{\text{int}} = \sum_{\mathbf{k}} \psi_{\mathbf{k}}^\dagger e v_{\text{F}} (\tau_z \sigma_x A_x + \sigma_y A_y) \psi_{\mathbf{k}} \quad .$$

For completeness we give the current operator in the $\mathbf{q} \rightarrow 0$ limit

$$\mathbf{j} = \sum_{\mathbf{k}} \psi_{\mathbf{k}}^\dagger \mathbf{j}_{\mathbf{k}} \psi_{\mathbf{k}} \quad \mathbf{j}_{\mathbf{k}} = e v_{\text{F}} \begin{pmatrix} \tau_z \sigma_x \\ \sigma_y \end{pmatrix}$$

and the full Hamiltonian

$$H = H_0 + H_{\text{int}} = \sum_{\mathbf{k}} \psi_{\mathbf{k}}^\dagger H_{\mathbf{k}} \psi_{\mathbf{k}} \\ H_{\mathbf{k}} = v_{\text{F}} [\tau_z \sigma_x (\hbar k_x + e A_x) + \sigma_y (\hbar k_y + e A_y)] \quad . \quad (2.6)$$

2.1.4. Including dissipation and formulating the master equation⁴

Here we characterize the dissipation of our system and formulate the actual master equation for the time evolution of electrons in driven graphene. We use the von Neumann equation for the unitary part of the time evolution and include interactions as well as other damping and dephasing effects by including Lindblad operators. At each momentum point \mathbf{k} the full time evolution of the density matrix is then governed by the master equation [158]

$$\frac{d}{dt} \rho_{\mathbf{k}} = \frac{i}{\hbar} [\rho_{\mathbf{k}}, H_{\mathbf{k}}] - \frac{1}{2} \sum_{\alpha} (L^{\alpha\dagger} L^{\alpha} \rho_{\mathbf{k}} + \rho_{\mathbf{k}} L^{\alpha\dagger} L^{\alpha} - 2 L^{\alpha} \rho_{\mathbf{k}} L^{\alpha\dagger}) \quad .$$

The first part of this equation describes the unitary part of the time evolution, fully determined by the Hamiltonian of the system. The second part with the Lindblad operators L^{α} accounts for dissipation effects.

Each momentum mode is modeled by a two-level system, remember Fig. 2.1(a). So far we have only considered the two singly-occupied modes $\psi_k = (|01\rangle \quad |10\rangle)$. The dissipation additionally couples to the empty and fully occupied mode. We explicitly extend our state

⁴Large parts of this section have been published in the appendix of Ref. [N2]. The corresponding section in Ref. [N2] has mainly been written by the author of this thesis.

space to these two modes and obtain

$$\Psi_{\mathbf{k}} = \left(|11\rangle \quad |01\rangle \quad |10\rangle \quad |00\rangle \right) \quad ,$$

where $|11\rangle = c_{\mathbf{k},A}^\dagger c_{\mathbf{k},B}^\dagger |0\rangle$.

Here we repeat the definitions of the previous sections, extending them to the larger 4×4 state space. To this end we introduce a set of Pauli-type matrices

$$\begin{aligned} \sigma_x &= \begin{pmatrix} 0 & 0 & 0 & 0 \\ 0 & 0 & 1 & 0 \\ 0 & 1 & 0 & 0 \\ 0 & 0 & 0 & 0 \end{pmatrix} & \sigma_y &= \begin{pmatrix} 0 & 0 & 0 & 0 \\ 0 & 0 & -i & 0 \\ 0 & i & 0 & 0 \\ 0 & 0 & 0 & 0 \end{pmatrix} \\ \sigma_z &= \begin{pmatrix} 0 & 0 & 0 & 0 \\ 0 & 1 & 0 & 0 \\ 0 & 0 & -1 & 0 \\ 0 & 0 & 0 & 0 \end{pmatrix} & \sigma_z^{(0)} &= \begin{pmatrix} 0 & 0 & 0 & 0 \\ 0 & 0 & 0 & 0 \\ 0 & 0 & 1 & 0 \\ 0 & 0 & 0 & -1 \end{pmatrix} \\ \sigma_z^{(2)} &= \begin{pmatrix} 1 & 0 & 0 & 0 \\ 0 & -1 & 0 & 0 \\ 0 & 0 & 0 & 0 \\ 0 & 0 & 0 & 0 \end{pmatrix} & \sigma_g &= \begin{pmatrix} 0 & 0 & 0 & 0 \\ 0 & 1/2 & 0 & 0 \\ 0 & 0 & 1/2 & 0 \\ 0 & 0 & 0 & 0 \end{pmatrix} \quad . \end{aligned}$$

For the linearized dispersion relation the Hamiltonian for each momentum point further splits into a sum of three terms

$$H_{\mathbf{k}}(t) = H_{0,\mathbf{k}} + H_{\text{dr},\mathbf{k}}(t) + H_{L,\mathbf{k}}(t) \quad . \quad (2.7)$$

The first contribution is the equilibrium Hamiltonian without any light field applied. Explicitly including the chemical potential we obtain

$$H_{0,\mathbf{k}} = \Psi_{\mathbf{k}}^\dagger \left[\hbar v_F (\tau_z k_x \sigma_x + k_y \sigma_y) - \mu (1 + \sigma_z + \sigma_z^{(0)} + \sigma_z^{(2)}) \right] \Psi_{\mathbf{k}} \quad .$$

The second and third term in Eq. 2.7 arise from the coupling to the light field. We include two different light fields, one representing the circularly polarized driving pulse and the other representing a longitudinal bias field. We split the vector potential into the parts for these two field contributions

$$\mathbf{A}(t) = \mathbf{A}_{\text{dr}}(t) + \mathbf{A}_L(t) \quad .$$

For the linearized system we can then accordingly split the interaction part of the Hamiltonian into these two parts

$$H_{\text{int},\mathbf{k}} = H_{\text{dr},\mathbf{k}} + H_{\text{L},\mathbf{k}} \quad .$$

For the driving pulse we use a circularly polarized pulse with either Gaussian $\mathbf{A}_{\text{dr}}(t) = \mathbf{A}_{\text{circ,gaus}}(t)$ or tanh-type $\mathbf{A}_{\text{dr}}(t) = \mathbf{A}_{\text{circ,tanh}}(t)$ envelope. For the longitudinal bias field we use $\mathbf{A}_{\text{L}}(t) = s_{\text{switch}}(t)\mathbf{A}_{\text{uniform}}(t)$, where s_{switch} denotes a slow switch-on term during the first 100 fs.

In addition to the unitary time evolution governed by the Hamiltonian $H_{\mathbf{k}}(t)$ we include Lindblad operators defined in the basis that diagonalizes the instantaneous Hamiltonian $H_{\mathbf{k}}(t)$

$$\Psi_{\mathbf{k}} = U_{\mathbf{k}}\Phi_{\mathbf{k}} \quad ,$$

where

$$U_{\mathbf{k}} = \begin{pmatrix} 1 & 0 & 0 & 0 \\ 0 & 1/\sqrt{2} & 1/\sqrt{2} & 0 \\ 0 & e^{i\phi_{\mathbf{k}}}/\sqrt{2} & -e^{i\phi_{\mathbf{k}}}/\sqrt{2} & 0 \\ 0 & 0 & 0 & 1 \end{pmatrix} \quad (2.8)$$

and $\phi_{\mathbf{k}}$ is defined via

$$|\mathbf{k} + e/\hbar\mathbf{A}| e^{i\phi_{\mathbf{k}}} = \left(\tau_z(k_x + \frac{e}{\hbar}A_x) + i(k_y + \frac{e}{\hbar}A_y) \right) \quad .$$

In this basis we introduce

$$L^\alpha = \sqrt{c_\alpha} \begin{pmatrix} 0 & \delta_{\alpha,1} & \delta_{\alpha,3} & 0 \\ \delta_{\alpha,2} & 0 & \delta_{\alpha,5} & \delta_{\alpha,7} \\ \delta_{\alpha,4} & \delta_{\alpha,6} & 0 & \delta_{\alpha,9} \\ 0 & \delta_{\alpha,8} & \delta_{\alpha,10} & 0 \end{pmatrix} \quad \text{for } \alpha = 1, 2, \dots, 10$$

$$L^{11} = \sqrt{\gamma_z}\sigma_z \quad ,$$

with for now arbitrary constants c_α . Here c_5 and c_6 correspond to decay effects and γ_z corresponds to dephasing effects in the singly occupied sector. Additionally we explicitly allow for exchange of particles with the back gate. The time scale and dynamics for the exchange of particles are set by the dissipation constants $c_1 - c_4$ and $c_7 - c_{10}$. We do not allow for simultaneous loss or gain of two particles which would correspond to entries in

the top right and bottom left of the matrix.

We note that the transformation in Eq. 2.8 is ill-defined when $|\mathbf{k} + e/\hbar\mathbf{A}| = 0$. In this case $H_{\mathbf{k}} = 0$ and the instantaneous Hamiltonian is diagonal with respect to any basis. We choose to implement the same Lindblad operators as above in the original AB -basis for this case.

We find that the resulting equations of motion for the density matrix decouple into different sectors and write the density matrix in the sector that is relevant for computing the current as

$$\begin{aligned} \rho_{\mathbf{k}} = & \sigma_y + \rho_{\mathbf{k},x}\sigma_x + \rho_{\mathbf{k},y}\sigma_y + \rho_{\mathbf{k},z}\sigma_z \\ & + \rho_{\mathbf{k},0}\sigma_z^{(0)} + \rho_{\mathbf{k},2}\sigma_z^{(2)} \quad . \end{aligned}$$

The resulting equations of motion are

$$\begin{aligned} \hbar\partial_t\rho_{\mathbf{k},x} = & \delta_{\mathbf{k}+e\mathbf{A}}\rho_{\mathbf{k},z} - \epsilon_{\mathbf{k}+e\mathbf{A}}\rho_{\mathbf{k},y} - [\Gamma + (c_1 + c_3 + c_8 + c_{10})/2] \rho_{\mathbf{k},x} \\ \hbar\partial_t\rho_{\mathbf{k},y} = & \epsilon_{\mathbf{k}+e\mathbf{A}}\rho_{\mathbf{k},x} - [\Gamma + (c_1 + c_3 + c_8 + c_{10})/2] \rho_{\mathbf{k},y} \\ \hbar\partial_t\rho_{\mathbf{k},z} = & \delta_{\mathbf{k}+e\mathbf{A}}\rho_{\mathbf{k},x} + c_3(1/2 + \rho_{\mathbf{k},0} - \rho_{\mathbf{k},z}) - c_4\rho_{\mathbf{k},2} + c_5(1/2 + \rho_{\mathbf{k},0} - \rho_{\mathbf{k},z}) \\ & - c_6(1/2 + \rho_{\mathbf{k},z} - \rho_{\mathbf{k},2}) - c_7\rho_{\mathbf{k},0} - c_8(1/2 + \rho_{\mathbf{k},z} - \rho_{\mathbf{k},2}) \\ \hbar\partial_t\rho_{\mathbf{k},0} = & -(c_7 + c_9)\rho_{\mathbf{k},0} - c_{10}(1/2 + \rho_{\mathbf{k},0} - \rho_{\mathbf{k},z}) - c_8(1/2 + \rho_{\mathbf{k},z} - \rho_{\mathbf{k},2}) \\ \hbar\partial_t\rho_{\mathbf{k},2} = & -(c_2 + c_4)\rho_{\mathbf{k},2} + c_3(1/2 + \rho_{\mathbf{k},0} - \rho_{\mathbf{k},z}) + c_1(1/2 + \rho_{\mathbf{k},z} - \rho_{\mathbf{k},2}) \quad , \end{aligned}$$

where

$$\begin{aligned} \Gamma = & (c_5 + c_6)/2 + 2\gamma_z \tag{2.9} \\ \epsilon_{\mathbf{k}+e\mathbf{A}} = & 2\tau_z v_F [\hbar|\mathbf{k}| + e\mathbf{k} \cdot \mathbf{A}/|\mathbf{k}|] \\ \delta_{\mathbf{k}+e\mathbf{A}} = & 2\tau_z v_F [e\mathbf{A} \times \mathbf{k}/|\mathbf{k}|] \quad . \end{aligned}$$

We note that while we give the equations of motion in the basis diagonalizing $H_{0,\mathbf{k}}$ here, we implement them in the original AB -basis in the numerical simulations.

We choose the damping constants Boltzmann distributed

$$\begin{aligned} \Gamma = & 1/T_2 \\ c_5 = & c_6 \exp(-2\beta\epsilon) & c_5 + c_6 = & 1/T_1 \\ c_1 = & c_2 \exp(-\beta(-\epsilon - \mu)) & c_1 + c_2 = & 1/T_p \\ c_3 = & c_4 \exp(-\beta(\epsilon - \mu)) & c_3 + c_4 = & 1/T_p \\ c_7 = & c_8 \exp(-\beta(\epsilon - \mu)) & c_7 + c_8 = & 1/T_p \end{aligned}$$

$$\text{and } c_9 = c_{10} \exp(-\beta(-\epsilon - \mu)) \quad c_9 + c_{10} = 1/T_p \quad ,$$

where $\epsilon = v_F \sqrt{(\hbar k_x + eA_x)^2 + (\hbar k_y + eA_y)^2}$ are the instantaneous eigenenergies. This ensures that the ground state of the system without the light field is Fermi distributed with chemical potential μ and inverse temperature $\beta = 1/(k_B T)$. Note that T_1 and T_2 are commonly introduced decoherence measures. In analogy we define a third time scale T_p for the exchange of particles with the back gate.

We solve the master equation numerically and then compute the current for each momentum point as

$$\langle \mathbf{j}_{\mathbf{k}} \rangle = \text{Tr}(\rho_{\mathbf{k}} \mathbf{j}_{\mathbf{k}}) \quad .$$

The longitudinal and transverse conductivities are then obtained as

$$\begin{aligned} \sigma_{xx}(\mathbf{k}) &= \lim_{E_L \rightarrow 0} J_{x,\mathbf{k}}/E_L \\ \sigma_{xy}(\mathbf{k}) &= \lim_{E_L \rightarrow 0} J_{y,\mathbf{k}}/E_L \quad . \end{aligned}$$

We perform the calculation of j_y at experimentally realistic values of E_L , and have checked that these values realize the linear-response limit. Finally, we define the conductivity density

$$\tilde{\sigma}_{xy} = \frac{\sigma_{xy}(\mathbf{k})}{A} \quad ,$$

with the lattice size A and the full conductivity

$$\sigma_{xy} = \sum_{\mathbf{k}} \tilde{\sigma}_{xy} \quad .$$

2.2. Floquet bands and their occupations in driven graphene

Before we study the transport properties of driven graphene we take a look at its properties without applying the longitudinal bias field. When driving graphene with circularly polarized light it is well established that a gap opens in the effective band structure at the Dirac point in the high-frequency limit⁵ [76, 77]. In this regime the effective Hamiltonian

⁵The assumption is that the eigenenergies of the system can be neglected compared to the driving frequency.

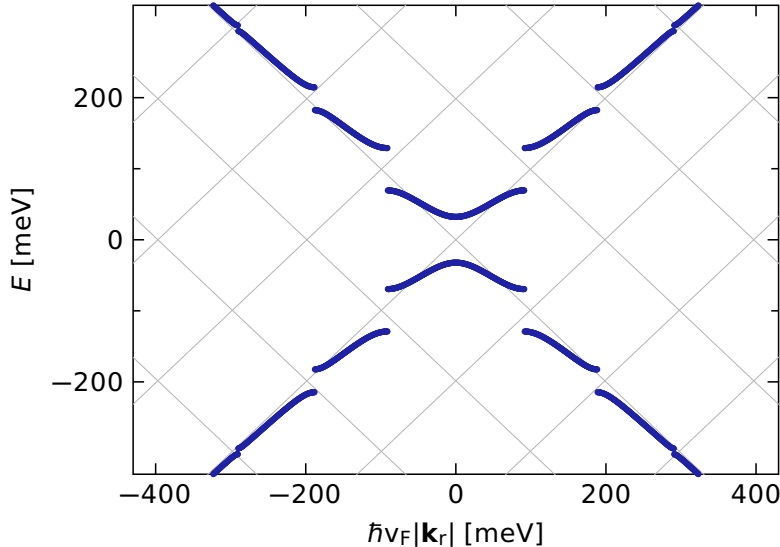


Figure 2.3 – Floquet band structure as a function of momentum times $\hbar v_F$ (Note that $\hbar v_F k = 400$ meV corresponds to $k \approx 0.06 \text{ \AA}^{-1}$). Grey lines show Floquet replica of the undriven band structure. Blue lines show the numerically computed Floquet band structure for $E_{\text{dr}} = 20 \text{ MV m}^{-1}$ and $\omega_{\text{dr}} = 2\pi \cdot 48 \text{ THz}$. We show only those bands that are adiabatically connected to the undriven band structure. We explain the numerical algorithm used for this plot in Sec. 2.2.1.

becomes

$$H_{\text{eff},\mathbf{k}} = H_{0,\mathbf{k}} - \tau_z \sigma_{\text{pol}} \Delta_{\text{hf}} \psi_{\mathbf{k}}^\dagger \sigma_z \psi_{\mathbf{k}} \quad , \quad (2.10)$$

where $2\Delta_{\text{hf}} = 2(\hbar e E_{\text{dr}} v_F)^2 / (\hbar \omega_{\text{dr}})^3$ is the size of the gap at the Dirac point. At finite driving frequency additional gaps open at each resonance, where $2v_F k = \omega_{\text{dr}}$. Within Floquet theory this can be understood as follows: the electronic band structure acquires new states that result from dressing one of the original states with a photon. These new states are called Floquet replica and have the same dispersion as the original bands but are shifted by a multiple of the photon energy $\hbar \omega_{\text{dr}}$, see Fig. 2.3. Depending on the exact form of the driving term, the light field couples different Floquet replica. This coupling leads to a hybridization of the eigenstates at each band crossing and as a result avoided crossings and the opening of band gaps.

The effective Hamiltonian above is obtained from the Magnus expansion [159–163] by taking the high-frequency limit. Here we show that a slightly better result can be obtained without the high-frequency approximation within the Magnus expansion. Additionally we use the Magnus expansion for obtaining a similar result valid close to the first resonance. We compare these results to our numerical prediction obtained by truncating the quasi-energy operator in the extended Floquet-Hilbert space.

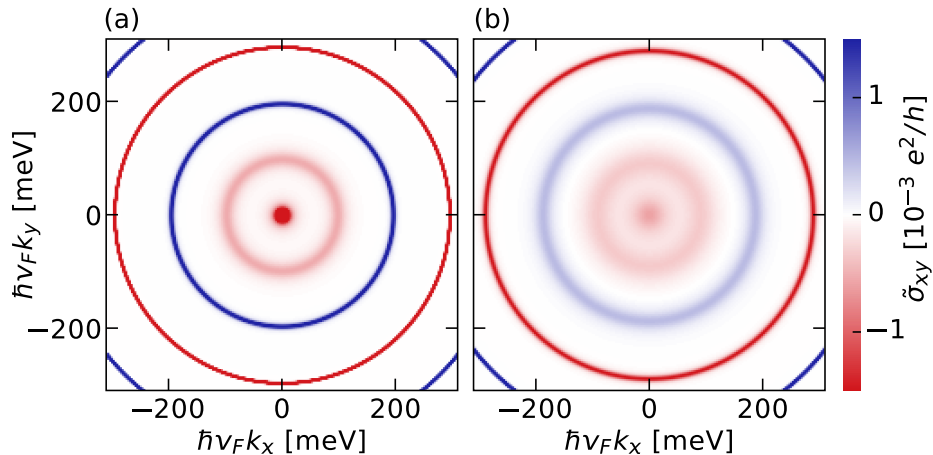


Figure 2.4 – Momentum-resolved Berry curvature at $\omega_{\text{dr}} = 2\pi \cdot 48$ THz and $E_{\text{dr}} = 10$ MV m $^{-1}$ in panel (a) and $E_{\text{dr}} = 26$ MV m $^{-1}$ in panel (b). We see that the Berry curvature is localized around each resonance at $E_{\text{dr}} = 10$ MV m $^{-1}$. For larger electric field strength the contribution of each resonance broadens and for $E_{\text{dr}} = 26$ MV m $^{-1}$ the resonances already start overlapping.

We also compute the Berry curvature both numerically and analytically within our approximations. We find that the Berry curvature is well localized at the Dirac point and at individual resonances for low electric field strength E_{dr} , see Fig. 2.4(a). In this regime it is meaningful to integrate the Berry curvature for individual resonances and the Dirac point and affiliate a pseudo-Chern number to each of them⁶. For larger electric field strength Berry curvatures arising from individual resonances start overlapping and therefore the corresponding pseudo-Chern numbers deviate from integers significantly, see Fig. 2.4(b).

When including dissipation we find from numerical simulations of the single-particle correlation function that the spectrum agrees well with the effective Floquet band structure. In contrast, the occupations of the respective bands are profoundly different from those of a static system. Also when applying a bias to the back gate of graphene and hence effectively changing the chemical potential, we do not observe the expected plateau in the electron density within the gap at the Dirac point.

⁶Strictly speaking these are no Chern numbers, since Chern numbers are defined as the integral of the Berry curvature over the entire band. We will see that these pseudo-Chern numbers are indeed quantized in the low-fluence limit and will find an analytic formula for the pseudo-Chern number of the Dirac point $c_0 = -2$ and the first resonance $c_1 = -4$. For larger fluence the pseudo-Chern numbers deviate from their quantized values.

2.2.1. Dissipationless graphene: band structure and Berry curvature within Floquet theory

Here we do a perturbative computation of the effective Floquet Hamiltonian starting from the high-frequency limit and extending it to lower driving frequencies by expanding around the first resonance. To this end we will need the Hamiltonian in the interaction picture.

Hamiltonian for driven graphene in the interaction picture

We start from the Hamiltonian for graphene driven with circularly polarized light with no additional envelope (see Eqs. 2.5 and 2.6)

$$\begin{aligned}
 H_{\text{circular},\mathbf{k}} &= H_{0,\mathbf{k}} + H_{1,\mathbf{k}} \tag{2.11} \\
 H_{0,\mathbf{k}} &= \hbar v_F (\tau_z k_x \sigma_x + k_y \sigma_y) \\
 H_{1,\mathbf{k}} &= \frac{e E_{\text{dr}} v_F}{\omega_{\text{dr}}} (\tau_z \sigma_{\text{pol}} \sin(\omega_{\text{dr}} t) \sigma_x - \cos(\omega_{\text{dr}} t) \sigma_y) \quad .
 \end{aligned}$$

The corresponding Schrödinger equation is

$$i\hbar \partial_t |\psi\rangle = H_{\text{circular},\mathbf{k}} |\psi\rangle \quad .$$

In the eigenbasis of the undriven system we obtain

$$U_{\mathbf{k}}^\dagger H_{1,\mathbf{k}} U_{\mathbf{k}} = \frac{e E_{\text{dr}} v_F}{\omega_{\text{dr}}} \begin{pmatrix} s_1 & -ic_1 \\ ic_1 & -s_1 \end{pmatrix} \quad ,$$

$$\begin{aligned}
 \text{where } s_1 &= \sin(\tau_z \sigma_{\text{pol}} \omega_{\text{dr}} t - \phi_{\mathbf{k}}) \\
 c_1 &= \cos(\tau_z \sigma_{\text{pol}} \omega_{\text{dr}} t - \phi_{\mathbf{k}})
 \end{aligned}$$

and $U_{\mathbf{k}}$ has been defined in Eq. 2.3. Finally, we get the Schrödinger equation in the interaction picture as

$$\begin{aligned}
 i\hbar \partial_t |\psi_I\rangle &= H_{I,\mathbf{k}} |\psi_I\rangle \\
 H_{I,\mathbf{k}} &= \frac{e E_{\text{dr}} v_F}{\omega_{\text{dr}}} \begin{pmatrix} s_1 & -ie^{2iv_F kt} c_1 \\ ie^{-2iv_F kt} c_1 & -s_1 \end{pmatrix} \quad .
 \end{aligned}$$

Floquet-perturbative expansion around the Dirac point

We apply the Floquet-Magnus expansion [159–163] up to second order in the interaction Hamiltonian. Up to second order, the Magnus terms for the effective Hamiltonian are

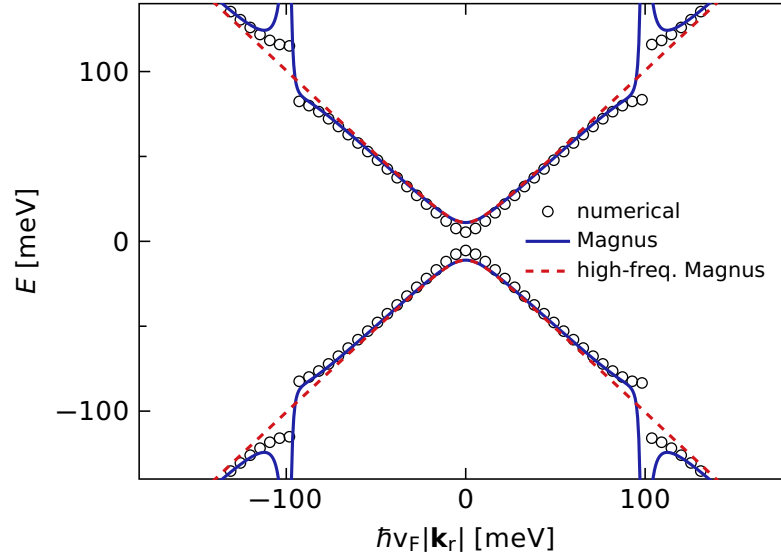


Figure 2.5 – Comparison of numerical band structure (open circles) and analytical approximations for $E_{\text{dr}} = 10 \text{ MV m}^{-1}$ and $\omega_{\text{dr}} = 2\pi \cdot 48 \text{ THz}$. We show the result within the second-order Magnus expansion (solid blue line) as well as its high-frequency limit (dashed red line).

(see e.g. [160])

$$H_{I,\text{eff},\mathbf{k}}(t) = H_{I,\mathbf{k}}(t) - \frac{1}{2i\hbar} \int^t dt' [H_{I,\mathbf{k}}(t'), H_{I,\mathbf{k}}(t)] \quad .$$

We only keep those terms that are time independent upon going back to the Schrödinger picture. As all terms of $H_{I,\mathbf{k}}$ oscillate with the driving frequency the first order does not contribute to the effective Hamiltonian. For the second-order term we obtain

$$H_{I,\text{eff},\mathbf{k}} = \left(\frac{eE_{\text{dr}}v_{\text{F}}}{\omega_{\text{dr}}} \right)^2 \frac{1}{\hbar [(2v_{\text{F}}k)^2 - \omega_{\text{dr}}^2]} \begin{pmatrix} v_{\text{F}}k & \frac{2\omega_{\text{dr}}^2 - (2v_{\text{F}}k)^2}{2\omega_{\text{dr}}} \tau_z \sigma_{\text{pol}} e^{2iv_{\text{F}}kt} \\ \frac{2\omega_{\text{dr}}^2 - (2v_{\text{F}}k)^2}{2\omega_{\text{dr}}} \tau_z \sigma_{\text{pol}} e^{-2iv_{\text{F}}kt} & -v_{\text{F}}k \end{pmatrix} \quad .$$

Upon returning to the Schrödinger picture and the AB-basis this results in

$$H_{\text{eff},\mathbf{k}} = \hbar v_{\text{F}} (\tau_z k_x \sigma_x + k_y \sigma_y) \left[1 + \left(\frac{eE_{\text{dr}}v_{\text{F}}}{\hbar\omega_{\text{dr}}} \right)^2 \frac{1}{(2v_{\text{F}}k)^2 - \omega_{\text{dr}}^2} \right] + \frac{\tau_z \sigma_{\text{pol}}}{2\hbar\omega_{\text{dr}}} \left(\frac{eE_{\text{dr}}v_{\text{F}}}{\omega_{\text{dr}}} \right)^2 \frac{2\omega_{\text{dr}}^2 - (2v_{\text{F}}k)^2}{(2v_{\text{F}}k)^2 - \omega_{\text{dr}}^2} \sigma_z \quad ,$$

which indeed recovers Eq. 2.10 in the limit $\omega_{\text{dr}} \gg 2v_{\text{F}}k$.

It is often convenient to rewrite a 2×2 Hamiltonian in the form

$$H = d_0 \mathbb{1} + d_x \sigma_x + d_y \sigma_y + d_z \sigma_z \quad . \quad (2.12)$$

The object $\mathbf{d} = (d_x, d_y, d_z)$ can then be interpreted as a three-dimensional vector and both the eigenvectors and eigenvalues $\epsilon_{\pm} = d_0 \pm |\mathbf{d}|$ can be expressed in terms of \mathbf{d} . This vector is also commonly plotted on the Bloch sphere, a representation that is established in quantum optics [164].

For our case

$$d_x = \hbar v_F \tau_z k_x \left[1 + \left(\frac{e E_{\text{dr}} v_F}{\hbar \omega_{\text{dr}}} \right)^2 \frac{1}{(2v_F k)^2 - \omega_{\text{dr}}^2} \right] \quad (2.13)$$

$$d_y = \hbar v_F k_y \left[1 + \left(\frac{e E_{\text{dr}} v_F}{\hbar \omega_{\text{dr}}} \right)^2 \frac{1}{(2v_F k)^2 - \omega_{\text{dr}}^2} \right] \quad (2.14)$$

$$d_z = \frac{\tau_z \sigma_{\text{pol}}}{2\hbar \omega_{\text{dr}}} \left(\frac{e E_{\text{dr}} v_F}{\omega_{\text{dr}}} \right)^2 \frac{2\omega_{\text{dr}}^2 - (2v_F k)^2}{(2v_F k)^2 - \omega_{\text{dr}}^2} \quad . \quad (2.15)$$

We compare the resulting perturbative band structure to the numerically obtained one in Fig. 2.5. We see that close to the Dirac point both approximations are valid, while for larger \mathbf{k} -values the second-order Magnus result makes a slightly better approximation until it diverges at the first resonance. In fact, the divergence of the Magnus expansion at the first resonance is only lifted when going to infinite order.

The decomposition in form of Eq. 2.12 is helpful for computing the Berry curvature as well. The Berry curvature is obtained as

$$F_{ij} = \frac{\epsilon_{abc} d_a \partial_i d_b \partial_j d_c}{2d^3} \quad .$$

While it is straightforward to evaluate the Berry curvature F_{xy} for Eqs. 2.13-2.15, the resulting equations are rather lengthy. We therefore present the corresponding results for the high-frequency limit. The lower and upper bands have equal and opposite curvature. The one for the lower band is

$$F_{xy}(\mathbf{k}) = -F_{yx}(\mathbf{k}) = -\frac{2\sigma_{\text{pol}} \hbar^2 v_F^2 A}{[\hbar^2 v_F^2 k^2 + 4A^2]^{3/2}} \quad ,$$

where $A = \frac{1}{2\hbar \omega_{\text{dr}}} \left(\frac{e E_{\text{dr}} v_F}{\omega_{\text{dr}}} \right)^2 \quad .$

Note that we have summed this expression over the valley index τ_z already⁷ and the factor

⁷Both valleys contribute with the same sign and equal magnitude.

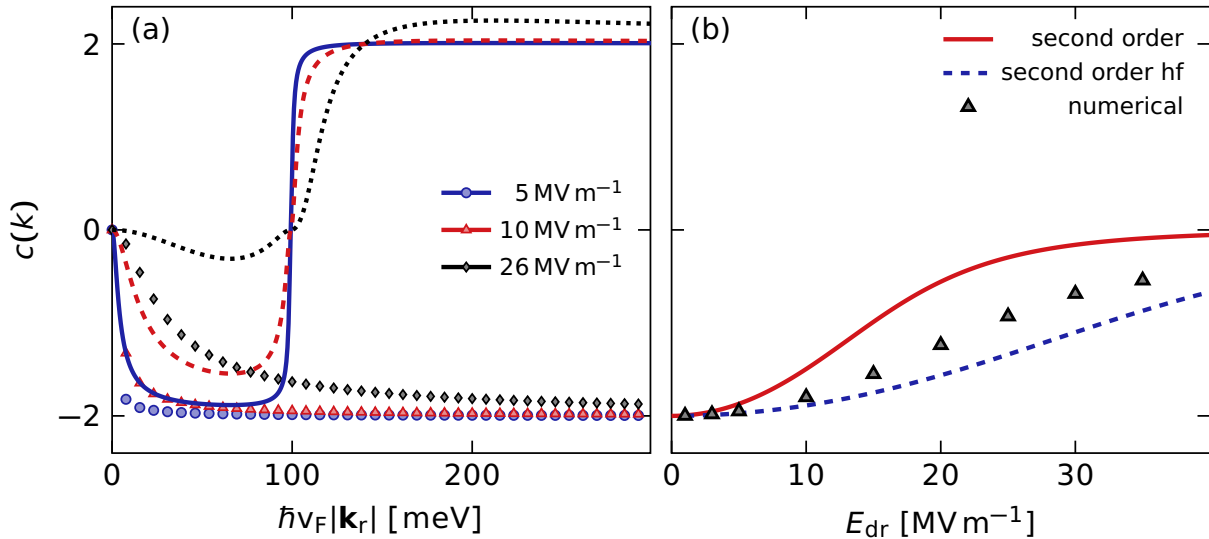


Figure 2.6 – Chern integral $c(k)$ for the lower graphene band. (a) We show the Chern integral as a function of momentum for three different driving field strengths E_{dr} as indicated in the legend. Lines show the Chern integral computed from the second-order Magnus expansion, while symbols show the corresponding high-frequency limit. (b) We show the contribution of the Dirac point to the Chern number $c(k = \omega_{\text{dr}}/(2v_{\text{F}}))$ as a function of driving field strength E_{dr} . The solid red line shows the second-order Magnus expansion, the dashed blue line its high-frequency limit and black triangles show the numerically exact value. For both panels $\omega_{\text{dr}} = 2\pi \cdot 48$ THz and $\sigma_{\text{pol}} = 1$.

of 2 has been included for the spin degeneracy. The Chern number is obtained by integrating the Berry curvature. In order to investigate which momentum modes contribute most to the Berry curvature it is useful to truncate the integration at a threshold momentum, such that the Chern number $c = \lim_{k \rightarrow \infty} c(k)$, $\mathbf{k} = (k \cos(\phi), k \sin(\phi))$ and for the lower band we obtain

$$c(k) = \frac{1}{2\pi} \int_0^k dk' \int_0^{2\pi} d\phi k' F_{xy}(k') = \frac{2\sigma_{\text{pol}}}{\sqrt{1 + \left(\frac{\hbar v_{\text{F}} k \hbar \omega_{\text{dr}} \omega_{\text{dr}}^2}{(e E_{\text{dr}} v_{\text{F}})^2}\right)^2}} - 2\sigma_{\text{pol}} \quad .$$

We compare this equation to the full second-order expression in Fig. 2.6(a). We see that both equations are similar for small momenta, but differ significantly close to the first resonance. From our numerical simulations we find that the first resonance should contribute -4 to the Chern number. We confirm that neither of the two expressions gives the right result for the Chern number contribution of the first resonance. This was expected due to their failure to capture the band structure correctly at the first resonance.

For small electric field strength the contribution of the Dirac point is well localized and hence can be obtained by considering $c(k = \omega_{\text{dr}}/(2v_{\text{F}}))$. In the limit of vanishing field strength both analytic expressions do indeed approach the correct value of -2 for the con-

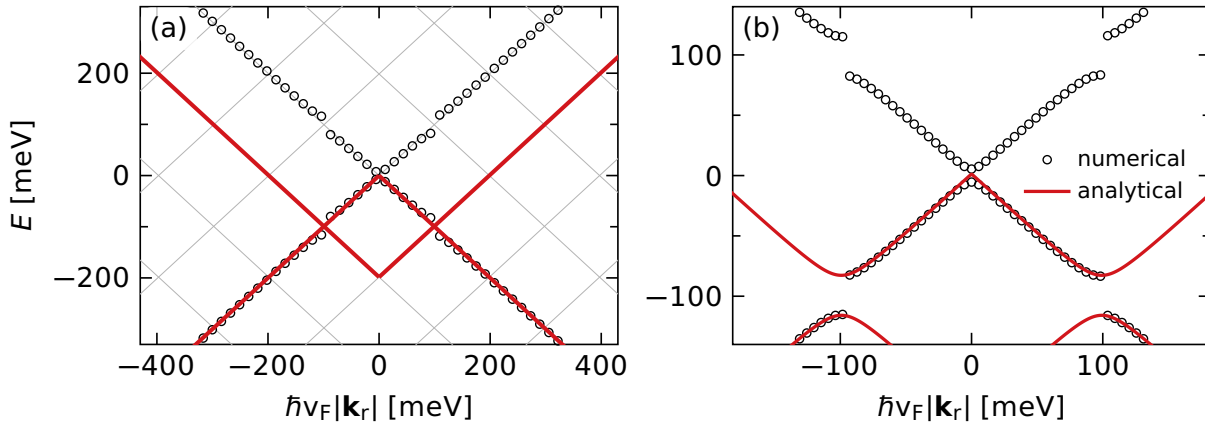


Figure 2.7 – (a) Floquet replica of the undriven graphene band structure (gray lines) highlighting the two bands in red that hybridize when applying the additional unitary transformation U_{dr} . For comparison open circles show the numerically computed driven band structure. (b) Comparison of the Magnus approximation (red line) and the numerically computed band structure (black circles). Both panels show $E_{\text{dr}} = 10 \text{ MV m}^{-1}$ and $\omega_{\text{dr}} = 2\pi \cdot 48 \text{ THz}$.

tribution of the Dirac point to the Chern number. In order to quantify the localization of the Berry curvature around the Dirac point we evaluate $c(\omega_{\text{dr}}/(2v_F))$ for $\omega_{\text{dr}} = 2\pi \cdot 48 \text{ THz}$ as a function of E_{dr} in Fig. 2.6(b). For larger E_{dr} the Berry curvature is less localized in momentum space and hence $c(\omega_{\text{dr}}/(2v_F))$ reduces. We see a significant reduction for $E_{\text{dr}} > 10 \text{ MV m}^{-1}$. This result needs to be taken with care since it is pushing the limit of validity of the second-order Magnus expansion.

Floquet-perturbative expansion around the first resonance

We have seen that the second-order Magnus expansion is neither able to capture the band structure nor the Berry curvature close to the first resonance. Here we therefore apply a trick in order to obtain results valid near the first resonance. Before applying the Magnus approximation we now go to the rotating frame by using the additional unitary transformation

$$U_{\text{dr}} = \begin{pmatrix} e^{-i\omega_{\text{dr}}t} & 0 \\ 0 & 1 \end{pmatrix} .$$

This amounts to choosing the two bands that hybridize from different Floquet replica, as exemplarily shown in Fig. 2.7(a). In this case the first-order Magnus expansion already contains static terms and hence it is sufficient to go to this order. Already transforming

back to the Schrödinger picture we obtain for the effective Hamiltonian

$$H_{\text{eff},\mathbf{k}} = -\frac{\hbar\omega_{\text{dr}}}{2} + \left(\hbar v_{\text{F}}k - \frac{\hbar\omega_{\text{dr}}}{2} \right) \sigma_z + \frac{eE_{\text{dr}}v_{\text{F}}}{2\omega_{\text{dr}}} [\cos(\phi_{\mathbf{k}})\sigma_x + \tau_z\sigma_{\text{pol}}\sin(\phi_{\mathbf{k}})\sigma_y] \quad .$$

Upon transforming back to the AB basis and using the notation from Eq. 2.12 we get

$$\begin{aligned} d_0 &= -\frac{\hbar\omega_{\text{dr}}}{2} \\ d_1 &= \hbar\left(v_{\text{F}} - \frac{\omega_{\text{dr}}}{2k}\right)k_x + \sigma_{\text{pol}}\tau_z S_{\text{dr}} \frac{k_y^2}{2k^2} \\ d_2 &= \hbar\left(v_{\text{F}} - \frac{\omega_{\text{dr}}}{2k}\right)k_y - \sigma_{\text{pol}} S_{\text{dr}} \frac{k_x k_y}{2k^2} \\ d_3 &= S_{\text{dr}} \frac{\tau_z k_x}{2k} \\ S_{\text{dr}} &= \frac{eE_{\text{dr}}v_{\text{F}}}{\omega_{\text{dr}}} \end{aligned}$$

and the eigenenergies are obtained as

$$\epsilon_{\mathbf{k},\pm} = -\frac{\hbar\omega_{\text{dr}}}{2} \pm \frac{1}{2} \sqrt{S_{\text{dr}}^2 + \hbar^2 (\omega_{\text{dr}} - 2v_{\text{F}}k)^2} \quad . \quad (2.16)$$

This approximation for the band structure is shown in Fig. 2.7(b). We see that it indeed gives a good approximation close to the first resonance. The corresponding Berry curvature for the lower band is

$$F_{xy} = -\frac{2\hbar v_{\text{F}} S_{\text{dr}} [S_{\text{dr}}\sigma_{\text{pol}} + \hbar(\omega_{\text{dr}} - 2v_{\text{F}}k) \cos(\phi_{\mathbf{k}})]}{k [S_{\text{dr}}^2 + \hbar^2(2v_{\text{F}}k - \omega_{\text{dr}})^2]^{3/2}} \quad . \quad (2.17)$$

The second term depends on the driving phase of the circularly polarized field. It is an artifact of the Floquet-Magnus expansion that is related to the 'kick' operators, see e.g. [165]. The approximation made here is in fact (up to this spurious term in the Berry curvature) equivalent to mapping the graphene Hamiltonian onto the Rabi problem. We will discuss this further in chapter 2.4.2. We neglect the second term in Eq. 2.17 and integrate in order to obtain the momentum-resolved contribution to the Chern number of the lower band

$$c(k) = 2\sigma_{\text{pol}} \frac{\hbar(\omega_{\text{dr}} - 2v_{\text{F}}k)}{\sqrt{S_{\text{dr}}^2 + \hbar^2(\omega_{\text{dr}} - 2v_{\text{F}}k)^2}} - 2\sigma_{\text{pol}} \frac{\hbar\omega_{\text{dr}}}{\sqrt{S_{\text{dr}}^2 + (\hbar\omega_{\text{dr}})^2}} \quad .$$

We plot this quantity in Fig. 2.8. The result for the Chern number contribution of the first resonance of -4 (including spin and valley degeneracy) agree with our numerical simulations. We also observe that for $E_{\text{dr}} = 26 \text{ MV m}^{-1}$ the Berry-curvature contribution

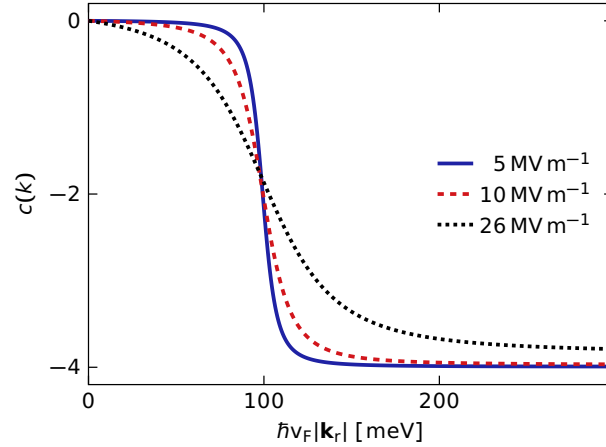


Figure 2.8 – Chern integral $c(k)$ for the lower band as a function of momentum. We use $\omega_{\text{dr}} = 2\pi \cdot 48$ THz, $\sigma_{\text{pol}} = 1$ and three different driving field strengths E_{dr} as indicated in the legend. We show the result for the first-order Magnus expansion expanded around the first resonance.

of the first resonance shows significant overlap with both the Berry-curvature contribution of the Dirac point and the second resonance at $\hbar v_F k \approx 200$ meV.

Numerical calculations of Floquet-band structure and Berry curvature

Here we present the numerical algorithm that has been used in the preceding sections for the calculation of Berry curvatures and band structures. For our calculations we use the quasi-energy operator Q in the extended Floquet-Hilbert space, for details see for example [166]. At each momentum \mathbf{k} we can write this operator as

$$Q = \begin{pmatrix} \ddots & \vdots & \vdots & \vdots & \ddots \\ \cdots & H_0 - \hbar\omega_{\text{dr}} & H_1 & 0 & \cdots \\ \cdots & H_{-1} & H_0 & H_1 & \cdots \\ \cdots & 0 & H_{-1} & H_0 + \hbar\omega_{\text{dr}} & \cdots \\ \ddots & \vdots & \vdots & \vdots & \ddots \end{pmatrix},$$

where

$$H_m = \int_{t_0}^{t_0+T} dt e^{-im\omega_{\text{dr}}t} H_{\text{circular},\mathbf{k}}$$

and the integral is performed over a period T of the driving field. The quasi-energy operator is one way to write an effective time-independent Hamiltonian at the cost of increasing the size of the Hilbert space. For obtaining the band structure and Berry curvature we can now apply methods designed for static Hamiltonians to the quasi-energy

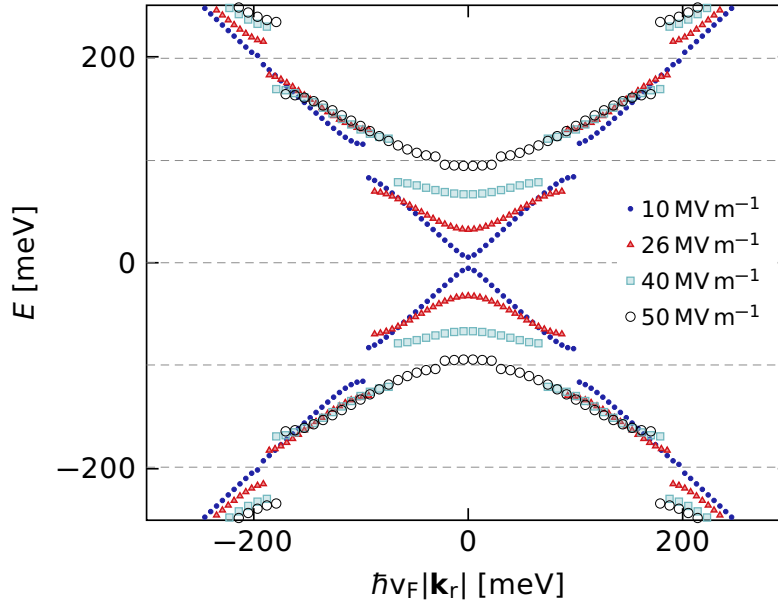


Figure 2.9 – We show the Floquet bands computed numerically for $\omega_{\text{dr}} = 2\pi \cdot 48$ THz and several values of E_{dr} as indicated in the legend. Dashed gray lines, with spacing $\hbar\omega_{\text{dr}}/2$, indicate the resonances.

operator. In order to get the Floquet eigenstates and eigenenergies we truncate and subsequently diagonalize Q . Floquet replica with larger values of m give corrections to the $H_{m=0}$ to higher order in $E_{\text{dr}}/\omega_{\text{dr}}$. In our case it turns out that truncation such that $-7 \leq m \leq 7$ is a sufficient approximation. The Floquet band structure is obtained from combining the eigenenergies of different momentum points. In later chapters we will also need the Floquet band velocity. This we obtain by numerically computing the momentum derivative of the Floquet eigenenergies.

We show the numerically obtained band structure in Fig. 2.9. For low driving field strength the first resonance has the largest gap. When increasing the field strength the gap increases while simultaneously moving inward towards the Dirac point. At even larger field strength the size of the gap starts decreasing again. At $E_{\text{dr}} \approx 52 \text{ MV m}^{-1}$ the ring of momenta that are resonant contracts to a point and merges at the Dirac point. Generally higher-order resonances open for larger values of the field strength but show the same life cycle of increasing gap size, then decreasing gap size and merging at the Dirac point.

Besides the band structure we are also interested in the Berry curvature. We use the method presented in [167] in order to determine the Berry curvature numerically. Within this numerical formalism we can now compute Chern numbers. From previous chapters we know that the contribution to Chern numbers is localized around each resonance. It

is therefore helpful to define the pseudo-Chern numbers for individual resonances by

$$c_0 = \frac{1}{2\pi} \int_0^{k=\omega_{\text{dr}}/4/v_{\text{F}}} dk \int_0^{2\pi} d\phi k F_{xy}(k, \phi)$$

$$c_n = \frac{1}{2\pi} \int_{k=(n-1/2)\omega_{\text{dr}}/2/v_{\text{F}}}^{k=(n+1/2)\omega_{\text{dr}}/2/v_{\text{F}}} dk \int_0^{2\pi} d\phi k F_{xy}(k, \phi) \quad .$$

The pseudo-Chern numbers of individual resonances have also been analyzed analytically in [168]. There it has been shown that $c_n = (-1)^n \cdot 4n$, $n \geq 1$, where the factor of 4 arises due to the spin and valley degeneracies. This result is in agreement with our result for c_1 in Sec. 2.2.1. For the examples shown in Fig. 2.4 we can now compute the resulting pseudo-Chern numbers and compare to the analytical results. For $E_{\text{dr}} = 10 \text{ MV m}^{-1}$ we obtain $c_0 = -1.8$, $c_1 = -4.05$, $c_2 = 7.8$, $c_3 = -11.97$. We see that even for this comparatively low field strength the pseudo-Chern numbers for the Dirac point and the first few resonances deviate from the analytical results. For the Dirac point the pseudo-Chern number only slowly approaches the expected value of -2 when further reducing the field strength. We get $c_0 = 1.95$ for $E_{\text{dr}} = 5 \text{ MV m}^{-1}$ and $c_0 = 1.98$ for $E_{\text{dr}} = 3 \text{ MV m}^{-1}$. At higher field strength, $E_{\text{dr}} = 26 \text{ MV m}^{-1}$, the pseudo-Chern numbers deviate further from their analytical values. Since neighboring resonances always have opposite Berry curvature, these contributions start overlapping and cancel. For this field strength we obtain $c_0 = -0.9$, $c_1 = -4.2$, $c_2 = 6.8$ and $c_3 = -11.6$.

At this point we would also like to remind the reader of our discussion in footnote 6. The only reason why the pseudo-Chern numbers are allowed to deviate from integers is that the actual Chern number is the one for the entire band, i.e. the sum of all the pseudo-Chern numbers of one band. Note that this is a large but finite sum when taking into account the full graphene dispersion and hence the finite bandwidth.

2.2.2. Dissipative driven graphene: Single-particle correlation function reveals the band structure⁸

So far we have only considered periodically driven graphene without dissipation. We are now interested to what extent dissipative graphene can still be described within Floquet theory. We simulate the effective, driven band structure of graphene by computing the single-particle correlation function, for details see Ref. [N2]. The peaks of the single-particle correlation function agree perfectly with the Floquet band structure computed in

⁸The results in this section have been published in Ref. [N2]. While the results on the single-particle correlation function are based on the description of graphene and the damping and dephasing formalism, developed in this thesis, the actual calculations for this part have been performed by my colleague Lukas Broers.

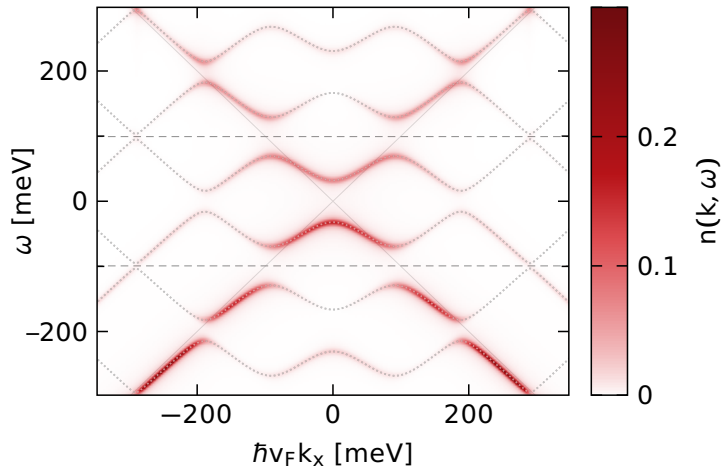


Figure 2.10 – Single-particle correlation function $n(\mathbf{k}, \omega)$ as a function of momentum times $\hbar v_F$. (Note that $\hbar v_F k = 400$ meV corresponds to $k \approx 0.06$ Å.) Dotted gray lines show the numerically computed Floquet band structure. The peaks of the single-particle correlation function agree perfectly with the Floquet band structure. The correlation function is shown after a steady state is achieved for a tanh-type ramp to the driven state. We show a slice along the k_x -direction of the band structure shown in Fig. 2.1. Dashed gray lines separate the different Floquet replica, while faint solid gray lines indicate the Dirac cone for undriven graphene. The parameters are inspired by experimental ones used in [86]. We use $E_{\text{dr}} = 26$ MV m $^{-1}$, $\omega_{\text{dr}} = 2\pi \cdot 48$ THz ≈ 200 meV/ \hbar , $T_1 = 1$ ps, $T_2 = 0.2$ ps and $T_p = 0.4$ ps. This figure has been published in Ref. [N2].

Sec. 2.2.1, see Fig. 2.10. It is obvious that not all of the Floquet replica can be occupied, since the number of states per momentum is infinitely large and not 2 as for the undriven band structure. We see that instead only those modes have significant occupation that are adiabatically connected to the undriven band structure. This was expected, at least for low electric field strengths, since for $E_{\text{dr}} \rightarrow 0$ the occupations have to approach the undriven case. We observe that significant heating occurs at the Dirac point, where the lower and upper band have almost equal population. Additional excitations occur at each resonance. Here the lower and upper bands are connected by multiples of the driving frequency and hence can easily be excited. It is interesting and not obvious to note that at the second resonance the first Floquet replica ($m = +1$) has significantly larger occupation than the zeroth Floquet replica ($m = 0$). This supports the statement that only the modes adiabatically connected to the undriven band structure obtain significant occupation. It is, however, counterintuitive from a perturbation theory perspective, where the excitation from $m = -1$ to $m = 0$ is a first-order effect, while the excitation to $m = +1$ is only possible in second order in the driving field strength.

Finally, we note that the single-particle correlation function is also accessible for experiments. Similar results could be obtained by angle-resolved photoemission spectroscopy

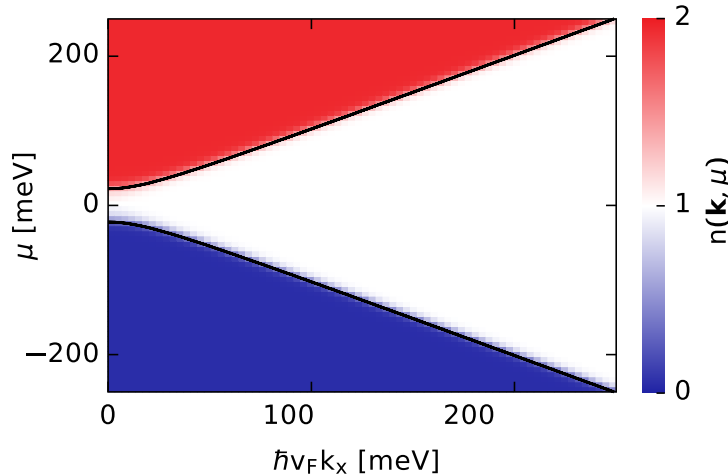


Figure 2.11 – Sum of the occupation of the lower and upper graphene bands $n(\mathbf{k}, \mu)$ as a function of chemical potential μ and momentum times $\hbar v_F$ for the effective high-frequency system. We use the static high-frequency Hamiltonian from Eq. 2.10 for the dynamics and ramp the effective gap Δ_{hf} from 0 to its final value. The occupation is rotationally symmetric and we exemplarily show a cut along the k_x -direction. The black line shows the corresponding effective Floquet band structure. As expected for a static system the changes in $n(\mathbf{k}, \mu)$ reflect the band structure and the opening of the band gap. We use $E_{\text{dr}} = 20 \text{ MV m}^{-1}$, $\omega_{\text{dr}} = 2\pi \cdot 48 \text{ THz}$, $T_1 = 1 \text{ ps}$, $T_2 = 0.2 \text{ ps}$, $T_p = 0.25 \text{ ps}$ and $T = 15 \text{ K}$.

(ARPES) [169]. The main difference is the appearance of a dark corridor [170–172], which could be easily included in our calculations. At this point it is interesting to note the connection to the discussion in Sec. 3.1, where we obtain an expression for the time-of-flight signal when releasing atoms from an optical lattice. The angular dependence of this expression is closely related to the dark corridor in ARPES-type experiments. In both cases, the origin is the interference of the signal arising from each of the two sublattices.

2.2.3. Chemical-potential bias in driven graphene

After finding such good agreement between the effective Floquet band structure and the single-particle correlation function, we consider how close driven graphene behaves to a static system when applying a chemical-potential bias. This can be achieved by putting graphene onto a substrate and applying a voltage bias to the substrate. We will find that dissipative driven graphene reacts profoundly different from an effective static system when applying a chemical-potential bias. Instead of the gaps of the effective Floquet band structure the bare Rabi frequency $eE_{\text{dr}}v_F/\omega_{\text{dr}}$ plays a crucial role in determining which momentum modes are occupied at a given chemical-potential bias.

Before considering the actual driven case we take a look at the effective high-frequency

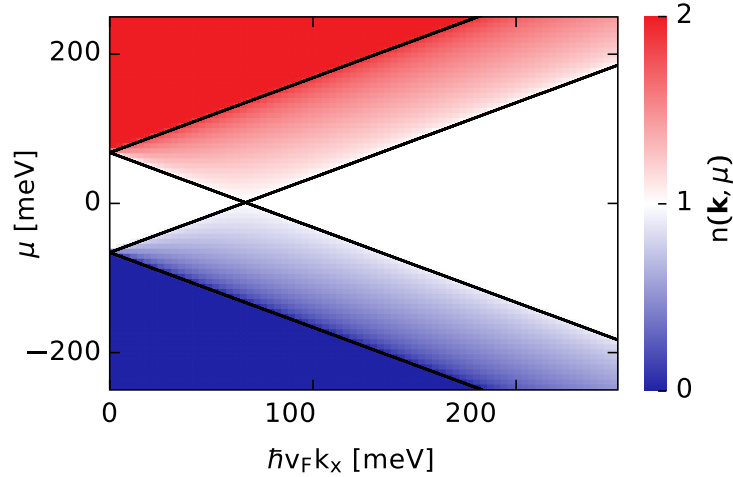


Figure 2.12 – Sum of the occupation of the lower and upper graphene bands $n(\mathbf{k}, \mu)$ as a function of chemical potential μ and momentum times $\hbar v_F$ for driven graphene. We show a cut along the k_x -direction. Black lines show the minimum and maximum of the generalized momentum $\pm(\hbar v_F k \pm e E_{\text{dr}} v_F / \omega_{\text{dr}})$. We use the same parameters as for Fig. 2.11. We show the occupation after the steady state is achieved for a tanh-type ramp to the driven state.

static system from Eq. 2.10. We consider the total occupation of each momentum mode

$$n(\mathbf{k}, \mu) = \text{Tr} \left[\rho_{\mathbf{k}}(\mu) \left(c_{\mathbf{k},A}^\dagger c_{\mathbf{k},A} + c_{\mathbf{k},B}^\dagger c_{\mathbf{k},B} \right) \right] .$$

For our simulation we initialize the system at $\Delta_{\text{hf}} = 0$ then increase Δ_{hf} towards its final value using a tanh-type ramp protocol and wait until a steady state has been achieved. The results for the effective static system are shown in Fig. 2.11. For all cases considered in this section the occupation is particle-hole symmetric and we therefore only discuss $\mu > 0$. As expected for a static system we see that the total occupation of all momentum modes is 1 for $\mu = 0$ and remains at that value when changing the chemical potential within the band gap. Furthermore for each momentum mode the total occupation increases to 2 when increasing the chemical potential above the corresponding upper band energy.

We show the corresponding plot for the driven system in Fig. 2.12. We see that the total occupation is dramatically different from that of a static system. In fact, no signs of the Dirac-point gap and resonance gaps can be seen in this observable. Instead the instantaneous generalized momentum $\mathbf{k} - e\mathbf{A}$ of the system plays a crucial role. For circularly polarized light the generalized momentum moves on a circle with radius $e E_{\text{dr}} v_F / \omega_{\text{dr}}$ around the bare momentum \mathbf{k} . Hence the absolute value of the generalized momentum oscillates periodically. When the chemical potential is below the minimum of the generalized momentum $\mu < |\hbar v_F k - e E_{\text{dr}} v_F / \omega_{\text{dr}}|$ the corresponding momentum mode has unit occupation. For larger chemical potential the occupation increases and, when it is above

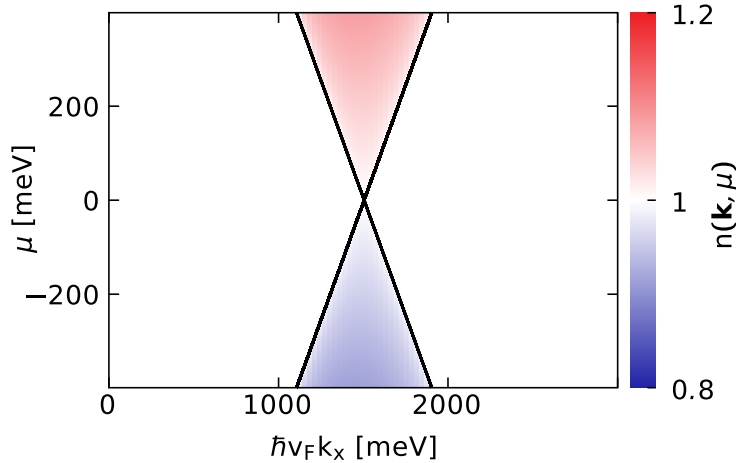


Figure 2.13 – Sum of the occupation of the lower and upper graphene bands $n(\mathbf{k}, \mu)$ as a function of chemical potential μ and momentum times $\hbar v_F$ for driven graphene. We show a cut along the k_x -direction. Black lines show the minimum and maximum of the generalized momentum $\pm(\hbar v_F k \pm eE_{\text{dr}}v_F/\omega_{\text{dr}})$. We use the same damping as in Fig. 2.12, but significantly higher $E_{\text{dr}} = 225 \text{ GV m}^{-1}$, $\omega_{\text{dr}} = 2\pi \cdot 24 \text{ PHz}$ and $T = 80 \text{ K}$. We show the occupation after the steady state is achieved for a tanh-type ramp to the driven state.

the maximum $\mu > |\hbar v_F k + eE_{\text{dr}}v_F/\omega_{\text{dr}}|$, the system reaches double occupancy. As a result when increasing the chemical potential the first modes that are occupied are those at $\hbar v_F k = eE_{\text{dr}}v_F/\omega_{\text{dr}}$, which we call the bare Rabi frequency⁹. This behavior is robust even for very high driving frequencies, when increasing the field strength simultaneously, see Fig. 2.13. Finally, we find that the total occupation of all momentum modes $\sum_{\mathbf{k}} n(\mathbf{k}, \mu)$ is for any chemical potential, independent of the driving field strength E_{dr} . This is again in contrast to the effective static system where for small positive chemical potential the occupation reduces from a value larger than 1 to 1 when the gap at the Dirac point opens.

2.3. Numerical conductivity simulations and comparison to experiments

After considering the spectrum and the occupations of driven graphene we now turn towards analyzing the Hall conductivity. It has been predicted that graphene driven with circularly polarized light has a quantized topological Hall conductivity in the high-frequency limit [76–80]. Here we consider low-frequency driving as used in Ref. [86]. For all our simulations we show the conductivity dichroism, defined as the difference of the conductivity for positive and negative circularly polarized light. We show the momentum-

⁹This nomenclature will become clear later in Sec. 2.4.2.

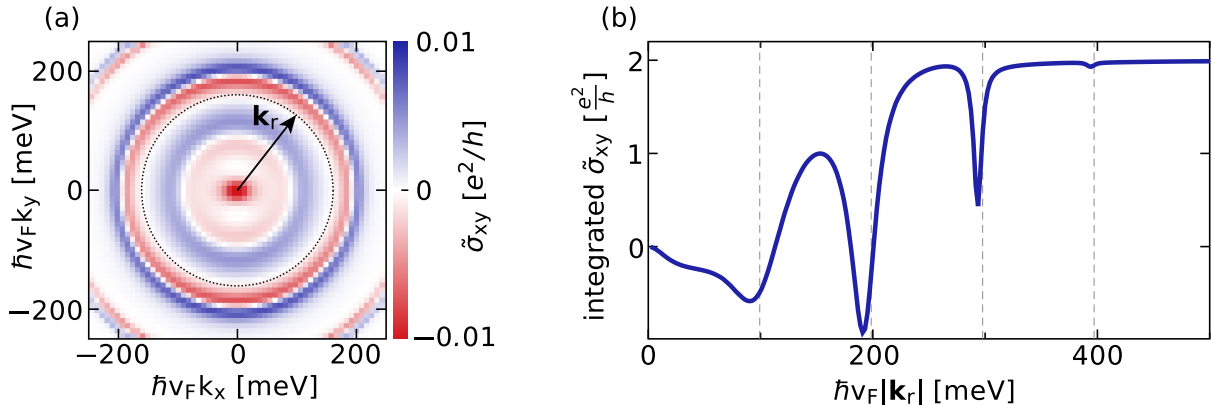


Figure 2.14 – Circular dichroism of the Hall conductivity. (a) We show the conductivity density $\tilde{\sigma}_{xy}$ as a function of momentum averaged over contributions from opposing momentum modes. Panel (b) shows the same data as (a) but radially integrated as a function of threshold momentum $|\mathbf{k}_r|$. The first four resonances are indicated by dashed lines. For both panels we use $E_{\text{dr}} = 20 \text{ MV m}^{-1}$, $\omega_{\text{dr}} = 2\pi \cdot 48 \text{ THz} \approx 200 \text{ meV}/\hbar$, $T_1 = 1 \text{ ps}$, $T_2 = 200 \text{ fs}$, $T_p = 250 \text{ fs}$, $T = 1 \text{ K}$, $E_L = 1.7 \text{ kV m}^{-1}$ and $\mu = 0$. We show the conductivity density after a steady state is achieved for a tanh-type ramp of the driving field strength.

resolved dichroism of the conductivity density in Fig. 2.14(a). In addition to the negative contribution of the Dirac point resonant contributions occur at multiples of the driving frequency $2v_F k = m\omega_{\text{dr}}$. Each resonance has negative conductivity contribution for momentum modes smaller than the resonance $2v_F k < m\omega_{\text{dr}}$, and positive contribution for momenta larger than the resonance $2v_F k > m\omega_{\text{dr}}$. This effect can be understood from a harmonic-oscillator perspective: for a driven harmonic oscillator the response switches sign when driven below and above the eigenfrequency. In graphene the eigenfrequency has the momentum dependence $2v_F k$. Hence momenta smaller and larger than the resonance contribute with opposite sign to the conductivity.

We show the radially integrated conductivity density $\tilde{\sigma}_{xy}$ in Fig. 2.14(b). The plateau for large $|\mathbf{k}_r|$ gives the full conductivity dichroism. We see that the major contribution to the conductivity arises from resonances. Only the small decrease in the integrated $\tilde{\sigma}_{xy}$ for momenta smaller than 50 meV reflects the contribution of the Dirac point. The alternating negative and positive contributions from resonances lead to decreasing integrated $\tilde{\sigma}_{xy}$ before the resonance and increasing $\tilde{\sigma}_{xy}$ after the resonance. The larger increase than decrease reflects that each resonance has a net positive contribution. For higher-order resonances the contributions are more focused around the resonance and the magnitude of the net contribution is smaller. For the chosen parameter set only the first two resonances have a significant net contribution to the conductivity. Higher-order resonances do not contribute.

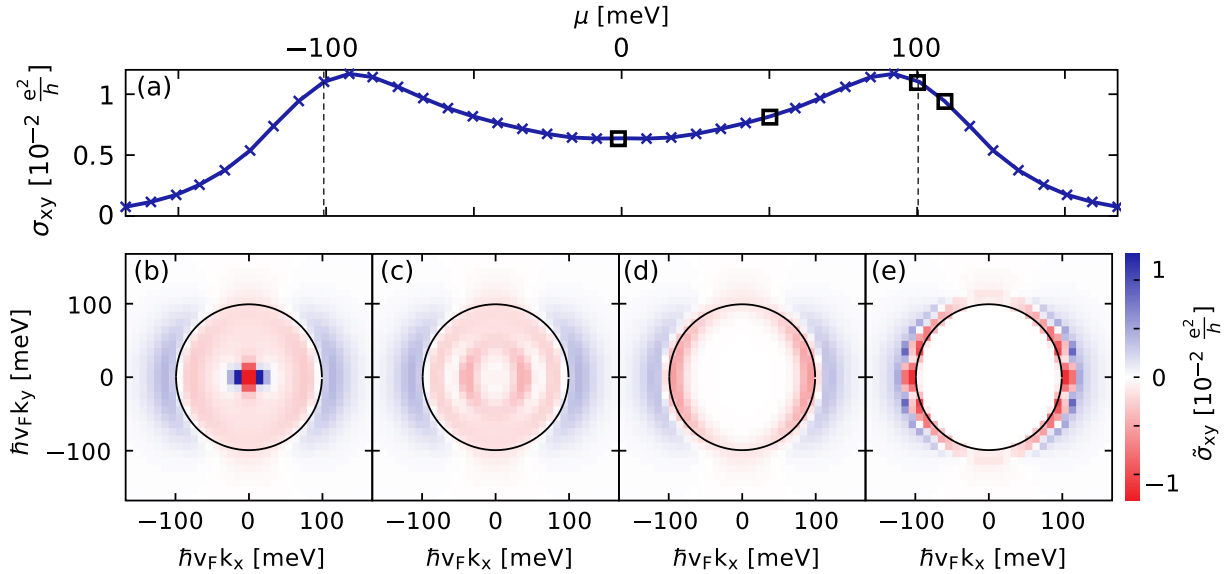


Figure 2.15 – Circular dichroism of the transverse conductivity. Panel (a) shows the total conductivity as a function of applied chemical potential. Dashed lines indicate the position of the first resonance $2v_F k = \omega_{\text{dr}}$. Panels (b)-(e) show the momentum-resolved conductivity density averaged over opposite momentum modes for increasing chemical potential as indicated by black squares in panel (a). Black circles denote the position of the first resonance. The center of each panel $(0, 0)$ is positioned at the Dirac point. The parameters for all panels are $E_{\text{dr}} = 1 \text{ MV m}^{-1}$, $\omega_{\text{dr}} = 2\pi \cdot 48 \text{ THz}$, $T_1 = 100 \text{ fs}$, $T_2 = 20 \text{ fs}$, $T_p = 25 \text{ fs}$, $T = 80 \text{ K}$, $E_L = 840 \text{ V m}^{-1}$ and $g_{\text{env}}(t)$ is a Gaussian envelope with full width half maximum $t_{\text{FWHM}} = 1 \text{ ps}$. This figure has been published in Ref. [N2].

The momentum-resolved conductivity allows to identify the different contributions to the transverse current. In experiment, however, such data is not easily accessible. Instead it is possible to tune the applied back gate, i.e. the chemical potential [86]. When increasing the chemical potential for the effective static system, momenta close to the Dirac point are fully occupied and due to Pauli blocking do not contribute to the conductivity. As we have learned in Sec. 2.2.3 changing the chemical potential in driven graphene behaves profoundly different, inserting extra electrons at the Rabi frequency, i.e. $\hbar v_F \mathbf{k} = e E_{\text{dr}} v_F / \omega_{\text{dr}}$, instead of the Dirac point, i.e. $\mathbf{k} = 0$. For low electric field strength E_{dr} the bare Rabi frequency is small, hence its difference to $\mathbf{k} = 0$ negligible, and the system behaves similar to the static system. We show this case in Fig. 2.15. For momentum modes smaller than the first bare resonance negative contributions to the conductivity dominate. When increasing the chemical potential the conductivity of these modes becomes suppressed and the total conductivity increases. Near the first resonance the situation reverses. Now momentum modes above the resonance become fully occupied and increasing the chemical potential further leads to decreasing total conductivity. Hence the chemical-potential

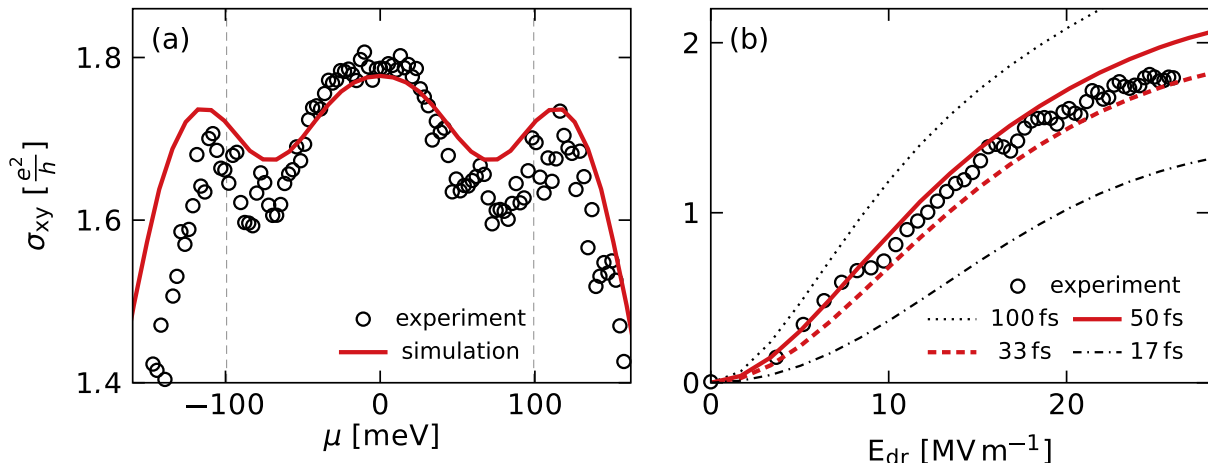


Figure 2.16 – (a) Chemical-potential-resolved circular dichroism of the transverse conductivity. The data from the numerical simulation (red line) and experimental data [86] (open circles) agree quantitatively. (b) Electric field strength dependence of the current dichroism for several values of the particle-exchange time scale T_p as indicated in the legend. We see that a value of $T_p = 30 - 50$ fs is consistent with the experiment. The parameters for the numerical simulation are $\omega_{\text{dr}} = 2\pi \cdot 48$ THz ≈ 200 meV/ \hbar , $T_1 = 100$ fs, $T_2 = 20$ fs, $T = 80$ K, $E_L = 1.7$ kV m $^{-1}$ and the driving pulse has Gaussian envelope with electric field strength FWHM of $\sqrt{2}$ ps, corresponding to intensity FWHM of 1 ps. Finally, $E_{\text{dr}} = 26$ MV m $^{-1}$ and $T_p = 36$ fs in panel (a) and chemical potential $\mu = 0$ in panel (b). This figure has been published in Ref. [N2].

dependence of the transverse conductivity reflects the resonant behavior. Although the mapping between chemical potential and occupied momentum modes is more convoluted for larger field strengths we can still see a clear signature of the resonances in this regime. In Fig. 2.16 we compare our results to experimental results obtained in [86]. We find that both the fluence dependence as well as the chemical-potential dependence for high fluence agree quantitatively with just a single free parameter. All parameters except for the dissipation rates agree with those in [86]. The dissipation rates T_1 and T_2 are inspired by a different measurement on graphene [173]¹⁰. Only the third decay rate T_p is adjusted to match the experimental data. We find that depending on the electric field strength values of 30 – 50 fs are appropriate.

For the simulation of the experiment from [86] it is crucial to work at fixed chemical potential instead of fixed density. To illustrate the difference we show a simulation enforcing fixed density for each momentum mode during the time evolution in Fig. 2.17. The parameters are the same as in Fig. 2.16. The shape of the curve is fundamentally different from the experimental data. When working at fixed particle number we fill the undriven system according to the chosen chemical potential and then keep the total number of elec-

¹⁰Similar dissipation rates have also been obtained in a range of other publications [174–178].

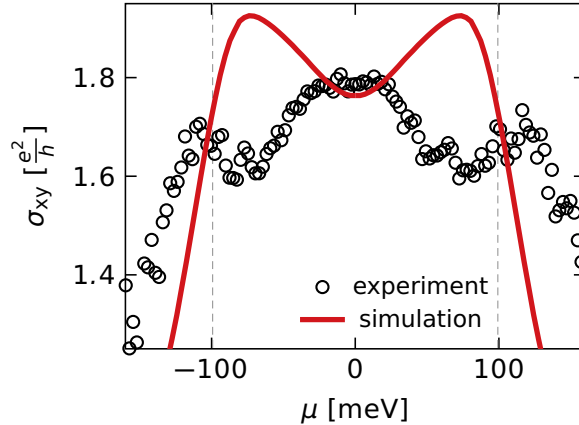


Figure 2.17 – Chemical-potential-resolved circular dichroism of the transverse conductivity. Black circles show experimental data from [86] and the solid red line shows results from our numerical simulation. Here μ is the chemical potential of the initial state and we do not allow for the exchange of particles during the simulation. The parameters for the numerical simulation are $E_{\text{dr}} = 26 \text{ MV m}^{-1}$, $\omega_{\text{dr}} = 2\pi \cdot 48 \text{ THz} \approx 200 \text{ meV}/\hbar$, $T_1 = 100 \text{ fs}$, $T_2 = 20 \text{ fs}$, $T = 80 \text{ K}$, $T_p = 36 \text{ fs}$, $E_L = 1.7 \text{ kV m}^{-1}$ and the driving pulse has Gaussian envelope with electric-field-strength FWHM of $\sqrt{2} \text{ ps}$, corresponding to intensity FWHM of 1 ps . This figure has been published in Ref. [N2].

trons in each momentum mode constant when switching the driving field on. In contrast to the experimental data the simulated conductivity increases when tuning the chemical potential away from zero. This effect is quite general for the system at fixed particle number as in this case the momentum modes close to the Dirac points are the first modes that are filled and hence do not contribute to the current. As we have seen in Fig. 2.15 the momentum modes inside the circle of the first resonance contribute dominantly negative and hence when blocking these modes the conductivity increases. We conclude that the exchange of electrons with unilluminated regions of the graphene sample as well as with the substrate is important even on the short time scales of the circularly polarized pulse.

We note that the experiments presented in Ref. [86] have been performed using a driving pulse with Gaussian envelope. For the comparisons to experiment we use the same setup for our simulations. We find, however, that the width of the Gaussian envelope is sufficiently long, such that the electrons remain close to the steady-state at all times for the given set of dissipation parameters. We therefore focus on the steady-state properties in the following chapters by considering a tanh-type ramp.

2.4. Hall conductivity in driven graphene in the low-fluence limit

We have seen that our model describes the Hall conductivity in driven dissipative graphene. Next we analyze the origin of the Hall conductivity. We find that a major contribution to the Hall conductivity in graphene is a Berry curvature effect. In the infinite-frequency limit the Berry curvature is well localized around the Dirac point. At finite frequency there are additional contributions originating from resonances. In fact, we find that in most cases these contributions dominate the conductivity. At low driving field strength E_{dr} the dominant contribution to the Hall conductivity originates from the first resonance where $2v_{\text{F}}k = \omega_{\text{dr}}$. This is because at low E_{dr} all other gaps are small compared to temperature, damping and dephasing time scales. We call these gaps closed (this will be explained in detail in Sec. 2.6). Therefore we first consider the contribution of the first resonance in the limit of low field strengths where mapping the graphene Hamiltonian onto the Rabi problem can give intuitive insights. We confirm our proposal that the Hall conductivity is approximately given by the sum of the Berry-curvature and band-velocity contributions, see Eq. 2.1, for the regime of low field strengths.

2.4.1. The Rabi problem

For completeness we give a brief description of the Rabi problem. A more detailed description can be found in Rabi's original work [179] and in Ref. [180]. We start from the Jaynes-Cummings-Paul model for a driven two-level system within the rotating-wave approximation¹¹

$$H_0 = \begin{pmatrix} \hbar\omega_0/2 & 0 \\ 0 & -\hbar\omega_0/2 \end{pmatrix} \quad (2.18)$$

$$H' = \hbar\lambda \begin{pmatrix} 0 & e^{-i\omega_{\text{dr}}t} \\ e^{i\omega_{\text{dr}}t} & 0 \end{pmatrix}, \quad (2.19)$$

where ω_0 is the level spacing of the atom and ω_{dr} is the frequency of the electric field. The resulting Schrödinger equation is commonly solved by applying the rotating-wave approximation, i.e. applying the unitary transform

$$U_{\text{rotating-wave}} = \begin{pmatrix} e^{-i\omega_{\text{dr}}t} & 0 \\ 0 & 1 \end{pmatrix}.$$

¹¹Usually the Hamiltonian is written as $H_0 = \begin{pmatrix} \hbar\omega_0 & 0 \\ 0 & 0 \end{pmatrix}$. Here we introduce a constant energy offset as this will make the comparison to graphene easier.

The solution is

$$\psi(t) = \begin{pmatrix} e^{-i\omega_{\text{dr}}t/2} \left[a \cos(\Omega_{\text{R}}t) + i \frac{a\Delta - b\lambda}{\Omega_{\text{R}}} \sin(\Omega_{\text{R}}t) \right] \\ e^{i\omega_{\text{dr}}t/2} \left[b \cos(\Omega_{\text{R}}t) - i \frac{b\Delta + a\lambda}{\Omega_{\text{R}}} \sin(\Omega_{\text{R}}t) \right] \end{pmatrix},$$

where we have defined the detuning

$$\Delta = \frac{\omega - \omega_0}{2}$$

and the Rabi frequency

$$\Omega_{\text{R}} = \sqrt{\Delta^2 + \lambda^2}.$$

The integration constants a, b are fixed from the normalization of the wave function and the initial condition. Note that the above wave function is normalized for $a = \sin(\chi)$ and $b = \cos(\chi)$.

2.4.2. Mapping driven graphene onto the Rabi problem

We use the solution obtained for the Rabi problem in the previous section to solve the Schrödinger equation in driven graphene within the rotating wave approximation. This yields a good estimate close to the first resonance.

As in Sec. 2.2.1 we start from the graphene Hamiltonian with no longitudinal field, see Eq. 2.11. Again we go to the basis that diagonalizes the undriven Hamiltonian and obtain

$$U_{\mathbf{k}}^\dagger H_{0,\mathbf{k}} U_{\mathbf{k}} = 2\hbar v_F k \sigma_z \tag{2.20}$$

$$U_{\mathbf{k}}^\dagger H_{1,\mathbf{k}} U_{\mathbf{k}} = \frac{eE_{\text{dr}}v_{\text{F}}}{\omega_{\text{dr}}} \begin{pmatrix} s_1 & -ic_1 \\ ic_1 & -s_1 \end{pmatrix},$$

$$\begin{aligned} \text{where } s_1 &= \sin(\tau_z \sigma_{\text{pol}} \omega_{\text{dr}} t - \phi_{\mathbf{k}}) \\ c_1 &= \cos(\tau_z \sigma_{\text{pol}} \omega_{\text{dr}} t - \phi_{\mathbf{k}}). \end{aligned}$$

Next we do the rotating wave approximation, keeping only those terms, non-oscillatory in the rotating frame. Then

$$H_{\text{dr},\mathbf{k}}(t) \approx \frac{eE_{\text{dr}}v_{\text{F}}}{2\omega_{\text{dr}}} \begin{pmatrix} 0 & -ie^{-i\omega_{\text{dr}}t + i\tau_z \sigma_{\text{pol}} \phi_{\mathbf{k}}} \\ ie^{i\omega_{\text{dr}}t - i\tau_z \sigma_{\text{pol}} \phi_{\mathbf{k}}} & 0 \end{pmatrix}. \tag{2.21}$$

Equations 2.20 and 2.21 closely resemble Eqs. 2.18 and 2.19 and can therefore be solved

analytically in analogy to the Rabi problem. The solution can be written as

$$|\psi_{\text{R}}(t)\rangle = |\psi_{\text{R},+}(t)\rangle e^{i\Omega_{\text{R}}t} + |\psi_{\text{R},-}(t)\rangle e^{-i\Omega_{\text{R}}t} \quad ,$$

where

$$|\psi_{\text{R},\pm}(t)\rangle = \begin{pmatrix} -ie^{i\tau_z\sigma_{\text{pol}}\phi_{\mathbf{k}}} \left(a \pm \frac{a\Delta - b\lambda}{\Omega_{\text{R}}} \right) \\ \left(b \mp \frac{b\Delta + a\lambda}{\Omega_{\text{R}}} \right) e^{i\omega_{\text{dr}}t} \end{pmatrix} e^{-i\omega_{\text{dr}}t/2}$$

and

$$\begin{aligned} \Delta &= \frac{\omega_{\text{dr}} - 2v_{\text{F}}k}{2} \\ \lambda &= \frac{eE_{\text{dr}}v_{\text{F}}}{2\hbar\omega_{\text{dr}}} \quad . \end{aligned}$$

Also note that

$$\sigma_{\text{pol}} e^{i\tau_z\sigma_{\text{pol}}\phi_{\mathbf{k}}} = \frac{\tau_z(\sigma_{\text{pol}}k_x + ik_y)}{k}$$

and we obtain the bare Rabi frequency, i.e. the one for zero detuning, as $2\Omega_{\text{R}}(\Delta = 0) = eE_{\text{dr}}v_{\text{F}}/\omega_{\text{dr}}$, where the factor of 2 has been included for convenience. The eigenenergies can be read off from the eigenstates as

$$E_{\text{R},\pm} = -\hbar\omega_{\text{dr}}/2 \pm \hbar\Omega_{\text{R}} \quad .$$

This result is indeed in agreement with Eq. 2.16. This emphasizes that the Magnus expansion in the rotating frame is closely related to the Rabi problem.

For completeness we note that the band velocity is obtained as

$$\mathbf{v}^{\pm}(\mathbf{k}) = \nabla_{\mathbf{k}} E_{\text{R},\pm}(k) \quad .$$

Next we determine the instantaneous Berry curvature. For this we need the eigenstates with respect to the original AB -basis

$$|\psi_{\text{R},\pm}^{AB}(t)\rangle = U_{\mathbf{k}} |\psi_{\text{R},\pm}(t)\rangle \quad .$$

The Berry connection is now given by

$$A_j^{\pm}(t) = i\langle \psi_{\text{R},\pm}^{AB}(t) | \frac{\partial}{\partial k_j} | \psi_{\text{R},\pm}^{AB}(t) \rangle$$

and as a result we obtain the Berry curvature as

$$\begin{aligned}
 F_{\mathbf{R}}^{\pm}(\mathbf{k}, t) &= \frac{\partial}{\partial k_y} A_x(t) - \frac{\partial}{\partial k_x} A_y(t) \\
 &= \mp \frac{\sigma_{\text{pol}} v_F \lambda^2}{2k \Omega_{\mathbf{R}}^3} \mp \frac{\text{Re} [(k_y + i\sigma_{\text{pol}} k_x) e^{i\omega_{\text{dr}} t}] v_F \lambda \Delta}{2k^2 \Omega_{\mathbf{R}}^3} .
 \end{aligned} \tag{2.22}$$

The first contribution is the same as the result within the Magnus expansion in the rotating frame, see Eq. 2.17. For now we neglect the second time-dependent part of the Berry curvature. This will be discussed in Sec. 2.4.3. Finally, we note that given a density matrix $\rho_{\mathbf{k}}$ we can compute the occupations of the Rabi bands as

$$n_{\mathbf{R},\pm}(\mathbf{k}, t) = \langle \psi_{\mathbf{R},\pm}^{AB}(t) | \rho_{\mathbf{k}}(t) | \psi_{\mathbf{R},\pm}^{AB}(t) \rangle .$$

2.4.3. Interpretation of the Hall conductivity in terms of Rabi Berry curvature and Rabi band velocity

We are now ready to compare the full conductivity to the Rabi-Berry-curvature and band-velocity contributions. To this end we use the results for the Rabi Berry curvature, Rabi band velocity and Rabi occupations from the previous section and insert them into Eq. 2.1. We find that the Rabi-Berry-curvature contribution switches sign at the first resonance, see Fig. 2.18(a). This is a result of occupying different Rabi bands with opposite Berry curvature on each side of the resonance. Most of this contribution cancels. Damping leads, however, to slightly higher occupation on the outside of the resonance and hence there is a net positive contribution from Rabi Berry curvature, see Fig. 2.18(c). Comparing the Rabi Berry curvature to the full conductivity in Fig. 2.18(b) we find qualitatively good agreement. Only the contribution from the Dirac point in the full conductivity is not captured by the Rabi-Berry-curvature contribution. This is expected since the rotating-wave approximation is only valid close to the first resonance. A quantitative comparison in Fig. 2.18(c) shows that about half of the full conductivity is due to Rabi Berry curvature. An additional contribution is due to the band velocity of Rabi states. This effect is similar to the population-imbalance effect presented in Ref. [N5]. We see that roughly 80% of the full conductivity is captured by the sum of the Berry-curvature and band-velocity contributions.

We show results for lower damping and dephasing time scales in Fig. 2.19. We see that the sum of Berry-curvature and band-velocity contributions shows better agreement with the full conductivity in this regime. We therefore conclude that the identification $\sigma_{xy} \approx \Phi_{xy}$, see Eq. 2.1, is particularly well founded in the weakly damped regime. For all damping strengths there is a finite contribution from Rabi band velocity. Hence, band-

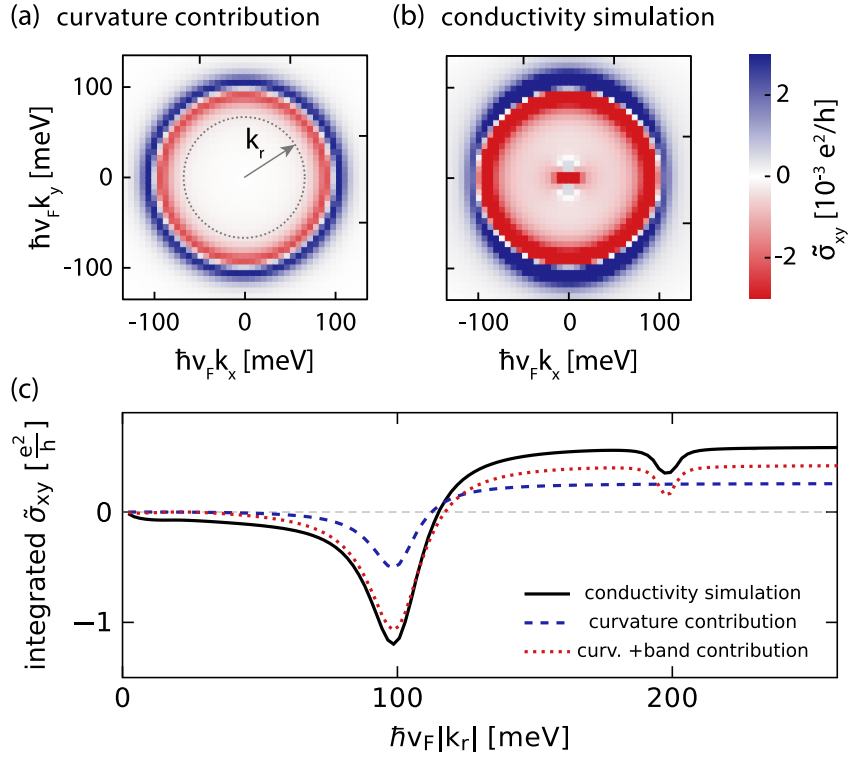


Figure 2.18 – Circular dichroism of the Rabi-Berry-curvature and Rabi-band-velocity contributions and the full conductivity. (a) Rabi-Berry-curvature contribution to the conductivity dichroism. We show the Berry curvature computed according to Eq. 2.22 weighted with the respective Rabi occupations. (b) Circular dichroism of the simulated Hall conductivity density $\tilde{\sigma}_{xy}$. Panels (a) and (b) are averaged over opposing momentum modes. (c) Comparison of the integrated Hall conductivities. We show the conductivity density $\tilde{\sigma}_{xy}$ integrated over all momenta smaller than the threshold value $|\mathbf{k}_r|$. The solid black line shows the simulated full conductivity, the dashed blue line shows the Rabi-Berry-curvature contribution and the dotted red line shows the sum of Rabi-Berry-curvature and Rabi-band-velocity contributions. In all plots we use $E_{\text{dr}} = 5 \text{ MV m}^{-1}$, $\omega_{\text{dr}} = 2\pi \cdot 48 \text{ THz} \approx 200 \text{ meV}/\hbar$, $T_1 = 1 \text{ ps}$, $T_2 = 200 \text{ fs}$, $T_p = 200 \text{ fs}$, $T = 80 \text{ K}$, $E_L = 1.7 \text{ kV m}^{-1}$ and $\mu = 0$. All observables are shown after a steady state is achieved for a tanh-type ramp of the driving field strength. Panels (a) and (b) have been published in Ref. [N2].

velocity and Berry-curvature contributions occur simultaneously. This is in contrast to topological insulators, where the band gap leads to vanishing band-velocity contribution in the topological regime.

Finally, we consider the time-dependent Berry-curvature contributions we found in Eq. 2.22. Since the density matrix and the Rabi eigenstates are time dependent the occupations of Rabi bands $n_{R,\pm}(\mathbf{k}, t)$ will also contain an oscillatory contribution. The resulting time dependence may cancel and therefore there is a time-independent contribution from time-dependent curvature and occupations. We have checked that this

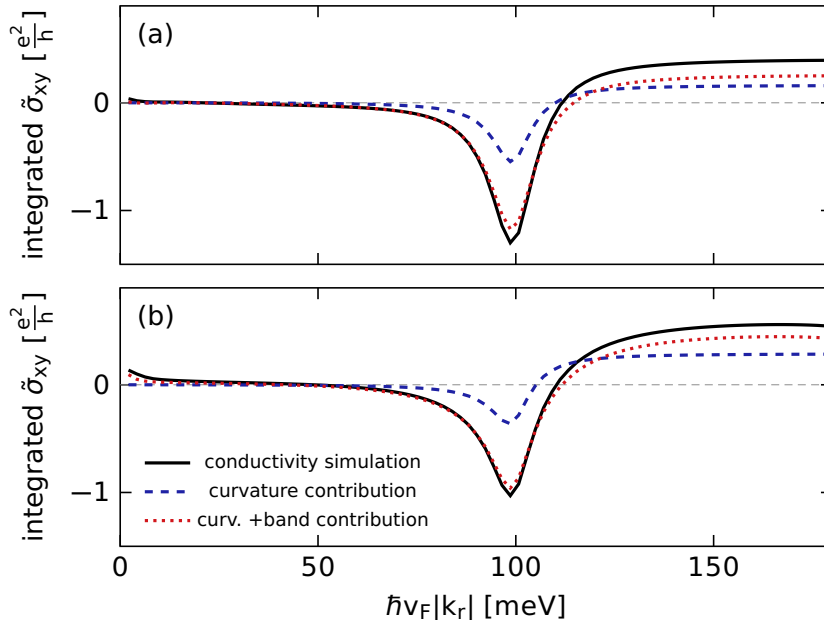


Figure 2.19 – Comparison of the integrated Hall conductivity dichroisms. We show the conductivity density $\tilde{\sigma}_{xy}$ integrated over all momenta smaller than the threshold value $|k_r|$. The solid black line shows the simulated full conductivity, the dashed blue line shows the Rabi-Berry-curvature contribution and the dotted red line shows the sum of Rabi-Berry-curvature and Rabi-band-velocity contributions. We have added an offset to all curves such that they are zero at $\hbar v_F |k_r| = 20$ meV. In all plots we use $E_{\text{dr}} = 5$ MV m $^{-1}$, $\omega_{\text{dr}} = 2\pi \cdot 48$ THz ≈ 200 meV/ \hbar , $T = 80$ K, $E_L = 1.7$ kV m $^{-1}$ and $\mu = 0$. Panel (a) shows $T_1 = 4$ ps, $T_2 = 0.8$ ps, $T_p = 1.6$ ps and panel (b) shows $T_1 = 20$ ps, $T_2 = 4$ ps, $T_p = 8$ ps. All observables are shown after a steady state is achieved for a tanh-type ramp of the driving field strength. Panel (a) has been published in Ref. [N2].

contribution is several orders of magnitude smaller than the contribution arising due to time-independent Berry curvature and hence the quantities can be averaged independently $\overline{F_{xy}(k, t)n(k, t)} \approx \overline{F_{xy}(k, t)} \overline{n(k, t)}$. Hence it was well founded to drop the second, time-dependent contribution to the Berry curvature.

2.5. Hall conductivity in driven graphene for larger fluence

The analysis using the Rabi solution gives intuitive insight for the contribution of the first resonance. At larger electric field strength higher-order resonance gaps open and the Rabi approximation is not valid any more. In analogy to the above considerations using the Rabi solution, we can now use Floquet theory in order to obtain the Berry-curvature and band-velocity contributions. The occupations of individual Floquet bands

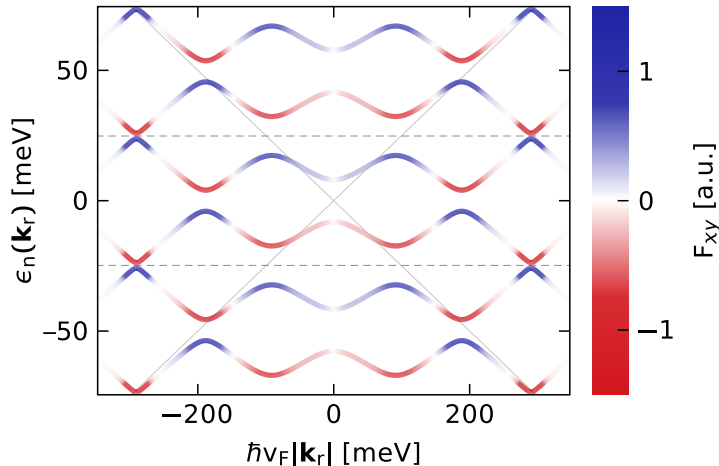


Figure 2.20 – Floquet band structure colored by Berry curvature. Berry curvatures are integrated over ring segments of the 2-d momentum space. Dashed gray lines separate the different Floquet replica, while faint solid gray lines indicate the Dirac cone for undriven graphene. We use $E_{\text{dr}} = 26 \text{ MV m}^{-1}$ and $\omega_{\text{dr}} = 2\pi \cdot 48 \text{ THz} \approx 200 \text{ meV}/\hbar$. This figure has been published in Ref. [N2].

are obtained by integrating the respective sectors of the single-particle correlation function shown in Fig. 2.10, for details see the appendix of Ref. [N2]. The Floquet Berry curvature and Floquet band velocities are computed numerically using the procedure presented in Sec. 2.2.1.

In Fig. 2.10 we see that those Floquet bands obtain the largest occupation that are adiabatically connected to the undriven lower Dirac cone. For these bands the following pattern repeats at each resonance: momenta smaller than the resonance have dominant occupation in the band above the resonance and momenta larger than the resonance in the band below. A split band picture emerges where the dominantly occupied band changes at each resonance. Additionally we consider the Floquet Berry curvature, shown in Fig. 2.20. The latter is always positive in the band below the resonance and negative in the band above. Combining this with the occupations we find that the Hall-conductivity contribution according to Eq. 2.1 is negative for momenta smaller than the resonance and positive for momenta larger. The pattern of the first resonance repeats. This is in agreement with the alternating sign of the Hall conductivity density, remember Fig. 2.14.

We turn to a quantitative comparison of the Floquet-Berry-curvature and Floquet-band-velocity contributions with the full current. The resulting fluence dependence of the Hall conductivity is shown in Fig. 2.21. For all fluences a significant part of the simulated conductivity is due to Floquet Berry curvature, while an additional contribution comes from Floquet band velocities. At low fluence the band-velocity contribution dominates. At higher fluence there is a crossover and the Hall conductivity is dominated by Berry-

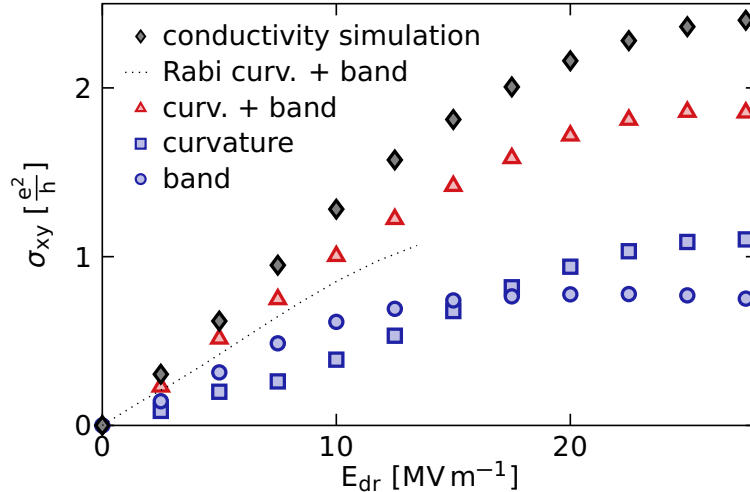


Figure 2.21 – Comparison of the electric field strength dependence of the conductivity dichroism and the Berry-curvature and band-velocity contributions. Black diamonds show the simulated full conductivity, the faint dashed line the sum of Berry-curvature and band-velocity contributions computed from Rabi states, red triangles show the same computed from Floquet states, blue squares show only the Berry-curvature and blue circles only the band-velocity contribution computed from Floquet states. We use $\omega_{\text{dr}} = 2\pi \cdot 48 \text{ THz} \approx 200 \text{ meV}/\hbar$, $T_1 = 1 \text{ ps}$, $T_2 = 0.2 \text{ ps}$ and $T_p = 0.4 \text{ ps}$, $T = 80 \text{ K}$, $E_L = 1.7 \text{ kV m}^{-1}$ and $\mu = 0$. All observables are shown after a steady state is achieved for a tanh-type ramp of the driving field strength. This figure has been published in Ref. [N2].

curvature contributions.

We find that a similar comparison for smaller dephasing-type damping, shown in Fig. 2.22, yields even better agreement of the Hall conductivity and the sum of Floquet-Berry-curvature and Floquet-band-velocity contributions. This suggests that dephasing-type dissipation is responsible for the deviation of the two quantities in Fig. 2.21.

2.6. Resolving the Hall conductivity of individual resonances

We have identified the main contribution to the Hall conductivity to be arising from individual resonances and the Dirac point. For low values of E_{dr} the conductivity density is well localized around individual resonances and there is no contribution to the conductivity in between resonances. Hence in between resonances the integrated conductivity shown in Fig. 2.23 is constant. In this regime we can define contributions of the Dirac point and individual resonances by integrating the conductivity density over the respective sectors. This is similar to the integrals for pseudo-Chern numbers defined in Sec. 2.2.1.

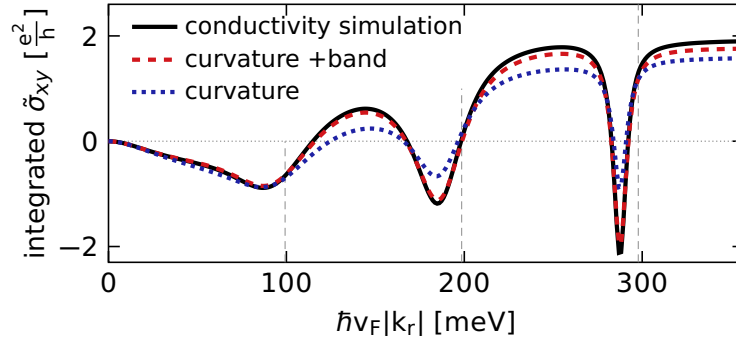


Figure 2.22 – Comparison of the electric-field-strength dependence of the conductivity dichroism and the Berry-curvature and band-velocity contributions for small dephasing-type damping. We show the circular dichroism of the integrated Hall-conductivity density. The solid black line shows the simulated full conductivity, the dashed red line the sum of Berry-curvature and band-velocity contributions computed from Floquet states and the dotted blue line shows only the Berry-curvature contribution. Dashed vertical lines indicate the first three resonances. The parameters are the same as in Fig. 2.21 except for $T_2 = 2$ ps. This figure has been published in Ref. [N2].

We define

$$\sigma_{\text{Dirac}} = \int_0^{k=\omega_{\text{dr}}/4/v_F} d^2\mathbf{k} \tilde{\sigma}_{xy} \quad (2.23)$$

$$\sigma_{\text{n-th resonance}} = \int_{k=(n-1/2)\omega_{\text{dr}}/2/v_F}^{k=(n+1/2)\omega_{\text{dr}}/2/v_F} d^2\mathbf{k} \tilde{\sigma}_{xy} \quad . \quad (2.24)$$

For larger field strength we can still apply this procedure. In this regime the contributions of resonances start overlapping, however, and it is therefore not as well founded. Since the contribution from resonances is always negative below and positive above the resonance, overlapping resonances lead to canceling contributions.

Keeping the applicability regime in mind we use the above procedure in order to analyze the driving-field-strength dependence of the contribution of individual resonances and the Dirac point. The contribution in the high-frequency limit without damping has been analyzed in [76–80]. In this limit there are no resonant contributions and the total Hall conductivity originates from the gap at the Dirac point and is $\sigma_{xy} = -2e^2/h$. For this result a fully occupied lower and an empty upper graphene band is assumed. Under experimental conditions finite-frequency driving leads to excitations into the upper graphene band. Depending on the strength of damping and dephasing effects one obtains a steady state with significant occupation in the upper graphene band close to the Dirac point, see Fig. 2.10. The upper band has opposite Berry curvature and hence contributes to the Hall conductivity with opposite sign. As a result the Hall conductivity arising from the Dirac point is reduced significantly for experimental conditions. Since the occupation

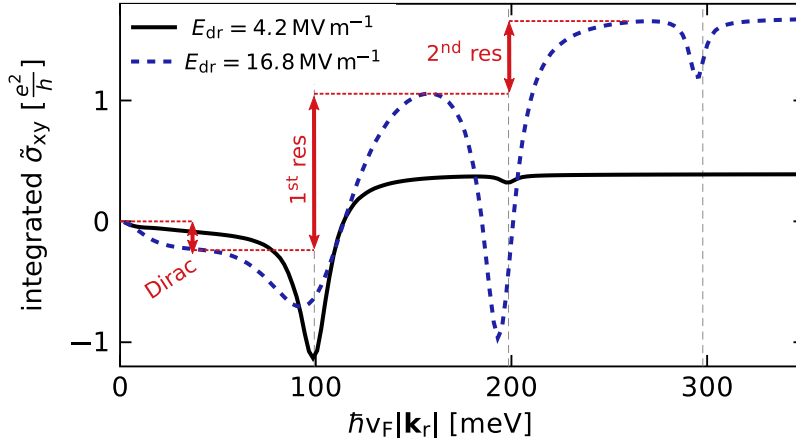


Figure 2.23 – Circular dichroism of the integrated Hall conductivity density. We show the conductivity density $\tilde{\sigma}_{xy}$ integrated over all momenta smaller than the threshold value $|\mathbf{k}_r|$ for two different driving field strengths as indicated in the legend. The first, second and third resonance are indicated by dashed lines. Red arrows mark the conductivity contribution of the Dirac point, the first and the second resonance for $E_{dr} = 16.8 \text{ MV m}^{-1}$. We use $\omega_{dr} = 2\pi \cdot 48 \text{ THz} \approx 200 \text{ meV}/\hbar$, $T_1 = 1 \text{ ps}$, $T_2 = 200 \text{ fs}$, $T_p = 200 \text{ fs}$, $T = 80 \text{ K}$, $E_L = 1.7 \text{ kV m}^{-1}$ and $\mu = 0$. All observables are shown after a steady state is achieved for a tanh-type ramp of the driving field strength.

of the lower band is always larger than the one of the upper band, the net contribution from the Dirac point is always negative. Hence the sign agrees with the one expected in the high-frequency limit, but the magnitude is reduced.

We have noted in the previous section that all resonances give net positive contribution. We show the resulting field-strength dependence of the contributions of different resonances and the Dirac point in Fig. 2.24(a). We see that only the first resonance contributes for electric field strengths smaller than 8 MV m^{-1} . In this regime the conductivity is well described by the Rabi Berry curvature. For low field strengths the gaps at higher-order resonances are still small compared to temperature, damping and dephasing effects, see Fig. 2.24(b). Therefore the lower and upper Floquet bands near the resonance have equal occupation and hence the corresponding contributions to the conductivity cancel due to the opposite sign of the Berry curvature and band velocity. We call these resonance gaps that do not contribute to the conductivity closed.

For field strengths larger than 10 MV m^{-1} the second-order gap starts to open and hence contributes to the conductivity. We expect the conductivity arising from the first resonance to saturate in this regime. We see, however, a reduction in Fig. 2.24(a). This is due to the above mentioned resonance broadening that leads to canceling contributions of the first and second resonance and hence a reduction of the conductivity in the momentum range of the first resonance.

As the second resonance opens we see a further increase of the Hall conductivity. At

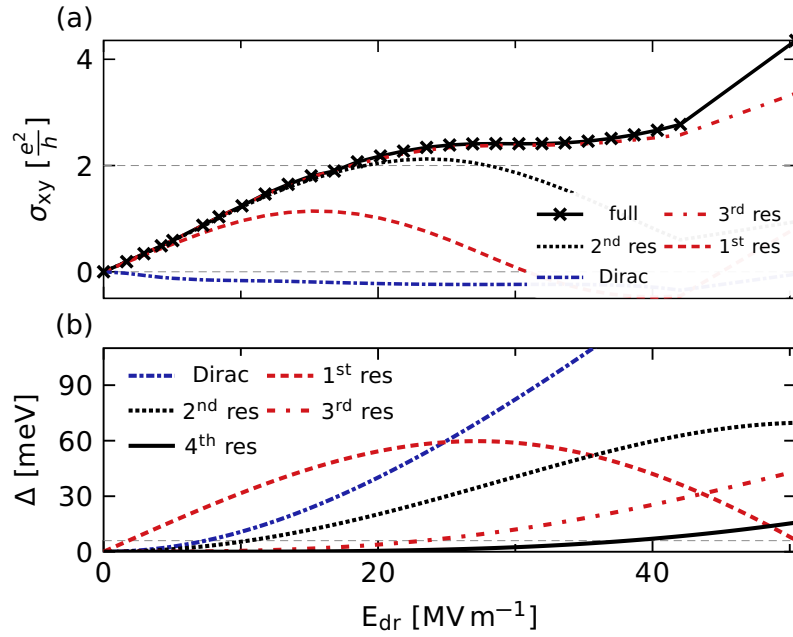


Figure 2.24 – (a) Resonance-resolved conductivity dichroism as a function of electric field strength. The solid black line shows the full conductivity, while the dash-dotted blue line shows the contribution of the Dirac point and other lines show the contributions up to and including the n -th resonance as indicated in the legend. (b) Gap sizes as a function of electric field strength. The dash-dotted blue line shows the gap at the Dirac point, while other lines show the gaps at the n -th resonance as indicated in the legend. The dashed gray line shows the approximate scale of temperature, damping and dephasing effects $k_B T \approx \hbar/T_1 \approx 6$ meV. The parameters used are $\omega_{\text{dr}} = 2\pi \cdot 48$ THz ≈ 200 meV/ \hbar , $T_1 = 1$ ps, $T_2 = 200$ fs, $T_p = 400$ fs, $T = 80$ mK, $E_L = 1.7$ kV m^{-1} and $\mu = 0$. All observables are shown after a steady state is achieved for a tanh-type ramp of the driving field strength. This figure has been published in Ref. [N2].

even higher field strengths, higher-order gaps open subsequently and lead to a series of plateaus and further increasing conductivity. Still, for the field strengths considered, only a small fraction of the total number of resonances contributes to the conductivity. For $E_{\text{dr}} = 26$ MV m^{-1} we find that summing the contribution of the Dirac point and the first 4 resonances accounts for 99.8% of the full Hall conductivity. The net contribution of each resonance is negative and therefore the total resonant contribution is opposite to the high-frequency contribution. Furthermore we find numerically that the magnitude of the high-frequency contribution is usually smaller than the magnitude of the resonant contributions. This is in agreement with the sign of the conductivity of experimental data in Ref. [86].

2.7. Geometric Hall conductivity of the Dirac-point gap

So far we have seen that the transverse Hall conductivity is dominated by resonant contributions and the contribution of the Dirac point is highly suppressed by dissipation in the experimentally realistic regime. Here we are interested in the question under which circumstances the contribution of the Dirac point can become significant. We consider three different regimes: increasing driving frequency, decreasing dissipation and the transient response for short times. We find that for increasing driving frequency the system approaches a high-temperature state with equal occupation in the lower and upper band and hence vanishing Hall conductivity. In contrast, for reduced dissipation and in the transient response the system approaches a regime in which the Dirac-point contribution approaches the value of $\sigma_{xy} = -2e^2/h$, which is expected in the high-frequency limit.

2.7.1. High-frequency limit

We compare the conductivity in a realistic system with the effective high-frequency limit in Fig. 2.25(a). We model the latter with the effective static Hamiltonian from Eq. 2.10. We confirm that the sign of the conductivity is opposite. When increasing the driving frequency we keep the size of the gap at the Dirac point $\Delta_{\text{hf}} \propto E_{\text{dr}}^2/\omega_{\text{dr}}^3$ fixed by simultaneously increasing the electric field strength E_{dr} . This is important in order to ensure that the gap remains open, i.e. large compared to damping and dephasing effects. We see in Fig. 2.25(a) that for the given range of frequencies the system approaches the high-frequency limit for increasing driving frequency.

For larger driving frequency we need to take smaller time steps for our numerical integration routines. Increased field strength additionally leads to current arising from larger momenta and hence an increased window in momentum space that needs to be simulated. Therefore the regime of high electric field strengths and frequencies is numerically challenging and we can not go to higher driving frequency for the full conductivity in Fig. 2.25(a). Instead we focus on the contribution of the Dirac point in Fig. 2.25(b). For $\omega_{\text{dr}} = 2\pi \cdot 50$ THz and $\omega_{\text{dr}} = 2\pi \cdot 100$ THz we still see the onset of the first resonance. For larger driving frequencies the plateau at larger threshold momenta gives the Dirac-point contribution to the conductivity. In the high-frequency limit it is expected to converge towards $-2e^2/h$. Dissipation dramatically changes this result. We observe in Fig. 2.25(b) for increasing driving frequencies that the conductivity reduces to 0 instead. The interplay of driving and dissipation leads to the formation of a high-temperature state with almost equal occupation of the lower and upper graphene band. Since both bands have

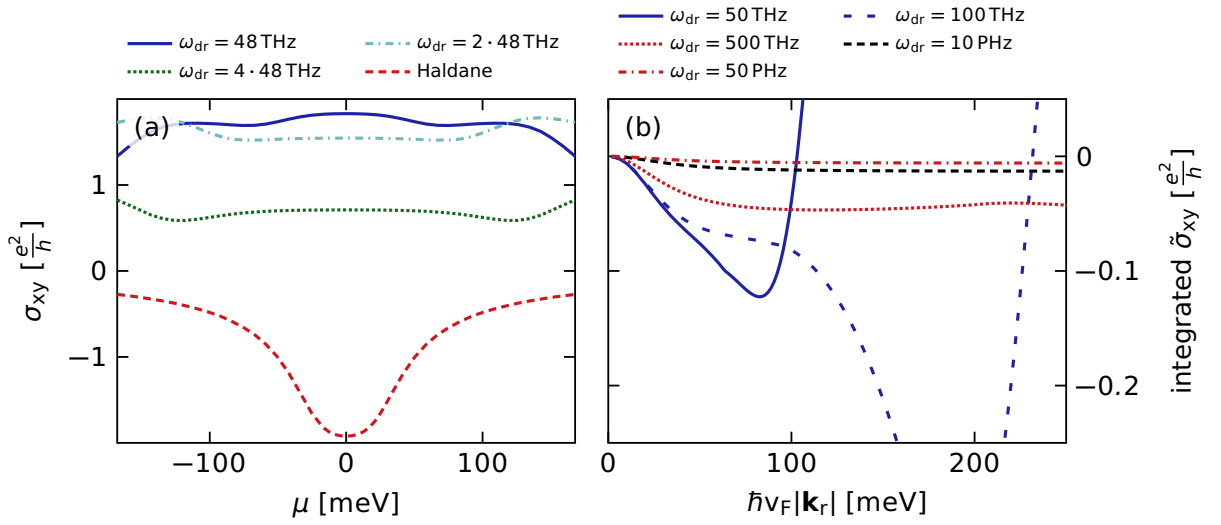


Figure 2.25 – Increasing the driving frequency for fixed Dirac-point gap. We show the circular dichroism of the transverse conductivity. Panel (a) shows the total conductivity as a function of applied chemical potential and panel (b) the conductivity density $\tilde{\sigma}_{xy}$ integrated over all momenta smaller than the threshold value $|\mathbf{k}_r|$. The driving frequencies for both panels are indicated in the legends. The electric field strength is $E_{\text{dr}} = 20 \text{ MV m}^{-1}$ for $\omega_{\text{dr}} = 2\pi \cdot 48 \text{ THz}$ and is adjusted such that $E_{\text{dr}}^2/\omega_{\text{dr}}^3$ — corresponding to the gap in the high-frequency limit — is the same for all choices of ω_{dr} . For comparison we show the conductivity of the effective high-frequency system in (a). The remaining parameters for all panels are $T_1 = 100 \text{ fs}$, $T_2 = 20 \text{ fs}$, $T_p = 25 \text{ fs}$, $T = 80 \text{ K}$ and $E_L = 840 \text{ V m}^{-1}$. All observables are shown after a steady state is achieved for a tanh-type ramp of the driving field strength.

opposite Berry curvature and band velocity the resulting Hall conductivity vanishes.

2.7.2. Geometric Hall conductivity for low dissipation

Next we consider a different route for recovering the geometric Hall conductivity of the Dirac-point gap. Instead of increasing the driving frequency we reduce dissipation. We find for fixed driving frequency that dissipation greatly inhibits the Hall-conductivity contribution of the Dirac-point gap. At the same time the contributions of resonances are enhanced by some dissipation mechanisms. We can identify a regime of low dissipation and intermediate electric field strengths where the Hall-conductivity contribution of the Dirac point approaches $-2e^2/h$.

In this and the following section we switch off the coupling to the back gate ($T_p = \infty$), hence we work at fixed particle number, enforcing unit occupation of each momentum mode. The computations with decoupled back gate are more efficient and hence allow to investigate a wider parameter regime. Apart from being numerically more feasible we have several other reasons motivating the decoupled back gate: experimentally this could

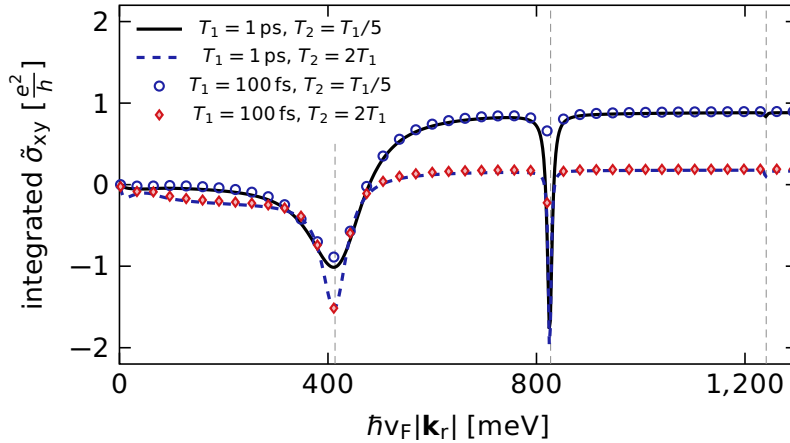


Figure 2.26 – Circular dichroism of the integrated Hall conductivity densities for several different values of the dissipation as indicated in the legend. We show the conductivity density $\tilde{\sigma}_{xy}$ integrated over all momenta smaller than the threshold value $|\mathbf{k}_r|$. The first, second and third resonance are indicated by dashed lines. We use $E_{\text{dr}} = 84 \text{ MV m}^{-1}$, $\omega_{\text{dr}} = 2\pi \cdot 200 \text{ THz}$, $T_p = \infty$, $T = 80 \text{ mK}$, $E_L = 1.7 \text{ kV m}^{-1}$ and $\mu = 0$. All observables are shown after a steady state is achieved for a tanh-type ramp of the driving field strength.

be achieved by using free-standing graphene, i.e. graphene without a substrate. Also we expect that at zero chemical potential the results are qualitatively similar to those with coupled back gate. Finally, it is an interesting question on its own to ask whether decay-type damping inhibits the geometric Hall conductivity of the gap at the Dirac point.

First we focus on the role of dephasing-type damping, i.e. T_2 . In order to resolve the contributions of individual resonances we use larger driving frequency as compared to previous sections. We observe in Fig. 2.26 that the relative scale of T_1 and T_2 crucially influences the Hall-conductivity contributions of the Dirac point and the first resonance. Large dephasing type damping, i.e. small T_2 , suppresses the contribution from the Dirac point, while at the same time enhancing the contribution of the first resonance. Compared to this effect the overall time scale of damping at fixed T_2/T_1 plays a negligible role for $100 \text{ fs} < T_1 < 1 \text{ ps}$. We note that there is an upper bound $T_2/T_1 \leq 2$, since there is a finite amount of dephasing for each decay process. This can also be motivated from Eq. 2.9, where we see, when setting the bare dephasing-type damping $\gamma_z = 0$ to zero, that at low temperature

$$\frac{1}{T_2} = \Gamma = \frac{c_6}{2} \approx \frac{1}{2T_1} \quad .$$

Hence, in order to find a regime where the contribution of the Dirac point to the Hall conductivity becomes large, we consider only cases where $T_2 = 2T_1$. We show the driving-field-strength dependence of the Dirac-point contribution for different T_1 in Fig. 2.27. In

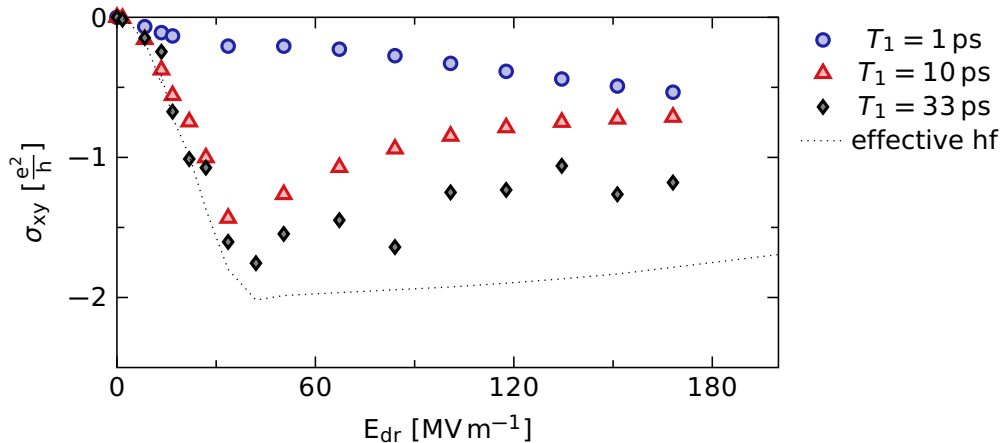


Figure 2.27 – Contribution of the Dirac point to the Hall conductivity dichroism, as defined in Eq. 2.23, for different damping time scales as indicated in the legend. For comparison we show the results for the effective high-frequency limit at $T_1 = 1$ ps (dotted line). We use $\omega_{dr} = 2\pi \cdot 200$ THz, $T_2 = 2T_1$, $T_p = \infty$, $T = 80$ mK, $E_L = 1.7$ kV m $^{-1}$ and $\mu = 0$. All observables are shown after a steady state is achieved for a tanh-type ramp of the driving field strength. The simulations for the low dissipation cases are numerically quite challenging and we expect this to be the origin of the wiggles in the $T_1 = 33$ ps data.

the effective high-frequency limit (modeled by Eq. 2.10) the contribution of the Dirac point to the Hall conductivity is small for low electric field strength, increases to approximately $-2e^2/h$ and then reduces again for even larger field strengths. At low field strength the size of the gap is still small compared to dissipation and temperature and therefore does not contribute to the conductivity. The origin of the reduction for large field strength is the one noted in Sec. 2.6: the conductivity contribution spreads out in momentum space and hence extends beyond the regime that we affiliate with the Dirac point. At intermediate field strengths we find a plateau at $-2e^2/h$ for the effective high-frequency system. We note that the dissipation has only minor influence on the effective high-frequency system, since it is a static system with the chemical potential inside a band gap. For the experimentally realistic system, driven at finite frequency, we see that decay-type damping has strong influence on the Hall conductivity of the Dirac point. For large decay-type damping, i.e. small T_1 , the Dirac-point contribution is reduced significantly. For larger values of T_1 the contribution of the Dirac point agrees with the one computed for the effective high-frequency system for low values of the driving field strength. When further increasing T_1 the range in which the two contributions agree extends to larger and larger field strength. For $T_1 = 33$ ps we nearly recover the quantized value of $-2e^2/h$ at intermediate field strengths. Hence, the Hall-conductivity contribution of the Dirac point converges towards its high-frequency limit when reducing dissipation.

2.7.3. Geometric Hall conductivity in the transient response

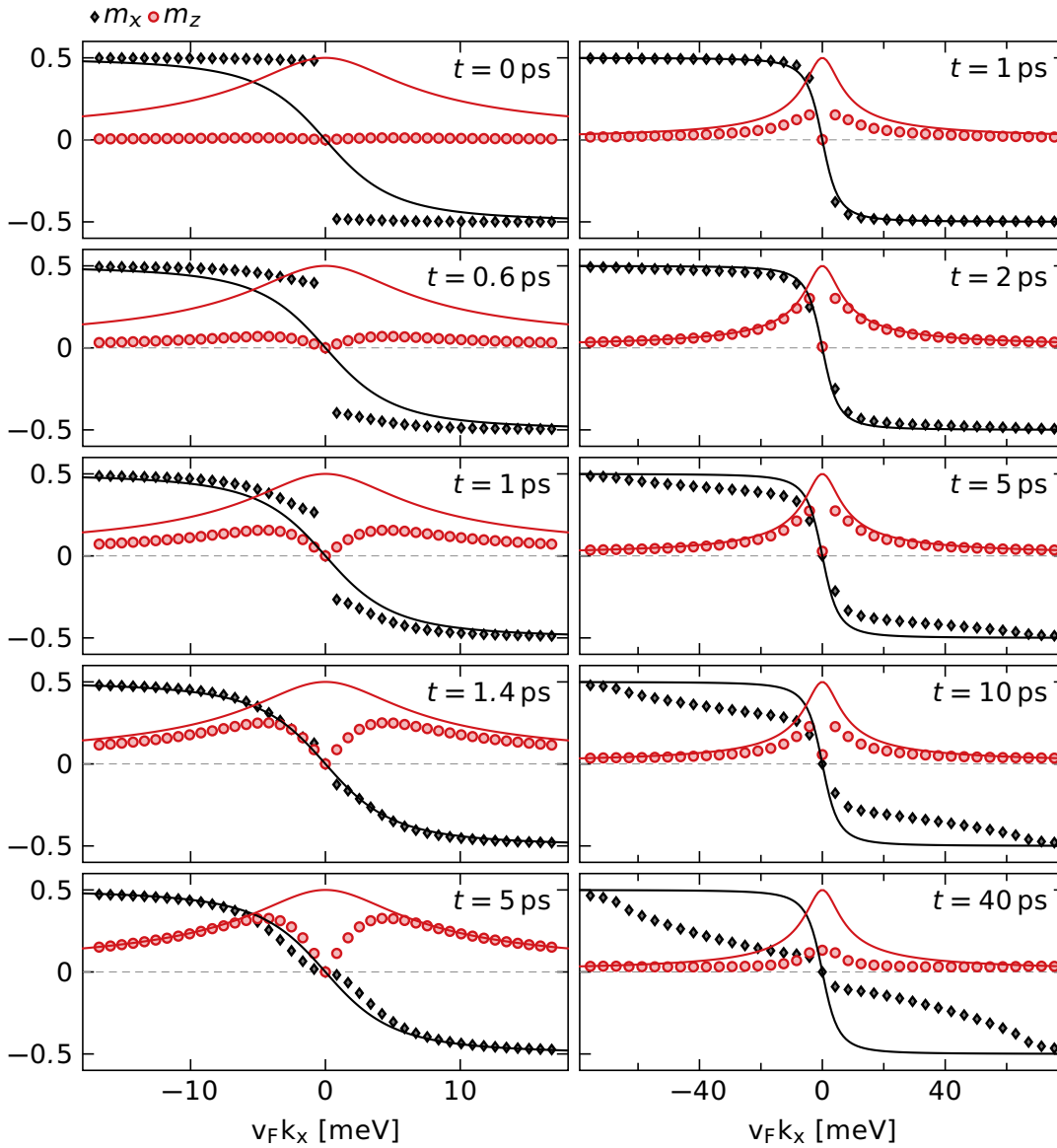


Figure 2.28 – Coefficients of the density matrix for a cut along the k_x -direction at different snapshots in time as indicated in the legend. For comparison we show the ground state of the effective high-frequency system with solid lines. We show m_x by black triangles and m_z by red circles, we do not show m_y since it is negligible along the k_x -direction. The left column shows the undamped system while the right column shows $T_1 = 10$ ps, $T_2 = 2T_1$ and $T_p = \infty$. For all panels $E_{\text{dr}} = 84$ MV m $^{-1}$, $\omega_{\text{dr}} = 2\pi \cdot 200$ THz, $T = 80$ mK, $E_L = 0$ and the envelope of the driving pulse is a tanh-type interpolation from 0 to 1, that reaches 1 after 1 ps.

A second route to increase the contribution of the Dirac point to the Hall conductivity is to look at the transient response before the system equilibrates. We find that in the transient regime the contribution of the Dirac point is approximately $-2e^2/h$ for a wide

range of different damping time scales $T_1 > 1/2$ ps.

In order to get an intuitive understanding of the transient regime we first consider the time evolution of the density matrix without an applied longitudinal field. When decoupling the back gate ($T_p = \infty$) the system has unit filling and hence can be described by a 2×2 density matrix

$$\rho_{\mathbf{k}} = 1/2 + m_x(\mathbf{k})\sigma_x + m_y(\mathbf{k})\sigma_y + m_z(\mathbf{k})\sigma_z \quad .$$

We show the coefficients of the density matrix for a cut along the k_x -direction in Fig. 2.28. We do not show $m_y(\mathbf{k})$ since it is negligible for $k_y = 0$. We first consider the undamped case which is shown in the left column of Fig. 2.28. Initially the density matrix correctly shows the dependence for undriven graphene where $m_x = -k_x/|\mathbf{k}|$ and $m_z = 0$. Subsequently the system evolves towards the ground state of the driven effective high-frequency system shown by solid lines in Fig. 2.28. For large momenta it reaches this value after about 5 ps. Here the quench is adiabatic since the time scale of the quench of about $t_{\text{quench}} = 1$ ps ($\hbar/t_{\text{quench}} \approx 0.7$ meV) is slow compared to the bandwidth of undriven graphene $2\epsilon_{\mathbf{k}} = 2\hbar v_F k$. Directly at the Dirac point the bands of undriven graphene touch and hence the quench can not be adiabatic. The time scale of the quench determines the range around the Dirac point where the quench is nonadiabatic. For longer quench time scales the region where the response deviates from the ground state of the high-frequency system is more confined around the Dirac point. Finite m_z -component around the Dirac point is important for having finite Berry curvature and hence a finite Hall conductivity. With dissipation momentum points that are nonadiabatic may relax towards the ground-state value of the high-frequency system, see right column of Fig. 2.28. At the same time dissipation leads to a reduction of all coefficients of the density matrix. We find that this reduction is stronger for larger dissipation. This overall reduction also reduces the Hall conductivity. In the right column of Fig. 2.28 we consider a regime where the quench duration is faster than the relaxation time scale T_1 . Then there are two different time scales. First the system approaches the ground state of the high-frequency system for all momentum modes that are adiabatic within the first 5 ps. Then on a longer time scale the density matrix components of all momenta approach the steady state which is reached after about 40 ps. At intermediate times the m_z component of the density matrix at the Dirac point has already nonzero value while at the same time the density-matrix components of larger momenta are still close to the effective high-frequency system. This is the regime where we expect the quantized Hall response of the Dirac point.

We show the time-resolved contribution of the Dirac point to the Hall conductivity in Fig. 2.29. The net Hall conductivity is negative for all dissipation strengths and times. We

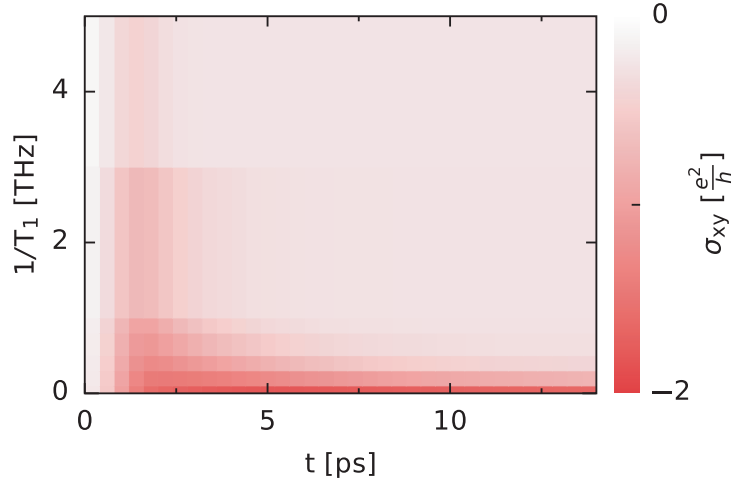


Figure 2.29 – Contribution of the Dirac point to the Hall conductivity dichroism, as defined in Eq. 2.23, as a function of time t and inverse dissipation time $1/T_1$. We use $E_{\text{dr}} = 84 \text{ MV m}^{-1}$, $\omega_{\text{dr}} = 2\pi \cdot 200 \text{ THz}$, $T_2 = 2T_1$, $T_p = \infty$, $T = 80 \text{ mK}$, $E_L = 1.7 \text{ kV m}^{-1}$, $\mu = 0$ and the envelope of the driving pulse is a tanh-type interpolation from 0 to 1, that reaches 1 after 1 ps. Note that the sharp transitions in the plot are a result of using a course grid of times and dissipation strengths.

see that the Hall conductivity reaches the high-frequency value of $-2e^2/h$ in the transient regime for a range of dissipation strengths $T_1 > 1/2 \text{ ps}$. The duration of the plateau where the Hall conductivity is $-2e^2/h$ is longer for small dissipation strength, i.e. larger T_1 .

2.8. Characterization of resonant contributions in the low- and high-frequency limit

So far we have mainly considered a driving regime that is inspired by the experiments in [86]. In this regime one obtains a sizable gap at the Dirac point for experimentally feasible conditions. We have seen that this also shows significant resonant contributions to the Hall conductivity. In order to further characterize these resonant contributions we consider different driving frequencies ω_{dr} at fixed driving-field strength E_{dr} in Fig. 2.30. For larger frequency the main contribution comes from the bare resonances, see Fig. 2.30(e). At low driving field strength the bare resonances overlap significantly and hence are suppressed. In this regime we observe a new resonance at the bare Rabi frequency $eE_{\text{dr}}v_F/\omega_{\text{dr}}$. We give an intuitive explanation of the Rabi resonance by considering the motion of electrons in momentum space. The circularly polarized field moves an electron with momentum \mathbf{k} on a circle with radius $eE_{\text{dr}}v_F/\omega_{\text{dr}}$. Hence electrons with momentum $|\mathbf{k}| > eE_{\text{dr}}v_F/\omega_{\text{dr}}$ do encircle the Dirac point while electrons with $|\mathbf{k}| < eE_{\text{dr}}v_F/\omega_{\text{dr}}$ do not. The motion around the Dirac point leads to an extra Berry phase of π , which reflects itself in a sign change

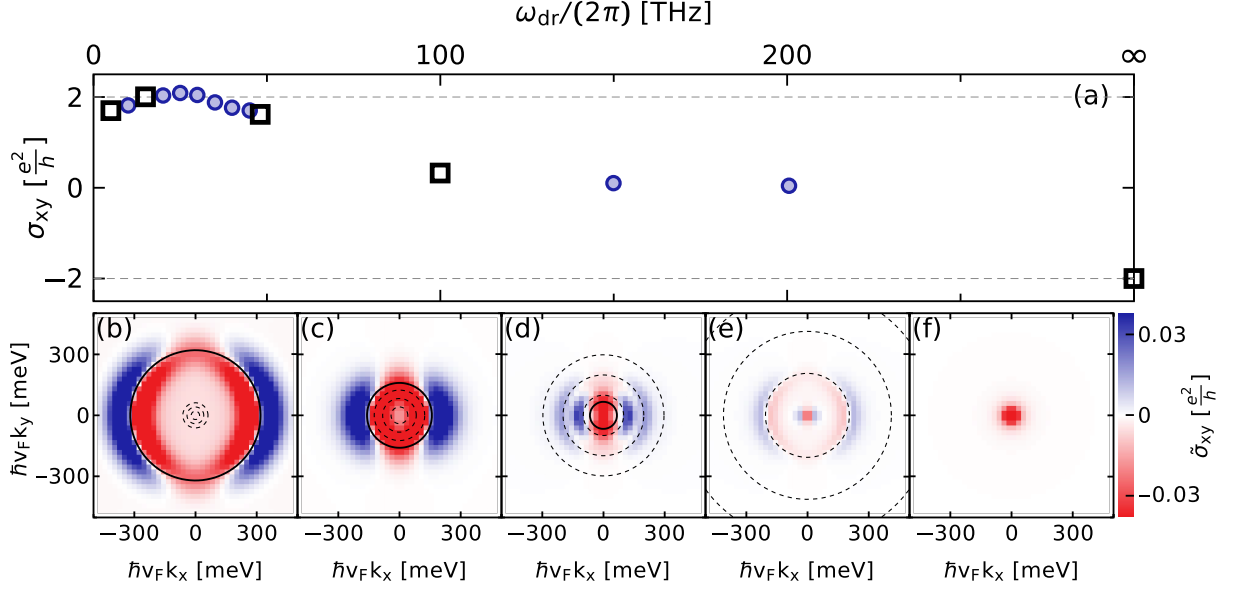


Figure 2.30 – Hall-conductivity dichroism for low- and high-frequency driving. Panel (a) shows the total circular dichroism of the Hall conductivity. Panels (b)-(f) show the momentum-resolved conductivity density for several different driving frequencies, indicated by black squares in panel (a). Dashed circles denote the position of the first three bare resonances $2v_F k = n\omega_{dr}$, $n = 1, 2, 3$ and the solid circle denotes the resonance at the Rabi frequency $v_F k = \Omega_R = ev_F E_{dr}/(\hbar\omega_{dr})$. For panels (b)-(f) we average the conductivity of opposite momentum modes. The corresponding values of the driving frequency $\omega_{dr}/(2\pi)$ are 10 THz (b), 20 THz (c), 48 THz (d) and 100 THz (e). Panel (f) shows the conductivity dichroism for the effective high-frequency Hamiltonian for $E_{\text{eff}}^2 = (\hbar v_F e E_{dr})^2 / (\hbar\omega_{dr})^3 = 22.5 \text{ meV}$. Inspired by Ref. [86] we choose the following parameters for all panels: $E_{dr} = 20 \text{ MV m}^{-1}$, $T_1 = 100 \text{ fs}$, $T_2 = 20 \text{ fs}$, $T_p = 25 \text{ fs}$, $T = 80 \text{ K}$, $\mu = 0$ and $E_L = 840 \text{ V m}^{-1}$. All observables are shown after a steady state is achieved for a tanh-type ramp of the driving field strength.

of the conductivity at the resonance.

In the regime where the conductivity is dominated by the Rabi resonance we observe a plateau of the conductivity at $2e^2/h$. This may be a hint towards an underlying topological origin. We note, however, that also in this regime the occupations of Floquet bands are highly nonequilibrium and therefore we do not expect to see quantized response from the Chern numbers of individual bands. Also we find that the observed value of $2e^2/h$ is not robust with respect to changes in dissipation and the driving field strength.

Finally, we note that the experiments in Ref. [86] are in a regime where the bare Rabi frequency has roughly the same magnitude as the first resonance and therefore the two resonances overlap.

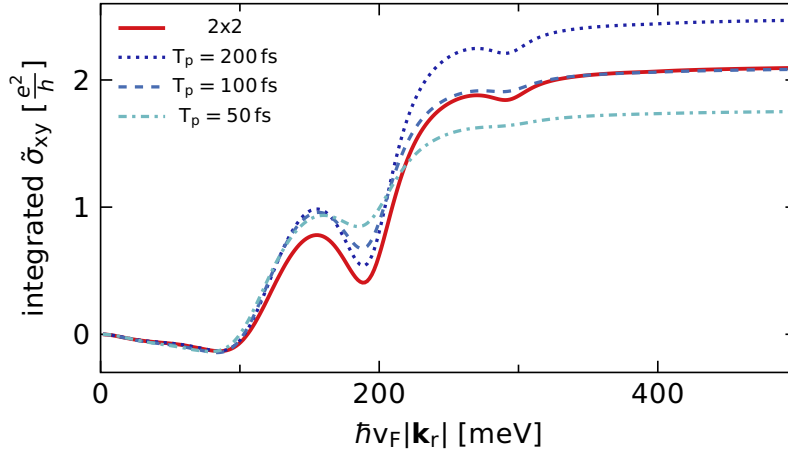


Figure 2.31 – Comparison of the integrated Hall conductivity density for the 2×2 and the 4×4 model for several different values of the timescale for the exchange of particles with the back gate T_p , as indicated in the legend. We show the circular dichroism of the conductivity density $\tilde{\sigma}_{xy}$ integrated over all momenta smaller than the threshold value $|\mathbf{k}_r|$. We use $E_{\text{dr}} = 20 \text{ MV m}^{-1}$, $\omega_{\text{dr}} = 2\pi \cdot 48 \text{ THz}$, $T_1 = 100 \text{ fs}$, $T_2 = 20 \text{ fs}$, $T = 80 \text{ mK}$, $E_L = 8.4 \text{ kV m}^{-1}$ and $\mu = 0$. All observables are shown after a steady state is achieved for a tanh-type ramp of the driving field strength.

2.9. Comparison of the 2×2 and 4×4 model for zero chemical potential

We note that a similar model for the dissipation has been used in Ref. [N5]. The key difference to our model is that Ref. [N5] uses a model based on an effective 2×2 density matrix for each momentum mode, while at the same time dropping the restriction that the density matrix has unit trace. Instead the trace of the density matrix reflects the filling fraction of each momentum mode. This introduces an effective coupling to the back gate and we find that the results are qualitatively similar, see Fig. 2.31. The coupling strength to the back gate can, however, not be tuned independently of T_1 and T_2 . Here we use a more rigorous approach that explicitly includes the empty and the doubly occupied mode in the density matrix. As a result we obtain a 4×4 density matrix for each momentum mode and explicitly introduce a third coupling strength T_p for the exchange of particles with the back gate. As we have seen in Sec. 3.4.1 this third coupling strength is crucial in order to obtain quantitative agreement with experiments. While the comparison to the experimental data showed that a value of $T_p \approx 30 - 50 \text{ fs}$ we find that the effective coupling of the 2×2 model is closer to $T_p \approx 100 \text{ fs}$.

We also show a comparison of the effective 2×2 and 4×4 models at significantly weaker dissipation in order to check how well the results we obtained within the 2×2 model in Secs. 2.7.2 and 2.7.3 hold for the 4×4 model, see Fig. 2.32. We see that finite back gate

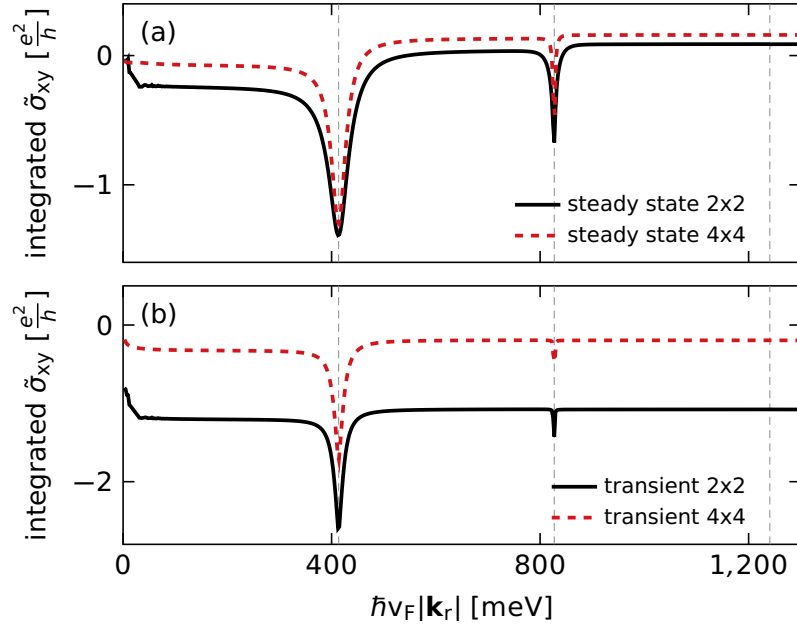


Figure 2.32 – Comparison of the integrated Hall conductivity dichroism for the 2×2 and the 4×4 model for low dissipation. We show the conductivity density $\tilde{\sigma}_{xy}$ integrated over all momenta smaller than the threshold value $|\mathbf{k}_r|$. Panel (a) shows the conductivity after a steady state has been achieved for a tanh-type ramp of the driving field strength, while panel (b) shows the transient response. We use $E_{\text{dr}} = 30 \text{ MV m}^{-1}$, $\omega_{\text{dr}} = 2\pi \cdot 200 \text{ THz}$, $T_1 = 10 \text{ ps}$, $T_2 = 2 \text{ ps}$, $T_p = 4 \text{ ps}$, $T = 80 \text{ mK}$, $E_L = 1.7 \text{ kV m}^{-1}$ and $\mu = 0$.

damping T_p within the 4×4 model significantly reduces the contribution of the Dirac point. While the overall magnitude is reduced the conductivity in the transient regime is still larger than the corresponding steady-state result.

3. Detection of topological Bloch-state defects in ultracold-atom systems¹

As explained in the introduction geometric and topological properties are of major importance for the properties of solids as well as for understanding the underlying principles of fundamental physical phenomena. Ultracold-atom experiments can give deeper insight into the underlying mechanisms of topology and geometry. It is therefore important to develop tools that allow direct access to geometric properties such as Berry curvature and winding numbers. In recent years ultracold atoms in optical lattices have emerged as a versatile model system with tunable topological properties [38]. A range of methods has been developed that allows access to topological and geometric properties such as Berry curvature and winding numbers [84, 85, 117–123]. These methods are, however, either inefficient for covering the full Brillouin zone, cannot resolve the position of the defects, or only work in specific systems such as Floquet systems.

Here we present an alternative method for the detection of topological defects. The method is applicable to an almost arbitrary two-band system², i.e. a system with two lattice sites per unit cell. It allows to map out the azimuthal phase profile of the pseudo-spin texture for all momentum states simultaneously. The azimuthal phase is the relative phase of the eigenstates on the two sublattices. The phase windings of this phase are related to topological defects.

We apply our method to ultracold fermions on the hexagonal lattice, which is the lattice structure for both boron nitride and graphene. The hexagonal lattice features topological defects at the two inequivalent Dirac points. These defects are quantized vortices in the azimuthal phase, see Fig. 3.1(a), and are responsible for the special electronic transport properties of graphene, see [48, 50]. Our method is based on a time-of-flight image after a periodic modulation of the lattice depth, see Fig. 3.2. We show in Sec. 3.1 that a time-of-

¹Parts of this chapter have been published in Ref. [N1].

²It can also be applied to systems where the lowest two bands are well separated from the rest and hence the system can be approximated by only two bands.

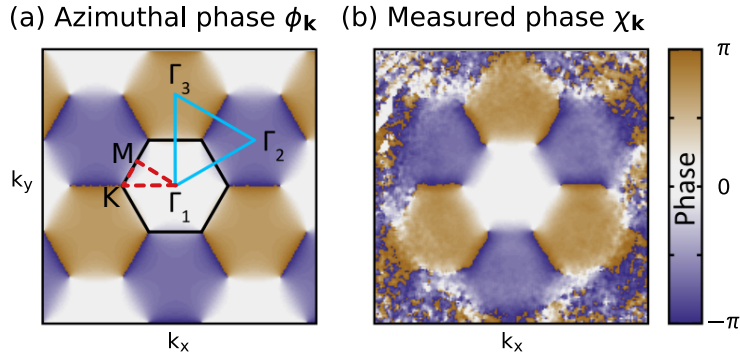


Figure 3.1 – Comparison of the measurement and the theoretical prediction of the azimuthal phase profile. (a) Expected azimuthal phase $\phi_{\mathbf{k}}$ in momentum space. The black hexagon marks the first Brillouin zone and solid blue and dashed red triangles denote high-symmetry paths for later reference. (b) Experimentally obtained phase $\chi_{\mathbf{k}}$. The parameters are $\omega = 2\pi \cdot 5500$ Hz, $J = \hbar \cdot 520$ Hz, $J_{AA} = \hbar \cdot 99$ Hz, $\Delta_{AB} = \hbar \cdot 6056$ Hz, $J_{AA}^{(d)} = 0.3 J_{AA}$, $J^{(d)} = 0.18 J$ and $\Delta_{AB}^{(d)} = 0.22 \Delta_{AB}$. A similar version of this figure has been published in Ref. [N1].

flight image for an unperturbed lattice already contains information about the azimuthal phase for a lattice with two sites per unit cell. By adding the periodic lattice modulation before the time-of-flight image we can disentangle this information from the remaining dependencies on the properties of the lattice. We show in Sec. 3.3 that in this case the time-of-flight density oscillates with the driving frequency for each point in momentum space. The relative momentum-dependent phase of this oscillation is in the red-detuned limit given by

$$\chi_{\mathbf{k}} = \text{Arg} [\cos(\phi_{\mathbf{k}}) + iP_{\mathbf{k}} \sin(\phi_{\mathbf{k}})] \quad , \quad (3.1)$$

where $\text{Arg}(z)$ gives the argument of a complex number z and $P_{\mathbf{k}}$ is a distortion factor given later in Eq. 3.20. For near-resonant driving $P_{\mathbf{k}} \approx 1$ and the two phases $\phi_{\mathbf{k}}$ and $\chi_{\mathbf{k}}$ agree. The experimental measurement for this case is shown in Fig. 3.1(b). It closely resembles the azimuthal phase profile shown in Fig. 3.1(a). A quantitative comparison in Fig. 3.3 shows that the experimental measurement of $\chi_{\mathbf{k}}$, the theoretical prediction for $\chi_{\mathbf{k}}$ and the azimuthal phase $\phi_{\mathbf{k}}$ agree quantitatively. The data is shown along the high-symmetry path that encircles the Dirac point once and indeed all three phases show the correct phase winding of 2π . The nonequivalent second Dirac point has the opposite phase winding. The phase winding of $\pm 2\pi$ gives rise to a Berry phase of $\pm\pi$ when encircling the respective Dirac point.

An application of our method is the measurement of the motion of topological defects when changing the lattice properties. For example the Dirac points in graphene move when changing the relative strength of the nearest-neighbor hopping parameters. In

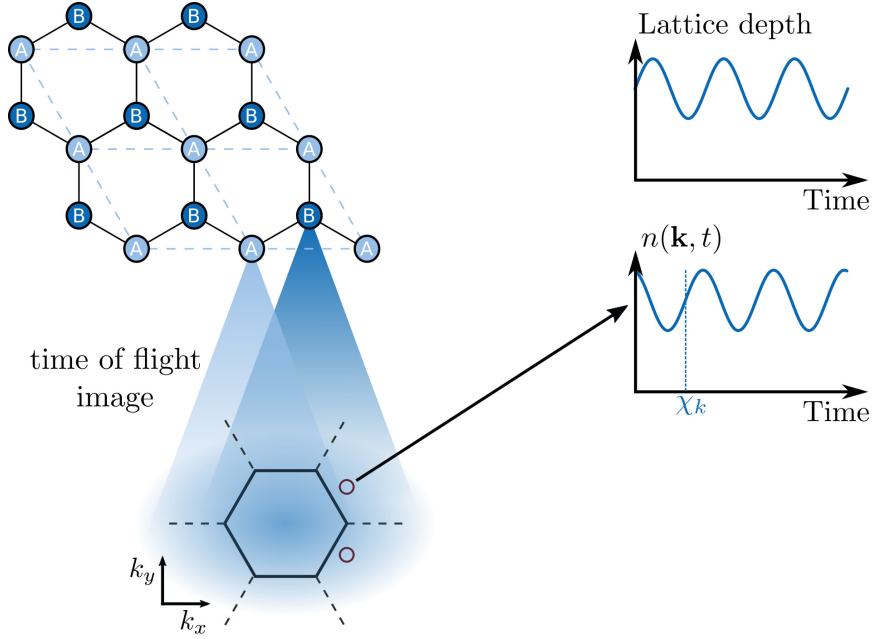


Figure 3.2 – Sketch of our method for measuring the azimuthal phase. We perform a time-of-flight image after a periodic modulation of the lattice depth. The relative phase of the time-of-flight density oscillation and the lattice-depth oscillation is closely related to the azimuthal phase. A similar version of this figure has been published in Ref. [N1].

solid-state graphene minor changes of the nearest-neighbor hopping can be obtained by twisting the lattice. In ultracold atoms tuning the relative intensity of the laser beams can impose a significant imbalance of the nearest-neighbor hopping. For such a scenario the Dirac points move in momentum space until they merge at the M -points of the lattice. Our method has been used to measure this merging transition of the Dirac points in a hexagonal lattice in Ref. [N1].

3.1. Time of flight images

In ultracold-atom experiments time-of-flight images give access to the momentum distribution of the atoms in a lattice. The key idea is that atoms are released from the lattice and freely expand. Except for gravity no forces act on the atoms. Hence, in the directions perpendicular to the gravitational force and for sufficiently long expansion times the position of the atoms is solely determined by their initial momentum. For lattices with a single lattice site per unit cell, time-of-flight images therefore show the momentum distribution of the atoms. For lattices with several sites per unit cell, atoms originating from the different sublattices will interfere. The resulting interference pattern does not only contain information about the momentum distribution of the atoms but also about

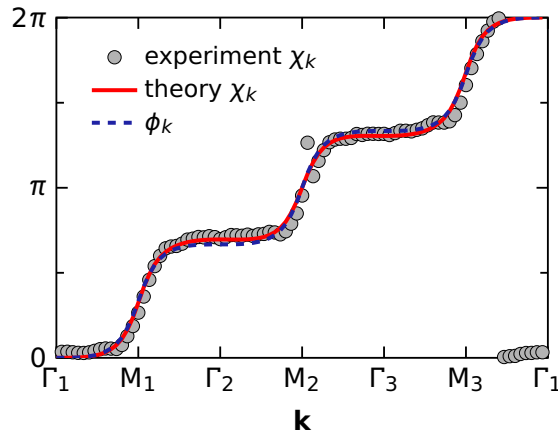


Figure 3.3 – Quantitative comparison of the measurement and the theoretical prediction of the azimuthal phase profile along the high-symmetry paths, see Fig. 3.1(a). We show the experimentally measured phase $\chi_{\mathbf{k}}$, averaged over the three equivalent paths of which only one is shown in Fig. 3.1(a), the theoretical prediction for $\chi_{\mathbf{k}}$, which is based on a perturbative approach as described in Sec. 3.3, and the expected azimuthal phase $\phi_{\mathbf{k}}$. The experimentally measured $\chi_{\mathbf{k}}$ matches well with the theoretical prediction, which we also find for other red-detuned driving frequencies. Furthermore, for the chosen parameters, the difference between $\chi_{\mathbf{k}}$ and $\phi_{\mathbf{k}}$ is experimentally indiscernible. The parameters are the same as in Fig. 3.1. A similar version of this figure has been published in Ref. [N1].

the relative phases of atoms on different sublattices. Here we will focus on the case of two atoms per unit cell and will derive that the time-of-flight density is

$$n(\mathbf{r} = \hbar\tau\mathbf{k}/m) \approx \sum_{CD} \langle c_{\mathbf{k},C}^\dagger c_{\mathbf{k},D} \rangle \quad ,$$

where τ is the expansion time, m is the mass of the atoms, $c_{\mathbf{k},C}^\dagger$ ($c_{\mathbf{k},C}$) creates (annihilates) a particle with momentum \mathbf{k} on the sublattice C and the sum runs over all sublattices.

For completeness we note that there is a second, similar method giving access to the momentum distribution in ultracold-atom systems. It is called band mapping and we will use this technique in chapter 4. In both cases the atoms are released from the lattice and expand freely. The key difference between band mapping and time-of-flight images is the speed for switching off the lattice. For band mapping the lattice is switched off slowly. The slow switch-off allows the eigenstates to adiabatically transform into the eigenstates of free space. Therefore atoms occupying the individual bands of the lattice will be mapped onto the corresponding Brillouin zones [146, 181–185]. For a time-of-flight image the lattice is rapidly switched off instead. This leads to an interference pattern containing information about the phases of atoms on different sublattices. As we will see this interference pattern is periodically repeating with a Gaussian envelope.

We first consider a time-of-flight image with a single lattice site per unit cell in two dimensions. The atoms localized at the individual lattice sites are well described by the corresponding Wannier wave functions. We approximate the Wannier wave functions by a Gaussian wave packet in two dimensions. By solving the Schrödinger equation in free space we obtain the time dependence for the expansion of each individual Wannier function

$$w(\mathbf{r}, \tau) = \frac{d}{\sqrt{2\pi}|\Delta(\tau)|} \exp\left(-\frac{\mathbf{r}^2}{4\Delta^2(\tau)}\right) \quad (3.2)$$

$$\Delta^2(\tau) \approx d^2 + i\tau\hbar/(2m) \quad , \quad (3.3)$$

where d is the initial width of the wave function. The density measured in a time-of-flight experiment is then given by

$$n(\mathbf{r}, \tau) = \sum_{nm} w^*(\mathbf{r} - \mathbf{r}_m, \tau) w(\mathbf{r} - \mathbf{r}_n, \tau) \langle c_m^\dagger c_n \rangle \quad , \quad (3.4)$$

where \mathbf{r}_n are the positions of the lattice sites, c_n^\dagger (c_n) creates (annihilates) an atom on site n and the sum runs over all lattice sites. We use the so-called far-field approximation, assuming that the cloud of atoms has expanded much further than all initial positions of the atoms $\mathbf{r} \gg \mathbf{r}_n$ and that the expansion time is much longer than the initial width of the Wannier wave functions $\frac{\hbar\tau}{2m} \gg d^2$. Inserting Eq. 3.2 into Eq. 3.4, making the far-field approximation and Fourier transforming to momentum space we obtain

$$n(\mathbf{r}, \tau) = \frac{d^2}{2\pi \left[d^4 + \left(\frac{\tau\hbar}{2m} \right)^2 \right]} \frac{1}{M} \sum_{nmk} e^{-\left(\frac{m\mathbf{d}\mathbf{r}}{\hbar\tau} \right)^2} e^{i(\mathbf{k} - \frac{m\mathbf{r}}{\hbar\tau})(\mathbf{r}_m - \mathbf{r}_n)} \langle c_k^\dagger c_k \rangle \quad , \quad (3.5)$$

where M is the total number of unit cells. Hence we identify $\mathbf{k} \sim \frac{m\mathbf{r}}{\hbar\tau}$ and up to a Wannier envelope the time-of-flight signal indeed shows the momentum distribution of the atoms

$$n(\mathbf{r} = \hbar\tau\mathbf{k}/m) \approx \langle c_k^\dagger c_k \rangle \quad .$$

Outside the first Brillouin zone the distribution repeats periodically except for the overall Gaussian envelope $e^{-\left(\frac{m\mathbf{d}\mathbf{r}}{\hbar\tau} \right)^2}$.

For a lattice with several sites per unit cell the expression for the time-of-flight density is slightly altered

$$n(\mathbf{r}, \tau) = \sum_{nmCD} w^*(\mathbf{r} - \mathbf{r}_n - \delta_C, \tau) w(\mathbf{r} - \mathbf{r}_m - \delta_D, \tau) \langle c_{n,C}^\dagger c_{m,D} \rangle \quad ,$$

where δ_C is the vector pointing from the origin of the unit cell³ to the position of the corresponding sublattice site C within that unit cell. Again we employ the far-field limit and obtain

$$= \frac{d^2}{2\pi \left[d^4 + \left(\frac{\tau\hbar}{2m} \right)^2 \right]} \frac{1}{M} \sum_{nmkCD} e^{-\left(\frac{m\mathbf{d}\mathbf{r}}{\hbar\tau} \right)^2} e^{i(\mathbf{k} - \frac{m\mathbf{r}}{\hbar\tau})(\mathbf{r}_m + \delta_D - \mathbf{r}_n - \delta_C)} \langle c_{\mathbf{k},C}^\dagger c_{\mathbf{k},D} \rangle \quad .$$

Upon identification of $\mathbf{k} \sim m\mathbf{r}/(\hbar\tau)$ we obtain

$$n(\mathbf{r} = \hbar\tau\mathbf{k}/m) \approx \sum_{CD} \langle c_{\mathbf{k},C}^\dagger c_{\mathbf{k},D} \rangle \quad . \quad (3.6)$$

We see that not only the occupations $\langle c_{\mathbf{k},C}^\dagger c_{\mathbf{k},C} \rangle$, but also the correlations between different lattice sites $\langle c_{\mathbf{k},C}^\dagger c_{\mathbf{k},D} \rangle$ for $C \neq D$ enter the time-of-flight expression.

As an example we consider an arbitrary lattice with two lattice sites per unit cell. We use the same convenient notation as in Sec. 2.2.1, Eq. 2.12

$$h_{\mathbf{k}} = d_0 \mathbb{1} + d_{\mathbf{k},x} \sigma_x + d_{\mathbf{k},y} \sigma_y + d_{\mathbf{k},z} \sigma_z \quad .$$

It is then convenient to write the vector $\mathbf{d} = (d_{\mathbf{k},x}, d_{\mathbf{k},y}, d_{\mathbf{k},z})$ in spherical coordinates

$$\begin{aligned} d_{\mathbf{k},x} &= R_{\mathbf{k}} \sin(\theta_{\mathbf{k}}) \cos(\phi_{\mathbf{k}}) \\ d_{\mathbf{k},y} &= R_{\mathbf{k}} \sin(\theta_{\mathbf{k}}) \sin(\phi_{\mathbf{k}}) \\ d_{\mathbf{k},z} &= R_{\mathbf{k}} \cos(\theta_{\mathbf{k}}) \\ R_{\mathbf{k}} &= \sqrt{d_{\mathbf{k},x}^2 + d_{\mathbf{k},y}^2 + d_{\mathbf{k},z}^2} \quad . \end{aligned}$$

The creation and annihilation operators diagonalizing H are then

$$\begin{pmatrix} c_{\mathbf{k},+} \\ c_{\mathbf{k},-} \end{pmatrix} = \begin{pmatrix} \cos(\theta_{\mathbf{k}}/2) & \sin(\theta_{\mathbf{k}}/2)e^{-i\phi_{\mathbf{k}}} \\ -\sin(\theta_{\mathbf{k}}/2)e^{i\phi_{\mathbf{k}}} & \cos(\theta_{\mathbf{k}}/2) \end{pmatrix} \begin{pmatrix} c_{\mathbf{k},A} \\ c_{\mathbf{k},B} \end{pmatrix} \quad (3.7)$$

and Eq. 3.6 becomes

$$n(\mathbf{r} = \hbar\tau\mathbf{k}/m) \approx A_{\mathbf{k},+} n_{\mathbf{k},+} + A_{\mathbf{k},-} n_{\mathbf{k},-} + \text{Re} \left[B_{\mathbf{k}} \langle c_{\mathbf{k},+}^\dagger c_{\mathbf{k},-} \rangle \right] \quad , \quad (3.8)$$

where $n_{\mathbf{k},C} = \langle c_{\mathbf{k},C}^\dagger c_{\mathbf{k},C} \rangle$ for $C \in \{A, B, +, -\}$. The prefactors

$$A_{\mathbf{k},\pm} = 1 \mp \cos \phi_{\mathbf{k}} \sin \theta_{\mathbf{k}} \quad (3.9)$$

³We can choose an arbitrary point as the origin of the unit cell, as long as we choose it consistent among all unit cells.

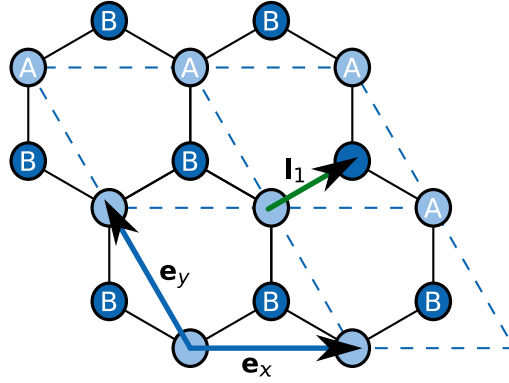


Figure 3.4 – Sketch of the hexagonal lattice with unit vectors $\mathbf{e}_x = (d, 0)^T$ and \mathbf{e}_y and lattice constant d . Solid black lines show the hexagonal lattice of Wigner-Seitz unit cells. The dashed blue parallelograms show an equivalent lattice spanned by \mathbf{e}_x and \mathbf{e}_y . Both lattices contain two sites, A and B , per unit cell, which are connected by the vector \mathbf{l}_1 . This figure has been published in the Supplemental Material to Ref. [N1].

$$\text{and } B_{\mathbf{k}} = \cos(\theta_{\mathbf{k}}) \cos(\phi_{\mathbf{k}}) + i \sin(\phi_{\mathbf{k}}) \quad (3.10)$$

contain information about the azimuthal phase $\phi_{\mathbf{k}}$ and the mixing phase $\theta_{\mathbf{k}}$ which, however, cannot be disentangled by a single measurement of the density. We will see that it is possible to get access to the azimuthal phase by additionally applying a periodic lattice modulation.

3.2. The hexagonal lattice: transition from graphene to boron-nitride

Our goal for Secs. 3.2 and 3.3 is to detect the azimuthal phase $\phi_{\mathbf{k}}$ of the eigenstates in a hexagonal lattice by a lattice modulation. In this section we introduce the Hamiltonian of the undriven system, its diagonalization and how we couple to the lattice modulation.

3.2.1. Undriven properties⁴

Here we use a slightly different tight-binding Hamiltonian than in Sec. 2.1.1 as we include next-nearest-neighbor hopping and a potential offset between the A and the B sites

$$H_{\text{init}} = H_J + H_{\Delta}$$

⁴Significant parts of this section have been published in the Supplemental Material to Ref. [N1]. The corresponding section in the Supplemental Material to Ref. [N1] has mainly been written by the author of this thesis.

$$\begin{aligned}
 H_J &= -J \sum_{\langle \mathbf{n}x, \mathbf{m}y \rangle_n} c_{\mathbf{n},x}^\dagger c_{\mathbf{m},y} + J_{AA} \sum_{\langle \mathbf{n}A, \mathbf{m}A \rangle_{nn}} c_{\mathbf{n},A}^\dagger c_{\mathbf{m},A} \\
 H_\Delta &= \Delta_{AB}/2 \sum_{\mathbf{n}} c_{\mathbf{n},A}^\dagger c_{\mathbf{n},A} - c_{\mathbf{n},B}^\dagger c_{\mathbf{n},B} \quad ,
 \end{aligned}$$

where $c_{\mathbf{n},x}$ annihilates a particle in the \mathbf{n} -th unit cell at the sublattice site $x = A, B$ and obeys the anti-commutator $\{c_{\mathbf{n},x}^\dagger, c_{\mathbf{m},y}\} = \delta_{\mathbf{nm}}\delta_{xy}$ for $x = A, B$. The Hamiltonian has two contributions: the hopping part H_J with nearest- and next-nearest-neighbor hopping J and J_{AA} and the potential-offset part H_Δ with Δ_{AB} being the energy offset between the A and B sublattice sites. The next-nearest-neighbor hopping between the B sublattice sites J_{BB} is negligible for $\Delta_{AB} \ll J$. Finally, $\langle \mathbf{n}x, \mathbf{m}y \rangle_n$ denotes the sum over nearest neighbors and $\langle \mathbf{n}A, \mathbf{m}A \rangle_{nn}$ the sum over next-nearest neighbors.

In the remaining part of this chapter we present the diagonalization of the Hamiltonian. In a first step we block-diagonalize the Hamiltonian by introducing the quasi-momentum operators $c_{\mathbf{k},x} = \frac{1}{\sqrt{M}} \sum_n e^{-i\mathbf{k}(\mathbf{n}+\delta_x)} c_{\mathbf{n},x}$. Here, $\delta_A = 0$ and $\delta_B = \mathbf{1}_1$, $\mathbf{1}_1$ is defined in Fig. 3.4 and M is the number of unit cells. With these definitions the Hamiltonian in momentum space is

$$H_{\text{init}} = \sum_{\mathbf{k}} \begin{pmatrix} c_{\mathbf{k},A}^\dagger & c_{\mathbf{k},B}^\dagger \end{pmatrix} \begin{pmatrix} \Delta_{AB}/2 + 2J_{AA}g_{\mathbf{k}} & -Jf_{\mathbf{k}}^* \\ -Jf_{\mathbf{k}} & -\Delta_{AB}/2 \end{pmatrix} \begin{pmatrix} c_{\mathbf{k},A} \\ c_{\mathbf{k},B} \end{pmatrix} , \quad (3.11)$$

where

$$\begin{aligned}
 f_{\mathbf{k}} &= e^{-i\mathbf{k}\mathbf{1}_1} (1 + e^{i\mathbf{k}\mathbf{e}_x} + e^{i\mathbf{k}(\mathbf{e}_x + \mathbf{e}_y)}) \\
 g_{\mathbf{k}} &= (\cos(\mathbf{k}\mathbf{e}_x) + \cos(\mathbf{k}\mathbf{e}_y) + \cos(\mathbf{k}(\mathbf{e}_x + \mathbf{e}_y)))
 \end{aligned}$$

and the basis vectors \mathbf{e}_x and \mathbf{e}_y are defined in Fig. 3.4. We now define

$$\begin{aligned}
 \theta_{\mathbf{k}} &= 2 \arccos \left[\frac{|Jf_{\mathbf{k}}|}{\sqrt{(\epsilon_{\mathbf{k}} - \Delta_{AB}/2 - J_{AA}g_{\mathbf{k}})^2 + |Jf_{\mathbf{k}}|^2}} \right] \\
 \epsilon_{\mathbf{k}} &= \sqrt{(\Delta_{AB}/2 + J_{AA}g_{\mathbf{k}})^2 + |Jf_{\mathbf{k}}|^2}
 \end{aligned}$$

and $\phi_{\mathbf{k}}$ is the complex phase of $f_{\mathbf{k}}$. Using these definitions the Hamiltonian in momentum space can be rewritten as

$$H_{\text{tb},\mathbf{k}} = \epsilon_{\mathbf{k}} \begin{pmatrix} c_{\mathbf{k},A}^\dagger & c_{\mathbf{k},B}^\dagger \end{pmatrix} \begin{pmatrix} \cos(\theta_{\mathbf{k}}) + J_{AA}g_{\mathbf{k}} & \sin(\theta_{\mathbf{k}})e^{-i\phi_{\mathbf{k}}} \\ \sin(\theta_{\mathbf{k}})e^{i\phi_{\mathbf{k}}} & -\cos(\theta_{\mathbf{k}}) + J_{AA}g_{\mathbf{k}} \end{pmatrix} \begin{pmatrix} c_{\mathbf{k},A} \\ c_{\mathbf{k},B} \end{pmatrix} \quad (3.12)$$

and is then diagonalized by the transformation defined in Eq. 3.7. The eigenenergies are

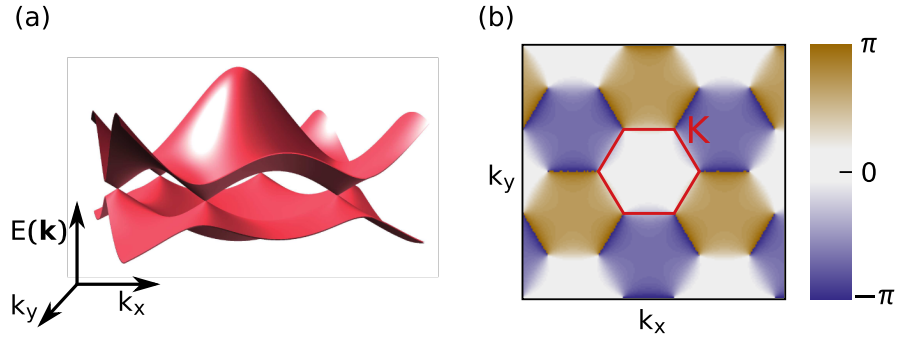


Figure 3.5 – Sketch of the graphene band structure (a) and the corresponding azimuthal phase profile (b).

given by

$$E_{\mathbf{k},\pm} = J_{AA}g_{\mathbf{k}} \pm \epsilon_{\mathbf{k}} \quad .$$

The Hamiltonian in Eq. 3.11 is a tight-binding model of a hexagonal lattice. For graphene there is no imbalance between the A and the B sublattice and hence $\Delta_{AB} = 0$. The corresponding band structure is shown in Fig. 3.5(a). Boron nitride does have a finite sublattice imbalance $\Delta_{AB} > 0$. This leads to a gapped band structure as shown in Fig. 3.6(a). The sublattice imbalance can be tuned in ultracold-atom systems and hence both cases can be realized. Note that for any sublattice imbalance the phase structure of the azimuthal phase will be the same. This can be exemplarily seen by comparing Figs. 3.5(b) and 3.6(b).

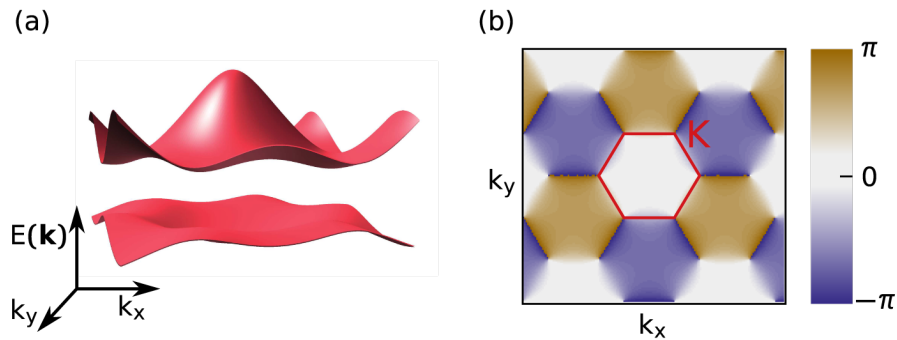


Figure 3.6 – Sketch of the boron-nitride band structure (a) and the corresponding azimuthal phase profile (b).

3.2.2. Applying a lattice modulation⁵

In addition to the initial Hamiltonian we now apply a periodic lattice modulation which can be represented by making all tight-binding parameters time dependent

$$\begin{aligned} J &\rightarrow J + J^{(d)} \sin(\omega t) \\ J_{AA} &\rightarrow J_{AA} + J_{AA}^{(d)} \sin(\omega t) \\ \Delta_{AB} &\rightarrow \Delta_{AB} + \Delta_{AB}^{(d)} \sin(\omega t) \quad . \end{aligned}$$

The lattice modulation is such that the lattice imbalance Δ_{AB} is modulated out of phase with respect to the tunneling strengths J and J_{AA} ($\Delta_{AB}^{(d)} < 0$). We write the full Hamiltonian in the basis that diagonalizes the initial Hamiltonian

$$H = \begin{pmatrix} c_{\mathbf{k},+}^\dagger & c_{\mathbf{k},-}^\dagger \end{pmatrix} (H_{\text{init}} + H_{\text{d}}) \begin{pmatrix} c_{\mathbf{k},+} \\ c_{\mathbf{k},-} \end{pmatrix} \quad (3.13)$$

$$H_{\text{init}} = \begin{pmatrix} E_{\mathbf{k},+} & 0 \\ 0 & E_{\mathbf{k},-} \end{pmatrix} \quad (3.14)$$

$$H_{\text{d}} = \sin(\omega t) \begin{pmatrix} E_{\mathbf{k},+}^{(d)} & E_{\mathbf{k}}^{(d)} \\ E_{\mathbf{k}}^{(d)} & E_{\mathbf{k},-}^{(d)} \end{pmatrix} \quad . \quad (3.15)$$

For the Hamiltonian from Eq. 3.11 we obtain

$$\begin{aligned} E_{\mathbf{k},\pm}^{(d)} &= J_{AA}^{(d)} g_{\mathbf{k}} \pm \frac{J J^{(d)} |f_{\mathbf{k}}|^2 + \left(\frac{\Delta_{AB}}{2} + J_{AA} g_{\mathbf{k}}\right) \left(\frac{\Delta_{AB}^{(d)}}{2} + J_{AA}^{(d)} g_{\mathbf{k}}\right)}{\epsilon_{\mathbf{k}}} \\ E_{\mathbf{k}}^{(d)} &= \frac{J |f_{\mathbf{k}}| \left(\frac{\Delta_{AB}^{(d)}}{2} + J_{AA}^{(d)} g_{\mathbf{k}}\right) - J^{(d)} |f_{\mathbf{k}}| \left(\frac{\Delta_{AB}}{2} + J_{AA} g_{\mathbf{k}}\right)}{\epsilon_{\mathbf{k}}} \quad . \end{aligned}$$

3.3. Time-of-flight expression for a periodic lattice modulation in perturbation theory⁶

We have seen in Sec. 3.1 that a time-of-flight image for a lattice with two sites per unit cell does already contain information about the azimuthal phase $\phi_{\mathbf{k}}$, see Eq. 3.8. This information is, however, not directly accessible since there is an additional unknown phase $\theta_{\mathbf{k}}$. In order to disentangle this information we now apply a periodic lattice modulation. The

⁵This section has been published in the Supplemental Material to Ref. [N1]. The corresponding section in the Supplemental Material to Ref. [N1] has mainly been written by the author of this thesis.

⁶Parts of this section have been published in the Supplemental Material to Ref. [N1]. The corresponding section in the Supplemental Material to Ref. [N1] has mainly been written by the author of this thesis.

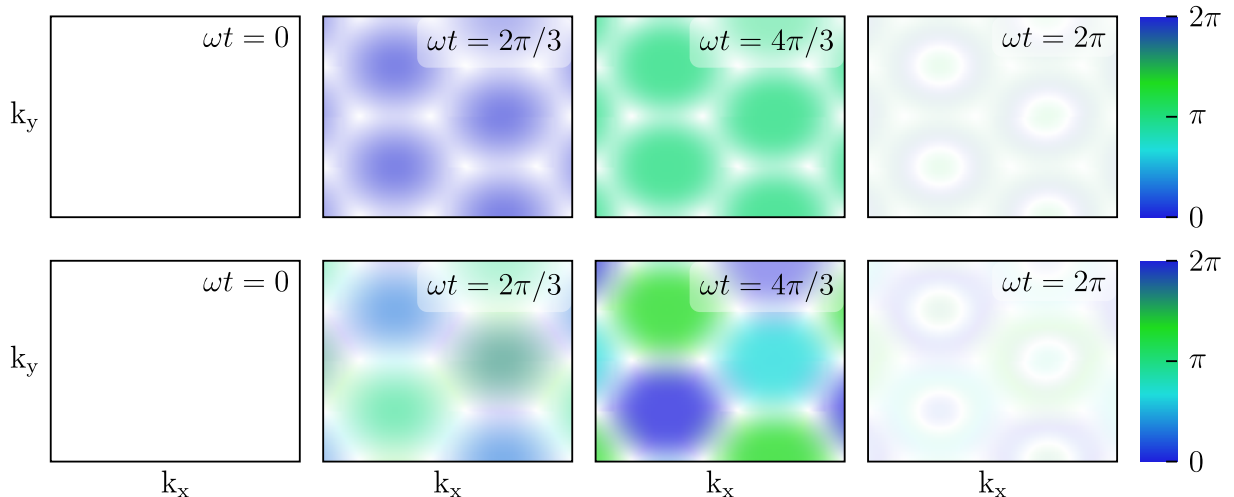


Figure 3.7 – We sketch $\langle c_{\mathbf{k},+}^\dagger(t)c_{\mathbf{k},-}(t) \rangle$ in the top row and $B_{\mathbf{k}}\langle c_{\mathbf{k},+}^\dagger(t)c_{\mathbf{k},-}(t) \rangle$ in the bottom row as a function of momentum. The intensity of the color shows the amplitude and the color the phase of the oscillation. The amplitude of the oscillation vanishes at the edge of the Brillouin zone. Hence white hexagons indicate the repetition of the Brillouin zone. Different columns show different snapshots in time as indicated in the panels. While $\langle c_{\mathbf{k},+}^\dagger(t)c_{\mathbf{k},-}(t) \rangle$ oscillates in phase with the frequency of the lattice modulation, the quantity $B_{\mathbf{k}}$ imprints the azimuthal phase onto that oscillation.

idea is the following: we employ a periodic lattice modulation such that the correlation $\langle c_{\mathbf{k},+}^\dagger(t)c_{\mathbf{k},-}(t) \rangle$ obtains a periodic phase modulation, see top row in Fig. 3.7. The quantity $B_{\mathbf{k}}$ in the coherence part of the unperturbed time-of-flight density, see Eq. 3.10, already contains information about $\phi_{\mathbf{k}}$. In fact, the phase of $B_{\mathbf{k}}$ is closely related to $\phi_{\mathbf{k}}$. This phase information is revealed by the periodic oscillation of $\langle c_{\mathbf{k},+}^\dagger(t)c_{\mathbf{k},-}(t) \rangle$ as is shown in the bottom row of Fig. 3.7. For a more thorough derivation of this fact we employ perturbation theory.

We assume that the corrections to the initial Hamiltonian are small and apply time-dependent perturbation theory in the Heisenberg picture. For an uncorrelated initial state, i.e. $\langle c_{\mathbf{k},+}^\dagger c_{\mathbf{k},-} \rangle = 0$, we obtain to first order in the perturbation Hamiltonian for the expectation values of the time evolved operators

$$\begin{aligned} \langle c_{\mathbf{k},+}^\dagger(t)c_{\mathbf{k},+}(t) \rangle &\approx n_{\mathbf{k},+} \\ \langle c_{\mathbf{k},-}^\dagger(t)c_{\mathbf{k},-}(t) \rangle &\approx n_{\mathbf{k},-} \end{aligned}$$

$$\langle c_{\mathbf{k},+}^\dagger(t)c_{\mathbf{k},-}(t) \rangle \approx \frac{E_{\mathbf{k}}^{(d)}}{4\epsilon_{\mathbf{k}}^2 - \omega^2} \times \left[2\epsilon_{\mathbf{k}} \sin(\omega t) - i\omega \cos(\omega t) + i\omega e^{2i\epsilon_{\mathbf{k}}t} \right] (n_{\mathbf{k},+} - n_{\mathbf{k},-}) \quad .^7$$

We now replace the second-quantization operators in Eq. 3.8 by the corresponding time-dependent operators and insert the results from perturbation theory. A short calculation shows that

$$n_{\text{TOF}}(\mathbf{k}, t) = n_{\text{eq},\mathbf{k}} - \delta n_{\mathbf{k}} \sin(\omega t + \chi_{\mathbf{k}}) - \delta \tilde{n}_{\mathbf{k}} \sin(2\epsilon_{\mathbf{k}}t + \xi_{\mathbf{k}}) \quad , \quad (3.16)$$

where

$$\chi_{\mathbf{k}} = \text{Arg} [\cos(\phi_{\mathbf{k}}) + iP_{\mathbf{k}} \sin(\phi_{\mathbf{k}})] + \text{Arg} [D_{\mathbf{k}}] \quad (3.17)$$

$$n_{\text{eq},\mathbf{k}} = n_{\mathbf{k},+} + n_{\mathbf{k},-} + \sin(\theta_{\mathbf{k}}) \cos(\phi_{\mathbf{k}}) (n_{\mathbf{k},+} - n_{\mathbf{k},-}) \quad (3.18)$$

$$\delta n_{\mathbf{k}} = \left| D_{\mathbf{k}} \sqrt{4\epsilon_{\mathbf{k}}^2 \cos^2(\theta_{\mathbf{k}}) \cos^2(\phi_{\mathbf{k}}) + \omega^2 \sin^2(\phi_{\mathbf{k}})} \right| \quad (3.19)$$

$$P_{\mathbf{k}} = \frac{\omega}{2\epsilon_{\mathbf{k}} \cos(\theta_{\mathbf{k}})} \quad (3.20)$$

$$D_{\mathbf{k}} = \frac{2E_{\mathbf{k}}^{(d)}}{4\epsilon_{\mathbf{k}}^2 - \omega^2} (n_{\mathbf{k},-} - n_{\mathbf{k},+}) \quad (3.21)$$

$$\delta \tilde{n}_{\mathbf{k}} = |F_{\mathbf{k}}| \quad (3.22)$$

$$\xi_{\mathbf{k}} = \text{Arg}[F_{\mathbf{k}}] \quad (3.23)$$

$$F_{\mathbf{k}} = -\omega D_{\mathbf{k}} [\cos(\theta_{\mathbf{k}}) \cos(\phi_{\mathbf{k}}) + i \sin(\phi_{\mathbf{k}})] \quad . \quad (3.24)$$

The above equations are valid for an almost arbitrary Hamiltonian⁸ with two lattice sites per unit cell that is diagonalized by Eq. 3.7. For any such Hamiltonian the measured phase χ_k is closely related to the azimuthal phase ϕ_k and in particular the two phases have the same winding number, see Fig. 3.8. We will explain the different driving regimes in more detail in Sec. 3.4.2.

⁷All calculations in this section have been performed by the author of this thesis. Still we note that these perturbation theory expressions have been obtained before as part of Ref. [186].

⁸While the equations presented in this chapter are valid for an almost arbitrary Hamiltonian, we note that for the Hamiltonian from Eq. 3.13 a finite offset Δ_{AB} is always required. In this case we can compute $\cos(\theta_{\mathbf{k}}) = (\Delta_{AB}/2 + J_{AA}g_{\mathbf{k}})/\epsilon_{\mathbf{k}}$ and therefore $P_{\mathbf{k}} = \omega / (\Delta_{AB} + 2J_{AA}g_{\mathbf{k}})$. A finite offset is required, as otherwise the next-nearest-neighbor hopping between the B -sites J_{BB} is equal to J_{AA} and hence can not be neglected. This leads to a modified driving Hamiltonian and the driving amplitude $E_{\mathbf{k}}^{(d)}$ vanishes.

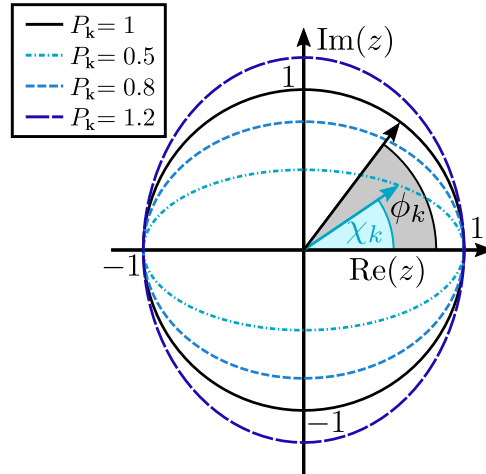


Figure 3.8 – Illustration of the relation of the measured phase $\chi_{\mathbf{k}}$ and the azimuthal phase $\phi_{\mathbf{k}}$. We plot the real and imaginary part of $z = \cos(\phi_{\mathbf{k}}) + iP_{\mathbf{k}} \sin(\phi_{\mathbf{k}})$ for several values of $P_{\mathbf{k}}$ as indicated in the legend. Each angle $\phi_{\mathbf{k}}$ is represented by the complex phase of the corresponding point on the $P = 1$ circle as shown by the gray shaded region in the figure. The related angle $\chi_{\mathbf{k}}$ is then obtained by choosing the point on the circle with the appropriate P value that has the same value of $\text{Re}(z)$. We see that for each $\phi_{\mathbf{k}}$ the vector $\cos(\phi_{\mathbf{k}}) + iP_{\mathbf{k}} \sin(\phi_{\mathbf{k}})$ remains in the same quadrant of the complex plane for all $P_{\mathbf{k}}$ and therefore the phase winding of $\phi_{\mathbf{k}}$ is preserved in $\chi_{\mathbf{k}}$. This figure has been published in the Supplemental Material to Ref. [N1].

3.4. Comparison of experimental, numerical and perturbative results

3.4.1. Numerical simulation

For our numerical simulation we compute the exact time evolution for the creation and annihilation operators according to the Heisenberg equations of motion. We then obtain a numerical solution for the time-of-flight density in the far-field limit by inserting the result into Eq. 3.8.

The Heisenberg equation for the creation and annihilation operators is given by

$$\partial_t \begin{pmatrix} c_{\mathbf{k},+}(t) \\ c_{\mathbf{k},-}(t) \end{pmatrix} = \begin{pmatrix} E_+ & E_i \\ E_i & E_- \end{pmatrix} \begin{pmatrix} c_{\mathbf{k},+}(t) \\ c_{\mathbf{k},-}(t) \end{pmatrix},$$

$$\text{where } E_+ = -\frac{i}{\hbar} \left(E_{\mathbf{k},+} + \sin(\omega t) E_{\mathbf{k},+}^{(d)} \right)$$

$$E_- = -\frac{i}{\hbar} \left(E_{\mathbf{k},-} + \sin(\omega t) E_{\mathbf{k},-}^{(d)} \right)$$

$$E_i = -\frac{i}{\hbar} \sin(\omega t) E_{\mathbf{k}}^{(d)}$$

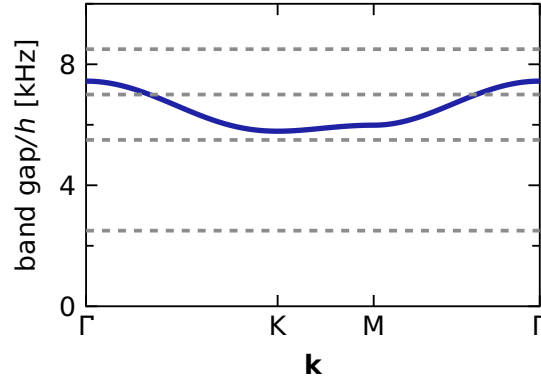


Figure 3.9 – Comparison of band gap $E_{\mathbf{k},+} - E_{\mathbf{k},-} = 2\epsilon_{\mathbf{k}}$ and driving frequencies along the high-symmetry path indicated by the dashed red line in Fig. 3.1(a). Dashed gray lines show the driving frequencies used in this section: $\omega/(2\pi) = 2500$ Hz, 5500 Hz, 7500 Hz and 8500 Hz. We use $J = h \cdot 520$ Hz, $J_{AA} = h \cdot 99$ Hz and $\Delta_{AB} = h \cdot 6056$ Hz.

and the remaining quantities were defined in Sec. 3.2.2.

We introduce the time evolution matrix $U(t)$

$$\begin{pmatrix} c_{\mathbf{k},+}(t) \\ c_{\mathbf{k},-}(t) \end{pmatrix} = U(t) \begin{pmatrix} c_{\mathbf{k},+} \\ c_{\mathbf{k},-} \end{pmatrix},$$

solve for $U(t)$ in the interaction picture and insert the results for $c_{\mathbf{k},\pm}$ into Eq. 3.8 to obtain numerical results for the time-of-flight density.

3.4.2. Driving regimes⁹

We have seen in Sec. 3.3 that the phase of the periodic oscillation of the time-of-flight density $\chi_{\mathbf{k}}$ is closely related to the azimuthal phase $\phi_{\mathbf{k}}$. In Fig. 3.3 we have shown the ideal case of near-resonant red-detuned driving. In this case the two phases agree almost perfectly. In other driving regimes the two phases are still related but not identical. Here we show a more detailed discussion of the different driving regimes.

We assume that initially all atoms are in the lower band $n_{\mathbf{k},-} = 1$, $n_{\mathbf{k},+} = 0$ and recall the relation between $\phi_{\mathbf{k}}$ and $\chi_{\mathbf{k}}$ from Eq. 3.17

$$\chi_{\mathbf{k}} = \text{Arg} [\cos(\phi_{\mathbf{k}}) + iP_{\mathbf{k}} \sin(\phi_{\mathbf{k}})] + \text{Arg} [D_{\mathbf{k}}] \quad (3.25)$$

$$P_{\mathbf{k}} = \frac{\omega}{2\epsilon_{\mathbf{k}} \cos(\theta_{\mathbf{k}})} \quad (3.26)$$

⁹Parts of this section have been published in the Supplemental Material to Ref. [N1]. The corresponding section in the Supplemental Material to Ref. [N1] has mainly been written by the author of this thesis.

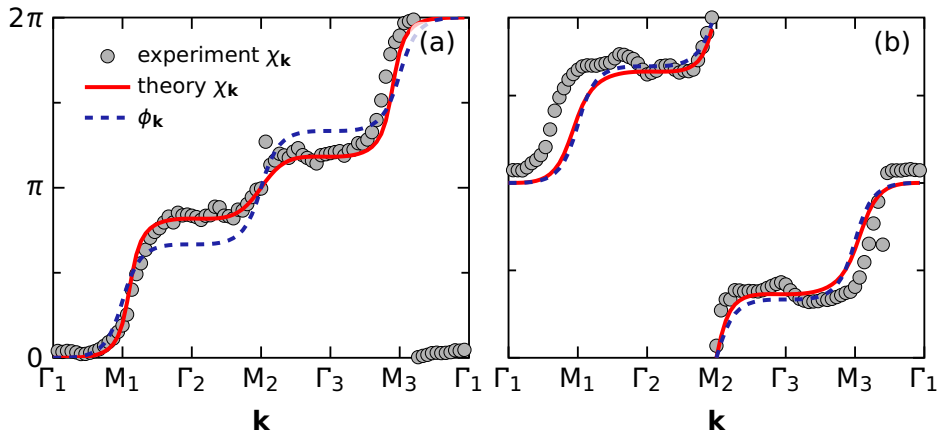


Figure 3.10 – Comparison of the measurement, the theoretical prediction $\chi_{\mathbf{k}}$ and the expected azimuthal phase $\phi_{\mathbf{k}}$ along the high-symmetry path indicated by the solid, blue lines in Fig. 3.1(a). The parameters are $J = h \cdot 520$ Hz, $J_{AA} = h \cdot 99$ Hz, $\Delta_{AB} = h \cdot 6056$ Hz, $J_{AA}^{(d)} = 0.3J_{AA}$, $J^{(d)} = 0.18J$ and $\Delta_{AB}^{(d)} = 0.22\Delta_{AB}$ for both panels. Furthermore $\omega = 2\pi \cdot 2500$ Hz in panel (a) and $\omega = 2\pi \cdot 8500$ Hz in panel (b). The different driving frequencies are indicated in Fig. 3.9.

$$D_{\mathbf{k}} = \frac{2E_{\mathbf{k}}^{(\text{dr})}}{4\epsilon_{\mathbf{k}}^2 - \omega^2} . \quad (3.27)$$

For red-detuned driving $\omega < 2\epsilon_{\mathbf{k}}$, then $D_{\mathbf{k}} > 0$ and therefore $\text{Arg}[D_{\mathbf{k}}] = 0$. This term is therefore omitted in Eq. 3.1. The only difference between $\phi_{\mathbf{k}}$ and $\chi_{\mathbf{k}}$ is now the distortion for $P_{\mathbf{k}} \neq 1$. For the graphene lattice described in Sec. 3.2.1

$$\cos(\theta_{\mathbf{k}}) = \frac{\Delta_{AB}/2 + J_{AA}g_{\mathbf{k}}}{\sqrt{(\Delta_{AB}/2 + J_{AA}g_{\mathbf{k}})^2 + |Jf_{\mathbf{k}}|^2}} .$$

In the experiment considered in Ref. [N1] $\Delta_{AB} \gg J$ and therefore $\cos(\theta_{\mathbf{k}}) \approx 1$. In this regime $P_{\mathbf{k}} = 1$ when the driving frequency is resonant ($\omega = 2\epsilon_{\mathbf{k}}$). We will see later, however, that resonant driving frequencies are not ideal for other reasons. Therefore it is ideal to consider near-resonant driving, where the distortion between $\phi_{\mathbf{k}}$ and $\chi_{\mathbf{k}}$ is still small. We show an example for even smaller driving frequency in Fig. 3.10(a). The experimentally measured $\chi_{\mathbf{k}}$ still agrees with the theoretical prediction from perturbation theory. One can, however, observe a significant distortion between $\phi_{\mathbf{k}}$ and $\chi_{\mathbf{k}}$.

In order to avoid the resonant regime but still have good agreement between $\phi_{\mathbf{k}}$ and $\chi_{\mathbf{k}}$ it can be beneficial to use a slightly smaller value of Δ_{AB} such that $\cos(\theta_{\mathbf{k}}) < 1$. In this case the condition for $P_{\mathbf{k}} = 1$ occurs for driving frequencies below the resonance $\omega = 2\epsilon_{\mathbf{k}} \cos(\theta_{\mathbf{k}}) < 2\epsilon_{\mathbf{k}}$. As we always have $\cos(\theta_{\mathbf{k}}) \leq 1$ we identify the red-detuned regime as the best regime for measuring the azimuthal phase.

Next we consider the blue-detuned limit. Now $D_{\mathbf{k}} < 0$ and therefore $\text{Arg}[D_{\mathbf{k}}] = \pi$,

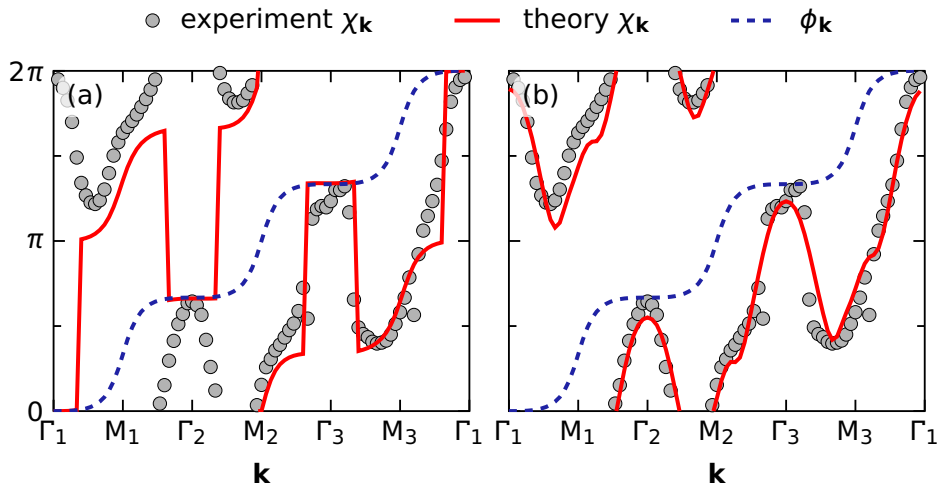


Figure 3.11 – Comparison of the measurement, the theoretical prediction $\chi_{\mathbf{k}}$ and the expected azimuthal phase $\phi_{\mathbf{k}}$ along the high-symmetry path indicated by the solid, blue lines in Fig. 3.1(a). The parameters are $\omega = 2\pi \cdot 7000$ Hz, $J = h \cdot 520$ Hz, $J_{AA} = h \cdot 99$ Hz, $\Delta_{AB} = h \cdot 6056$ Hz, $J_{AA}^{(d)} = 0.3J_{AA}$, $J^{(d)} = 0.18J$ and $\Delta_{AB}^{(d)} = 0.22\Delta_{AB}$ for both panels. In panel (a) the phase $\chi_{\mathbf{k}}$ is computed within perturbation theory as explained in Sec. 3.3, while we show the full numerical result as explained in Sec. 3.4.1 for $\chi_{\mathbf{k}}$ in panel (b).

meaning that the measured phase $\chi_{\mathbf{k}}$ is shifted by π with respect to the azimuthal phase $\phi_{\mathbf{k}}$. We show an example of near-resonant blue-detuned driving in Fig. 3.10(b). The agreement between $\phi_{\mathbf{k}}$, measured and experimental $\chi_{\mathbf{k}}$ is again very good. In general there are two caveats of blue-detuned driving. The first is that we always have $\cos(\theta_{\mathbf{k}}) \leq 1$ and therefore it can be impossible to achieve $P_{\mathbf{k}} = 1$ for blue-detuned driving in some cases. The second is that coupling to higher bands can occur for blue-detuned driving. This is likely the reason for the discrepancy between the experimental and theoretical curves in Fig. 3.10(b).

Finally, we consider resonant driving. Along a chosen path in momentum space each time the driving frequency becomes resonant with the band gap, the quantity $D_{\mathbf{k}}$ switches sign and the measured phase $\chi_{\mathbf{k}}$ jumps by π . An example of this behavior is shown in Fig. 3.11(a). For this case the agreement between the theoretical prediction from perturbation theory and the experimental data is not perfect. This is because perturbation theory breaks down in the resonant regime. A fit, obtained from our numerical calculations and shown in Fig. 3.11(b), agrees with the experimental data.

In general it is important to note that for all cases, even for the resonant regime, the phase winding of $\phi_{\mathbf{k}}$ is always preserved in $\chi_{\mathbf{k}}$. Therefore any regime is sufficient to detect the topological defects of the azimuthal phase $\phi_{\mathbf{k}}$. An illustration of this behavior based on our perturbation theory results was given in Fig. 3.8.

3.4.3. Cross-check of experimental fitting routine

Here we explain the experimental fitting routine by applying it to data from our numerical simulation. We find that except for the resonant regime fitting the phase with a single fixed frequency reproduces the phase of the oscillation as predicted from perturbation theory. Furthermore we find that higher-order effects become relevant for the modulation amplitude of $\sim 20\%$ used in Ref. [N1]. While these effects may lead to dramatic changes of the amplitude of the oscillation of the time-of-flight density, the modulation phase remains consistent with perturbation theory.

For a cross-check of the experimental fitting routine, we apply the routine used in Ref. [N1] to data from our numerical simulation, see Sec. 3.4.1. The time-of-flight density $n_{\text{TOF}}(\mathbf{k})$ is fitted with a single-frequency sinusoidal oscillation

$$n_{\text{TOF}}(\mathbf{k}, t) = n_{\text{eq},\mathbf{k}} - \delta n_{\mathbf{k}} \sin(\omega t + \chi_{\mathbf{k}}) \quad . \quad (3.28)$$

Only the amplitude $n_{\text{eq},\mathbf{k}}$ and phase $\chi_{\mathbf{k}}$ of the oscillation as well as a constant offset $n_{\text{eq},\mathbf{k}}$ are used as fit parameters. The frequency of the oscillation is set to the driving frequency.

We compare the resulting fit to the full numerical solution and the corresponding perturbative result from Eq. 3.16. For the latter we neglect the second oscillation with frequency $2\epsilon_{\mathbf{k}}/h$. The fit is based on a separation of frequency scales between the driving frequency ω and other frequencies which are dominated by the frequency of the band gap $2\epsilon_{\mathbf{k}}/h$. For red-detuned driving the oscillation with frequency $2\epsilon_{\mathbf{k}}/h$ is faster than ω . Therefore the time-of-flight density has extra 'wiggles'. This is shown in Fig. 3.12(a,b,e,f). When fitting the oscillation over several cycles the extra 'wiggles' average out and the fit agrees with the perturbative result. For blue-detuned driving the extra oscillation with frequency $2\epsilon_{\mathbf{k}}/h$ is slower than ω , see Fig. 3.13. In this case it is important to fit over several oscillation cycles of this extra slow oscillation. In that case it averages out and again the fit is in good agreement with the perturbative results.

Panels (c) and (d) in Fig. 3.12 show the special case of $2\epsilon_{\mathbf{k}} = 2\hbar\omega$. In this case the oscillation from the fully numerical simulation does not match the perturbative prediction. This illustrates that at the perturbation amplitude of roughly 20% additional higher-order effects such as two-photon processes play a significant role already. We note, however, that even in this regime the phase of the oscillation is captured by perturbation theory.

In the resonant regime, i.e. $2\epsilon_{\mathbf{k}} = \hbar\omega$, see Fig. 3.14(a) and b, we see clear differences between the fit to numerical and the perturbative results for both the amplitude and the phase of the oscillation. As expected perturbation theory breaks down in this regime and the phase of the fitted oscillation does no longer resemble the azimuthal phase. For eigenfrequencies being 300 Hz away from resonance the phase of the oscillation is already

roughly matched by perturbation theory again, see Fig. 3.14(c) and (d). Finally, Fig. 3.14 (e) and (f) show that for eigenfrequencies being 500 Hz away from resonance we obtain good agreement between the fit to numerical and the perturbative oscillations.

In summary, we find that the fitting routine is based on a separation of frequency scales and works well as long as the driving frequency is well separated from the eigenfrequencies of the system.

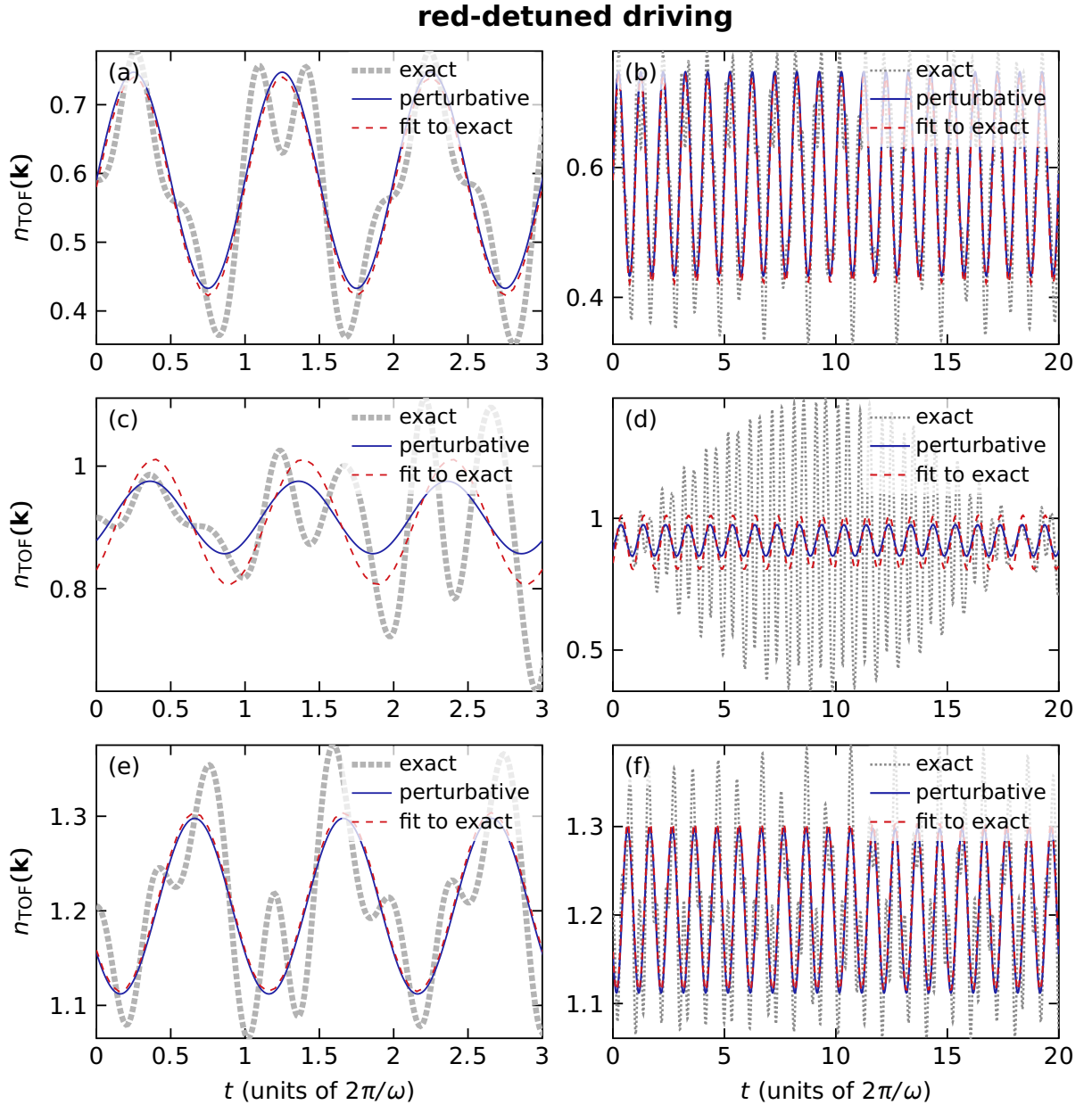


Figure 3.12 – Comparison of perturbative (solid blue line), numerically exact (dotted gray line) and a fit to the numerically exact (dashed red line) time-of-flight density. The parameters for all panels are $\omega = 2\pi \cdot 3000$ Hz, $J = h \cdot 520$ Hz, $J_{AA} = h \cdot 99$ Hz, $\Delta_{AB} = h \cdot 6056$ Hz, $J_{AA}^{(d)} = 0.3J_{AA}$, $J^{(d)} = 0.18J$ and $\Delta_{AB}^{(d)} = 0.22\Delta_{AB}$. Panels (a) and (b) show the oscillation at the Γ_1 - point, panels (c) and (d) at the M -point between Γ_1 and Γ_2 and panels (e) and (f) at the Γ_2 - point. The left and right column show the short- and long-time behavior, respectively.

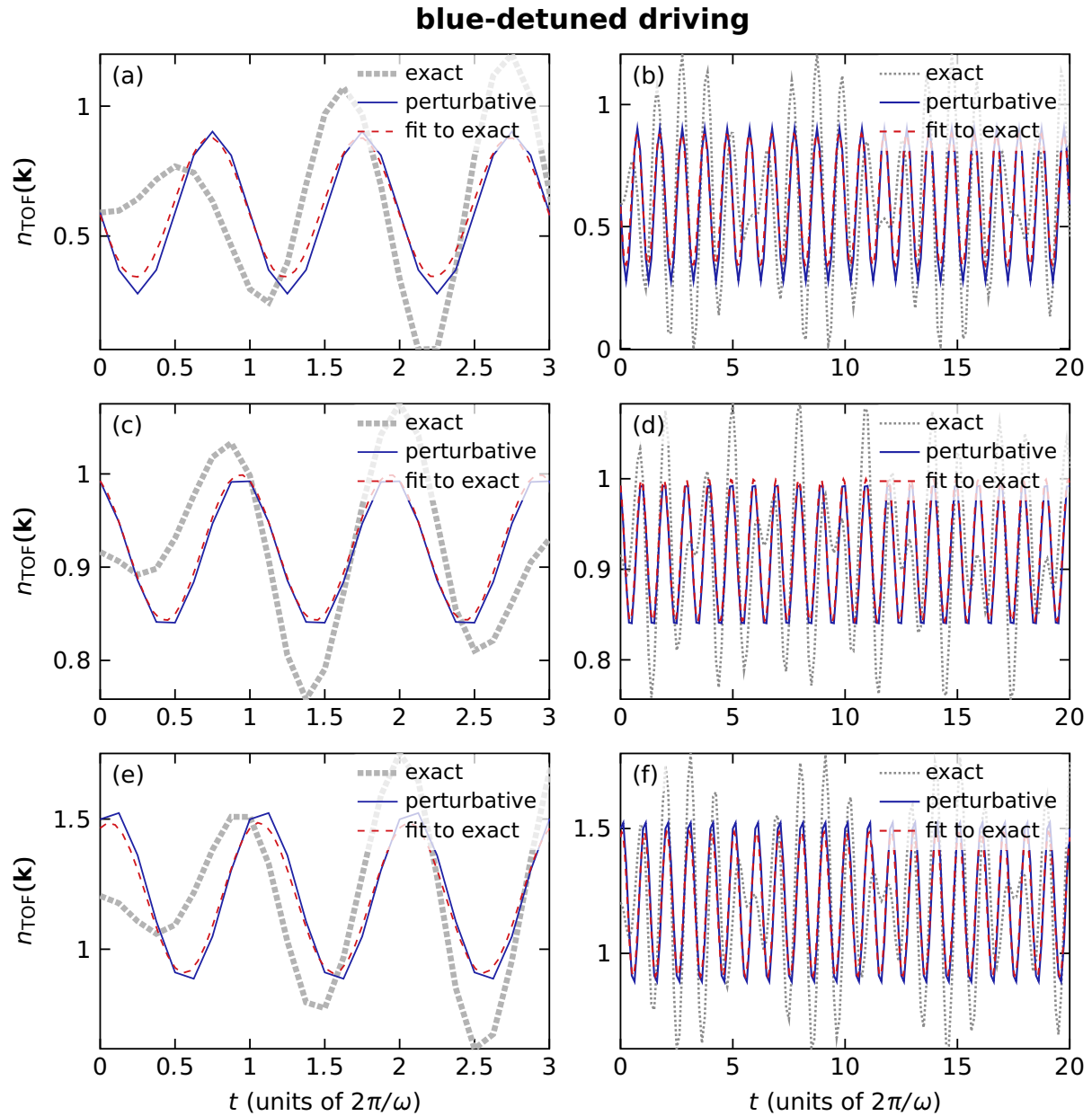


Figure 3.13 – Comparison of perturbative (solid blue line), numerically exact (dotted gray line) and a fit to the numerically exact (dashed red line) time-of-flight density. The parameters for all panels are $\omega = 2\pi \cdot 9000$ Hz, $J = h \cdot 520$ Hz, $J_{AA} = h \cdot 99$ Hz, $\Delta_{AB} = h \cdot 6056$ Hz, $J_{AA}^{(d)} = 0.3J_{AA}$, $J^{(d)} = 0.18J$ and $\Delta_{AB}^{(d)} = 0.22\Delta_{AB}$. Panels (a) and (b) show the oscillation at the Γ_1 - point, panels (c) and (d) at the M -point between Γ_1 and Γ_2 and panels (e) and (f) at the Γ_2 - point. The left and right column show the short- and long-time behavior, respectively.

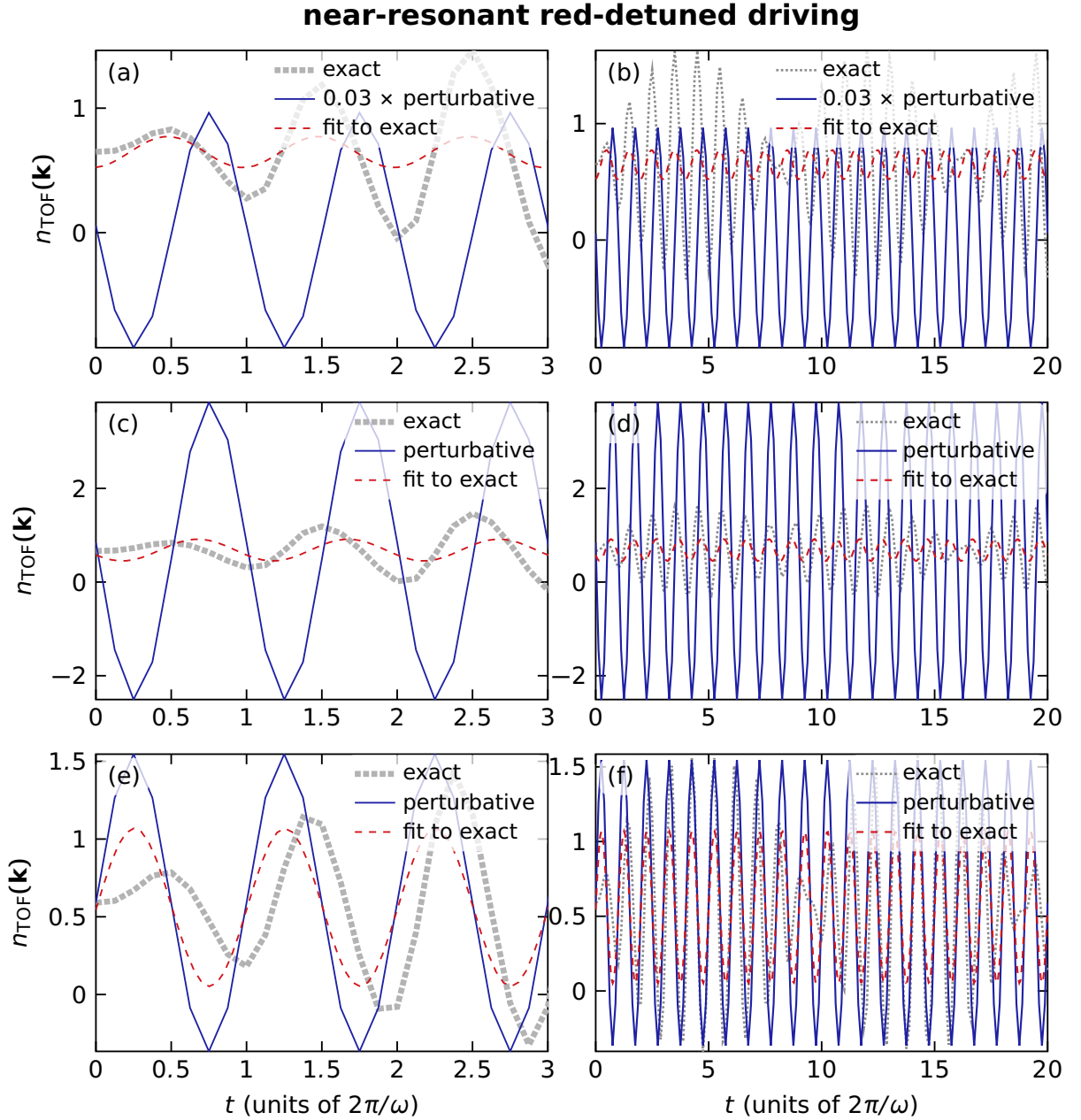


Figure 3.14 – Comparison of perturbative (solid blue line), numerically exact (dotted gray line) and a fit to the numerically exact (dashed red line) time-of-flight density. The parameters for all panels are $\omega = 2\pi \cdot 7000$ Hz, $J = h \cdot 520$ Hz, $J_{AA} = h \cdot 99$ Hz, $\Delta_{AB} = h \cdot 6056$ Hz, $J_{AA}^{(d)} = 0.3J_{AA}$, $J^{(d)} = 0.18J$ and $\Delta_{AB}^{(d)} = 0.22\Delta_{AB}$. All panels show momenta on the line between Γ_1 ($k_x = 0$) and Γ_2 ($k_x[2\pi/a] = 1$). Panels (a) and (b) are close to resonance with $k_x[2\pi/a] = 0.22$ corresponding to $2\epsilon_{\mathbf{k}} = 6900$ Hz. In panels (c) and (d) $k_x[2\pi/a] = 0.25$ and $2\epsilon_{\mathbf{k}} = 6700$ Hz, while and panels (e) and (f) show $k_x[2\pi/a] = 0.3$, corresponding to $2\epsilon_{\mathbf{k}} = 6500$ Hz. The left and right column show the short- and long-time behavior, respectively. On resonance the amplitude of the perturbative results diverges and is therefore scaled in panels (a) and (b).

4. Ultracold atoms in higher bands: the s - p_x - p_y -lattice¹

We consider a staggered square lattice. The key feature of this lattice is that the relative depth ΔV of adjacent lattice sites can be tuned, thus forming an A - and a B -sublattice. This allows to load the atoms in a regime where the A -sublattice is much deeper than the B -sublattice and atoms only occupy the former, see $\Delta V < 0$ in Fig. 4.1. A sudden quench that exchanges the depth of the A - and B -sublattice excites the atoms into higher bands [131–137]. In particular, it is possible to quench into a regime where p -orbitals on B -sublattice sites have similar energy than s -orbitals on A -sublattice sites, see $\Delta V = 0.86 V_0$ in Fig. 4.1. For sufficiently low initial temperature bosons condense at the two degenerate minima at the X -points of the second band. Here the atoms form a chiral phase pattern with alternating p -orbital chirality on B -sites [136], see $\Delta V_{\text{eq}} > 0$ in Fig. 4.1.

We use classical field theory in order to model the excitation scheme and the subsequent condensation and decay dynamics for bosons. Most notably we find in Sec. 4.2.5 that the chiral condensate in the second band prescribes a metastable state that self-stabilizes against relaxation to the first band. In fact, the chiral order of the condensate leads to destructive interference of different decay channels and hence inhibits relaxation. We identify four states connected by three different relaxation stages, see Fig. 4.2: immediately after the quench the atoms form an incoherent cloud in the second band (denoted *incoherent excited state* in Fig. 4.2). In stage I coherence increases and the atoms condense into a metastable state characterized by a chiral phase pattern (*coherent metastable state*). During stage II the chiral phase pattern of the condensate inhibits relaxation due to destructive interference. In fact, the condensate itself is a dark state showing perfect destructive interference and a pure condensate would be infinitely long-lived. Only the thermal fraction of atoms decays. Decaying atoms gain a large amount of energy. Eventually this lead to heating, a subsequent loss of coherence and hence, an increasingly populated *thermal excited state*. This is the onset of stage III, which is characterized by exponentially fast relaxation to the *thermal ground state*.

Within our model we identify the relevant decay mechanisms in Sec. 4.2.4. Close to

¹Parts of this section have been published in Ref. [N3]

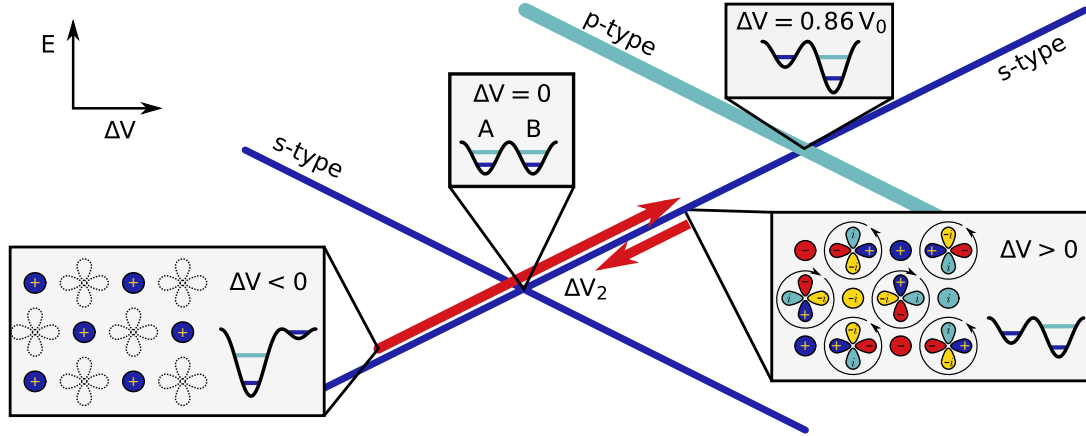


Figure 4.1 – Sketch of the mechanism for loading atoms into higher bands. Thick blue lines show the band structure as a function of potential imbalance ΔV . Away from the band crossings each of the bands can be affiliated with one of the orbitals on either A- or B-sublattice sites as indicated by labels s - and p -type. Bands corresponding to orbitals on A-sites increase with increasing ΔV , while those corresponding to B-sites decrease. The system is initialized at $\Delta V_{\text{init}} < 0$. Here A-sites are significantly deeper than B-sites and only s -orbitals on A-sites are occupied. The first fast quench to $\Delta V_{\text{eq}} = 0.43 V_0$ is performed across the first band crossing point where A- and B-sites are equally deep ($\Delta V = 0$). Afterwards a slow second quench to ΔV_f is performed, where ΔV_f can take any value between $\Delta V_f = 0$ and $\Delta V_f = 0.86 V_0$. In the light-gray boxes we show sketches of the depth of the A- and B-sites and for some cases sketches of the corresponding condensate wave functions. For $\Delta V > 0$ the phase pattern of the condensate in the second band has staggered chirality on B-sites, indicated by circular arrows. A similar version of this figures has been published in Ref. [N3].

the first band crossing at $\Delta V = 0$, see Fig. 4.1, both sublattices have similar depth and hence tunneling between the s -orbitals is the dominant decay channel. At the second band crossing for $\Delta V = 0.86 V_0$ p -orbitals on the B-sublattice have significant occupation. Here the dominant decay channel is interaction-induced. It is a scattering term where two p_x - or p_y -orbital atoms collide and scatter into the s -orbital on the same site. We show that the chiral phase pattern of the condensate leads to perfect destructive interference for both decay mechanisms individually.

We also investigate the lifetime of the atoms in Sec. 4.2.4. We find that the atoms decay fast close to the two band crossings at $\Delta V = 0$ and $\Delta V = 0.86 V_0$. In between there is a competition of the two decay mechanisms. The longest lifetime is obtained approximately half way in between the two band crossings. We show that the exact position shifts slightly depending on temperature. These results are in good agreement with experimental results from Refs. [131–137] and [N3].

So far we have considered a scenario where after the quench the atoms condense at both of the X -points of the second band. The relative phase between the wave function

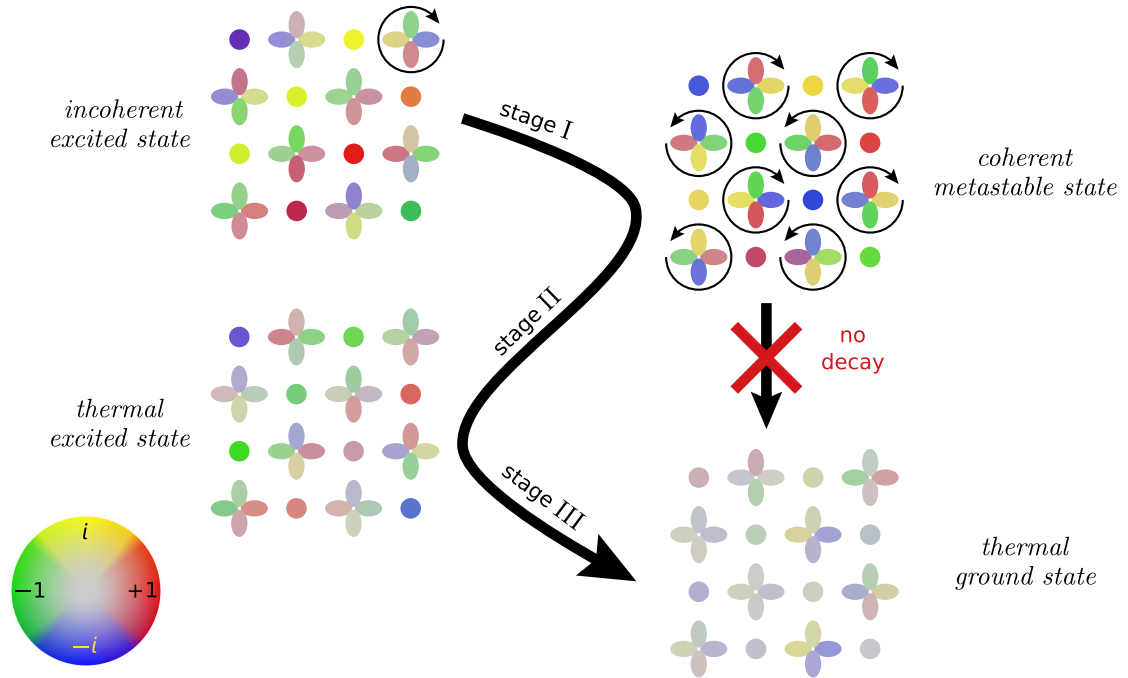


Figure 4.2 – Snapshots of real-space occupations, obtained from a numerical simulation, characterizing four states connected by three stages of relaxation (I),(II) and (III). For all states the plots show the occupations of s -orbitals (circles) and p -orbitals (dumbbells) for a snapshot of a single x - y -layer of our numerical simulation. Grey color indicates vanishing occupation of orbitals, while other colors denote the phase of the wave function. We show the idealized case of very low initial temperature ($T = 0.5$ nK) that leads to nearly perfect phase coherence. This figure has been published in Ref. [N3].

at the two X -points spontaneously chooses $+i$ or $-i$. When starting with a coherent cloud before the quench and performing a Bloch oscillation transferring the atoms to one of the X -points we can prepare a cloud of atoms at only one of the X -points of the lattice, see Sec. 4.2.6. The subsequent dynamics features — for low enough initial temperature — stable oscillation between the two X -points. Half-cycle in between reaching one of the X -points the atoms alternate between the $+i$ and $-i$ superposition of the X -points. We see several of these instanton-type flips between the two ground state condensate modes until eventually the oscillations are damped and the atoms pick one of the two minima spontaneously.

Finally, in Sec. 4.2.7 we also investigate different quench scenarios for optimizing towards a most efficient loading procedure.

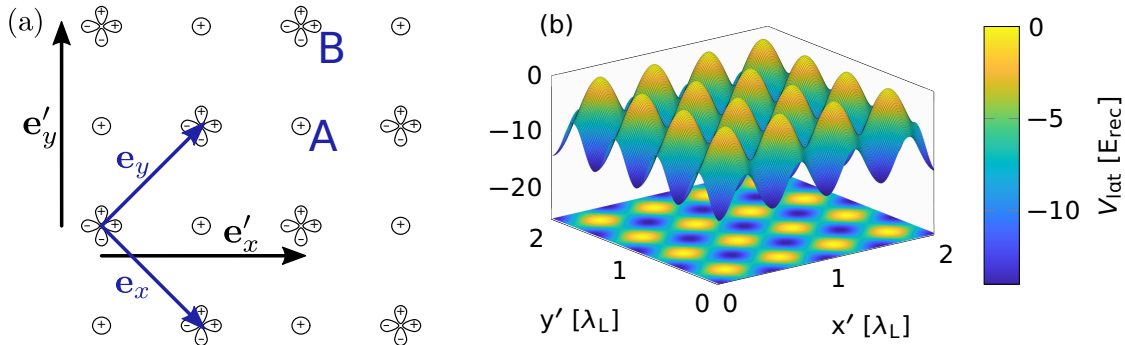


Figure 4.3 – (a) Sketch of the s - p_x - p_y -lattice. In the desired lattice configuration the s -band of one orbital is energetically close to the p -bands of neighboring orbitals. We therefore show a sketch of s - and p -orbitals on the A and B sites, respectively. (b) Lattice potential for $V_0 = -7E_{\text{rec}}$ and $\theta = 0.5\pi$.

4.1. Lattice structure and tight-binding Hamiltonian for the s - p_x - p_y -lattice

Our goal for this section is to construct a tight-binding Hamiltonian for the lattice structure used in the experiments in [131–137]. Tight-binding Hamiltonians are an approach to model the static and dynamic properties of atoms in a lattice. The idea is that, for a sufficiently deep lattice, atoms are localized at individual lattice sites. Using a set of such localized states we can write down a Hamiltonian consisting of hopping and interaction terms between nearby lattice sites. The Hamiltonian is then fully determined by a set of hopping and interaction strengths, called tight-binding parameters. Hopping terms model the kinetic energy of the Hamiltonian. For well-localized states they are short range and usually it is sufficient to consider nearest- and next-nearest-neighbor hopping terms. Tight-binding Hamiltonians are of particular importance for systems with short-range interactions. In that case the interaction terms of the tight-binding Hamiltonian can be approximated by only on-site terms. One approach to construct a tight-binding Hamiltonian is to compute Wannier states and determine the tight-binding parameters from the overlaps of these Wannier functions. Since the Wannier functions are not unique, neither are the tight-binding parameters. The choice of Wannier functions then determines how well the full Hamiltonian is approximated by the tight-binding Hamiltonian with only nearby hopping and interaction terms. This approach has been discussed in more detail in [N8].

Here we use a different approach to determine the tight-binding Hamiltonian. We compute the band structure of the full lattice and construct a tight-binding Hamiltonian comprising the noninteracting s - and p -orbitals on each lattice site. Then we adjust the parameters of this Hamiltonian such that we obtain the best fit of the tight-binding band

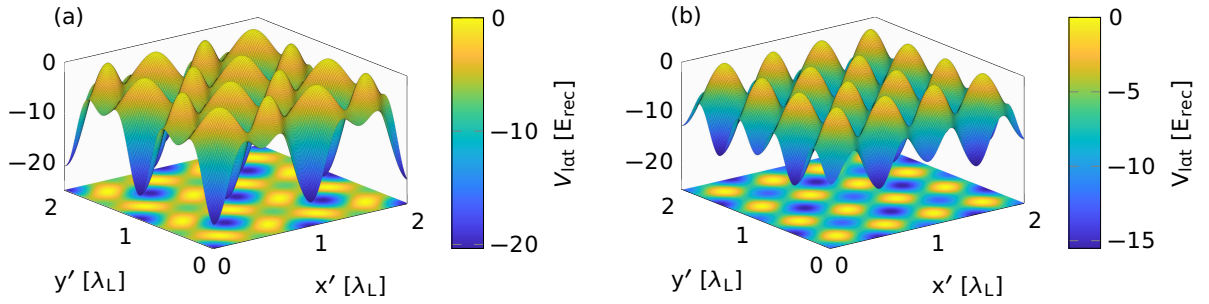


Figure 4.4 – Lattice potential for $V_0 = -7E_{\text{rec}}$ and $\theta = 0.35\pi$ in panel (a) and $\theta = 0.5345\pi$ in panel (b).

structure to the Bloch-band structure. We do this both by considering symmetry points of the lattice as well as by using numerical minimization routines.

We use the lattice potential from [131–137]

$$V(x', y') = -V_0/2 [\cos(2k_L x') + \cos(2k_L y')] - V_0 \cos(\theta) [\cos(k_L(x' + y')) + \cos(k_L(x' - y'))] \quad , \quad (4.1)$$

where V_0 is the lattice depth and $k_L = 2\pi/\lambda_L$ is the wave vector of the laser creating the lattice potential. The experiments use ^{87}Rb atoms and a laser wave length of $\lambda_L = 1064 \text{ nm}$, such that the recoil energy is $E_{\text{rec}} = h^2/(2m\lambda_L^2) \approx 2 h \cdot \text{kHz}$. The above lattice potential is written in terms of the unit vectors \mathbf{e}'_x and \mathbf{e}'_y shown in Fig. 4.3(a). These vectors fulfill $|\mathbf{e}'_x| = |\mathbf{e}'_y| = \lambda_L$. The angle θ can be tuned in experiment and determines the relative depth of the two inequivalent lattice sites in each unit cell. In fact, we find that the difference of the potential on A - and B -sites

$$\Delta V = V_A - V_B = -4V_0 \cos(\theta) \quad .$$

For $\theta = 0.5\pi$ we have $\cos(\theta) = 0$ and both sites have equal depth, see Fig. 4.3(b). Smaller values of theta are used for loading the atoms into the lattice. The lattice potential for $\theta = 0.35\pi$ ($\Delta V = -1.8V_0$) is shown in Fig. 4.4(a). In this regime, ground-state atoms are occupying the lower-lying lattice sites almost entirely. Figure 4.4(b) shows the situation for $\theta = 0.5345\pi$ ($\Delta V = 0.43 V_0$) where the p -orbitals of the deep lattice sites are similar in energy to the s -orbitals of the shallow lattice sites. Finally, at $\theta = 0.569\pi$ ($\Delta V = 0.86 V_0$) p -orbitals of deep lattice sites are degenerate with s -orbitals on shallow lattice sites. The ramp procedure explained in the introduction allows to load atoms into these excited bands.

The unit cell spanned by $\mathbf{e}'_{x,y}$ contains four lattice sites. Only two of these are not equivalent. It is therefore convenient to use the lattice spanned by $\mathbf{e}_{x,y}$, see Fig. 4.3(a).

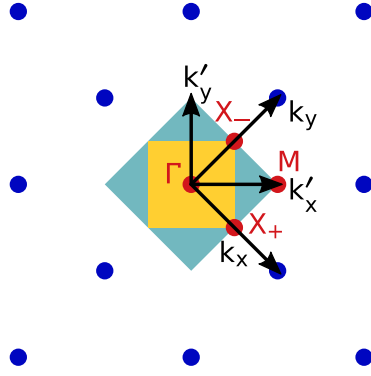


Figure 4.5 – Reciprocal lattice vectors and corresponding first Brillouin zones for the two choices of basis vectors $\mathbf{e}_{x,y}$ and $\mathbf{e}'_{x,y}$. We mark some of the symmetry points of the lattice in red.

The lattice potential in the new basis is

$$V(x, y) = -V_0/2 [\cos(k_L(x + y)) + \cos(k_L(x - y))] - V_0 \cos(\theta) [\cos(k_L x) + \cos(k_L y)] \quad .$$

The band structure² of the system in Fig. 4.6 and its sketch in Fig. 4.1 give further insight into the cross-over between the different lattices for different values of θ . Initially for $\theta = 0.35\pi$ ($\Delta V = -1.8V_0$) both the s - and the p -orbitals of the deeper A-sites are energetically lower than the s -orbitals on shallow B-sites. When increasing ΔV orbitals on A-sublattice sites increase in energy while orbitals on B-sublattice sites decrease. The first band crossing occurs at $\theta = 0.428\pi$ ($\Delta V = -0.9V_0$) when s -orbitals on B sites become degenerate with p -orbitals on A-sites. Next at $\theta = 0.5\pi$ ($\Delta V = 0$) both lattice sites are equally deep and hence all orbitals have the same energy on A- and B-sublattice sites. For increasing values of θ the s -orbitals on now shallow A-sites approach the p -orbitals on B-sites until they become resonant for $\theta = 0.569\pi$ ($\Delta V = 0.86V_0$).

4.1.1. Tight-binding model

Here we present which of the possible tight-binding terms we include in our Hamiltonian. Our goal is to find a set of parameters that gives a good approximation of the lowest four bands of the Hamiltonian. In general we can split the tight-binding Hamiltonian into the hopping or noninteracting part and the interaction part

$$H = H_{\text{non-int}} + H_{\text{int}} \quad . \quad (4.2)$$

In the following paragraphs we will show which terms we include.

²For details on how to compute band structures see for example [N8].

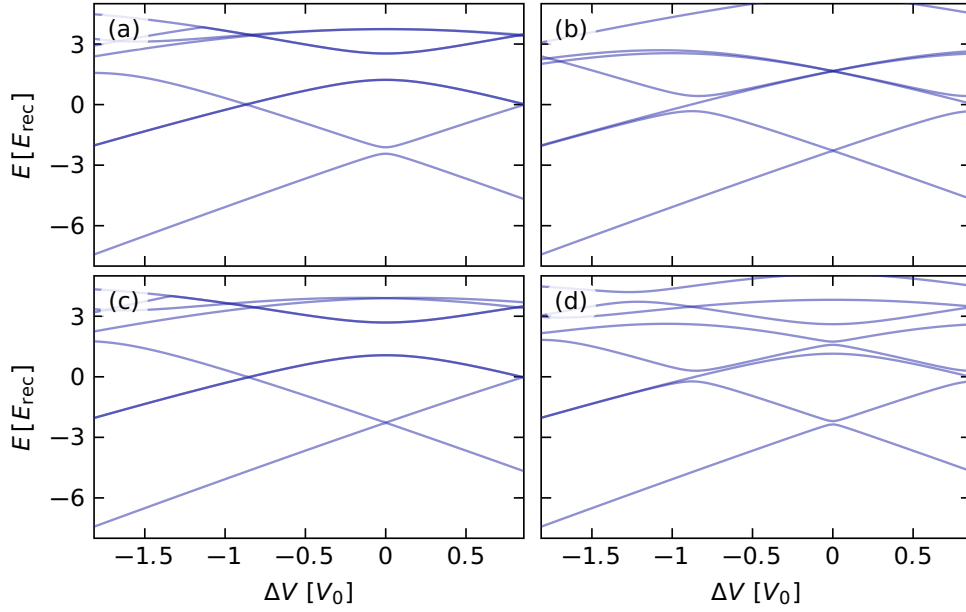


Figure 4.6 – Lowest 8 bands of the s - p_x - p_y -lattice as a function of ΔV at several high-symmetry points of the lattice. Panel (a) shows the Γ , panel (b) the X , panel (c) the M point and panel (d) the point half way between Γ and M . The positions of the symmetry points in the Brillouin zone are marked in Fig. 4.5. We show the bands with opacity such that degenerate bands appear in a slightly darker blue.

Hopping terms for the lattice with 3 orbitals per unit cell

When loading atoms into the second, third and fourth band for $0 \ll \Delta V < 0.86 V_0$ the atoms are mainly occupying s -orbitals on A-sites and p_x - and p_y -orbitals on B-sites. In this regime it is a good approximation to consider only these orbitals. We therefore make the following Ansatz for the tight-binding Hamiltonian, for a sketch of hopping parameters see Fig. 4.7,

$$H_{\text{non-int}} = H_{ss} + H_{sp_x} + H_{sp_y} + H_{p_x p_x} + H_{p_y p_y} + H_{p_x p_y} \quad (4.3)$$

$$\text{where } H_{ss} = -J_{ss} \sum_{\mathbf{R}_i \in A, \mathbf{R}_j = \pm \mathbf{e}_x, \pm \mathbf{e}_y} b_{s, \mathbf{R}_i + \mathbf{R}_j}^\dagger b_{s, \mathbf{R}_i} + \sum_{\mathbf{R}_i \in A} V_s b_{s, \mathbf{R}_i}^\dagger b_{s, \mathbf{R}_i} \quad (4.4)$$

$$H_{sp_x} = \sum_{\mathbf{R}_i \in B} -J_{sp_x} b_{s, \mathbf{R}_i + \mathbf{e}'_x/2}^\dagger b_{x, \mathbf{R}_i} + J_{sp-x} b_{s, \mathbf{R}_i - \mathbf{e}'_x/2}^\dagger b_{x, \mathbf{R}_i} + \text{h.c.} \quad (4.5)$$

$$H_{sp_y} = \sum_{\mathbf{R}_i \in B} -J_{sp_y} b_{s, \mathbf{R}_i + \mathbf{e}'_y/2}^\dagger b_{y, \mathbf{R}_i} + J_{sp-y} b_{s, \mathbf{R}_i - \mathbf{e}'_y}^\dagger b_{y, \mathbf{R}_i} + \text{h.c.} \quad (4.6)$$

$$H_{p_x p_x} = -J_{\parallel, x} \sum_{\mathbf{R}_i \in B, \mathbf{R}_j = \pm \mathbf{e}_x, \pm \mathbf{e}_y} b_{x, \mathbf{R}_i + \mathbf{R}_j}^\dagger b_{x, \mathbf{R}_i} + V_x \sum_{\mathbf{R}_i \in B} b_{x, \mathbf{R}_i}^\dagger b_{x, \mathbf{R}_i} \quad (4.7)$$

$$H_{p_y p_y} = -J_{\parallel, y} \sum_{\mathbf{R}_i \in B, \mathbf{R}_j = \pm \mathbf{e}_x, \pm \mathbf{e}_y} b_{y, \mathbf{R}_i + \mathbf{R}_j}^\dagger b_{y, \mathbf{R}_i} + V_y \sum_{\mathbf{R}_i \in B} b_{y, \mathbf{R}_i}^\dagger b_{y, \mathbf{R}_i} \quad (4.8)$$

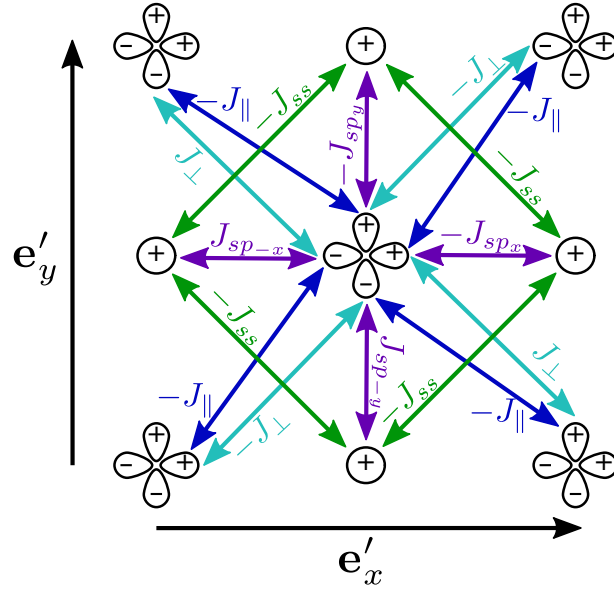


Figure 4.7 – Sketch of all hopping parameters used for the 3-orbital tight-binding model.

$$\begin{aligned}
 H_{p_x p_y} = & J_{\perp} \sum_{\mathbf{R}_i \in B, \mathbf{R}_j = \pm \mathbf{e}_x} b_{x, \mathbf{R}_i + \mathbf{R}_j}^{\dagger} b_{y, \mathbf{R}_i} + \text{h.c.} \\
 & - s_{\perp} J_{\perp} \sum_{\mathbf{R}_i \in B, \mathbf{R}_j = \pm \mathbf{e}_y} b_{x, \mathbf{R}_i + \mathbf{R}_j}^{\dagger} b_{y, \mathbf{R}_i} + \text{h.c.} \quad .
 \end{aligned} \tag{4.9}$$

The operator $b_{s,x,y,\mathbf{R}_i}^{\dagger}$ (b_{s,x,y,\mathbf{R}_i}) creates (annihilates) an atom on the site \mathbf{R}_i in the s - p_x - or p_y -orbital, respectively. Note that s_{\perp} has been introduced for later convenience in order to introduce an imbalance between J_{\perp} along \mathbf{e}_x and \mathbf{e}_y and for now we choose $s_{\perp} = 1$.

In later sections we will also need the tight-binding Hamiltonian into momentum space, which we obtain by applying the Fourier transformation

$$\begin{aligned}
 b_{\mathbf{R}_i} &= \frac{1}{\sqrt{N}} \sum_{\mathbf{k}} e^{i\mathbf{k} \cdot \mathbf{R}_i} b_{\mathbf{k}} \\
 b_{\mathbf{k}} &= \frac{1}{\sqrt{N}} \sum_{\mathbf{R}_i} e^{-i\mathbf{k} \cdot \mathbf{R}_i} b_{\mathbf{R}_i} \quad ,
 \end{aligned}$$

where the sum over \mathbf{k} runs over all momenta in the first Brillouin zone — the one spanned by $\mathbf{k}_{x,y}$ — and the sum over \mathbf{R}_i runs over all A -sublattice sites for s -orbitals and all B -sublattice sites for p -orbitals. N is the total number of unit cells. This leads to

$$H = \sum_{\mathbf{k}} H_{\mathbf{k}}$$

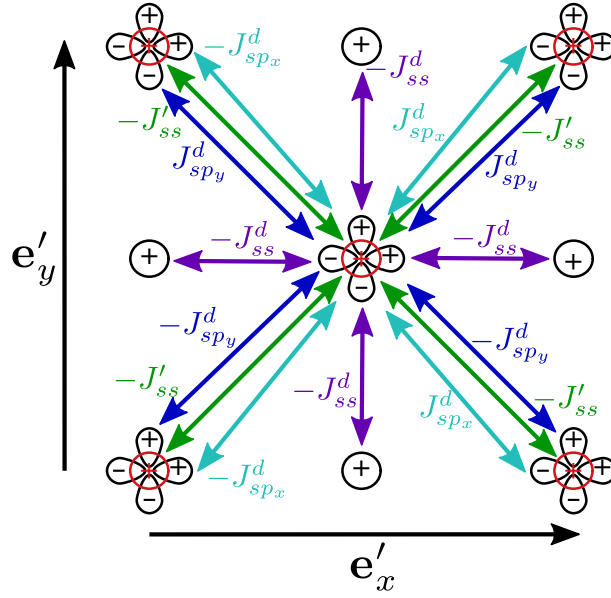


Figure 4.8 – Sketch of the lattice with the additional hopping parameters introduced for the s -orbitals on the A-sites. Red circles denote these s -orbitals.

and

$$H_{\mathbf{k}} = \begin{pmatrix} b_{s,\mathbf{k}}^\dagger & b_{x,\mathbf{k}}^\dagger & b_{y,\mathbf{k}}^\dagger \end{pmatrix} \begin{pmatrix} \epsilon_{\mathbf{k}}^{ss} & \epsilon_{\mathbf{k}}^{sp_x} & \epsilon_{\mathbf{k}}^{sp_y} \\ \epsilon_{\mathbf{k}}^{sp_x*} & \epsilon_{\mathbf{k}}^{p_x} & \epsilon_{\mathbf{k}}^{pp} \\ \epsilon_{\mathbf{k}}^{sp_y*} & \epsilon_{\mathbf{k}}^{p_y} & \epsilon_{\mathbf{k}}^{pp} \end{pmatrix} \begin{pmatrix} b_{s,\mathbf{k}} \\ b_{x,\mathbf{k}} \\ b_{y,\mathbf{k}} \end{pmatrix}$$

$$\begin{aligned}
 \epsilon_{\mathbf{k}}^{ss} &= -2J_{ss}(\cos(k_x a) + \cos(k_y a)) + V_s \\
 \epsilon_{\mathbf{k}}^{sp_x} &= -J_{sp_x} e^{-i\frac{k_x+k_y}{2}a} + J_{sp_{-x}} e^{i\frac{k_x+k_y}{2}a} \\
 \epsilon_{\mathbf{k}}^{sp_y} &= -J_{sp_y} e^{i\frac{k_x-k_y}{2}a} + J_{sp_{-y}} e^{-i\frac{k_x-k_y}{2}a} \\
 \epsilon_{\mathbf{k}}^{p_x} &= -2J_{\parallel,x} [\cos(k_x a) + \cos(k_y a)] + V_x \\
 \epsilon_{\mathbf{k}}^{p_y} &= -2J_{\parallel,y} [\cos(k_x a) + \cos(k_y a)] + V_y \\
 \epsilon_{\mathbf{k}}^{pp} &= 2J_{\perp} (\cos(k_x a) - s_{\perp} \cos(k_y a)) \quad .
 \end{aligned}$$

Hopping terms for the lattice with 4 orbitals per unit cell

When loading the atoms into the lattice at $\Delta V = -1.82 V_0$ all atoms occupy the s -orbitals on A-sites, which we label by s' . It is therefore important to include these orbitals in our simulations. As a result we need to include additional hopping terms in the Hamiltonian, which are sketched in Fig. 4.8. As an Ansatz for the tight-binding Hamiltonian we now use

$$H_{\text{non-int}} = H_{ss} + H_{sp_x} + H_{sp_y} + H_{p_x p_x} + H_{p_y p_y} + H_{p_x p_y} + H_{ss}^d + H_{sp_x}^d + H_{sp_y}^d \quad (4.10)$$

$$\text{where } H_{ss} = -J_{ss} \sum_{\mathbf{R}_i \in A, \mathbf{R}_j = \pm \mathbf{e}_x, \pm \mathbf{e}_y} b_{s, \mathbf{R}_i + \mathbf{R}_j}^\dagger b_{s, \mathbf{R}_i} + V_s \sum_{\mathbf{R}_i \in A} b_{s, \mathbf{R}_i}^\dagger b_{s, \mathbf{R}_i} - J'_{ss} \sum_{\mathbf{R}_i \in B, \mathbf{R}_j = \pm \mathbf{e}_x, \pm \mathbf{e}_y} b_{s, \mathbf{R}_i + \mathbf{R}_j}^\dagger b_{s, \mathbf{R}_i} + V'_s \sum_{\mathbf{R}_i \in B} b_{s, \mathbf{R}_i}^\dagger b_{s, \mathbf{R}_i} \quad (4.11)$$

$$H_{ss}^d = -J_{ss}^d \sum_{\mathbf{R}_i, \mathbf{R}_j = \pm \mathbf{e}'_x, \pm \mathbf{e}'_y} b_{s, \mathbf{R}_i + \mathbf{R}_j}^\dagger b_{s, \mathbf{R}_i} \quad (4.12)$$

$$H_{sp_x}^d = \sum_{\mathbf{R}_i \in B} J_{sp_x}^d \left(b_{s, \mathbf{R}_i - \mathbf{e}_y}^\dagger + b_{s, \mathbf{R}_i - \mathbf{e}_x}^\dagger - b_{s, \mathbf{R}_i + \mathbf{e}_y}^\dagger - b_{s, \mathbf{R}_i + \mathbf{e}_x}^\dagger \right) b_{x, \mathbf{R}_i} + \text{h.c.} \quad (4.13)$$

$$H_{sp_y}^d = \sum_{\mathbf{R}_i \in B} J_{sp_y}^d \left(b_{s, \mathbf{R}_i - \mathbf{e}_y}^\dagger + b_{s, \mathbf{R}_i + \mathbf{e}_x}^\dagger - b_{s, \mathbf{R}_i + \mathbf{e}_y}^\dagger - b_{s, \mathbf{R}_i - \mathbf{e}_x}^\dagger \right) b_{y, \mathbf{R}_i} + \text{h.c.} \quad (4.14)$$

and the remaining parts of the Hamiltonian have been defined in Eqs. 4.3–4.9. The corresponding Hamiltonian in momentum space is

$$H_{\mathbf{k}} = \begin{pmatrix} b_{s, \mathbf{k}}^\dagger & b_{x, \mathbf{k}}^\dagger & b_{y, \mathbf{k}}^\dagger & b_{s', \mathbf{k}}^\dagger \end{pmatrix} \begin{pmatrix} \epsilon_{\mathbf{k}}^s(J_{ss}, V_s) & \epsilon_{\mathbf{k}}^{sp_x} & \epsilon_{\mathbf{k}}^{sp_y} & \epsilon_{\mathbf{k}}^{sd} \\ \epsilon_{\mathbf{k}}^{sp_x*} & \epsilon_{\mathbf{k}}^{p_x} & \epsilon_{\mathbf{k}}^{pp} & \epsilon_{\mathbf{k}}^{sp_x d} \\ \epsilon_{\mathbf{k}}^{sp_y*} & \epsilon_{\mathbf{k}}^{pp} & \epsilon_{\mathbf{k}}^{p_y} & \epsilon_{\mathbf{k}}^{sp_y d} \\ \epsilon_{\mathbf{k}}^{sd} & \epsilon_{\mathbf{k}}^{sp_x d*} & \epsilon_{\mathbf{k}}^{sp_y d*} & \epsilon_{\mathbf{k}}^s(J'_{ss}, V'_s) \end{pmatrix} \begin{pmatrix} b_{s, \mathbf{k}} \\ b_{x, \mathbf{k}} \\ b_{y, \mathbf{k}} \\ b_{s', \mathbf{k}} \end{pmatrix}, \quad (4.15)$$

where

$$\begin{aligned} \epsilon_{\mathbf{k}}^s(J, V) &= -2J [\cos(k_x a) + \cos(k_y a)] + V \\ \epsilon_{\mathbf{k}}^{sd} &= -2J_{ss}^d [\cos((k_x + k_y)a/2) + \cos((k_x - k_y)a/2)] \\ \epsilon_{\mathbf{k}}^{sp_x d} &= 2iJ_{sp_x}^d [\sin(k_x a) + \sin(k_y a)] \\ \epsilon_{\mathbf{k}}^{sp_y d} &= 2iJ_{sp_y}^d [\sin(k_y a) - \sin(k_x a)] \quad . \end{aligned}$$

Diagonalizing the above Hamiltonian gives the tight-binding band structure. We can then compare the tight-binding band structure with the Bloch band-structure, shown in Fig. 4.6, in order to determine the tight-binding parameters. Before discussing the details of this procedure we present the interaction terms that we include in the Hamiltonian.

Interaction terms

So far we have only considered the hopping part of the tight-binding Hamiltonian. Here we will show which type of interaction terms we need to consider. Since the interaction in the experiments in [131–137] is sufficiently short range we only consider on-site interaction terms. Near the bottom of a lattice site the lattice potential resembles a harmonic trap. It is therefore often sufficient to use harmonic-oscillator wave functions for the determination

of interaction strengths. This is also the approach we take here.

The one-dimensional harmonic-oscillator wave function can be given in terms of the Hermite polynomials $H_n(x)$ as

$$\psi_n(x) = \frac{1}{2^n n! \sqrt{\pi} x_0} e^{-\frac{1}{2}(x/x_0)^2} H_n(x/x_0) \quad ,$$

where $x_0 = \sqrt{\hbar/m\omega}$ is the harmonic-oscillator wave length, m is the mass of the atoms and ω is the harmonic-oscillator frequency. The index n labels the subsequent solutions of the harmonic oscillator. The lowest eigenstate $n = 0$, due to its symmetry, corresponds to an s -orbital. The first excited state $n = 1$, which has one node in its wave function, is reminiscent of a p -orbital. The two-dimensional generalization of the harmonic oscillator is obtained from a product ansatz

$$\psi_{\mathbf{n}=(i,j)}(x, y) = \psi_i(x) \cdot \psi_j(y) \quad .$$

The weight of the possible interaction terms for the tight-binding Hamiltonian is determined from the overlap of the corresponding harmonic-oscillator wave functions

$$U_{\mathbf{ijnm}} = U_0 \iint dx dy \psi_i^*(x, y) \psi_j^*(x, y) \psi_{\mathbf{n}}(x, y) \psi_{\mathbf{m}}(x, y) b_i^\dagger b_j^\dagger b_{\mathbf{n}} b_{\mathbf{m}} \quad .$$

For our tight-binding model we are only interested in s -, p_x - and p_y -orbitals. By calculating the corresponding integrals we see that the only nonzero interaction terms are

$$\begin{aligned} U_{ssss} &= \frac{U_0}{2\pi x_0^2} b_s^\dagger b_s^\dagger b_s b_s \\ U_{xxxx} &= \frac{3U_0}{4} \frac{1}{2\pi x_0^2} b_x^\dagger b_x^\dagger b_x b_x & U_{yyyy} &= \frac{3U_0}{4} \frac{1}{2\pi x_0^2} b_y^\dagger b_y^\dagger b_y b_y \\ U_{xxyy} &= \frac{U_0}{4} \frac{1}{2\pi x_0^2} b_x^\dagger b_x^\dagger b_y b_y & U_{yyxx} &= \frac{U_0}{4} \frac{1}{2\pi x_0^2} b_y^\dagger b_y^\dagger b_x b_x \\ U_{xxss} &= \frac{U_0}{2} \frac{1}{2\pi x_0^2} b_x^\dagger b_x^\dagger b_s b_s & U_{ssxx} &= \frac{U_0}{2} \frac{1}{2\pi x_0^2} b_s^\dagger b_s^\dagger b_x b_x \\ U_{yyss} &= \frac{U_0}{2} \frac{1}{2\pi x_0^2} b_y^\dagger b_y^\dagger b_s b_s & U_{ssyy} &= \frac{U_0}{2} \frac{1}{2\pi x_0^2} b_s^\dagger b_s^\dagger b_y b_y \end{aligned}$$

and

$$\begin{aligned} U_{xyyx} + U_{yxxy} + U_{xyxy} + U_{yxyx} &= \frac{U_0}{2\pi x_0^2} b_y^\dagger b_y b_x^\dagger b_x \\ U_{xssx} + U_{sxxs} + U_{xsxs} + U_{sxsx} &= 2 \frac{U_0}{2\pi x_0^2} b_x^\dagger b_x b_s^\dagger b_s \end{aligned}$$

$$U_{yssi} + U_{sys} + U_{ysys} + U_{sysy} = 2 \frac{U_0}{2\pi x_0^2} b_y^\dagger b_y b_s^\dagger b_s \quad ,$$

where we use the shorthand notation $s = (0, 0)$, $x = (1, 0)$ and $y = (0, 1)$. We can therefore introduce interaction strengths for A - and B -sites of our tight-binding model U_A and U_B and write the interaction part of the tight-binding Hamiltonian as

$$\begin{aligned} H_{\text{int}} = & \frac{U_A}{2} \sum_{\mathbf{R}_i \in A} b_{s, \mathbf{R}_i}^\dagger b_{s, \mathbf{R}_i}^\dagger b_{s, \mathbf{R}_i} b_{s, \mathbf{R}_i} + \frac{U_B}{2} \sum_{\mathbf{R}_i \in B} b_{s, \mathbf{R}_i}^\dagger b_{s, \mathbf{R}_i}^\dagger b_{s, \mathbf{R}_i} b_{s, \mathbf{R}_i} \\ & + \frac{3}{4} \frac{U_B}{2} \sum_{\mathbf{R}_i \in B} \left[b_{x, \mathbf{R}_i}^\dagger b_{x, \mathbf{R}_i}^\dagger b_{x, \mathbf{R}_i} b_{x, \mathbf{R}_i} + b_{y, \mathbf{R}_i}^\dagger b_{y, \mathbf{R}_i}^\dagger b_{y, \mathbf{R}_i} b_{y, \mathbf{R}_i} \right] \\ & + \frac{U_B}{2} \sum_{\mathbf{R}_i \in B} b_{x, \mathbf{R}_i}^\dagger b_{x, \mathbf{R}_i} b_{y, \mathbf{R}_i}^\dagger b_{y, \mathbf{R}_i} + \frac{1}{4} \frac{U_B}{2} \sum_{\mathbf{R}_i \in B} \left[b_{x, \mathbf{R}_i}^\dagger b_{x, \mathbf{R}_i}^\dagger b_{y, \mathbf{R}_i} b_{y, \mathbf{R}_i} + \text{h.c.} \right] \\ & + \frac{1}{2} \frac{U_B}{2} \sum_{\mathbf{R}_i \in B} \left[b_{x, \mathbf{R}_i}^\dagger b_{x, \mathbf{R}_i}^\dagger b_{s, \mathbf{R}_i} b_{s, \mathbf{R}_i} + b_{y, \mathbf{R}_i}^\dagger b_{y, \mathbf{R}_i}^\dagger b_{s, \mathbf{R}_i} b_{s, \mathbf{R}_i} + \text{h.c.} \right] \\ & + 2 \frac{U_B}{2} \sum_{\mathbf{R}_i \in B} (b_{x, \mathbf{R}_i}^\dagger b_{x, \mathbf{R}_i} + b_{y, \mathbf{R}_i}^\dagger b_{y, \mathbf{R}_i}) b_{s, \mathbf{R}_i}^\dagger b_{s, \mathbf{R}_i} \quad . \end{aligned} \quad (4.16)$$

4.1.2. Determining tight-binding parameters

Hopping terms

In principle we could now proceed and directly use a numerical minimization routine in order to minimize the difference between the Bloch band structure and the tight-binding band structure at each point in momentum space. We can assume the lattice to be symmetric with respect to the x - and y -direction and hence assume that $J_{sp_x} = J_{sp_y} = J_{sp_{-x}} = J_{sp_{-y}} =: J_{sp}$, $J_{\parallel, x} = J_{\parallel, y} =: J_{\parallel}$, $J_{sp_x}^d = J_{sp_y}^d =: J_{sp}^d$ and $V_x = V_y =: V_p$. Even with these approximations the tight-binding Hamiltonian has 7 hopping parameters and 3 on-site potentials that need to be determined. Adjusting all by using a minimization routine is numerically quite challenging. Additionally we are interested in a scenario where the atoms are condensed at one of the symmetry points of the lattice. Hence, the band structure close to the symmetry points is of particular importance. Here we therefore take a different approach for determining the tight-binding parameters. We analytically compute the tight-binding bands at certain symmetry points of the Brillouin zone, identify the Bloch bands with the corresponding tight-binding bands and use the resulting equations to obtain analytical expressions for the tight-binding parameters. This approach works well for most of the tight-binding parameters. We determine the remaining set of parameters with a Monte-Carlo minimization routine.

First we need analytical expressions for the energies of tight-binding orbitals at certain

symmetry points. We start with considering the tight-binding Hamiltonian at the Γ -point, i.e. $k_x = k_y = 0$. In this case

$$H_\Gamma = \begin{pmatrix} b_{s,\mathbf{k}}^\dagger \\ b_{x,\mathbf{k}}^\dagger \\ b_{y,\mathbf{k}}^\dagger \\ b_{s',\mathbf{k}}^\dagger \end{pmatrix}^T \begin{pmatrix} -4J_{ss} + V_s & 0 & 0 & -4J_{ss}^d \\ 0 & -4J_\parallel + V_p & 0 & 0 \\ 0 & 0 & -4J_\parallel + V_p & 0 \\ -4J_{ss}^d & 0 & 0 & -4J_{ss}' + V_s' \end{pmatrix} \begin{pmatrix} b_{s,\mathbf{k}} \\ b_{x,\mathbf{k}} \\ b_{y,\mathbf{k}} \\ b_{s',\mathbf{k}} \end{pmatrix}$$

and the set of eigenvalues is

$$E_p^{(\Gamma)} = V_p - 4J_\parallel \quad (\text{two-fold degenerate}) \quad (4.17)$$

$$E_{ss',\pm}^{(\Gamma)} = \frac{V_s + V_s' - 4J_{ss} - 4J_{ss}''}{2} \pm \frac{\sqrt{[V_s - V_s' - 4(J_{ss} - J_{ss}')]^2 + 64J_{ss}^d}}{2}. \quad (4.18)$$

At the X -points, e.g. $k_x = \pi/a$, $k_y = 0$, we have

$$H_X = \begin{pmatrix} b_{s,\mathbf{k}}^\dagger \\ b_{x,\mathbf{k}}^\dagger \\ b_{y,\mathbf{k}}^\dagger \\ b_{s',\mathbf{k}}^\dagger \end{pmatrix}^T \begin{pmatrix} V_s & 2iJ_{sp} & -2iJ_{sp} & 0 \\ -2iJ_{sp} & V_p & -4J_\perp & 0 \\ 2iJ_{sp} & -4J_\perp & V_p & 0 \\ 0 & 0 & 0 & V_s' \end{pmatrix} \begin{pmatrix} b_{s,\mathbf{k}} \\ b_{x,\mathbf{k}} \\ b_{y,\mathbf{k}} \\ b_{s',\mathbf{k}} \end{pmatrix}$$

and the set of eigenvalues is

$$E_{p1}^{(X)} = V_p - 4J_\perp \quad (4.19)$$

$$E_{s'}^{(X)} = V_s' \quad (4.20)$$

$$E_{p2}^{(X)} = \frac{V_p - 4J_\perp + \sqrt{(4J_\perp + (V_p - V_s))^2 + 32J_{sp}^2}}{2} \quad (4.21)$$

$$E_s^{(X)} = \frac{V_p - 4J_\perp - \sqrt{(4J_\perp + (V_p - V_s))^2 + 32J_{sp}^2}}{2}. \quad (4.22)$$

At the M -points, e.g. $k_x = k_y = \pi/a$, we have

$$H_M = \begin{pmatrix} b_{s,\mathbf{k}}^\dagger \\ b_{x,\mathbf{k}}^\dagger \\ b_{y,\mathbf{k}}^\dagger \\ b_{s',\mathbf{k}}^\dagger \end{pmatrix}^T \begin{pmatrix} 4J_{ss} + V_s & 0 & 0 & 0 \\ 0 & 4J_\parallel + V_p & 0 & 0 \\ 0 & 0 & 4J_\parallel + V_p & 0 \\ 0 & 0 & 0 & 4J_{ss}' + V_s' \end{pmatrix} \begin{pmatrix} b_{s,\mathbf{k}} \\ b_{x,\mathbf{k}} \\ b_{y,\mathbf{k}} \\ b_{s',\mathbf{k}} \end{pmatrix}$$

and the set of eigenvalues is

$$E_p^{(M)} = V_p + 4J_{\parallel} \quad (\text{two-fold degenerate}) \quad (4.23)$$

$$E_s^{(M)} = V_s + 4J_{ss} \quad (4.24)$$

$$E_{s'}^{(M)} = V'_s + 4J'_{ss} \quad . \quad (4.25)$$

Finally, half way in between Γ and M , e.g. $k_x = k_y = \pi/(2a)$, we have

$$H_{\Gamma M} = \begin{pmatrix} b_{s,\mathbf{k}}^\dagger \\ b_{x,\mathbf{k}}^\dagger \\ b_{y,\mathbf{k}}^\dagger \\ b_{s',\mathbf{k}}^\dagger \end{pmatrix}^T \begin{pmatrix} V_s & 2iJ_{sp} & 0 & -2J_{ss}^d \\ -2iJ_{sp} & V_p & 0 & 4iJ_{sp} \\ 0 & 0 & V_p & 0 \\ -2J_{ss}^d & -4iJ_{sp} & 0 & V'_s \end{pmatrix} \begin{pmatrix} b_{s,\mathbf{k}} \\ b_{x,\mathbf{k}} \\ b_{y,\mathbf{k}} \\ b_{s',\mathbf{k}} \end{pmatrix} .$$

Here one eigenvalue is obviously V_p , while the others are not easily solved analytically.

We can use the above equations in order to express the tight-binding parameters in terms of energies of tight-binding bands at symmetry points. The energies of tight-binding bands are in turn set equal to those of the Bloch bands. In this process it is important to correctly associate the tight-binding bands with the corresponding Bloch bands. Away from the band crossings each of the tight-binding bands is predominantly occupying a single orbital and hence its energy scales with the potential offset of the corresponding orbital. We have already chosen our naming convention above accordingly, e.g. $E_p \propto V_p$. One case is slightly more involved, because the scaling of $E_{ss',\pm}^{(\Gamma)}$ depends on whether V_s or V'_s is larger. We can expect $V_s < V'_s$ while the s -lattice site is lower in energy than the s' -lattice site, i.e. for $\theta < 0.5\pi$, and $V_s \geq V'_s$ otherwise. Therefore

$$E_s^{(\Gamma)} = \begin{cases} E_{ss',-}^{(\Gamma)} & \text{for } \theta < 0.5\pi \\ E_{ss',+}^{(\Gamma)} & \text{for } \theta \geq 0.5\pi \end{cases}$$

$$E_{s'}^{(\Gamma)} = \begin{cases} E_{ss',+}^{(\Gamma)} & \text{for } \theta < 0.5\pi \\ E_{ss',-}^{(\Gamma)} & \text{for } \theta \geq 0.5\pi \end{cases} .$$

We can now turn to identifying the energies of Bloch bands with the corresponding energies of tight-binding bands. We identify the tight-binding band associated with the orbital with the lowest energy with the lowest Bloch band and proceed in the same way for higher Bloch bands. In this process it helps to keep Fig. 4.1 in mind. We obtain

$$E_s = \begin{cases} E_1^{(\text{Bloch})} & \text{for } \theta < 0.5\pi \\ E_2^{(\text{Bloch})} & \text{for } 0.5\pi \leq \theta < 0.569\pi \end{cases}$$

$$E_{s'} = \begin{cases} E_4^{(\text{Bloch})} & \text{for } \theta < 0.428\pi \\ E_2^{(\text{Bloch})} & \text{for } 0.428\pi \leq \theta < 0.5\pi \\ E_1^{(\text{Bloch})} & \text{for } 0.5\pi \leq \theta < 0.569\pi \end{cases}$$

$$E_p = \begin{cases} E_2^{(\text{Bloch})} & \text{for } \theta < 0.428\pi \\ E_3^{(\text{Bloch})} & \text{for } 0.428\pi \leq \theta < 0.569\pi \end{cases} .$$

Note that due to the degeneracy of the p -bands we only identify the lower of the two corresponding Bloch bands. For the p -orbitals an extra subtlety arises. In our model we only include p -orbitals on B -sites, but not the ones on A -sites. For $\theta < 0.5\pi$ the p -orbitals on A -sites are, however, energetically lower than the p -orbitals on B -sites. The identification above makes the seemingly wrong identification with p -orbitals on A -sites for $\theta < 0.5\pi$. This ensures that the tight-binding band structure recovers the lowest four Bloch bands and is therefore the more natural choice. Also we do not expect that this choice is important for the results of our numerical simulation since neither of the p -orbitals obtain significant occupations for $\theta < 0.5\pi$.

Finally, we are ready to actually compute the tight-binding parameters. We use the p -type bands at the Γ - and M -points to obtain

$$V_p = \frac{E_p^{(\Gamma)} + E_p^{(M)}}{2}$$

$$J_{\parallel} = \frac{E_p^{(M)} - E_p^{(\Gamma)}}{8} .$$

We could now in principle compute J_{\perp} from $E_p^{(X)}$. It also enters in $E_s^{(X)}$, however, and we therefore obtain better results by fixing this parameter in the Monte-Carlo minimization.

We further assume that we know the parameters for V'_s , J_{sp} and J_{sp}^d , which we will also fix with the Monte-Carlo minimization. We can then identify

$$J'_{ss} = \frac{E_{s'}^M - V'_s}{4}$$

$$V_s = \frac{E_s^{(\Gamma)} + E_{s'}^{(\Gamma)} - (V'_s - 4J'_{ss}) + E_s^{(M)}}{2}$$

$$J_{ss} = \frac{E_s^{(M)} - V_s}{4}$$

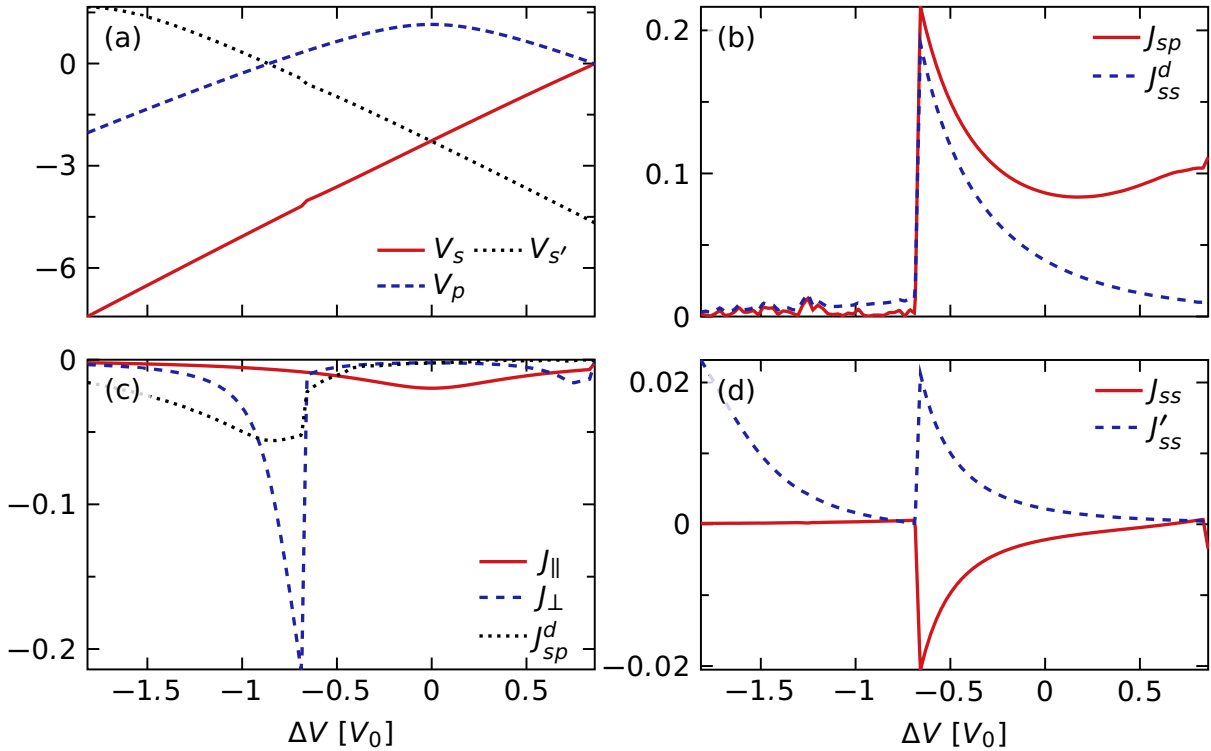


Figure 4.9 – Tight-binding parameters as a function of θ for $V_0 = 7E_{\text{rec}}$, $\lambda_L = 1064$ nm and the rubidium mass $m = 87m_p$. All parameters are given in units of E_{rec} .

$$J_{ss}^d = \begin{cases} \frac{\sqrt{j_{ss}^d}}{8} & \text{for } j_{ss}^d > 0 \\ 0 & \text{else} \end{cases},$$

$$\text{where } j_{ss}^d = \left(E_s^{(\Gamma)} - E_{s'}^{(\Gamma)}\right)^2 - [(V_s - 4J_{ss}) - (V_{s'} - 4J'_{ss})]^2.$$

The case distinction for J_{ss}^d is included to improve numeric convergence of the Monte-Carlo minimization.

Finally, we use the above set of equations in order to implement a Monte-Carlo minimization for V'_s , J_{sp} , J_{sp}^d and J_{\perp} . In each Monte-Carlo step we choose values for V'_s , J_{sp} , J_{sp}^d and J_{\perp} . Then we determine the remaining parameters from the symmetry-point equations above and compare the resulting tight-binding band structure to the Bloch band structure. Afterwards we choose the set of V'_s , J_{sp} , J_{sp}^d and J_{\perp} for the next step according to the Monte-Carlo procedure explained in more detail in App. A.1. We find that the results of the Monte-Carlo procedure are improved by enforcing $J_{sp} > 0$, $J_{sp}^d < 0$ and $J_{\perp} < 0$.

We note that it might seem intuitive to choose $V'_s = E_{s'}^{(X)}$. We have checked that this leads to a sudden jump of $V_{s'}$ at $\theta = 0.428\pi$ and rather unphysical results for V_s and $V_{s'}$ for $\theta < 0.428\pi$. As the s' -orbitals are the highest for these values of θ it is therefore

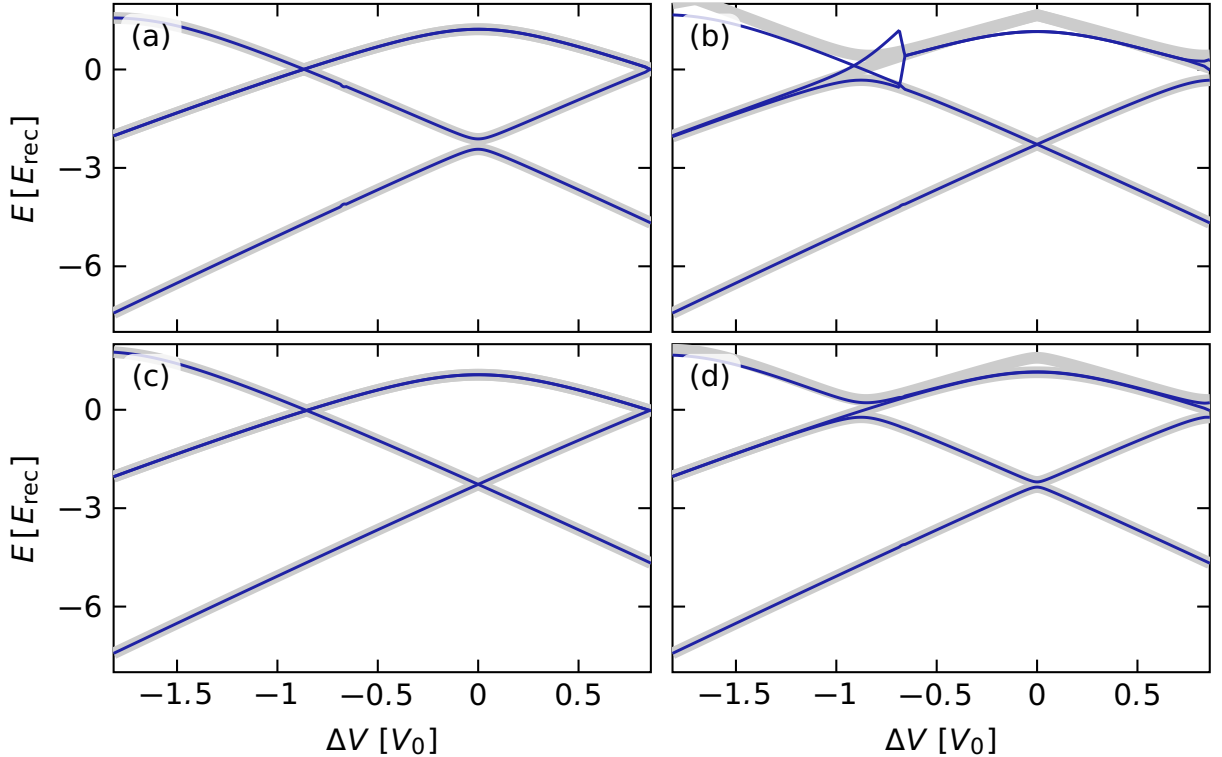


Figure 4.10 – Comparison of tight-binding and Bloch band structure as a function of θ for several high-symmetry points of the lattice. We show the Bloch band structure (wide gray lines) as well as the tight-binding band structure (narrow blue lines) for the Hamiltonian from Eq. 4.15. The tight-binding parameters are the ones giving the best fit to the Bloch bands. Their values are shown in Fig. 4.9. Panel (a) shows the Γ -, panel (b) the X -, panel (c) the M -point and panel (d) the point half way between Γ and M . The positions of the symmetry points in the Brillouin zone are marked in Fig. 4.5.

beneficial to relax the condition $V'_s = E_s^{(X)}$ and instead include V'_s in the minimization routine.

With this procedure we obtain the set of hopping parameters shown in Fig. 4.9. Here we use the parameters $V_0 = 7E_{\text{rec}}$, $\lambda_L = 1064 \text{ nm}$ and $m = 87m_p$, which are inspired by the experiments in Refs. [131–137]. This is also the set we use for all our calculations in sections 4.2 and 4.3. It leads to almost perfect agreement of the tight-binding and Bloch band structures for the lowest two bands, see Fig. 4.10. For the third and fourth band there are slight deviations in particular close to the X -points. The largest deviations are, however, in a regime of θ , where these bands are unoccupied during our simulations.

Interaction terms

So far we have adjusted the hopping parameters to match the noninteracting Bloch band structure. Now we will determine the prefactors U_A and U_B for the interaction part of

the Hamiltonian given in Eq. 4.16. In the experiments in Refs. [131–137] each lattice sites consists of a 1-d elongated tube. Our first goal is to compute the 1-d-interaction strength for each of these tubes. To do so we make the harmonic approximation at the bottom of the lattice potential, see Eq. 4.1, and use the corresponding harmonic-oscillator length in order to estimate the 1-d-interaction strength. Near the two inequivalent minima of the lattice potential, it can be approximated as

$$V_C(x', y') = \text{const.} + V_0 k_L^2 [1 + \sigma_C \cos(\theta)] (x^2 + y^2) \quad ,$$

where $\sigma_A = 1$ and $\sigma_B = -1$. By comparing to the harmonic-oscillator potential $V(x, y) = \frac{1}{2}m\omega^2(x^2 + y^2)$ we can identify

$$\begin{aligned} \omega_C &= \sqrt{\frac{2V_0 k_L^2 (1 + \sigma_C \cos(\theta))}{m}} \\ x_{0,C} &= \sqrt{\frac{\hbar}{\sqrt{2V_0 m (1 + \sigma_C \cos(\theta))}}} = \frac{\lambda_L}{2\pi} \frac{1}{\sqrt[4]{V_0/E_{rec} (1 + \sigma_C \cos(\theta))}} \quad . \end{aligned}$$

The 1-d interaction strength is then given by (see e.g. [187])

$$g_{1d,C} = \frac{2\hbar^2 a_{\text{scattering}}}{m x_{0,C}^2} \quad ,$$

where $a_{\text{scattering}}$ is the 3-d scattering length.

In ultracold-atom experiments one often speaks of two-dimensional experiments. Of course we are living in a three-dimensional world and there can not be truly two-dimensional experiments. What is meant instead is that the confinement in the third (in our case z -) direction is strong enough that only the lowest harmonic-oscillator state is occupied. In that case we could approximate

$$U_C = g_{1d,C} \int dz |\psi_0(z)|^4 \quad ,$$

where $\psi_0(z)$ is the ground-state wave function of the harmonic oscillator.

In our case this approximation is not valid. In fact, the contrary is the case. The experiments in [131–137] have a rather shallow trap in the z -direction. Additionally we excite atoms into higher bands and thereby insert a large amount of energy into the system. Atoms falling back to the lowest band can thereby obtain energies of several E_{rec} , which will also be shared with the degrees of freedom in the z -direction. This is actually beneficial for loading atoms into higher bands since the degrees of freedom in the z -direction act as a bath leading to thermalization of the atoms. We estimate that during

our simulations more than 10 harmonic-oscillator states can be excited in the z -direction.

Discretizing the z -direction

We therefore take a different approach for our numerical simulations. We artificially discretize the z -direction. In other words we assume to have a shallow lattice in the z -direction. This allows us to identify individual lattice sites and define hopping and interaction strengths between these sites. The lattice constant of this virtual lattice is called discretization length d_z . For this approach we need to estimate the effective occupation n_{eff} , hopping constant J_z and interaction strength U_{eff} for the virtual lattice model.

First we obtain an estimate for the density of the cloud in the center of the trap for a given total number of atoms in the trap. To this end we use the Thomas-Fermi approximation (see e.g. [187])

$$\begin{aligned} n(z) &= (\mu - V(z))/g_{1d} \\ V(z) &= \frac{1}{2}m\omega_z^2 z^2 \quad . \end{aligned}$$

For a given chemical potential the edge of the atomic cloud is at

$$z_{\text{max}} = \sqrt{\frac{2\mu}{m\omega_z^2}} \quad .$$

For a fixed number of atoms in each 1-d-tube N_{tube} we can obtain an expression for the chemical potential by integrating the density over the whole tube

$$\mu = \frac{1}{2} \sqrt[3]{\frac{9m\omega_z^2 g_{1d}^2 N_{\text{tube}}^2}{4}} \quad .$$

Finally, within the mean-field approximation, the density in the center of the cloud is given by

$$n(0) = \frac{\mu}{g_{1d}} = \frac{1}{2} \sqrt[3]{\frac{9m\omega_z^2 N_{\text{tube}}^2}{4g_{1d}}} \quad .$$

Then the effective density and interaction strength in the center of the trap are

$$n_{\text{eff}} = n(0)d_z \qquad U_{\text{eff}} = g_{1d}/d_z$$

such that the mean-field interaction energy agrees: $U_{\text{eff}}n_{\text{eff}} = g_{1d}n(0)$. Finally, we get

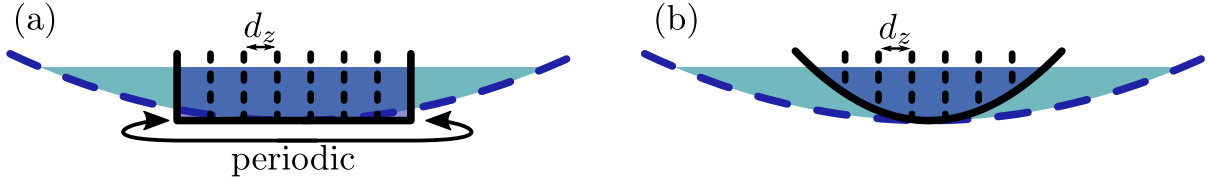


Figure 4.11 – Sketch of the lattice potential in the experiment (dashed blue line) and in our simulations (solid black line). We show two different implementations in panels (a) and (b). Dashed vertical lines indicate the artificial discretization with discretization length d_z that we use in our simulations.

an estimate for the hopping constant by comparing the dispersion relation of the tight-binding lattice model to the dispersion relation of free particles³

$$-2J_z \cos(kd_z) \approx -2J_z \left(1 - \frac{1}{2}k^2d_z^2 \right) \stackrel{!}{=} \frac{\hbar^2 k^2}{2m} - \mu \quad .$$

We can therefore identify

$$J_z = \frac{\hbar^2}{2md_z^2} \quad .$$

When discretizing the trap in the z -direction it is important to choose the discretization length small enough such that quantum and thermal fluctuation within each site can be neglected. As an estimate we can compare the discretization length to the healing length of the condensate (see e.g. [187])

$$\xi = \sqrt{\frac{\hbar^2}{2mg_{1d}n(0)}}$$

and the thermal de-Broglie wavelength

$$\lambda_T = \sqrt{\frac{2\pi\hbar^2}{mk_B T}} \quad .$$

For the experiments in [131–137] we have

³Since the harmonic trap in the z -direction is shallow its dispersion relation can be approximated by the free-particle dispersion.

param	value
λ_L	1064nm
E_{rec}	$2h \cdot \text{kHz}$
$a_{\text{scattering}}$	5nm
ω_z	$2\pi \cdot 79 \text{ Hz}$
V_0	$7E_{\text{rec}}$

such that for 300 atoms per tube and $\theta = 0.35\pi$ we obtain a size of the cloud of $2z_{\text{max}} \approx 20 \mu\text{m}$. At the same time we obtain $\xi \approx 0.15 \mu\text{m}$ and the thermal de-Broglie wavelength at temperature $T = 48 \text{ nK}$ is $\lambda_T = 0.85 \mu\text{m}$. Hence in order to model the full system we would have to use a total number of 200 sites with a discretization length of $d_z = 0.1 \mu\text{m}$. Modeling such a large number of sites, while at the same time including a sufficient number of lattice sites in the x - and y - direction is numerically challenging. We take two different approaches to avoid this problem. In the first approach we model only the dynamics in the center of the trap by using a box potential with periodic boundary conditions. The density is then chosen such that it matches the density in the center of the experimental harmonic trap, see Fig. 4.11(a). The second approach uses a steeper harmonic trap, such that we can match the density of the experimental and theoretical system in the center of the cloud. The steeper trap ensures that we reach zero density at the edge of the cloud with a sufficiently small number of lattice sites, see Fig. 4.11(b).

Unless stated otherwise we use for our numerical simulations in Sec. 4.2 a discretization length of $d_z = 0.13 \mu\text{m}$, implying $J_z = 1.7 E_{\text{rec}}$, 300 atoms per tube and

$\Delta V [V_0]$	$g_{1d,A} n_A(0) [E_{\text{rec}}]$	$n_{\text{eff},A}$	$U_{\text{eff},A} [E_{\text{rec}}]$	$U_{\text{eff},B} [E_{\text{rec}}]$
-1.8	1.405	2.9	0.491	0.301
-0.9	1.327	2.9	0.450	0.359
0	1.240	3.0	0.407	0.407
0.43	1.194	3.1	0.384	0.428
0.86	1.144	3.2	0.361	0.449

We only give the occupations on A -sites since these are the only occupied sites when we initialize the system at $\Delta V = -1.8V_0$.

Finally, we note that discretizing the z -direction changes the dispersion relation from quadratic to a cos-type dispersion relation. While this is a good approximation near the bottom of the band it is certainly not true any more for larger momenta. As an estimate of the validity we here give the bandwidth of the cos-type dispersion relation

$$\Delta\epsilon = 4J_z \approx 6.8 E_{\text{rec}}$$

for $d_z = 0.13 \mu\text{m}$. A slightly better approximation can be obtained by using the Bogoliubov energies

$$\Delta E = 4J_z \sqrt{1 + \frac{U_{\text{eff}} n_{\text{eff}}}{2J_z}} .$$

For the parameters above we obtain $\Delta E = 7.7 E_{\text{rec}}$, while for the same parameters but $d_z = 0.3 \mu\text{m}$ we obtain $\Delta E = 2.1 E_{\text{rec}}$ and for $d_z = 1 \mu\text{m}$ $\Delta E = 0.5 E_{\text{rec}}$. The distance between the first and second band, see Fig. 4.6, can be up to $5 E_{\text{rec}}$. Therefore a discretization length of $d_z = 0.3 \mu\text{m}$ is already too large.

4.2. Dynamics of atoms in excited bands

Loading atoms into the excited bands of an optical lattice gives rise to intriguing dynamics. In order to model these dynamics we use classical field theory. This method has been widely applied in ultracold-atom systems, for reviews see [188–193]. The main idea is that, in the limit of high occupation of individual quantum modes, the matter-wave field of each quantum-mechanical mode behaves like a classical field. In other words the integer mode occupations can be replaced by continuous complex numbers. The full quantum-mechanical time evolution can then be approximated by effective equations for the classical field.

We derive the equations of motion for bosons in the s - p_x - p_y -lattice within classical field theory. This allows us to compute the time evolution for arbitrary changes of the tight-binding parameters. We use the equations of motion to model the process of loading atoms into excited bands of the s - p_x - p_y -lattice and study the subsequent dynamics. For low enough initial temperature the atoms condense in the upper band, forming a chiral condensate with equal occupation on the two nonequivalent X -points of the lattice. On longer time scales the atoms decay back to the lowest band. We find that the coherence of the atoms inhibits decay and hence represents a self-stabilization mechanism of the condensate. We identify the underlying decay mechanisms and show that the origin of the self-stabilization is destructive interference of the respective decay channels. We also prepare the atoms in just one of the two X -points of the upper band and find coherent instanton-type oscillations between the two degenerate many-body ground states, i.e. the chiral condensates $|\Xi_{\pm}\rangle$. Finally, we investigate different schemes for preparing the atoms in the upper band.

4.2.1. Theory background: classical field theory

Here we give a brief introduction to classical field theory with a strong focus on the methods used in this thesis for describing the dynamics of atoms in higher bands. For a more detailed description of classical field theory we refer the reader to the excellent and extensive set of reviews on classical field theory [188–193].

PGPE-theory

For the projected Gross-Pitaevskii equation (PGPE) one considers the modes that are described by classical field equations to be strictly separated from the environment, hence the modes are described by a micro-canonical ensemble.

For our calculations we use the Hamiltonian from Eqs. 4.2, 4.10 and 4.16 and solve the Heisenberg equations of motion for the annihilation operators

$$\frac{db_j}{dt} = i \left[H - \mu b_j^\dagger b_j, b_j \right].$$

Here we include a chemical potential μ that is adjusted such that the desired particle number is reached. In these equations we replace the annihilation operators by complex numbers and solve the resulting ordinary differential equations (ODEs) for b_{s,\mathbf{R}_i} $\mathbf{R}_i \in A$ and b_{s,\mathbf{R}_i} , b_{x,\mathbf{R}_i} and b_{y,\mathbf{R}_i} $\mathbf{R}_i \in B$. Each of the ODEs consists of a sum of terms, where each term arises from one of the hopping or interaction terms of the Hamiltonian. Here we exemplarily give some of the resulting terms. The full set of equations is given in App. A.2.1. For example the terms corresponding to H_{sp_x} are

$$\frac{db_{s,\mathbf{R}_i}}{dt} = \dots + iJ_{sp_x} b_{x,\mathbf{R}_i - \mathbf{e}'_x/2} - iJ_{sp_{-x}} b_{x,\mathbf{R}_i + \mathbf{e}'_x/2} + \dots \quad (4.26)$$

$$\frac{db_{x,\mathbf{R}_i}}{dt} = \dots + iJ_{sp_x} b_{s,\mathbf{R}_i + \mathbf{e}'_x/2} - iJ_{sp_{-x}} b_{s,\mathbf{R}_i - \mathbf{e}'_x/2} + \dots, \quad (4.27)$$

while the equations for the interaction term

$$\frac{U_B}{2} \sum_{\mathbf{R}_i \in B} b_{x,\mathbf{R}_i}^\dagger b_{x,\mathbf{R}_i} b_{y,\mathbf{R}_i}^\dagger b_{y,\mathbf{R}_i} \quad (4.28)$$

are

$$\frac{db_{x,\mathbf{R}_i}}{dt} = \dots - \frac{iU_B}{2} b_{y,\mathbf{R}_i}^\dagger b_{y,\mathbf{R}_i} b_{x,\mathbf{R}_i} \dots \quad (4.29)$$

$$\frac{db_{y,\mathbf{R}_i}}{dt} = \dots - \frac{iU_B}{2} b_{x,\mathbf{R}_i}^\dagger b_{x,\mathbf{R}_i} b_{y,\mathbf{R}_i} \dots. \quad (4.30)$$

Initial state

For the initial state of the system we need to determine the set of complex numbers, where each of them corresponds to one of the annihilation operators $b_j = b_{\{s,x,y\},\mathbf{R}_i}$. We start from an empty lattice $b_j = 0$ and then vary all b_j according to a Monte-Carlo minimization procedure described in more detail in appendix A.1.1. For the Monte-Carlo procedure we use the Hamiltonian as the minimization functional and adjust the Monte-Carlo temperature to the desired temperature of the lattice. For our simulations we repeat this procedure and the subsequent time evolution many times. We average the observables over all of these Monte-Carlo trajectories. This procedure accounts for thermal fluctuations.

An improved description of the initial state can be obtained by sampling from the Wigner function of the system, see e.g. [188]. In particular, such a description accounts for quantum fluctuations in the initial state. For our case, however, the stochastic thermal sampling turns out to be sufficient.

SPGPE-theory

The stochastic projected Gross-Pitaevskii equation (SPGPE) is an extension of the PGPE, in which we also allow for exchange of energy and particles with the environment. The interactions with the environment are modeled by effective stochastic processes corresponding to gain and loss of atoms and energy. Here we mainly give the SPGPE for completeness. We model our system using this set of equations that gives a slightly more precise description of the interaction terms. For our purposes it would, however, be sufficient to use the PGPE. Still it would be an interesting direction for future work to explicitly include decay terms for the loss of atoms from the trap. As we mentioned above when atoms decay from one of the excited bands back into the lowest band they gain a large amount of energy. This energy can be larger than the trapping potential in the x - y -plane and hence the atoms can be lost from the trap in the experiments in [131–137]. In contrast, in our simulations the atoms always remain in the lowest band instead. Via scattering with excited band atoms the energy they gain in the decay process can be transferred to atoms in excited bands. This energy transfer is an additional source of heating for the excited band population. Including decay terms could therefore lead to an even better description of the experiments in [131–137].

For the derivation of the SPGP-equations we follow a procedure described in the appendix to [194]. Here we only show the calculation exemplarily for some of the terms of the tight-binding Hamiltonian. The full set of equations is given in App. A.2.2. Since our goal is to include effective stochastic gain and loss terms we start from the Lindblad

equation [158] for the density matrix

$$\frac{d}{dt}\rho = i[\rho, H] - \frac{1}{2} \sum_{\alpha} \{L^{\alpha\dagger}L^{\alpha}\rho + \rho L^{\alpha\dagger}L^{\alpha} - 2L^{\alpha}\rho L^{\alpha\dagger}\} \quad . \quad (4.31)$$

Apart from the Hamiltonian H , which we take to be the one from Eqs. 4.2, 4.10 and 4.16, and the density matrix ρ this equation contains Lindblad operators L^{α} . Here we are mainly interested in the Lindblad operator corresponding to loss of atoms

$$L^i = \sqrt{\gamma_i} b_{s, \mathbf{R}_i} \quad \text{for } \mathbf{R}_i \in B \quad .$$

We use the procedure described in [194] in order to map the terms in Eq. 4.31 to equations for the Wigner function W . For example a hopping term of the form

$$H = b_i^{\dagger} b_j + b_j^{\dagger} b_i$$

leads to⁴

$$\begin{aligned} \partial_t W &= -\frac{2}{\hbar} \text{Im} \left[\frac{\partial}{\partial \beta_i} \beta_j + \frac{\partial}{\partial \beta_j} \beta_i \right] W \\ &= -\frac{1}{\hbar} \left[\frac{\partial}{\partial x_i} y_j - \frac{\partial}{\partial y_i} x_j + \frac{\partial}{\partial x_j} y_i - \frac{\partial}{\partial y_j} x_i \right] W \quad , \end{aligned}$$

where we have replaced the operators b_i by complex numbers $\beta_i = x_i + iy_i$ and $x_i, y_i \in \mathcal{R}$. As explained in [194] the resulting equations for the Wigner function are Fokker-Planck equations and can therefore be recast in the form of stochastic differential equations (SDEs). For example for the above hopping term we obtain for $i \neq j$

$$\begin{aligned} \frac{\partial x_i}{\partial t} &= y_j & \frac{\partial y_i}{\partial t} &= -x_j \\ \frac{\partial x_j}{\partial t} &= y_i & \frac{\partial y_j}{\partial t} &= -x_i \quad . \end{aligned}$$

When evaluating these terms for H_{sp_x} and rewriting them with complex derivatives, we indeed get the same equations as Eqs. 4.26 and 4.27.

For the interaction term

$$H = b_i^{\dagger} b_j^{\dagger} b_j b_i$$

⁴Note that for a complex number $z = x + iy$: $\partial/\partial z = 1/2 \partial/\partial x - i/2 \partial/\partial y$ and $\partial/\partial z^* = 1/2 \partial/\partial x + i/2 \partial/\partial y$.

we obtain for $i \neq j$

$$\begin{aligned} \partial_t W &= -\frac{2}{\hbar} \text{Im} \left[\frac{\partial}{\partial \beta_j} |\beta_i|^2 \beta_j + \frac{\partial}{\partial \beta_i} |\beta_j|^2 \beta_i - \frac{1}{2} \frac{\partial}{\partial \beta_i} \beta_i - \frac{1}{2} \frac{\partial}{\partial \beta_j} \beta_j \right] W \\ &= -\frac{1}{\hbar} \left[\frac{\partial}{\partial x_i} y_i \left(x_j^2 + y_j^2 - \frac{1}{2} \right) + \frac{\partial}{\partial x_j} y_j \left(x_i^2 + y_i^2 - \frac{1}{2} \right) \right. \\ &\quad \left. + \frac{\partial}{\partial y_i} x_i \left(\frac{1}{2} - x_j^2 - y_j^2 \right) + \frac{\partial}{\partial y_j} x_j \left(\frac{1}{2} - x_i^2 - y_i^2 \right) \right] \end{aligned}$$

and

$$\begin{aligned} \frac{dx_i}{dt} &= y_i \left(x_j^2 + y_j^2 - \frac{1}{2} \right) & \frac{dy_i}{dt} &= x_i \left(\frac{1}{2} - x_j^2 - y_j^2 \right) \\ \frac{dx_j}{dt} &= y_j \left(x_i^2 + y_i^2 - \frac{1}{2} \right) & \frac{dy_j}{dt} &= x_j \left(\frac{1}{2} - x_i^2 - y_i^2 \right) \quad . \end{aligned}$$

Rewriting these in terms of complex derivatives and using the explicit interaction term from Eq. 4.28 we obtain

$$\begin{aligned} \frac{d\beta_{x,\mathbf{R}_i}}{dt} &= -\frac{iU_B}{2} \left[\beta_{y,\mathbf{R}_i}^* \beta_{y,\mathbf{R}_i} - \frac{1}{2} \right] \beta_{x,\mathbf{R}_i} \\ \frac{d\beta_{y,\mathbf{R}_i}}{dt} &= -\frac{iU_B}{2} \left[\beta_{x,\mathbf{R}_i}^* \beta_{x,\mathbf{R}_i} - \frac{1}{2} \right] \beta_{y,\mathbf{R}_i} \quad . \end{aligned}$$

We see by comparing to Eqs. 4.29 and 4.30 that an extra $1/2$ occurs in the equations. This factor accounts for the zero-point motion of the harmonic oscillator and hence leads to a slightly more appropriate description for modes with comparatively low occupations.

Finally, for the Lindblad term $L^i = \sqrt{\gamma_i} b_{s,\mathbf{R}_i}$ we obtain for the density matrix

$$\frac{d\rho}{dt} = -\frac{\gamma_i}{2} \left(b_{s,\mathbf{R}_i}^\dagger b_{s,\mathbf{R}_i} \rho + \rho b_{s,\mathbf{R}_i}^\dagger b_{s,\mathbf{R}_i} - 2b_{s,\mathbf{R}_i} \rho b_{s,\mathbf{R}_i}^\dagger \right) \quad .$$

This maps to

$$\begin{aligned} \frac{dW}{dt} &= \gamma_i \left\{ \text{Re} \left[\frac{\partial}{\partial \beta_{s,\mathbf{R}_i}} \beta_{s,\mathbf{R}_i} \right] + \frac{1}{2} \frac{\partial}{\partial \beta_{s,\mathbf{R}_i}} \frac{\partial}{\partial \beta_{s,\mathbf{R}_i}^*} \right\} W \\ &= \gamma_i \left[\frac{1}{2} \frac{\partial}{\partial x_{s,\mathbf{R}_i}} x_{s,\mathbf{R}_i} + \frac{1}{2} \frac{\partial}{\partial y_{s,\mathbf{R}_i}} y_{s,\mathbf{R}_i} + \frac{1}{8} \left(\frac{\partial^2}{\partial x_{s,\mathbf{R}_i}^2} + \frac{\partial^2}{\partial y_{s,\mathbf{R}_i}^2} \right) \right] W \end{aligned}$$

for the Wigner function and we obtain the SDEs

$$\frac{dx_{s,\mathbf{R}_i}}{dt} = -\frac{\gamma_i}{2} x_{s,\mathbf{R}_i} + \frac{\sqrt{\gamma_i}}{2} \mathcal{N}_{x,i}(t)$$

$$\frac{dy_{s,\mathbf{R}_i}}{dt} = -\frac{\gamma_i}{2}y_{s,\mathbf{R}_i} + \frac{\sqrt{\gamma_i}}{2}\mathcal{N}_{y,i}(t) \quad ,$$

where $\mathcal{N}(t)$ is, in each time step of the SDE-integration, randomly sampled from a Gaussian distribution with zero mean and unit standard deviation.

4.2.2. Quench protocol and parameter settings

Here we describe the set of parameters which is used for all simulations in this section. This set is motivated by the settings used in Refs. [131–137] and [N3]. We initialize the system with $12 \times 12 \times 25$ ($x \times y \times z$) lattice sites. We start from an empty lattice and fill the lattice using a variational Monte-Carlo minimization with 50000 Monte-Carlo steps, for details see App. A.1. We use periodic boundary conditions in the x - and y -direction. For the z -direction we use a harmonic trap such that the density of the atoms vanishes at the edge of the trap, see Sec. 4.1.2 and Fig. 4.11. We adjust the chemical potential such that the density in the center of the trap is similar to the one in Refs. [131–137]. All observables are averaged over the full trap. Hence, the resulting particle numbers are lower than the ones in the center. The discretization length for the z -direction is $d_z = 0.13 \mu\text{m}$. The values of the tight-binding parameters are given in Sec. 4.1.2. For the interaction strength we scale the estimates obtained in Sec. 4.1.2 by 0.9. This scaling factor approximately accounts for the higher particle number that we use for our simulations in order to ensure that we stay in the range of validity of classical field theory. The protocol for the quench is sketched by red arrows in Fig. 4.1. We initialize the system at $\Delta V_{\text{init}} = -1.8V_0$ and start the time evolution with a fast quench changing the value of ΔV from $\Delta V_{\text{init}} = -1.8V_0$ to $\Delta V_{\text{eq}} = 0.43V_0$ within the first 100 μs . Afterwards we let the system equilibrate at $\Delta V_{\text{eq}} = 0.43V_0$ for 20 ms before we perform a second slow quench during 4 ms, hence reaching ΔV_f after 24 ms. For the simulations from Ref. [N3] we compare to a different experimental setup, where we use a direct quench without the intermediate step of equilibration at $\Delta V_{\text{eq}} = 0.43V_0$.

4.2.3. Condensation in higher bands: the s - p_x - p_y -condensate

When loading atoms into a lattice with alternating deep and shallow lattice sites and then suddenly performing a quench exchanging the depth of the lattice sites the atoms are transferred to the second band (remember the sketch in Fig. 4.1). On intermediate time scales the atoms prethermalize in the second band before on even longer time scales they decay back to the first band. We show the occupations of each orbital after such a

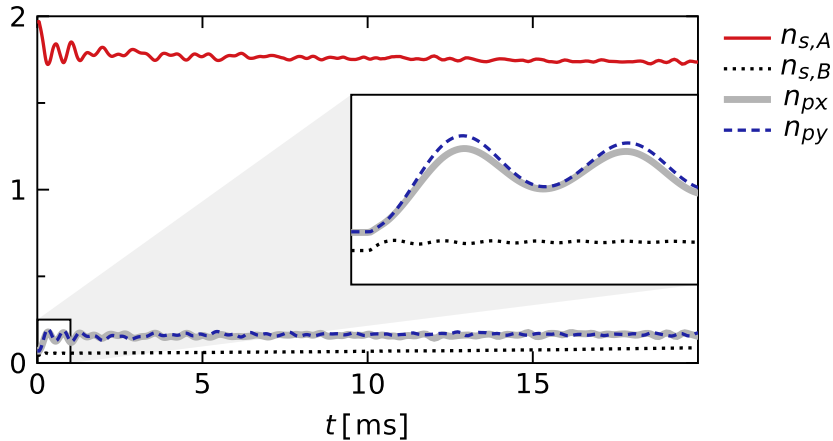


Figure 4.12 – Orbital occupations as a function of time for a single Monte-Carlo trajectory. We show the dynamics without doing a second quench, i.e. $\Delta V_{\text{eq}} = \Delta V_f = 0.43 V_0$. The inset shows a zoom of the region marked in the large figure. The system is initialized with temperature $T = 1/2 E_{\text{rec}}/k_B = 48$ nK.

quench in Fig. 4.12

$$n_{s,C} = \frac{1}{N_C} \sum_{\mathbf{R}_i \in C} \langle b_{s,\mathbf{R}_i}^\dagger b_{s,\mathbf{R}_i} \rangle \quad n_\sigma = \frac{1}{N_A} \sum_{\mathbf{R}_i \in A} \langle b_{\sigma,\mathbf{R}_i}^\dagger b_{\sigma,\mathbf{R}_i} \rangle \quad ,$$

where $\sigma \in \{p_x, p_y\}$, $C \in \{A, B\}$ and the sum runs over all sites of the A - or B -sublattice, respectively. Initially almost all atoms are located in the s -orbitals on A -sites (from now on called s_A -orbitals). Other orbitals only have small thermal occupations. After the quench to $\Delta V_f = 0.43 V_0$ the atoms relax almost instantaneously, after less than 1 ms, to an intermediate steady state. Almost no atoms are transferred to s_B -orbitals, while p -orbitals increase their thermal occupation due to the reduced energy difference between s_A - and p -orbitals.

The quench process will always lead to some heating. Still, for sufficiently low initial temperature, it is possible that thermalization within each tube in the z -direction leads to recondensation in the second band. Then the occupation of p -orbitals leads to a condensation mode that spontaneously breaks the symmetry of the lattice. The J_{sp} -hopping terms favor the alignment of neighboring s - and p -orbitals, see Fig. 4.13. This leads to the anti-alignment of s -orbitals with distance $\mathbf{e}'_{x,y}$. Two independent sublattices form. The relative phase between these sublattices is set by the interaction term $b_{x,\mathbf{R}_i}^\dagger b_{x,\mathbf{R}_i}^\dagger b_{y,\mathbf{R}_i} b_{y,\mathbf{R}_i} + \text{h.c.}$. The interaction is minimized for the chiral orientation of p -orbitals leading to two degenerate condensation modes $|\Xi_\pm\rangle$. In each initialization the system randomly picks one of these condensation modes with equal probability.

We would like to test the realization of the chiral condensate in our simulations. Our

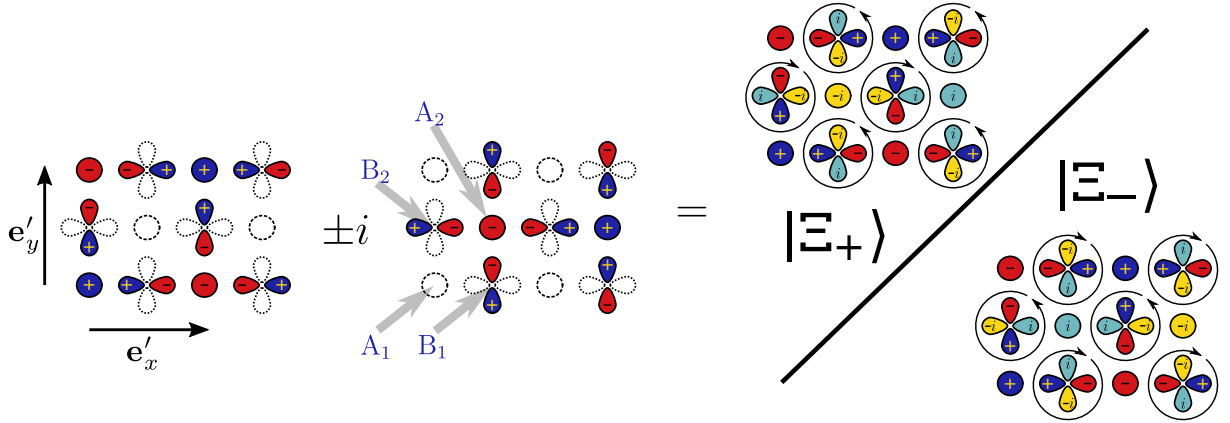


Figure 4.13 – Sketch of the condensation mode. Circles indicate s -orbitals while dumbbells indicate p -orbitals. There are two degenerate condensation modes that mix the two sublattices shown in the figure with relative phase $+i$ or $-i$. The condensation mode spontaneously breaks the symmetry of the lattice. We therefore introduce the site labels $A_{1,2}$ and $B_{1,2}$.

goal is to construct a correlation function that probes the relative orientation of the p -orbitals, allowing to detect their $p_x \pm ip_y$ -character. We first consider the single-particle correlation function between different orbitals

$$C^\sigma(\mathbf{d}) = \frac{1}{N_{A1}} \sum_{\mathbf{R}_i \in A_1} \frac{b_{s,\mathbf{R}_i}^\dagger b_{\sigma,\mathbf{R}_i+\mathbf{d}}}{\sqrt{\langle b_{s,\mathbf{R}_i}^\dagger b_{s,\mathbf{R}_i} \rangle \langle b_{\sigma,\mathbf{R}_i+\mathbf{d}}^\dagger b_{\sigma,\mathbf{R}_i+\mathbf{d}} \rangle}} \quad , \quad (4.32)$$

where $\sigma \in \{s, x, y\}$. For simplicity we have restricted ourselves to correlations of an s_{A1} -orbital with an arbitrary second orbital.

Within classical field theory the single-particle correlation function gives the phase difference between the two sites considered. In order to illustrate this behavior we consider a system with only two states and wave functions $\psi_1 = \sqrt{n_1}e^{i\phi_1}$ and $\psi_2 = \sqrt{n_2}e^{i\phi_2}$. Then

$$\left\langle \frac{b_1^\dagger b_2}{\sqrt{\langle b_1^\dagger b_1 \rangle \langle b_2^\dagger b_2 \rangle}} \right\rangle = e^{i(\phi_2 - \phi_1)} \quad .$$

For an s -condensate all phases are aligned and hence $C^s(\mathbf{d}) = 1$ for all \mathbf{d} .

We show a snapshot of the single-particle correlations after 40 ms in Fig. 4.14. Only the correlations on the first sublattice shown in Fig. 4.13 can be observed since the two orientations of the second sublattice average out when taking many initializations. The correlations on the visible sublattice are consistent with the chiral condensation mode. We find that this condensation mode is the ground state for all values $0 < \Delta V < 0.86V_0$.

In order to test the relative orientation of the two sublattices shown in Fig. 4.13, we

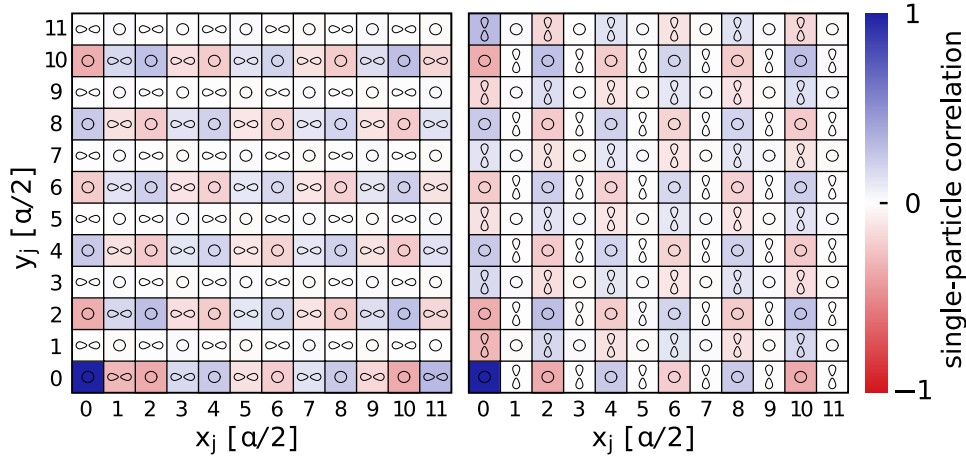


Figure 4.14 – Snapshot of the single-particle correlations at $t = 40$ ms. The resulting correlations are consistent with the condensation mode shown in Fig. 4.13. We show the real part of the single-particle correlation function $\text{Re}[\langle \mathcal{C}^\sigma \rangle(\mathbf{d}_j)]$ as a function of $d_j = (x_j, y_j)$. On A -sublattice sites we show the correlation with s -orbitals (i.e. $\sigma = s$) in both panels. On B -sublattice sites we show the correlation with p_x -orbitals (i.e. $\sigma = x$) in the left and with p_y -orbitals (i.e. $\sigma = y$) in the right panel. Small sketches on each site indicate which correlation is shown. The imaginary part of all correlations vanishes. For this simulation there is no second quench, i.e. $\Delta V_{\text{eq}} = \Delta V_f = 0.43 V_0$. The system is initialized with temperature $T = 1/2 E_{\text{rec}}/k_B = 48$ nK. All observables are averaged over 100 Monte-Carlo trajectories.

introduce the chirality of p -orbitals, i.e. the correlation of p_x - and p_y -orbitals on the same site,

$$\mathcal{C}_{\text{chir}}^C = \frac{1}{N_C} \sum_{\mathbf{R}_i \in C} \mathcal{I}_{\mathbf{R}_i} \quad ,$$

$$\text{where } \mathcal{I}_{\mathbf{R}_i} = \frac{1}{2i} \frac{b_{x,\mathbf{R}_i}^\dagger b_{y,\mathbf{R}_i} - b_{y,\mathbf{R}_i}^\dagger b_{x,\mathbf{R}_i}}{\sqrt{\langle b_{x,\mathbf{R}_i}^\dagger b_{x,\mathbf{R}_i} \rangle \langle b_{y,\mathbf{R}_i}^\dagger b_{y,\mathbf{R}_i} \rangle}}$$

and $C \in \{B_1, B_2\}$. We note that the anti-symmetrization of the operator is the analog of taking the imaginary part of the resulting expectation value.

We find that $\langle \mathcal{C}_{\text{chir}}^C \rangle = \pm 1$ for the $p_x \pm i p_y$ orientation on a given orbital. We say that this p -orbital has positive or negative chirality. Since the chiral condensate has alternating chirality on diagonally neighboring lattice sites, see Fig. 4.13, we need to evaluate the chirality for both B_1 - and B_2 -sites separately. Faint dashed lines in Fig. 4.15(a) show this observable for a single Monte-Carlo trajectory. Indeed the chirality is always opposite on B_1 - and B_2 -sites. We observe that the system does not only randomly pick one of the two condensation modes in each Monte-Carlo trajectory, but in fact even switches between the two condensation modes for a single initialization. Both effects result in

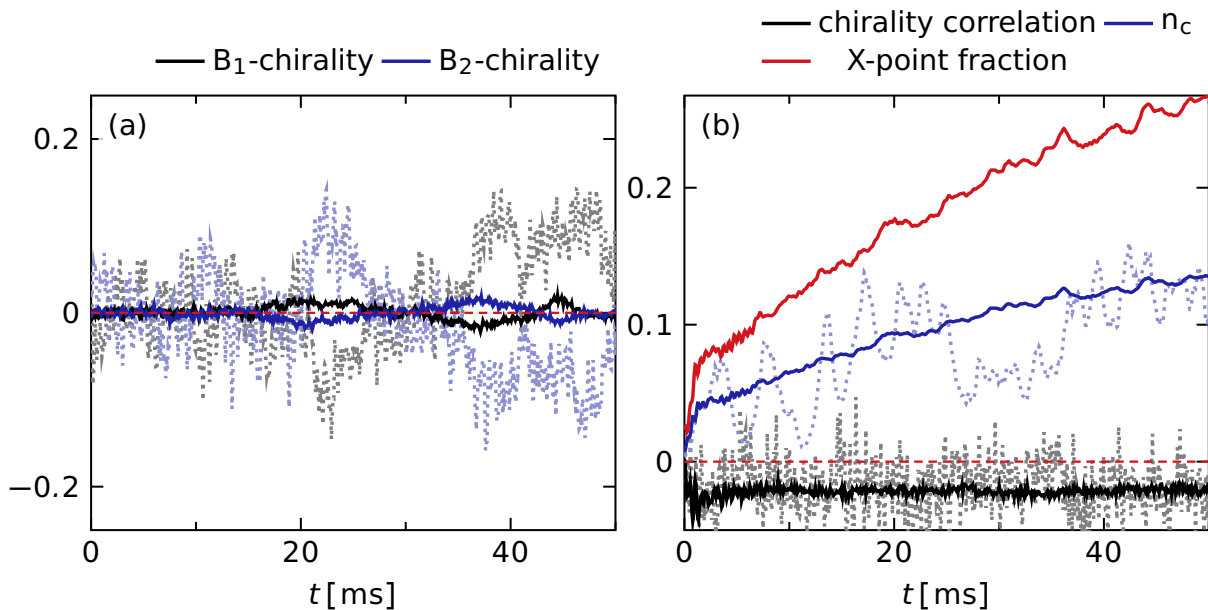


Figure 4.15 – Correlations as a function of time. Panel (a) shows the p-site chirality averaged over the B_1 - and B_2 - sublattice sites, $\mathcal{C}_{\text{chir}}^{B1,2}$. Panel (b) shows the averaged p-chirality correlation $\mathcal{C}_{\text{chir-chir}}$, the condensate fraction n_c and the fraction of atoms occupying the X-points in the second band $n_X^{(2)}/n$. We show the dynamics without doing a second quench, i.e. $\Delta V_{\text{eq}} = \Delta V_f = 0.43 V_0$. The system is initialized with temperature $T = 1/2 E_{\text{rec}}/k_B = 48 \text{ nK}$. Faint dashed lines show an example of a single random initialization of the system, while solid lines are averaged over 100 Monte-Carlo trajectories.

vanishing chirality when averaging over several Monte-Carlo trajectories, see solid lines in Fig. 4.15. In order to avoid this averaging effect and still obtain an estimate of how well the atoms are condensed one can look at the correlation of the chirality between neighboring p -orbitals

$$\mathcal{C}_{\text{chir-chir}} = \frac{1}{N_{B_1}} \sum_{\mathbf{R}_i \in B_1} \mathcal{I}_{\mathbf{R}_i} \mathcal{I}_{\mathbf{R}_i + \mathbf{e}_y} \quad .$$

This quantity is shown in Fig. 4.15(b). For a pure chiral condensate the chirality correlation $\mathcal{C}_{\text{chir}}^{xy} = -1$, while for a wave function where all p orbitals have the same orientation $\mathcal{C}_{\text{chir}}^{xy} = 1$. Just as the occupations the chirality correlations reach their equilibrium value almost instantaneously. The negative value of the chirality correlation reflects the staggered order of the chirality of the p -orbitals, which is indicated by circles with rotation directions in Fig. 4.13. The chirality correlation indicates how coherent the atoms are and hence gives an estimate for the condensate density.

A more exact way of computing the condensate density is to consider the relative phases and occupations of all orbitals. We obtain the condensate fraction for the chiral

condensate $|\Xi_{\pm}\rangle$, by summing all single-particle correlations weighted with the correct phase factor

$$n_c^{\pm} = \frac{1}{N^2} \sum_{\mathbf{R}_i, \mathbf{R}_j} \sum_{\sigma, \tau \in \{s, x, y\}} \frac{\langle b_{\sigma, \mathbf{R}_i}^{\dagger} b_{\tau, \mathbf{R}_j} \rangle e^{-i\Phi_{\sigma\tau}(\mathbf{R}_i, \mathbf{R}_j)}}{\sqrt{\langle b_{\sigma, \mathbf{R}_i}^{\dagger} b_{\sigma, \mathbf{R}_i} \rangle \langle b_{\tau, \mathbf{R}_j}^{\dagger} b_{\tau, \mathbf{R}_j} \rangle}} ,$$

where $\Phi_{\sigma\tau}(\mathbf{R}_i, \mathbf{R}_j)$ is the relative phase that the respective orbitals should have in the chiral condensate, see Fig. 4.13. Note that n_c^{\pm} is the condensate fraction and therefore $0 < n_c^{\pm} < 1$. We also define the fraction of atoms condensed in both modes by

$$n_c = n_c^+ + n_c^- .$$

In Fig. 4.15(b) we see that just as the chirality correlation the condensate fraction has a sharp initial increase on a time scale of less than a millisecond. In contrast to the chirality correlation it keeps increasing on longer time scales of about 40 ps. This reflects the buildup of long-range correlations.

Finally, we define a set of observables that is similar to the ones presented above but is closer to the observables that are accessible in experiments. In ultracold-atom experiments it is usually difficult to extract the occupations of individual sites and orbitals. The occupations of individual bands are, however, much more accessible via band mapping [146, 181–185].

In order to obtain the occupations of bands we diagonalize the tight-binding Hamiltonian in momentum space in order to obtain the Bloch functions for each band

$$|\psi_{\mathbf{k}}^{\alpha}\rangle .$$

From our simulation we extract the site-resolved wave function $|\phi_i\rangle$. Fourier transforming leads to the wave functions in momentum space

$$|\phi_k\rangle = \frac{1}{\sqrt{N}} \sum_i e^{i\mathbf{k}\mathbf{R}_i} |\phi_i\rangle .$$

We can now compute the overlap with the Bloch functions in order to extract the occupation of individual momentum modes for each band

$$n_k^{(\alpha)} = |\langle \psi_k^{\alpha} | \phi_k \rangle|^2 .$$

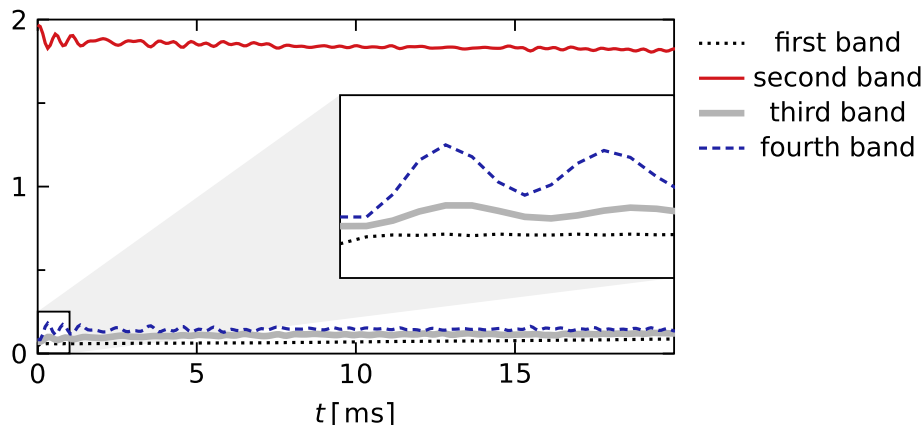


Figure 4.16 – Occupations $n^{(\alpha)}$ of the first to fourth band as a function of time for a single Monte-Carlo trajectory. We show the dynamics without doing a second quench, i.e. $\Delta V_{\text{eq}} = \Delta V_f = 0.43 V_0$. The inset shows a zoom of the region marked in the large figure. The system is initialized with temperature $T = 1/2 E_{\text{rec}}/k_B = 48 \text{ nK}$.

Summing over all momenta gives the occupations of bands

$$n^{(\alpha)} = \sum_k n_k^{(\alpha)} .$$

The minimum of the second band is at the X -points of the lattice. In experiments, it is common to define a region of interest around the X -points in order to obtain an estimate of the number of condensed atoms. We can imitate this approach by considering the occupation of the X -points $n_X^{(\alpha)}$. The condensate fraction can then be approximated by the normalized X -point occupation $n_X^{(\alpha)}/n$, where $n = \sum_\alpha n^{(\alpha)}$. We show this quantity in Fig. 4.15(b). Its time evolution is qualitatively similar to the one for the condensate fraction. Since there are also thermal atoms occupying the X -points it is generally slightly larger than the condensate fraction.

For the tight-binding model of the s - p_x - p_y -lattice we consider four orbitals in each unit cell and therefore obtain four bands. Often it will be helpful to look at the number of atoms in excited bands, we therefore define

$$n^{\text{ex}} = n^{(2)} + n^{(3)} + n^{(4)}$$

and similarly $n_X^{\text{ex}} = n_X^{(2)} + n_X^{(3)} + n_X^{(4)}$.

Away from the band crossings the occupations of bands agree well with the occupations of the corresponding orbitals, compare Figs. 4.12 and 4.16. Only near the band crossings different orbitals mix.

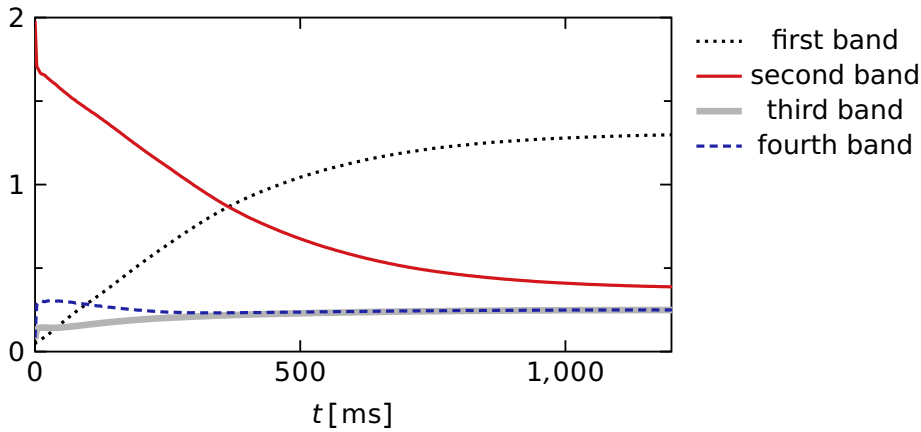


Figure 4.17 – Time evolution of the occupations $n^{(\alpha)}$ of the first four bands. We show the dynamics without doing a second quench, i.e. $\Delta V_{\text{eq}} = \Delta V_f = 0.43 V_0$. The system is initialized with temperature $T = 1/2 E_{\text{rec}}/k_B = 48$ nK and all observables are averaged over 300 Monte-Carlo trajectories.

4.2.4. Lifetime of atoms in higher bands

While the atoms form a stable condensate at intermediate time scales, they decay back to the thermal ground state of the lattice for longer times on the order of several hundred milliseconds. Their lifetime crucially depends on the control parameter θ and the temperature of the system. Here we will therefore investigate the lifetime of the atoms in the second band of the s - p_x - p_y -lattice.

We show the decay dynamics of the band occupations for longer times in Fig. 4.17. After the quench the excitation scheme prepares almost all atoms in the second band with an additional smaller occupation of the fourth band. Within about 1 s the atoms relax towards a thermal state with dominant occupation in the first band. Significant thermal occupations of higher bands remain due to the large energy that the atoms gain when decaying back to the first band.

In Fig. 4.18 we show the time dependence of the second-band occupation as well as its thermal and condensed fraction. We observe three different decay stages. In stage I the number of condensed atoms increases, in stage II there is a large number of condensed atoms and slow decay and stage III is characterized by exponential decay and a vanishing number of condensed atoms. The different decay stages and the resulting metastability of the condensate in the second band will be discussed in more detail in Sec. 4.2.5. Here we consider the speed of the exponential decay in stage III. We define the onset of stage III as the time where the condensate fraction drops below a threshold value and fit the total number of atoms with an exponential

$$f(t) = ae^{-t/T_{\text{decay}}} + b \quad ,$$

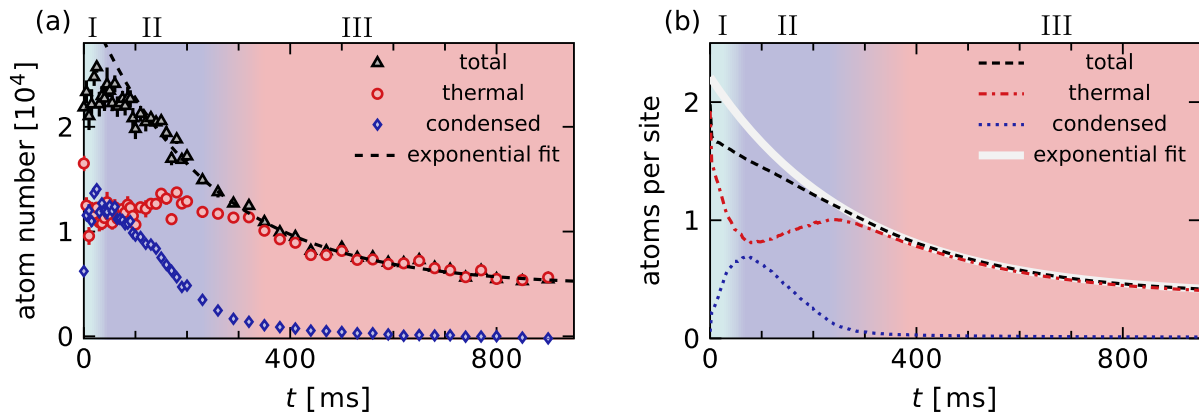


Figure 4.18 – (b) Time evolution of the total number of atoms in the second band $n^{(2)}$ as well as its condensate fraction $n_X^{(2)}$ and thermal fraction $n^{(2)} - n_X^{(2)}$ after a quench to $\Delta V = 0.43 V_0$. Panel (a) shows experimental data for comparison. Details on the experimental data can be found in Ref. [N3]. We identify three main decay stages: the coherence buildup stage (I), the inhibited relaxation stage (II) and the fast relaxation stage (III). The black lines show exponential fits to the data points in stage (III). The temperature of the initial state for both experiments and simulation is $T \approx 0.5 E_{\text{rec}}/k_B \approx 50$ nK. For the simulation all observables are averaged over 300 Monte-Carlo trajectories. This figure has been published in Ref. [N3].

where a, b and T_{decay} are fit parameters.

We extract the decay time scales T_{decay} as a measure for the atom’s lifetime.⁵ The extracted decay time scales as a function of the final potential offset between the two sublattice ΔV_f are shown in Fig. 4.19. The condensate is most stable at intermediate values of ΔV_f close to $\Delta V_f = 0.43 V_0$. Close to the band crossing points at $\Delta V_f = 0$ and $\Delta V_f = 0.86 V_0$ (remember Fig. 4.10) the condensate decays nearly two orders of magnitude faster. We first consider the decay close to $\Delta V_f = 0$. Here the s_A - and s_B -orbitals are almost degenerate. Therefore hopping between these orbitals is likely to occur. Second-order hopping processes via p -orbitals are strongly suppressed due to the high energy of p -orbitals. Therefore the only hopping processes transferring atoms from s_A - to s_B -orbitals are direct hopping terms between these orbitals, i.e. those proportional to J_{ss}^d . For larger value of ΔV_f the energy difference between s_A - and s_B -orbitals increases and these hopping processes are suppressed. Close to the second band crossing at $\Delta V_f = 0.86 V_0$ the energy of the s_B -orbitals is well detuned from both s_A - and p -orbitals. Hence we do not expect hopping-induced decay. Still the decay time scale is two orders of magnitude smaller than the one close to $\Delta V_f = 0.43 V_0$. In agreement with [195] we find that the main origin of decay are the p - s_B -interaction terms, which are $b_{s,\mathbf{R}_i}^\dagger b_{s,\mathbf{R}_i}^\dagger b_{x,\mathbf{R}_i} b_{x,\mathbf{R}_i} + b_{s,\mathbf{R}_i}^\dagger b_{s,\mathbf{R}_i}^\dagger b_{y,\mathbf{R}_i} b_{y,\mathbf{R}_i} +$

⁵We note that this is of course not the only time scale relevant for the lifetime of the atoms. Since the atoms only decay significantly during stage III, the onset of stage III is similarly important.

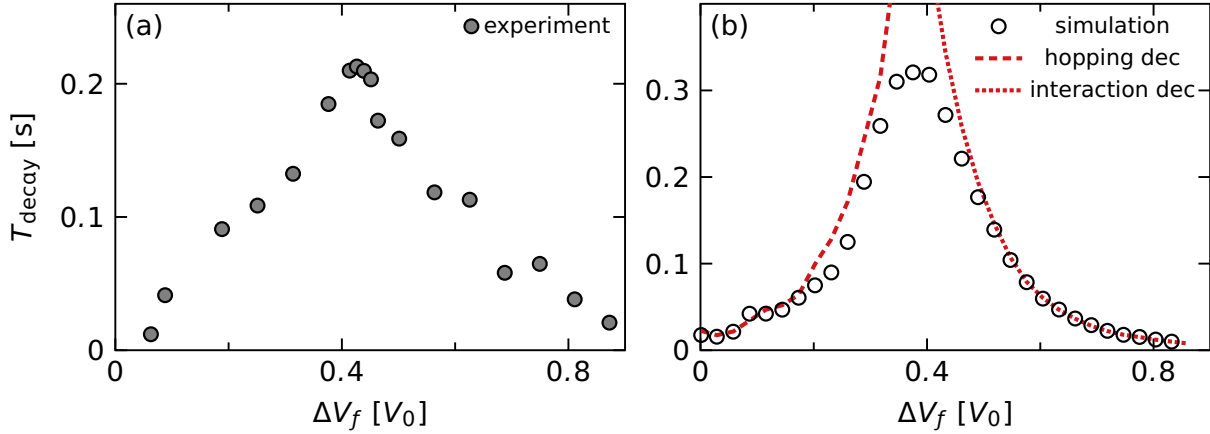


Figure 4.19 – Decay time scale as a function of final potential offset ΔV_f extracted from experiments (a) and numerical simulations (b). Red curves in panel (b) show a simulation where one of the two decay channels has been artificially switched off such that only hopping-induced decay (dashed curve) or only interaction-induced decay (dotted curve) remains. The temperature of the initial state for both experiments and simulation is $T \approx 0.5 E_{\text{rec}}/k_B \approx 50$ nK. For the simulation all observables are averaged over 300 Monte-Carlo trajectories. This figure has been published in Ref. [N3].

h.c.. These are scattering terms where 2 atoms in a p_x - or p_y -orbital collide and change their orbital character to s , ending up in s_B . Near the band crossing at $\Delta V_f = 0.86V_0$ the p -orbitals are close in energy to s_A -orbitals and therefore obtain large occupation, which leads to fast interaction-induced decay. In order to check the significance of the two decay processes at different values of ΔV_f we have artificially switched off each of the terms in our simulations, see Fig. 4.19. When switching the p - s_B -interaction terms off we observe nearly unchanged decay time scales close to $\Delta V_f = 0$, while the atoms become orders of magnitude more stable for $\Delta V_f > 0.43V_0$. The opposite happens when setting $J_{ss}^d = 0$. The decay time scale is nearly unchanged close to $\Delta V_f = 0.86V_0$ and increases by orders of magnitude for $\Delta V_f < 0.43V_0$. Hence we confirm that the main decay mechanism is due to J_{ss}^d -hopping close to $\Delta V_f = 0$ and due to p - s_B -interactions close to $\Delta V_f = 0.86V_0$.

4.2.5. Self-stabilization of condensates in higher bands⁶

So far we found that the lifetime of the atoms crucially depends on the final potential offset ΔV_f and have identified the decay mechanisms. We made the remark already that three different decay stages emerge. Here we analyze and characterize these decay stages.

Immediately after the quench that transfers the atoms to the second band they populate all available Bloch modes almost equally. In the subsequent thermalization dynamics the

⁶Significant parts of this section have been published in Ref. [N3]. The corresponding parts have mainly been written by the author of this thesis.

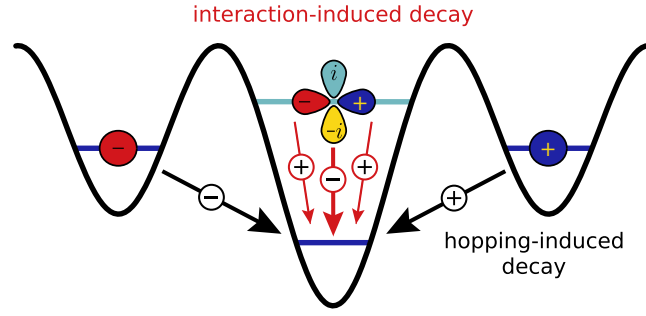


Figure 4.20 – Sketch of decay mechanisms and the inhibition of decay for the chiral condensate. For the hopping-induced decay destructive interference between opposite nearest-neighbor sites leads to the inhibition of decay. For the interaction-induced decay the decay channels of two colliding p_x -orbital atoms and two p_y -orbital atoms interfere destructively. This figure has been published in Ref. [N3]

tubes in the z -direction help the atoms to condense in the second band. Hence the first decay stage depicted in Fig. 4.18 is characterized by an increasing number of condensed atoms and decreasing number of thermal atoms. The number of condensed atoms increases until it reaches the equilibrium value corresponding to the temperature of the atoms. This is the onset of stage II. In the second stage there is a high condensate fraction and the decay is slower than exponential as we see from the exponential fits that agree in stage III, while deviating significantly in stage I and II. We see that in the crossover to stage III the condensate fraction reduces and simultaneously the decay of atoms from excited bands to the lowest band becomes faster. This indicates that the correlations of the condensate are responsible for the long lifetimes of the atoms. Indeed we find that the condensation mode shows destructive interference for both decay mechanisms that have been identified in the previous section. As a result the condensate represents a dark state, which leads to metastability of the atoms in the second band. To illustrate this behavior we consider a single s_B -orbital on site \mathbf{R} . For the hopping-induced decay there are four different terms that transfer atoms to this orbital

$$-J_{ss}^d \left(b_{s,\mathbf{R}}^\dagger b_{s,\mathbf{R}+\mathbf{e}'_x} + b_{s,\mathbf{R}}^\dagger b_{s,\mathbf{R}-\mathbf{e}'_x} + b_{s,\mathbf{R}}^\dagger b_{s,\mathbf{R}+\mathbf{e}'_y} + b_{s,\mathbf{R}}^\dagger b_{s,\mathbf{R}-\mathbf{e}'_y} + \text{h.c.} \right) .$$

Assuming that all atoms are condensed in the upper band, we know that s_A -orbitals on opposite sides of the s_B -orbital have opposite phase and hence the above hopping term vanishes, see Fig. 4.20. Hence there is perfect destructive interference for this decay mechanism. If we were able to prepare a perfect condensate in the upper band, it would not decay.

A similar explanation holds for the interaction-induced decay. Here we have identified

$$\frac{U_B}{4} \left[b_{s,\mathbf{R}}^\dagger b_{s,\mathbf{R}}^\dagger b_{x,\mathbf{R}} b_{x,\mathbf{R}} + b_{s,\mathbf{R}}^\dagger b_{s,\mathbf{R}}^\dagger b_{y,\mathbf{R}} b_{y,\mathbf{R}} + \text{h.c.} \right]$$

as the relevant decay mechanism. The condensation mode is characterized by the interaction-stabilized relative phase between p_x - and p_y -orbitals of $\pm i$. It also has the same occupation n_p in these orbitals. When evaluating the above interaction term for the condensate wave function $|\Xi_\pm\rangle$ we therefore obtain

$$\langle \Xi_\pm | a_{i,s}^\dagger a_{i,s}^\dagger (a_{i,x} a_{i,x} + a_{i,y} a_{i,y}) | \Xi_\pm \rangle = \langle \Xi_\pm | a_{i,s}^\dagger a_{i,s}^\dagger (n_p e^{i\phi} - n_p e^{i\phi}) | \Xi_\pm \rangle = 0 \quad .$$

We see that the condensation mode in the s - p_x - p_y -lattice has perfect destructive interference for both decay channels and hence does not decay. Only the thermal fraction decays. Decaying atoms gain an energy corresponding to the band gap between the first and second band, which for our lattice is on the order of E_{rec} . This energy thermalizes also among the atoms in the second band and hence leads to heating of the atoms. This heating effect together with the reduction of the number of atoms in the second band leads to a reduced phase-space density and hence lower condensate fraction. Eventually we cross the phase transition and only thermal atoms remain. This is the onset of stage III. Since now only thermal atoms remain there is no inhibition of decay and the remaining thermal atoms in the second band decay exponentially fast.

Higher initial temperature, shown in Fig. 4.21, leads to higher temperature after the quench and hence a lower condensate fraction. Now the crossover to stage III occurs significantly earlier and the exponential fit is a good approximation even for short times. This confirms that the coherent order of the condensate inhibits relaxation.

A simple two-fluid model for the decay of the atoms can give further insight into the dynamics. We consider only the atoms in the upper band and assume that we have a thermal fraction N_{th} and a condensed fraction N_c of atoms. The total number of atoms is $N_{\text{tot}} = N_{\text{th}} + N_c$. Furthermore we assume that the equilibration within the thermal and condensed atoms happens on a much faster time scale than the equilibration between the two, such that we can assume the equilibration within each fraction to be instantaneous. Without loss of generality we assume that the condensed atoms have zero energy. Following the description in chapter 2 of Ref. [187] we assume a generic density of states

$$g(\epsilon) = c_\alpha \epsilon^{\alpha-1} \quad .$$

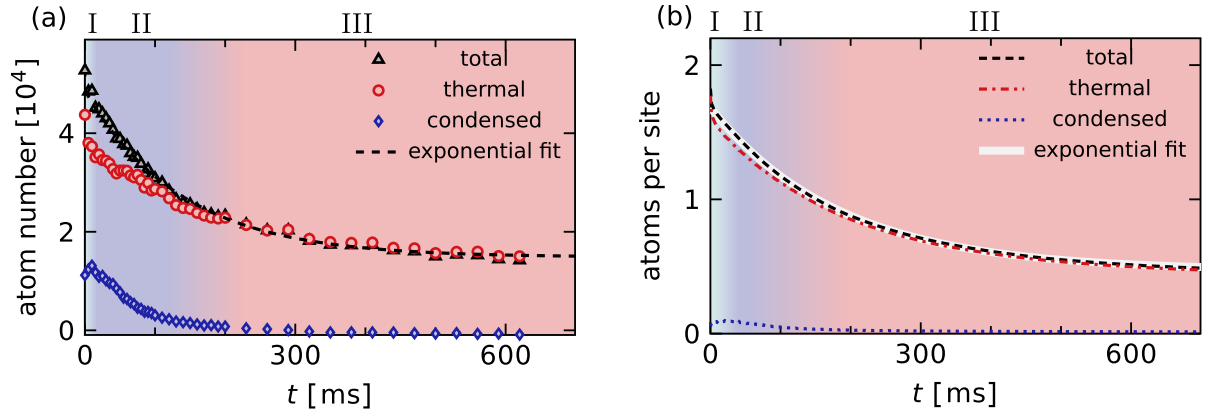


Figure 4.21 – (b) Time evolution of the total number of atoms in the second band $n^{(2)}$ as well as its condensate fraction $n_X^{(2)}$ and thermal fraction $n^{(2)} - n_X^{(2)}$ after a quench to $\Delta V = 0.43 V_0$ for high initial temperature. Panel (a) shows experimental data for comparison. Details on the experimental data can be found in Ref. [N3]. We identify three main decay stages: the coherence buildup stage (I), the inhibited relaxation stage (II) and the fast relaxation stage (III). The black lines show exponential fits to the data points in stage (III). The temperature of the initial state for both experiments and simulation is $T \approx 110$ nK. For the simulation all observables are averaged over 300 Monte-Carlo trajectories. This figure has been published in Ref. [N3].

We can then compute the total number of thermal atoms and the total energy E as

$$\begin{aligned}
 N_{\text{th}} &= \int d\epsilon g(\epsilon) \frac{1}{e^{\epsilon/(k_B T)} - 1} \propto T^\alpha \\
 E &= \int d\epsilon g(\epsilon) \frac{\epsilon}{e^{\epsilon/(k_B T)} - 1} \propto T^{\alpha+1} .
 \end{aligned}$$

We absorb the proportionality constants into the units of temperature and energy and therefore obtain

$$N_{\text{th}} = T^\alpha \qquad N_{\text{th}} T = E .$$

As we have seen above the condensed atoms do not decay due to perfect destructive interference. We therefore assume that only the thermal atoms decay with time scale $1/\gamma_{\text{dec}}$. Furthermore we assume that the thermal and condensed fraction equilibrate on a time scale of $1/\Gamma_{\text{eq}}$. On average whenever a thermal atom decays the total energy is decreased by the mean energy of a thermal atom E/N_{th} . Additionally the atom gains an energy ΔE corresponding to the energy difference between the upper and the lower band. We assume that this energy is redistributed to the atoms in the upper band and hence the energy of these atoms is increased by this amount. Hence the equations of motion for

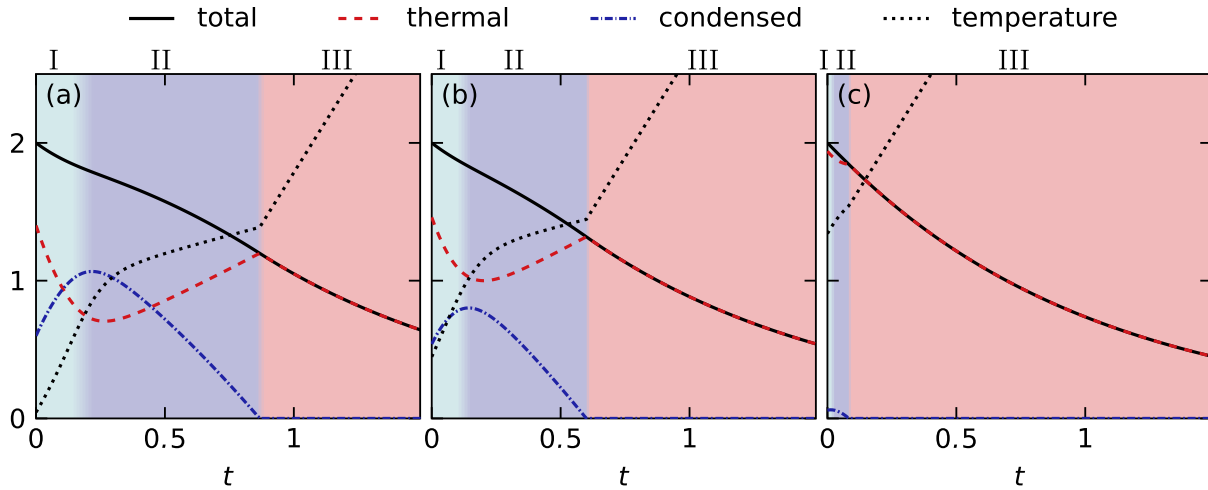


Figure 4.22 – Two-fluid model for self-stabilization at low (a), medium (b) and high (c) initial temperature. We show the total N_{tot} , thermal N_{th} and condensed $N_{\text{tot}} - N_{\text{th}}$ particle number as well as temperature T computed within a two-fluid model. The model shows qualitative agreement with experimental and simulated data shown in Figs. 4.18 and 4.21. All quantities within the toy model are dimensionless. We use $\gamma_{\text{dec}} = 1$, $\Gamma_{\text{eq}} = 3$, $\alpha = 2$ and $\Delta E = 3$. This figure has been published in Ref. [N3].

our model system are

$$\begin{aligned}
 \dot{N}_{\text{th}} &= -\gamma_{\text{dec}} N_{\text{th}} + \Gamma_{\text{eq}} (T^\alpha - N_{\text{th}}) \\
 \dot{N}_{\text{tot}} &= -\gamma_{\text{dec}} N_{\text{th}} \\
 \dot{E} &= \left(\Delta E - \frac{E}{N_{\text{th}}} \right) \gamma_{\text{dec}} N_{\text{th}} \quad .
 \end{aligned} \tag{4.33}$$

We derive the equation for the temperature of the system by taking the derivative of $T = E/N_{\text{th}}$. We obtain

$$\dot{T} = \gamma_{\text{dec}} \Delta E - \frac{\Gamma_{\text{eq}} T}{N_{\text{th}}} (T^\alpha - N_{\text{th}}) \quad . \tag{4.34}$$

These equations are of course only valid as long as the condensate fraction is finite, afterwards $N_{\text{tot}} = N_{\text{th}}$ and

$$\begin{aligned}
 \dot{N}_{\text{th}} &= -\gamma_{\text{dec}} N_{\text{th}} \\
 \dot{T} &= \gamma_{\text{dec}} \Delta E \quad .
 \end{aligned}$$

In our case having one harmonically trapped and two free dimensions we obtain $\alpha \approx 1/2 + 1/2 + 1 = 2$. We show the resulting time dependence in Fig. 4.22. We find that the results agree qualitatively with the simulations based on classical field theory. All main features of the three decay stages are also captured by the two-fluid model. Two

additional insights can be gained from the two-fluid model: firstly, we have easy access to the temperature in the two-fluid model and see that there is only a slow increase while there is still a large condensate fraction, and the temperature increases rapidly afterwards. This can be understood as follows: from Eq. 4.34 we can see that moving an atom from the condensate to the thermal cloud effectively cools the atoms. The reason is that the mean kinetic energy of thermal atoms is larger than the mean kinetic energy of condensed atoms. This cooling process counteracts the heating effect due to the decay of thermal atoms. Secondly, the two-fluid model has a sharp phase transition from a condensate to a purely thermal cloud showing a kink in the condensate fraction. By construction the decay of the two-fluid model is exponential when the condensate fraction vanishes. We also see from Fig. 4.22 that the inflection point of the curve for the total number of excited atoms is exactly the point where the condensate fraction vanishes. This seems to also hold for the experimental data and our classical-field-theory simulations, for these cases the phase transition is, however, smoothed due to the trapping potential.

Within the two-fluid model we can gain insight into the scaling of decay during the different relaxation stages. As we have noted the total number of atoms decays exponentially during stage III. Here we are interested in the scaling during stage II. Since at the onset of stage II the atoms have equilibrated already we can assume instantaneous equilibration, such that $N_{\text{th}} = T^\alpha$, during this stage. With this approximation we can solve Eq. 4.33 and obtain

$$E = (\Delta E - (\Delta E - T_0)e^{-\frac{\gamma}{\alpha+1}t})^{\alpha+1} \quad , \quad (4.35)$$

where $T_0 = E_0^{1/(\alpha+1)}$ is the initial value of the temperature and E_0 the one of the energy. Note that it is crucial to make the approximation $N_{\text{th}} = T^\alpha$ for the differential equation of the energy and not the temperature. In the latter case we would be neglecting the above mentioned change of temperature due to atoms that transfer between the condensate and the thermal fraction. Still we can derive the solution for the time dependence of temperature from Eq. 4.35

$$T = (\Delta E - (\Delta E - T_0)e^{-\frac{\gamma}{\alpha+1}t})^\alpha \quad .$$

The temperature always equilibrates towards a constant value of $T = \Delta E^\alpha$. We therefore consider the solution for the total number of atoms for fixed temperature, then

$$\dot{N}_{\text{tot}}(t) = -\gamma_{\text{dec}}T^\alpha$$

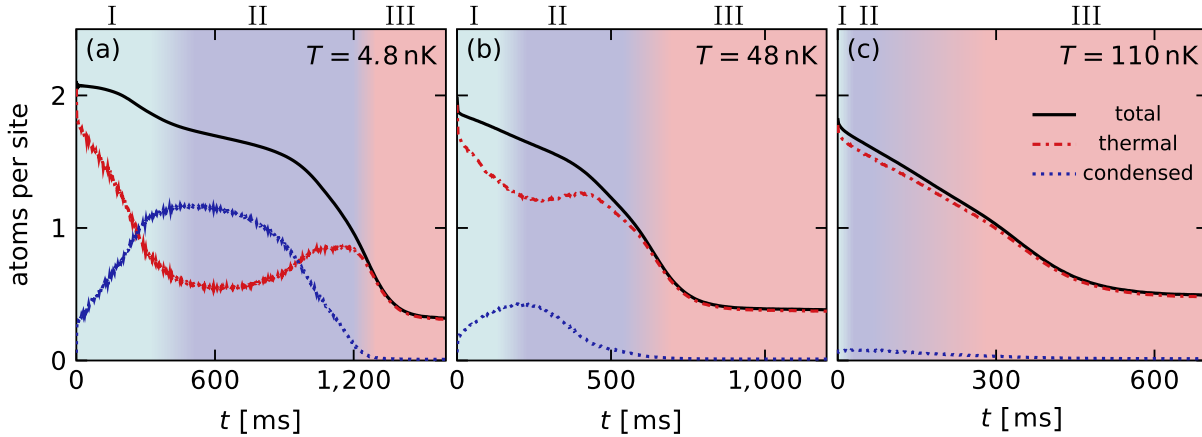


Figure 4.23 – Simulated time evolution of the total number of atoms in the second band $n^{(2)}$ as well as its condensate fraction $n_X^{(2)}$ and thermal fraction $n^{(2)} - n_X^{(2)}$ after a quench to $\Delta V = 0.25 V_0$ for three different temperatures as indicated in the panels. All observables are averaged over 200 Monte-Carlo trajectories. Panel (a) has been published in Ref. [N3].

and

$$N_{\text{tot}} = N_{\text{tot},0} - \gamma_{\text{dec}} T^\alpha t \quad .$$

where $N_{\text{tot},0}$ is the initial value of N_{tot} . Hence for any fixed temperature the total number of atoms decays linearly. This stresses the efficiency for the inhibition of decay, since we obtain linear instead of exponential scaling. Also we confirm that a perfect condensate at $T = 0$ represents a dark state without decay.

We return to our numerical simulations and take a closer look at the coherence-buildup stage. In the beginning of this stage there is a large thermal fraction, hence low coherence and therefore the atoms should decay fast. This effect can not be observed in Fig. 4.18. We do observe it, however, at significantly lower temperatures shown in Fig. 4.23(a) and also see a faint signature of this initial fast decay in the toy model in Fig. 4.22(a). The atoms initially decay fast until the condensate fraction becomes large and the amount of total atoms in the upper bands reaches a plateau with negligible decay. At significantly longer times, the condensate fraction reduces and we enter the fast decay stage. We therefore confirm the fast decay in the condensation stage and conclude that it is only a minor effect at the experimental temperature and therefore not observed in Fig. 4.18.

Finally, we show the decay time scale for several different temperatures in Fig. 4.24(a). We see that the decay time scale has no strong dependence on the initial temperature of the atomic cloud. For all temperatures the decay time scale is fast close to the two band crossings at $\Delta V = 0$ and $\Delta V = 0.86 V_0$. For intermediate values of ΔV there is a competition between the two decay channels. Depending on the relative size of

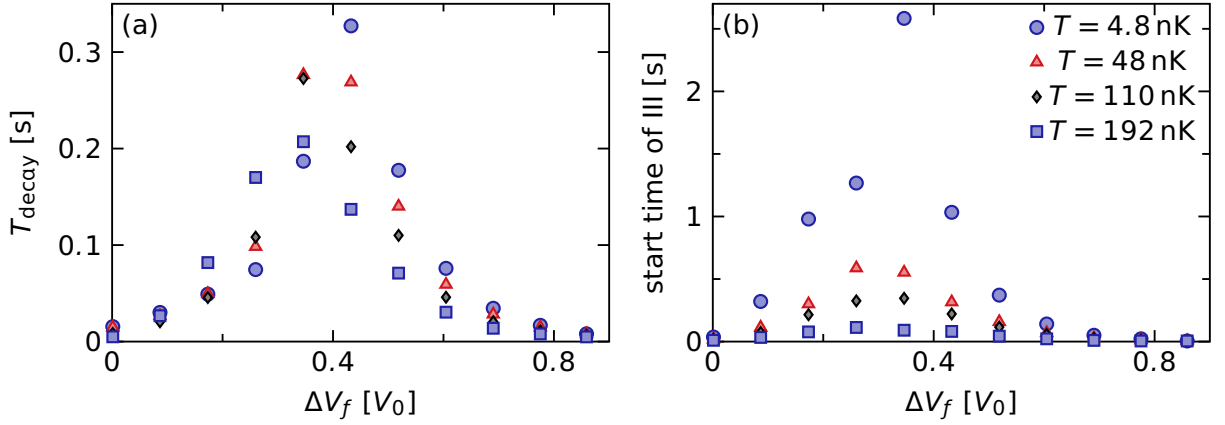


Figure 4.24 – (a) Simulated decay time scale as a function of final potential offset ΔV at several different temperatures as indicated in the legend. After loading the atoms into the second Bloch band they relax back to the lowest band. In stage III the decay is exponential and hence we extract the corresponding time scale. (b) Cross-over time from stage II to III. We extract the time where the condensate fraction drops below 3%, which indicates the cross-over from stage II to III and is the starting point for the exponential fits for the decay time scale. We see that the cross-over time crucially depends on temperature while the temperature dependence of the decay time scale is not as strong. All observables in this figure are averaged over 200 Monte-Carlo trajectories. This figure has been published in Ref. [N3].

the respective decay constants the longest lifetime is obtained close to the center point $\Delta V = 0.43 V_0$. Only the maximum of decay time scale shifts to slightly lower ΔV for higher temperatures. The lacking temperature dependence of the decay time scale can be explained as follows: the initial temperature of the cloud determines the condensate fraction at the beginning of stage II. Hence we expect larger coherence and slower decay during stage II. Subsequently heating leads to increasing temperature and hence reducing phase-space density. The onset of stage III is essentially determined by the time when the phase-space density has reduced below the critical value for condensation. Hence independent of the initial temperature the phase-space density in the beginning of stage III is always the same. Lower initial temperature only leads to a later cross-over from stage II to III. We confirm this by showing the cross-over time point from stage II to III in Fig. 4.24. We define the cross-over time point as the point where the condensate fraction drops below a certain threshold value. We see that indeed it changes dramatically with temperature, indicating significantly longer durations of stage II and as a result longer lifetimes of the condensate for lower initial temperature. Hence also the temperature dependence of the decay time scale and the crossover time point from stage II to III are consistent with the three different decay stages presented in this section.

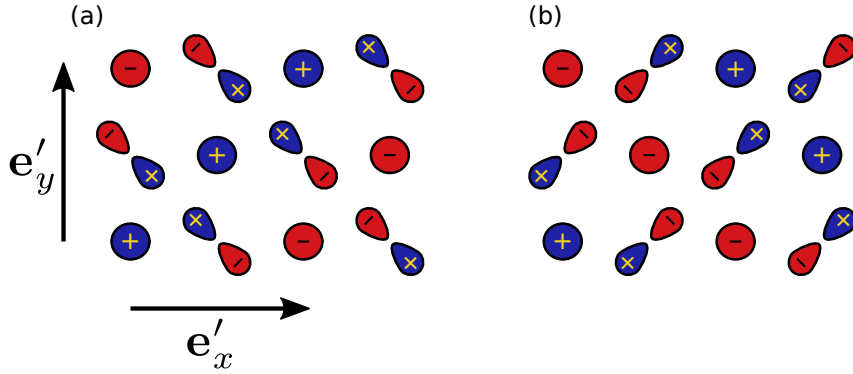


Figure 4.25 – Sketch of the phase pattern of the condensate wave function $|\psi_{\pm}\rangle$ at the X_+ -point in (a) and X_- -point in (b). Circles denote s - and dumbbells p -orbitals.

4.2.6. Oscillation between X -points.⁷

It has been proposed in Ref. [196] that a cloud of atoms prepared at one of the two degenerate minima of the second band, i.e. the X_+ - or X_- -point, see Fig. 4.5, will perform coherent oscillations between the two X -points that encode information about the relative strength of the involved interaction processes. While Ref. [196] used a minimal model considering only the two Bloch states $|\psi_{\pm}\rangle$ at the X_+ - and X_- -point, we study the resulting dynamics within our classical-field-theory simulations. Most notably we find instanton-type dynamics, where the condensate oscillates between the two many-body lowest-energy states $|\Xi_{\pm}\rangle$, which are characterized by chiral order. While the model from Ref. [196] makes precise predictions on the oscillation frequencies of the X -point dynamics these instanton-type oscillations are not observed.

We simulate the dynamics by starting at a moderate negative potential offset $\Delta V_{\text{init}} = -0.63 V_0$. This ensures that the lattice is sufficiently shallow such that the atoms can form a coherent condensate in the s -orbitals on A -sites. Subsequently we use a phase-imprinting technique in which we multiply each orbital with the phase corresponding to the state at the X_+ -point, as depicted in Fig. 4.25(a). This is the theoretical analogue of performing a half-cycle Bloch oscillation in experiments and exerts a momentum kick that moves the cloud of atoms to the X_+ -point. Only after this imprinting step we perform the quench that transfers the atoms to the second band. Here we perform a direct quench to the final imbalance ΔV_f within 100 μs . This protocol prepares the atoms in the Bloch state $|\psi_+\rangle$. The states $|\psi_+\rangle$ and $|\psi_-\rangle$ are, however, not the lowest-energy states of the interacting system. As we have seen in Sec. 4.2.3, the many-body lowest-energy state is the chiral condensate $|\Xi_{\pm}\rangle$ depicted in Fig. 4.13. So far we have characterized this state by its chiral superposition of the p -orbitals with relative phase $\pm i$. An alternative view on this state is that it mixes the Bloch functions $|\psi_{\pm}\rangle$ at the X_+ - and X_- -points with

⁷Parts of this section have been published in Ref. [N4]

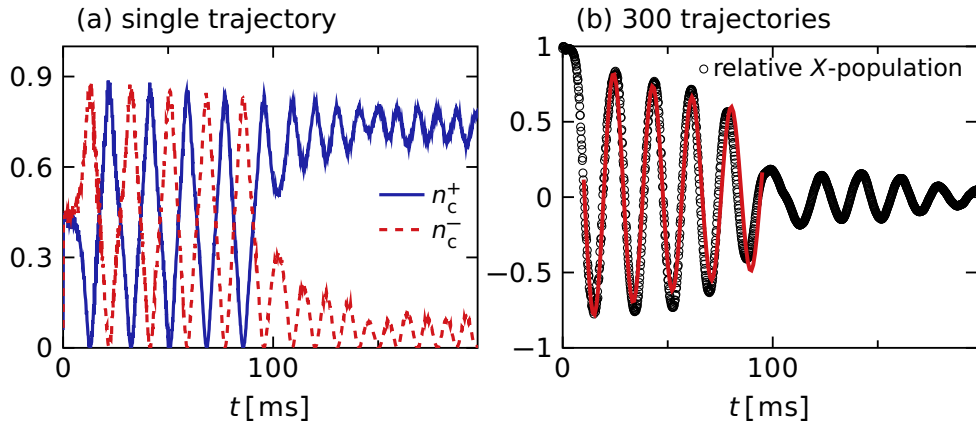


Figure 4.26 – Different representations of the oscillation between X_+ - and X_- -points. Panel (a) shows the number of condensed atoms n_c^\pm in the two degenerate condensate modes $|\Xi_\pm\rangle$, while panel (b) shows the relative occupation of X -points $(n_{X_+}^{\text{ex}} - n_{X_-}^{\text{ex}})/(n_{X_+}^{\text{ex}} + n_{X_-}^{\text{ex}})$. The solid red line in (b) shows a fit with a damped oscillation, as defined in Eq. 4.36. The example shown has a condensate density $n_c = n_c^+ + n_c^- \approx 0.9$. For both panels we initialize the system at $T = 0.005 E_{\text{rec}}/k_B \approx 0.5 \text{ nK}$ and $\Delta V_{\text{init}} = -0.63 V_0$ and perform a direct quench to $\Delta V_f = 0.35 V_0$. Panel (a) shows a single Monte-Carlo trajectory, while panel (b) is averaged over 300 trajectories.

relative phase $\pm i$, such that⁸

$$|\Xi_\pm\rangle = \frac{1}{\sqrt{2}} (|\psi_+\rangle \pm i|\psi_-\rangle) \quad .$$

The corresponding occupations n_c^\pm of $|\Xi_\pm\rangle$ and n_{X_+,X_-}^{ex} of $|\psi_\pm\rangle$ have been defined in Sec. 4.2.3.

In Fig. 4.26 we show the resulting dynamics for low initial temperature. After the quench the atoms recondense at the X_+ -point in the second band, such that the relative X -point occupation $(n_{X_+}^{\text{ex}} - n_{X_-}^{\text{ex}})/(n_{X_+}^{\text{ex}} + n_{X_-}^{\text{ex}}) = 1$. As a result the atoms form an equal superposition of the two interacting lowest-energy states $|\Xi_\pm\rangle$, such that $n_c^+ = n_c^- = n_c/2$. We observe two different stages in the resulting dynamics for $t < 100 \text{ ms}$ and $t > 100 \text{ ms}$, respectively. The first stage is characterized by coherent oscillations between both $|\Xi_\pm\rangle$ and $|\psi_\pm\rangle$. At the zero crossings of the relative X -point occupation the atoms alternate between maximal overlap with $|\Xi_+\rangle$ and $|\Xi_-\rangle$. Similarly, each time n_c^+ and n_c^- cross, the atoms have dominant overlap with either $|\psi_+\rangle$ or $|\psi_-\rangle$, such that $(n_{X_+}^{\text{ex}} - n_{X_-}^{\text{ex}})/(n_{X_+}^{\text{ex}} + n_{X_-}^{\text{ex}}) \approx \pm 1$. In each Monte-Carlo initialization the atoms randomly start with an oscillation towards either $|\Xi_+\rangle$ or $|\Xi_-\rangle$ with equal probability. Therefore

⁸With the convention shown in Figs. 4.13 and 4.25 there is an additional phase factor $(1 - i)/\sqrt{2}$, which we drop for better readability.

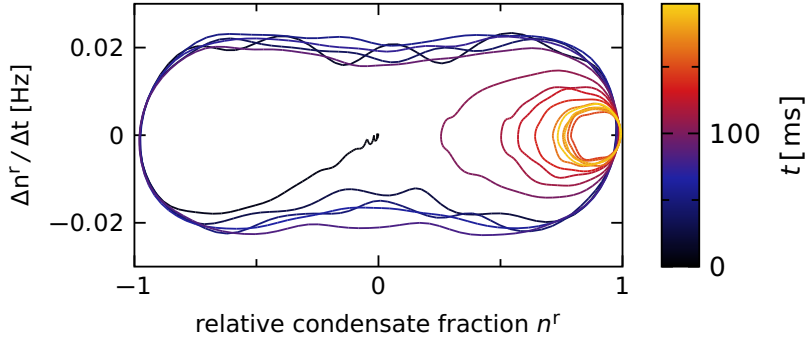


Figure 4.27 – Phase-space diagram of the oscillation between the two many-body lowest-energy states of the second band, which are the two chiral condensate modes $|\Xi_{\pm}\rangle$. We plot the relative condensate fraction $n^r = (n_c^+ - n_c^-) / (n_c^+ + n_c^-)$ on the x - and its numerically determined derivative on the y -axis. Time is encoded in the color scheme, as indicated by the color bar. We distinguish two different dynamical stages: during the first stage there are coherent oscillations between $|\Xi_+\rangle$ and $|\Xi_-\rangle$, see dark outer paths, and during the second stage $|\Xi_+\rangle$ obtains the dominant occupation, see red and yellow inner paths. We use the same set of parameters as in Fig. 4.26. In order to avoid noise we apply a Gaussian filter to n^r . This figure has been published in Ref. [N4].

the oscillations of n_c^{\pm} average out for many Monte-Carlo trajectories. This is the reason why we show these oscillations for a single trajectory in Fig. 4.26(a). In contrast, the oscillation always starts at the X_+ -point as a result of our preparation scheme. We show these oscillations averaged over 300 Monte-Carlo trajectories in Fig. 4.26(b). We see a more pronounced damping effect for the averaged oscillations. This is a result of several different frequency components involved in the oscillations. Depending on the random initialization of the system that accounts for thermal fluctuations, the resulting oscillations may have different frequencies. The dephasing between different frequency components leads to damping of the oscillations.

A different view on the dynamics can be obtained by plotting the oscillations between $|\Xi_+\rangle$ and $|\Xi_-\rangle$ in a phase-space diagram, as shown in Fig. 4.27. As the conjugate variable to the relative condensate fraction

$$n^r = \frac{n_c^+ - n_c^-}{n_c^+ + n_c^-}$$

we use its time derivative $\Delta n^r / \Delta t$. In the initial stage of the dynamics the atoms have almost unit overlap with $|\Xi_{\pm}\rangle$ once per cycle and hence perform oscillations between the two lowest-energy states of the system. This switching between the ground states is called instanton and plays an important role in high-energy physics [197, 198]. In Fig. 4.27 we observe a slight reduction in $\Delta n^r / \Delta t$ whenever $n^r = 0$. This is a result of the slow down

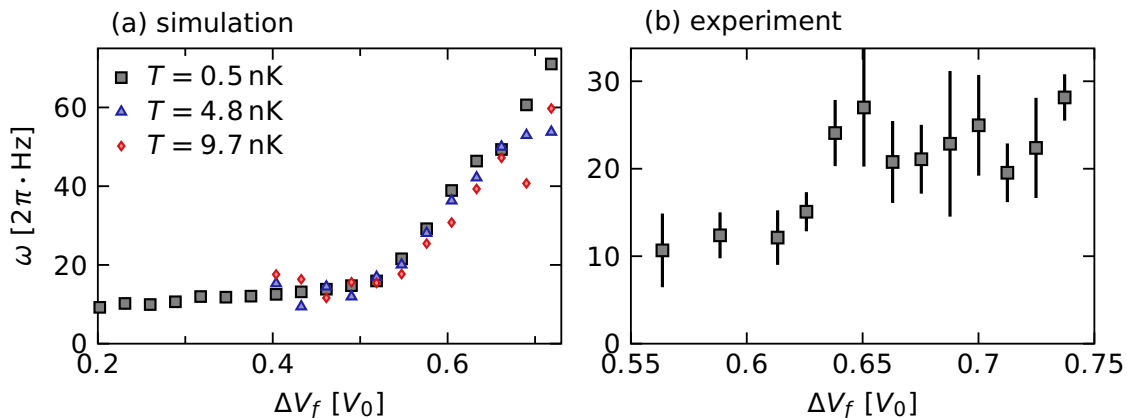


Figure 4.28 – (a) Oscillation frequencies, obtained from fitting the data from our classical-field-theory simulation, are plotted versus ΔV_f . We show the oscillation frequencies at three different initial temperatures, as indicated in the legend. For all three temperatures the obtained oscillation frequencies agree quantitatively. (b) For comparison we show experimental data taken by José Vargas from the group of Prof. Andreas Hemmerich. The temperature for this data is estimated to be 50 nK. For the high-temperature data it is more difficult to observe the low-frequency oscillations and hence we omit these data points in (a) and show a smaller range of ΔV_f in (b). To adjust the mean-field interaction energy to the experimental one we scale the interaction parameters obtained in Sec. 4.1.2 by 0.2 for panel (a). Before fitting all data is averaged over 300 Monte-Carlo trajectories. The experimental data presented in panel (b) has been published in Ref. [N4]. Refer to this reference for details on the experimental protocol.

due to a free-energy barrier between the two lowest-energy states $|\psi_{\pm}\rangle$. Eventually the atoms do not have sufficient energy to overcome this barrier. This is the onset of the second stage of the dynamics at $t \approx 100$ ms. During this stage the atoms are trapped in one of the free-energy minima and hence always have larger overlap with the same one of the states $|\Xi_{\pm}\rangle$. Which of the two states the atoms relax into depends on the initial parameters and the dissipation of the system.

This dynamics is reminiscent of a rigid pendulum swinging in a circle until dissipation reduces the energy far enough that the inverted position at the top of the circle is energetically forbidden. From that point onward the pendulum performs oscillations around the equilibrium position at the bottom of the circle. Depending on the initial conditions and damping the cross-over between the two types of oscillations may take a variable amount of time that leads to a phase jump between the two oscillations. A signature of this phase jump is the strong reduction of the amplitude of the oscillations, observed in Fig. 4.26(b): in each Monte-Carlo trajectory there is a slightly different phase jump. This leads to destructive interference of oscillations when averaging over many trajectories, resulting in significantly reduced amplitudes of the oscillation in the second stage of the dynamics for

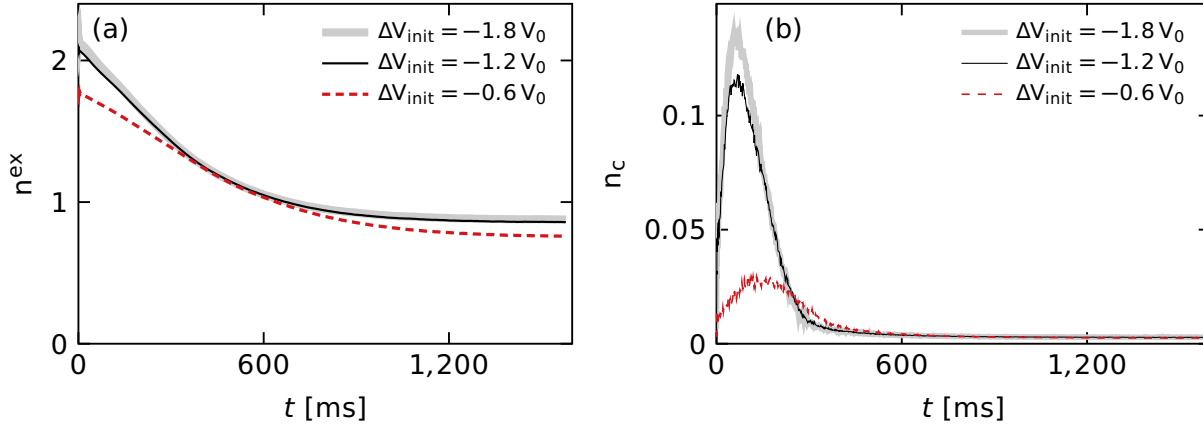


Figure 4.29 – Comparison of the excited band occupation n^{ex} in panel (a) and condensate fraction n_c in panel (b) for different initial values ΔV_{init} . For all cases we choose $\Delta V_{\text{eq}} = \Delta V_f = 0.43 V_0$. The system is initialized with temperature $T = 1/2 E_{\text{rec}}/k_B = 48$ nK and all observables are averaged over 100 Monte-Carlo trajectories.

$t > 100$ ms.

It was proposed in Ref. [196] that the observed oscillations give insight on the interaction properties of the system. In particular, it was predicted that the oscillation frequency depends on the relative strength of those interactions in which atoms exchange their momentum between X_+ and X_- as compared to those in which they keep the same momentum. The exchange-type interactions are related to the interaction terms that change the p -orbital character $b_{x,\mathbf{R}_i}^\dagger b_{x,\mathbf{R}_i}^\dagger b_{y,\mathbf{R}_i} b_{y,\mathbf{R}_i} + \text{h.c.}$ and hence are most pronounced for larger p -orbital occupations close to the band crossing at $\Delta V = 0.86 V_0$. In order to check this prediction we perform a fit to the oscillation between X -points as shown in Fig. 4.26(b). As a fit function we use a damped harmonic oscillation

$$f(t) = a \cos(\omega t + t_0) e^{-bt} + c \quad , \quad (4.36)$$

where a , b , c and t_0 denote fit parameters and ω is the fitted frequency of the oscillation. The resulting oscillation frequencies, shown in Fig. 4.28(a), increase as a function of ΔV_f as p -orbitals get occupied. Hence we confirm the predictions from Ref. [196]. We also obtain qualitative agreement with experimental data, shown in Fig. 4.28(b).

4.2.7. Optimizing the loading procedure

Inspired by the experiments in Refs. [131–137] we have so far mainly used the following quench protocol: we first quench from $\Delta V_{\text{init}} = -1.8 V_0$ to $\Delta V_{\text{eq}} = 0.43 V_0$ within $t_1 = 100 \mu\text{s}$, then wait for equilibration at $\Delta V_{\text{eq}} = 0.43 V_0$ for $t_{\text{eq}} = 20$ ms and perform a second

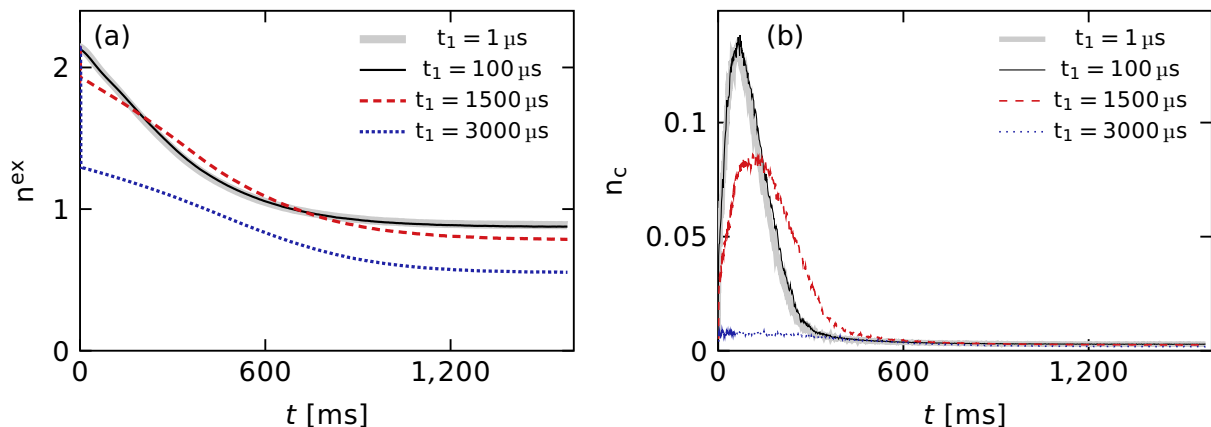


Figure 4.30 – Comparison of the excited band occupation n^{ex} in panel (a) and condensate fraction n_c in panel (b) for different quench-time scales t_1 at $\Delta V_{\text{eq}} = \Delta V_f = 0.43 V_0$. The system is initialized with temperature $T = 1/2 E_{\text{rec}}/k_B = 48 \text{ nK}$ and all observables are averaged over 100 Monte-Carlo trajectories.

quench to ΔV_f within $t_2 = 4 \text{ ms}$. In this section we analyze whether it is possible to obtain a larger condensate fraction or longer lifetime in the upper band by optimizing the quench protocol. We find that the protocol used in Refs. [131–137] is indeed well optimized with only minor options for further improvement.

First consider the starting point of the quench ΔV_{init} . We compare three different cases in Fig. 4.29. The curves for $\Delta V_{\text{init}} = -1.8 V_0$ and $\Delta V_{\text{init}} = -1.2 V_0$ look almost identical. Only the coherence of the condensate in the upper band is slightly better for $\Delta V_{\text{init}} = -1.8 V_0$, see Fig. 4.29(b). The differences for $\Delta V_{\text{init}} = -0.6 V_0$ are rather drastic. The atoms decay significantly faster to the lowest band and the condensate fraction in the upper band never exceeds 0.03. For $\Delta V_{\text{init}} = -0.6 V_0$ the A -sites are comparatively shallow with only a small offset to the B -sites. As a result the initial state has finite thermal occupation on s_B -orbitals, which is disadvantageous for three reasons. First of all this leads to fewer atoms in the upper band, since these atoms can not be transferred. Secondly these orbitals are rapidly lowered during the first quench, which leads to a significant amount of heating. Since the atoms on s_B -orbitals thermalize with the remaining atoms after the quench this leads to a higher temperature of the condensate and hence lower coherence. Thirdly the occupations on s_B orbitals combined with the shallow lattice leads to s-wave coherence of the initial state. This is, however, not the desired symmetry for the chiral condensate and hence leads to less efficient loading. In summary, we find that it is important to choose an initial quench parameter $\Delta V_{\text{init}} < -1.2 V_0$. We fix the value of $\Delta V_{\text{init}} = -1.8 V_0$ for all further simulations.

We note that we purposely choose $\Delta V_{\text{init}} = -0.63 V_0$ for the X -point oscillations. For that case it is important to have a phase-coherent initial state in order to make phase

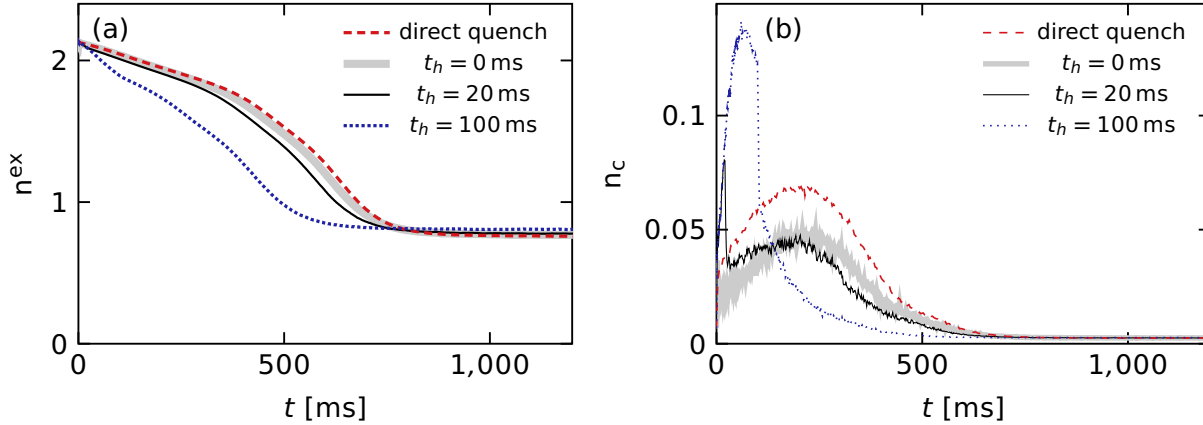


Figure 4.31 – Comparison of the excited band occupation n^{ex} in panel (a) and the condensate fraction n_c in panel (b) for different equilibration times t_{eq} . For the direct quench we choose $\Delta V_{\text{eq}} = \Delta V_f = 0.26 V_0$ and hence there is no holding time. For all other curves we use $\Delta V_{\text{eq}} = 0.43 V_0$ and $\Delta V_f = 0.26 V_0$. The system is initialized with temperature $T = 1/2 E_{\text{rec}}/k_B = 48$ nK and all observables are averaged over 100 Monte-Carlo trajectories.

imprinting possible.

Next we consider the influence of the initial quench duration t_1 . The quench should be slow compared to the harmonic-oscillator frequency of each lattice site ω_C , while at the same time being fast compared to the band splitting at the avoided-crossing point for $\Delta V = 0$. The first constraint ensures that the wave function can equilibrate within each lattice site during the quench. The second constraint ensures that the atoms are transferred from the first to the second band, instead of adiabatically following the first band. For our parameters, see Sec. 4.1.2, the harmonic-oscillator frequency is $\omega_C \approx 50 - 80$ kHz, depending on the value of ΔV and the site $C = A, B$ considered. This corresponds to a time scale of about $10 - 20$ μs . The band splitting of the lowest two bands at $\Delta V = 0$ is approximately $0.3E_{\text{rec}}$, corresponding to a time scale of about $t_{\text{splitting}} \approx 250$ μs . Hence the previously used time scale $t_1 = 100$ μs lies conveniently between the two constraints $10 \mu\text{s} < t_1 < 250 \mu\text{s}$. This value indeed leads to the highest coherence of the condensate within our simulations, see Fig. 4.30. A shorter time scale $t_1 = 1$ μs gives, however, similarly good results, although being much shorter than the time scale affiliated with the harmonic-oscillator frequency. This is to be expected since our simulations do not treat the dynamics within each lattice site. Therefore the atoms equilibrate infinitely fast within each lattice site and there is no lower bound on the quench duration t_1 within our simulations. For longer time scales $t_1 > t_{\text{splitting}} \approx 250$ μs indeed some of the atoms remain in the lowest band. For $t_1 = 3000$ μs more than half of the atoms are transferred to the lowest band during the quench and the remaining atoms fail to condense in the upper band. An interesting situation occurs for $t_1 = 1500$ μs . As $t_1 > t_{\text{splitting}}$ some of the atoms

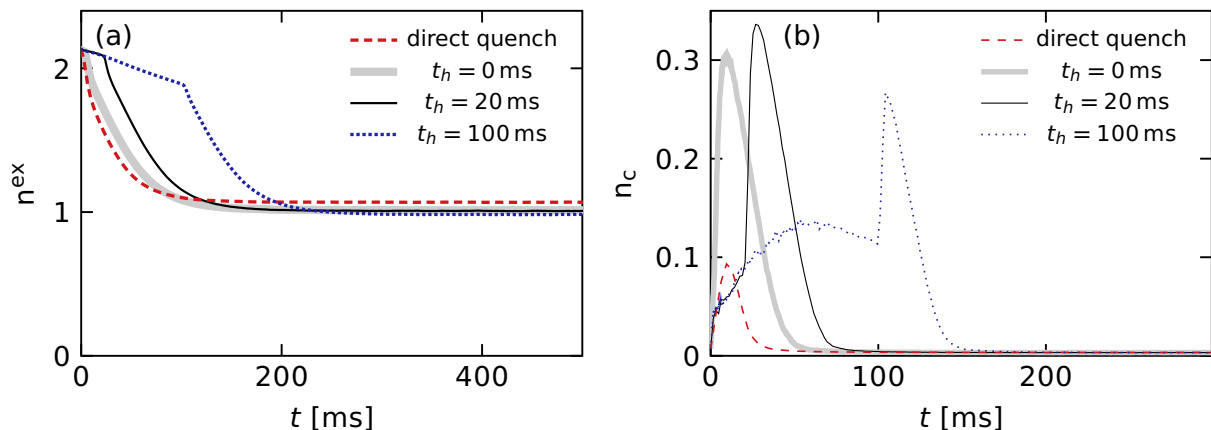


Figure 4.32 – Comparison of the excited band occupation n^{ex} in panel (a) and the condensate fraction n_c in panel (b) for different equilibration times t_{eq} . For the direct quench we choose $\Delta V_{\text{eq}} = \Delta V_f = 0.69 V_0$ and hence there is no holding time. For all other curves we use $\Delta V_{\text{eq}} = 0.43 V_0$ and $\Delta V_f = 0.69 V_0$. The system is initialized with temperature $T = 1/2 E_{\text{rec}}/k_B = 48$ nK and all observables are averaged over 100 Monte-Carlo trajectories.

remain in the lowest band, leading to initially lower coherence of the condensate. The coherence decays slower, however, and at intermediate time scales the s-site correlations are even larger than for $t_1 = 100 \mu\text{s}$, leading also to slower decay of the occupation in the upper band. We explain this as follows: the atoms decaying from the upper band to the lower band gain a large amount of energy and hence lead to heating. The fraction of atoms that has been transferred to the s_B -orbitals is cold compared to these atoms and hence can act as a cooling reservoir for the remaining atoms. On intermediate time scales this leads to lower temperatures and hence a larger condensate fraction. This has the trade off of having fewer atoms in the upper band with lower coherence on short time scales. For all further simulations we therefore keep the value of $t_1 = 100 \mu\text{s}$.

Up to now we have optimized the first quench that is independent of the final value ΔV_f which we want to achieve. Now we use the optimal parameters for the first quench and further optimize the equilibration time t_{eq} before the second quench and the quench duration t_2 of the second quench. We show results for two different values of ΔV_f : $\Delta V_f = 0.26 V_0$ and $\Delta V_f = 0.69 V_0$. The first value is smaller than the value of $\Delta V_{\text{eq}} = 0.43 V_0$, where we let the system equilibrate and hence the decay is mainly hopping induced. The second value is larger than $\Delta V_{\text{eq}} = 0.43 V_0$ and hence the decay is mainly interaction induced. A comparison of different holding times is shown in Figs. 4.31 and 4.32. For $\Delta V_f = 0.26 V_0$ a direct quench leads to the slowest decay of atoms to the lower band, while at the same time reaching the highest coherence of the condensate. Reducing the value of ΔV from $\Delta V_{\text{eq}} = 0.43 V_0$ to $\Delta V_f = 0.26 V_0$ implies lowering the energy of the

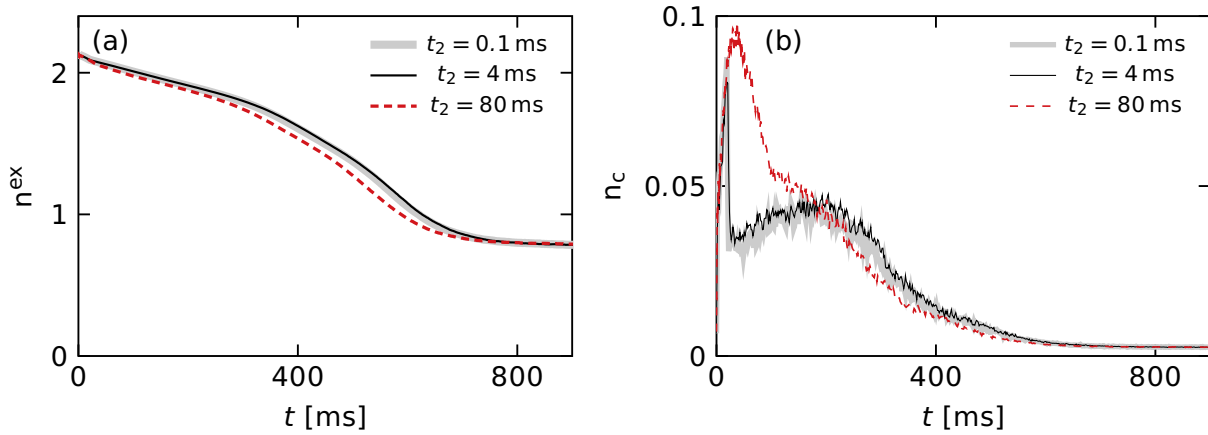


Figure 4.33 – Comparison of the excited band occupation n^{ex} in panel (a) and the condensate fraction n_c in panel (b) for different quench time scales t_2 . For all curves we use $\Delta V_{\text{eq}} = 0.43 V_0$ and $\Delta V_f = 0.26 V_0$. The system is initialized with temperature $T = 1/2 E_{\text{rec}}/k_B = 48$ nK and all observables are averaged over 100 Monte-Carlo trajectories.

predominantly occupied s_A -orbitals. This leads to additional heating. At the same time the condensate is similarly stable for $\Delta V = 0.26 V_0$ and $\Delta V = 0.43 V_0$. Therefore there is no benefit from waiting for condensation at $\Delta V = 0.43 V_0$. The contrary is true for $\Delta V_f = 0.69 V_0$. Here performing a direct quench leads to significant loss and as a result significant heating before the coherence of the condensate in the upper band is build up completely. It is therefore beneficial to wait for condensation at $\Delta V_{\text{eq}} = 0.43 V_0$ and then perform a slow second quench to $\Delta V_f = 0.69 V_0$. We find that holding times of about $20 \mu\text{s}$ are ideal.

We show results for different quench time scales t_2 in Figs. 4.33 and 4.34. For $\Delta V_f = 0.26 V_0$ the quench duration does not lead to significant differences for the coherence of the condensate and the decay time scale. In contrary, for $\Delta V_f = 0.69 V_0$ we find that a quench duration of $t_2 = 4$ ms is indeed well suited. Faster quenches result in overall lower coherences of the condensate, while slower quenches reach lower peak coherences.

In summary, we find that the parameter set $\Delta V_{\text{init}} = -1.8 V_0$, $t_1 = 100 \mu\text{s}$, $t_{\text{eq}} = 20$ ms and $t_2 = 4$ ms, which is inspired by Refs. [131–137], is already well optimized. In some cases it may be beneficial to use a slightly slower first quench $t_1 \approx 1500 \mu\text{s}$, which leads to a larger coherence of the condensate on intermediate time scales. Furthermore it may be beneficial to perform a direct quench without going to the intermediate point $\Delta V_{\text{eq}} = 0.43 V_0$ for values $\Delta V_f < 0.43 V_0$. Finally, we make the remark that in this section we have only generally optimized the quench protocol for high coherence of the condensate and long condensate lifetimes by comparing a series of different quench protocols. In the figures we have only shown a subset of these quench protocols that illustrates the general

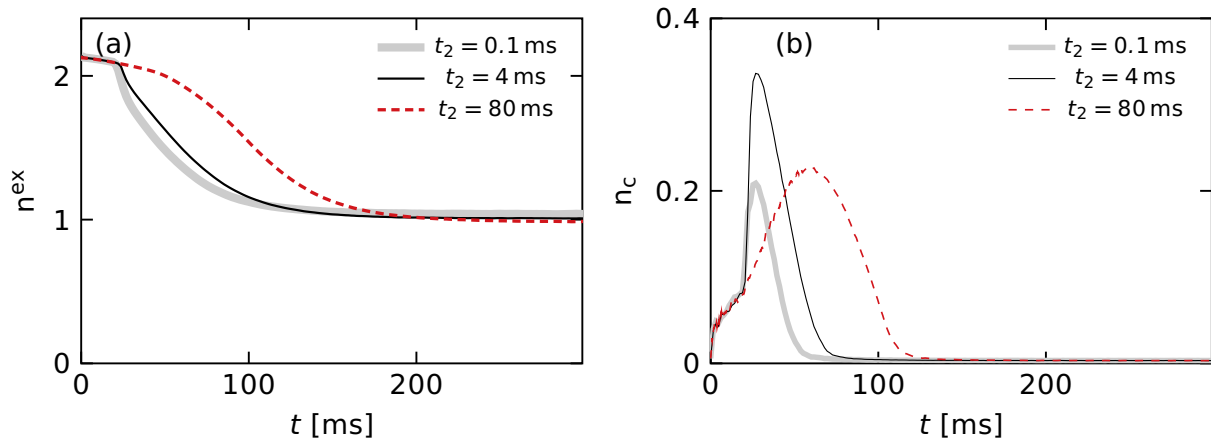


Figure 4.34 – Comparison of the excited band occupation n^{ex} in panel (a) and the condensate fraction n_c in panel (b) for different quench time scales t_2 . For all curves we use $\Delta V_{\text{eq}} = 0.43 V_0$ and $\Delta V_f = 0.69 V_0$. The system is initialized with temperature $T = 1/2 E_{\text{rec}}/k_B = 48$ nK and all observables are averaged over 100 Monte-Carlo trajectories.

behavior. But of course also the full set considered is not exhaustive and a more thorough investigation may be helpful for specific use cases.

4.2.8. Validity cross check

As a validity cross check for the discretization of the tubes in the z -direction we compare several different discretization lengths. In principle the results should agree for any system with the same physical length $N_z d_z$. We show three different cases with same physical length $25 \cdot 0.13 \approx 28 \cdot 0.116 \approx 20 \cdot 0.163$ in Figs. 4.35 and 4.36. Furthermore we note that we have artificially increased the steepness of the harmonic trap as compared to the experimental parameters. We therefore also show one comparison with the same discretization length but larger number of sites, corresponding to a larger system and hence a shallower trap. For all cases we obtain qualitative agreement, but differences on the quantitative level. These are likely due to being close to the limit of validity of classical field theory using rather low atom numbers per site. Increasing the discretization length increases the number of atoms on each site and hence improves the validity of classical field theory. Simultaneously it reduces the bandwidth of the effective band structure which may lead to slower decay as observed in Fig. 4.35.

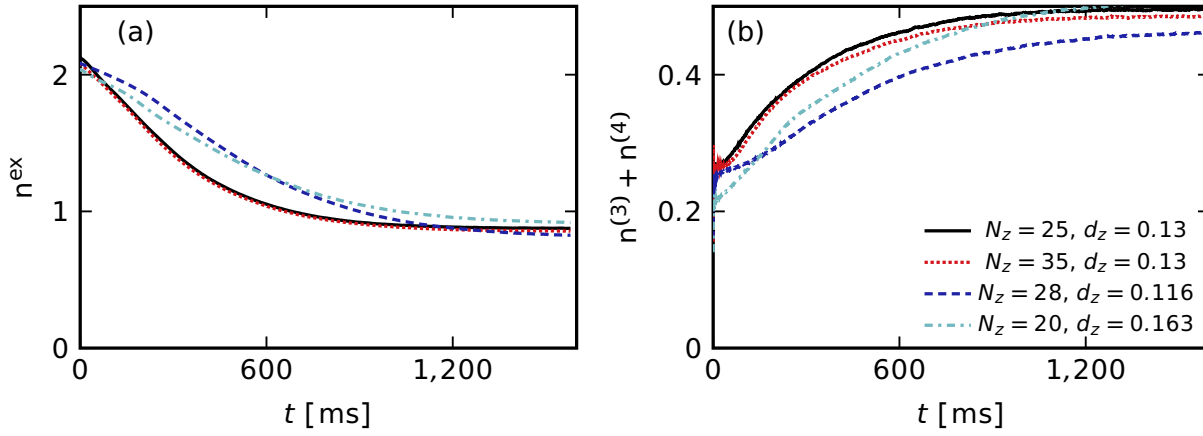


Figure 4.35 – Comparison of different numbers of sites in the z -direction N_z and different discretization lengths d_z for $\Delta V_{\text{eq}} = \Delta V_f = 0.43 V_0$. Panel (a) shows the excited-band occupation n^{ex} , while panel (b) shows the sum of the occupations of the third and fourth band $n^{(3)} + n^{(4)}$. The system is initialized with temperature $T = 1/2 E_{\text{rec}}/k_B = 48$ nK and all observables are averaged over 100 Monte-Carlo trajectories.

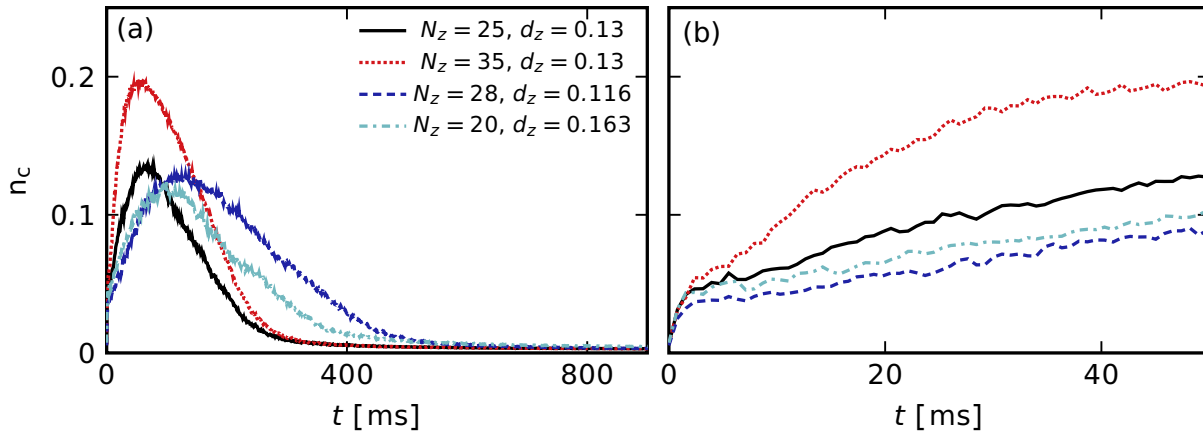


Figure 4.36 – Comparison of different numbers of sites in the z -direction N_z and different discretization lengths d_z for $\Delta V_{\text{eq}} = \Delta V_f = 0.43 V_0$. Panel (a) shows the condensate fraction n_c , while panel (b) shows the same data for shorter times. The system is initialized with temperature $T = 1/2 E_{\text{rec}}/k_B = 48$ nK and all observables are averaged over 100 Monte-Carlo trajectories.

4.3. Excitation spectra for atoms in higher bands

We apply Bogoliubov theory in order to determine the many-body lowest-energy states of the s - p_x - p_y -lattice in the weakly interacting limit. We show how Bogoliubov theory can be applied to an arbitrary system numerically even if the noninteracting Hamiltonian can not be solved analytically. We use this approach in order to confirm that the chiral condensate is indeed the many-body lowest-energy state in the second band of the s - p_x - p_y -lattice. Finally, we show how an imbalance in the hopping parameters breaks the degeneracy between the X_+ - and X_- -points and hence leads to condensation with unequal population of the two X -points.

4.3.1. Multi-mode Gross-Pitaevskii and Bogoliubov theory

Consider a three-dimensional gas of bosons. When lowering the temperature there is a second-order phase transition and below the critical temperature T_C the bosons form a Bose-Einstein condensate. In this state the bosons condense into a single wave function that obtains macroscopic occupation. For temperatures approaching T_C from below most of the atoms are still occupying the condensation mode with only minor occupations of other modes.

For a theoretical description of bosons at low temperatures it is therefore beneficial to exploit the macroscopic occupation of the ground-state wave function. In some cases it is even sufficient to only consider the condensation mode. This is the main approximation made within Gross-Pitaevskii theory. Additionally the low-energy excitations of the condensate can be obtained within Bogoliubov theory.

There are many established descriptions of Gross-Pitaevskii and Bogoliubov theory, see e.g. [187, 199–201]. Here we focus on the description of the multi-orbital case and the chiral condensate.

Gross-Pitaevskii theory

Our eventual goal is to determine the ground state of the s - p_x - p_y -Hamiltonian, see Eqs. 4.2, 4.10 and 4.16. An approximate solution for the ground state is obtained by solving the Gross-Pitaevskii equation. Here we will give a brief introduction to multi-mode Gross-Pitaevskii theory by presenting model systems of increasing complexity.

We start with a single mode Hamiltonian with on-site interactions

$$H_{sm} = \sum_k \epsilon_k b_k^\dagger b_k + U \sum_{k,p,q} b_{k+p}^\dagger b_{k-p}^\dagger b_{k+q} b_{k-q} \quad . \quad (4.37)$$

We assume that the bosons condense in the $b_{k=0}$ mode and that this mode has large occupation such that we can replace $b_{k=0}$ by a complex number Ψ . Then

$$H_{sm} - \mu \sum_k b_k^\dagger b_k = (\epsilon_0 - \mu)|\Psi|^2 + U|\Psi|^4$$

and by doing a variation with respect to Ψ^* we obtain the Gross-Pitaevskii equation

$$\mu = \epsilon_0 + 2n_0U \quad , \quad (4.38)$$

where $n_0 = |\Psi|^2$. For later convenience we note that an equivalent approach is to expand around the condensation mode and require that the linear order vanishes. The Hamiltonian expanded up to linear order around $b_0 = \Psi$ is

$$\begin{aligned} H_{sm} - \mu \sum_k b_k^\dagger b_k &= (\epsilon_0 - \mu)|\Psi|^2 + U|\Psi|^4 + \sum_{k \neq 0} b_k \Psi^* [(\epsilon_0 - \mu) + 2U|\Psi|^2] \\ &+ \sum_{k \neq 0} b_k^\dagger \Psi [(\epsilon_0 - \mu) + 2U|\Psi|^2] + \mathcal{O}(b_k^2) \quad . \end{aligned}$$

Demanding that the linear order vanishes indeed recovers Eq. 4.38.

Next consider the case of two modes and a density-density-type interaction term

$$H_{tm1} = \sum_k \epsilon_{k,x} b_{k,x}^\dagger b_{k,x} + \epsilon_{k,y} b_{k,y}^\dagger b_{k,y} + U \sum_{k,p,q} b_{k+p,x}^\dagger b_{k-p,y}^\dagger b_{k+q,y} b_{k-q,x} \quad .$$

Now it is not so obvious any more which mode the bosons condense in. We therefore perform a unitary transformation and then minimize the energy with respect to both the condensation mode and the parameters of the unitary transformation. We use

$$\begin{aligned} \begin{pmatrix} b_+ \\ b_- \end{pmatrix} &= \begin{pmatrix} u & v \\ -v^* & u^* \end{pmatrix} \begin{pmatrix} b_x \\ b_y \end{pmatrix} \\ \begin{pmatrix} b_x \\ b_y \end{pmatrix} &= \begin{pmatrix} u^* & -v \\ v^* & u \end{pmatrix} \begin{pmatrix} b_+ \\ b_- \end{pmatrix} \quad , \end{aligned}$$

with the constraint $|u|^2 + |v|^2 = 1$. We then assume condensation in the mode $b_- = \Psi$ and up to zeroth order in the condensation mode obtain

$$H_{tm1} - \mu \sum_{k,z=x,y} b_{k,z}^\dagger b_{k,z} = (\epsilon_{k,x} - \mu)|v|^2|\Psi|^2 + (\epsilon_{k,y} - \mu)|u|^2|\Psi|^2 + U|v|^2|u|^2|\Psi|^4 \quad .$$

In order to obtain the Gross-Pitaevskii equations for this system we now not only minimize

with respect to the condensation mode Ψ^* , but also with respect to the parameters of the unitary transformation u^* and v^* . We obtain

$$\frac{\delta H}{\delta \Psi^*} = 0 = \Psi [(\epsilon_{k,x} - \mu)|v|^2 + (\epsilon_{k,y} - \mu)|u|^2 + 2U|v|^2|u|^2|\Psi|^2] \quad (4.39)$$

$$\frac{\delta H}{\delta u^*} = 0 = u|\Psi|^2 [(\epsilon_{k,y} - \mu) + U|v|^2|\Psi|^2] \quad (4.40)$$

$$\frac{\delta H}{\delta v^*} = 0 = v|\Psi|^2 [(\epsilon_{k,x} - \mu) + U|u|^2|\Psi|^2] \quad . \quad (4.41)$$

Equation 4.39 is redundant and hence we obtain

$$0 = (\epsilon_{k,y} - \mu) + U|v|^2|\Psi|^2 \quad (4.42)$$

$$0 = (\epsilon_{k,x} - \mu) + U|u|^2|\Psi|^2 \quad . \quad (4.43)$$

An alternative procedure giving the same results without having to apply the unitary transformation is to immediately assume the condensation modes $b_x \rightarrow \Psi_x$ and $b_y \rightarrow \Psi_y$. We then obtain

$$H_{tm1} - \mu \sum_{k,z=x,y} b_{k,z}^\dagger b_{k,z} = (\epsilon_x - \mu)|\Psi_x|^2 + (\epsilon_y - \mu)|\Psi_y|^2 + U|\Psi_x|^2|\Psi_y|^2$$

and the variation with respect to Ψ_x and Ψ_y yields

$$\begin{aligned} \frac{\delta H}{\delta \Psi_x^*} &= 0 = \Psi_x [\epsilon_x - \mu + U|\Psi_y|^2] \\ \frac{\delta H}{\delta \Psi_y^*} &= 0 = \Psi_y [\epsilon_y - \mu + U|\Psi_x|^2] \quad , \end{aligned}$$

which is equivalent to Eqs.4.42 and 4.43.

Next we consider a two-mode Hamiltonian with a density-density- and a pairing-type interaction term

$$\begin{aligned} H_{tm2} &= \sum_k \epsilon_{k,x} b_{k,x}^\dagger b_{k,x} + \epsilon_{k,y} b_{k,y}^\dagger b_{k,y} + U \sum_{kpq} b_{k,x}^\dagger b_{q-k,x}^\dagger b_{p,x} b_{q-p,x} + U \sum_{kpq} b_{k,y}^\dagger b_{q-k,y}^\dagger b_{p,y} b_{q-p,y} + \\ &U_2 \sum_{kpq} b_{k,x}^\dagger b_{q-k,x}^\dagger b_{p,y} b_{q-p,y} + U_2 \sum_{kpq} b_{k,y}^\dagger b_{q-k,y}^\dagger b_{p,x} b_{q-p,x} \quad . \end{aligned}$$

For $U_2 = 0$ the two modes decouple and the Gross-Pitaevskii equation for each of them is simply

$$\mu = \epsilon_0 + 2n_0U \quad .$$

For $U_2 > 0$ the two modes couple. The phase of one of the two modes can be chosen arbitrarily. We make the assumption $b_{k=0,x} = \sqrt{n_x}$ and $b_{k=0,y} = \sqrt{n_y}e^{i\phi}$, with real $n_{x,y}$. The grand-canonical potential becomes

$$H_{tm2} - \mu \sum_{k,z=x,y} b_{k,z}^\dagger b_{k,z} = (\epsilon_x - \mu)n_x + (\epsilon_y - \mu)n_y + U(n_x^2 + n_y^2) + 2U_2 n_x n_y \cos(2\phi) \quad (4.44)$$

and the Gross-Pitaevskii equation is now

$$\begin{aligned} \epsilon_{0,x} - \mu + Un_x + U_2 n_y e^{2i\phi} &= 0 \\ \epsilon_{0,y} - \mu + Un_y + U_2 n_x e^{2i\phi} &= 0 \end{aligned} .$$

Taking the imaginary part of these equations we immediately see that $\phi = 0$ or $\phi = \pm\pi/2$. Inserting into Eq. 4.44 we find that only $\phi = \pm\pi/2$ is a minimum of the energy. Hence the condensation mode is

$$\sqrt{n_x} \pm i\sqrt{n_y} \quad (4.45)$$

and we have identified the interaction term that gives rise to the relative phase of $\pm i$ that also occurs for the chiral condensate.

Bosonic Bogoliubov theory

Bogoliubov theory can be applied to both bosons and fermions. In this thesis we will apply it to bosons only and hence we limit our considerations to this case. Bosonic Bogoliubov theory computes the possible excitations of the condensation mode obtained from Gross-Pitaevskii theory. Hence it gives the spectrum of the weakly interacting system. It is well known for its application to the weakly interacting single-mode Bose Gas, see e.g. [201]. The main steps of Bogoliubov theory involve the approximation that most atoms are condensed with only a small thermal fraction. This leads to a Hamiltonian quadratic in the creation and annihilation operators. For the weakly interacting single-mode Bose Gas the resulting Hamiltonian is 2×2 and can easily be diagonalized analytically. In the diagonalization it is crucial to ensure that the resulting diagonal modes are still bosonic, i.e. the resulting creation and annihilation operators fulfill bosonic commutation relations. For bosons this implies that the matrix diagonalizing the Hamiltonian need not be unitary. For more complicated cases (such as the s - p_x - p_y -condensate), where it is not possible to analytically diagonalize the Bogoliubov matrix, it is therefore not sufficient to use standard diagonalization routines for the Hamiltonian. Instead we will follow an

approach presented in [202, 203] that allows for the numerical diagonalization of quadratic Hamiltonians.

We start, however, by revisiting the simplest case of single-mode Bogoliubov theory. In contrast to standard textbooks, see e.g. [201], we will work in the grand-canonical ensemble instead of the canonical one. In other words we allow the exchanges of particles with a bath and therefore explicitly introduce the chemical potential. Consider the grand-canonical potential

$$H_{sm} - \mu \sum_k b_k^\dagger b_k \quad ,$$

where H_{sm} has been defined in Eq. 4.37. We assume condensation in the mode $b_0 = \Psi = \sqrt{n_0}$ and expand to quadratic order in the creation and annihilation operators

$$\begin{aligned} H_{sm} - \mu \sum_k b_k^\dagger b_k &\approx (\epsilon_0 - \mu)n_0 + Un_0^2 + \sum_{k \neq 0} (\epsilon_k - \mu)b_k^\dagger b_k \\ &+ 4Un_0 \sum_{k \neq 0} b_k^\dagger b_k + Un_0 \sum_{k \neq 0} \left(b_k^\dagger b_{-k}^\dagger + b_k b_{-k} \right) \quad . \end{aligned} \quad (4.46)$$

Here we have already used the fact that the linear order in the creation and annihilation operators vanishes when n_0 fulfills the Gross-Pitaevskii equation. In the canonical ensemble it is common to proceed by replacing the condensate density n_0 by the difference of the total particle number and the number of excitations. As we are working in the grand-canonical ensemble the total particle number is not fixed and one approach is to use the Gross-Pitaevskii equation in order to determine the condensate density

$$n_0 = \frac{\mu - \epsilon_0}{2U} \quad .$$

The equations for the Bogoliubov energies look more familiar, however, when keeping the condensate density and instead replacing the chemical potential in Eq. 4.46. We therefore take this approach, while keeping in mind that the condensate density is actually fixed to the chemical potential by the Gross-Pitaevskii equation. We obtain for Eq. 4.46, neglecting a constant energy offset,

$$H_{sm} - \mu \sum_k b_k^\dagger b_k \approx \frac{1}{2} \sum_{k \neq 0} \begin{pmatrix} b_k^\dagger \\ b_{-k} \end{pmatrix}^T \begin{pmatrix} \epsilon_k - \epsilon_0 + 2Un_0 & 2Un_0 \\ 2Un_0 & \epsilon_{-k} - \epsilon_0 + 2Un_0 \end{pmatrix} \begin{pmatrix} b_k \\ b_{-k}^\dagger \end{pmatrix} \quad .$$

This Hamiltonian is diagonalized by the Bogoliubov transformation

$$\begin{pmatrix} b_k \\ b_{-k}^\dagger \end{pmatrix} = U \begin{pmatrix} \beta_k \\ \beta_{-k} \end{pmatrix} ,$$

where $U = \begin{pmatrix} u_k & v_k \\ v_k^* & u_k^* \end{pmatrix}$

$$u_k^2 = \frac{-E_k + (\epsilon_k - \epsilon_0 + 2Un_0)}{2E_k}$$

$$v_k^2 = \frac{E_k + (\epsilon_k - \epsilon_0 + 2Un_0)}{2E_k}$$

$$u_k v_k = -\frac{Un_0}{E_k}$$

$$E_k = \sqrt{(\epsilon_k - \epsilon_0 + 2Un_0)^2 - 4U^2 n_0^2}$$

and $|v_k|^2 - |u_k|^2 = 1$. The resulting grand-canonical potential is

$$U^\dagger \left(H_{sm} - \mu \sum_k b_k^\dagger b_k \right) U \approx \sum_{k \neq 0} E_k \beta_k^\dagger \beta_k$$

and hence E_k is the energy of the quasi-particle excitations of the condensate.

For illustrative reasons we will now obtain the same solution using the approach described in [202] in chapter 3. We rewrite

$$H_{sm} - \mu \sum_k b_k^\dagger b_k \approx \frac{1}{4} \sum_{k \neq 0} \begin{pmatrix} a^\dagger & a \end{pmatrix} M_{sm} \begin{pmatrix} a \\ a^\dagger \end{pmatrix} ,$$

where $M_{sm} = \begin{pmatrix} \epsilon_k - \epsilon_0 + 2Un_0 & & & 2Un_0 \\ & \epsilon_{-k} - \epsilon_0 + 2Un_0 & 2Un_0 & \\ & 2Un_0 & \epsilon_k - \epsilon_0 + 2Un_0 & \\ 2Un_0 & & & \epsilon_{-k} - \epsilon_0 + 2Un_0 \end{pmatrix}$

and $a = \begin{pmatrix} b_k \\ b_{-k} \end{pmatrix}$.

It is shown in [202] that such a Hamiltonian can be diagonalized by diagonalizing ηM with

$$\eta = \begin{pmatrix} 1 & 0 \\ 0 & -1 \end{pmatrix} .$$

The resulting diagonal Hamiltonian then has twice E_k and twice $-E_k$ on the diagonal.

Hence we obtain the same quasi-particle excitations as in the previous analytical approach.

We turn a more complicating case: the two-mode Hamiltonian with pairing-type interactions H_{tm2} . From Gross-Pitaevskii theory we know that condensation occurs in the mode $\sqrt{n_x} \pm i\sqrt{n_y}$, see Eq. 4.45. Furthermore we know that the linear order in the operators must vanish for the condensate. Hence the next nonvanishing order is quadratic in the operators and we obtain for the Bogoliubov matrix

$$H_{tm2} - \mu \sum_k b_k^\dagger b_k \approx \frac{1}{2} \begin{pmatrix} b_{k,x}^\dagger \\ b_{k,y}^\dagger \\ b_{-k,x} \\ b_{-k,y} \end{pmatrix}^T M_{tm2} \begin{pmatrix} b_{k,x} \\ b_{k,y} \\ b_{-k,x}^\dagger \\ b_{-k,y}^\dagger \end{pmatrix},$$

where

$$M_{tm2} = \begin{pmatrix} \epsilon_{k,x} - \epsilon_{0,x} + 2Un_x + 2U_2n_y & 4iU_2\sqrt{n_x n_y} & 2Un_x - 2U_2n_y & 0 \\ -4iU_2\sqrt{n_x n_y} & \epsilon_{k,y} - \epsilon_{0,y} + 2Un_y + 2U_2n_x & 0 & -2Un_y + 2U_2n_x \\ 2Un_x - 2U_2n_y & 0 & \epsilon_{-k,x} - \epsilon_{0,x} + 2Un_x + 2U_2n_y & -4iU_2\sqrt{n_x n_y} \\ 0 & -2Un_y + 2U_2n_x & 4iU_2\sqrt{n_x n_y} & \epsilon_{-k,y} - \epsilon_{0,y} + 2Un_y + 2U_2n_x \end{pmatrix}.$$

While it is difficult to analytically determine the Bogoliubov transformation diagonalizing this matrix we can still numerically diagonalize ηM_{tm2} and thereby obtain the eigenenergies and -states of the excitation modes. To do so we again increase the size of the matrix to include the modes $(b_{k,x} \ b_{k,y} \ b_{-k,x} \ b_{-k,y} \ b_{k,x}^\dagger \ b_{k,y}^\dagger \ b_{-k,x}^\dagger \ b_{-k,y}^\dagger)$ and then apply the procedure described in [202].

The last case we consider is also the most general one: an arbitrary multi-mode system with a general interaction term. We assume that the noninteracting Hamiltonian $H_{k,\text{non-int}}$ is — for each momentum k — diagonalized by a unitary matrix U_k , such that

$$D_{k,\text{non-int}} = \sum_r \epsilon_{k,r} b'_{k,r}^\dagger b'_{k,r}$$

is diagonal. Here $b'_{k,r} = U_{k,sr}^* b_{k,s}$ and r, s are indices denoting different modes (e.g. s -, p_x - and p_y -orbitals). We write the interaction term of the Hamiltonian as

$$H_{\text{int}} = U \sum_{kpq} b_{k,r}^\dagger b_{q-k,s}^\dagger b_{p,t} b_{q-p,u} + \text{h.c.},$$

where r, s, t, u may denote arbitrary orbitals.

First we need to determine the condensation mode. We could do this by solving the Gross-Pitaevskii equation analytically, as presented above. This approach is, however, not possible if the diagonalization of the noninteracting Hamiltonian is only known numerically. Therefore we make an assumption for the condensation mode with variable

parameters and then minimize the energy of the condensation mode numerically. Without loss of generality we can assume that the atoms condense in the mode $c_{0,0} \approx \sqrt{n_0}$, where

$$b_{k,r} = (W_k c_k)_r = W_{k,rs} c_{k,s} = (U_k V_k c_k)_r \quad .$$

Note that we have introduced an arbitrary unitary transformation V here that allows for condensation in linear combinations of different noninteracting eigenmodes. We will indeed need this for the chiral condensate, since the atoms condense in a superposition of the Bloch functions at X_+ and X_- . We can now write the interaction term as

$$H_{\text{int}} = U \sum_{kpq,ijnm} W_{k,ir}^* W_{q-k,js}^* W_{p,tn} W_{q-p,um} c_{k,i}^\dagger c_{q-k,j}^\dagger c_{p,n} c_{q-p,m} + \text{h.c.} \quad .$$

For the full Hamiltonian we obtain to zeroth order in the excitation operators

$$H_{\text{non-int}} + H_{\text{int}} = n_0 \sum_r \epsilon_{0,r} V_{0,0r}^* V_{0,r0} + U n_0^2 (W_{0,0r}^* W_{0,0s}^* W_{0,t0} W_{0,u0} + \text{c.c.}) \quad .$$

We obtain the mean-field ground state, by parametrizing V appropriately and minimizing the above equation.

Our next goal is to construct the Bogoliubov Hamiltonian. For the Bogoliubov Hamiltonian we need to gather those terms where exactly two of the operators are evaluated in the condensation mode, hence

$$\begin{aligned} H_{\text{int}} \approx U n_0 \sum_{kpq,ijnm} & \left[W_{k,nr}^* W_{0,0s}^* W_{k,tm} W_{0,u0} c_{k,n}^\dagger c_{k,m} + W_{k,nr}^* W_{0,0s}^* W_{0,t0} W_{k,um} c_{k,n}^\dagger c_{k,m} \right. \\ & + W_{0,0r}^* W_{k,ns}^* W_{k,tm} W_{0,u0} c_{k,n}^\dagger c_{k,m} + W_{0,0r}^* W_{k,ns}^* W_{0,t0} W_{k,um} c_{k,n}^\dagger c_{k,m} \\ & \left. + W_{k,nr}^* W_{-k,ms}^* W_{0,t0} W_{0,u0} c_{k,n}^\dagger c_{-k,m}^\dagger + W_{0,0r}^* W_{0,0s}^* W_{k,tn} W_{-k,um} c_{k,n} c_{-k,m} + \text{h.c.} \right] \quad . \end{aligned}$$

The full Hamiltonian can now be rewritten in matrix form as

$$H_{\text{int}} \approx \frac{U n_0}{4} \sum_k \begin{pmatrix} c_k^\dagger \\ c_{-k}^\dagger \\ c_k \\ c_{-k} \end{pmatrix}^T \begin{pmatrix} \alpha(k) & 0 & 0 & \gamma(k) \\ 0 & \alpha(-k) & \gamma^T(k) & 0 \\ 0 & \gamma^*(k) & \alpha^*(k) & 0 \\ \gamma^\dagger(k) & 0 & 0 & \alpha^*(-k) \end{pmatrix} \begin{pmatrix} c_k \\ c_{-k} \\ c_k^\dagger \\ c_{-k}^\dagger \end{pmatrix}, \quad (4.47)$$

where c_k is a vector with components

$$(c_k)_n = c_{k,n}$$

and

$$\begin{aligned}
 \alpha_{nm}(k) &= \sum_r \epsilon_{k,r} V_{k,nr}^* V_{k,rm} + \left(W_{k,nr}^* W_{0,0s}^* W_{k,tm} W_{0,u0} + W_{k,nr}^* W_{0,0s}^* W_{0,t0} W_{k,um} \right. \\
 &\quad \left. + W_{0,0r}^* W_{k,ns}^* W_{k,tm} W_{0,u0} + W_{0,0r}^* W_{k,ns}^* W_{0,t0} W_{k,um} + \text{c.c.} \right) \\
 \gamma_{nm}(k) &= W_{k,nr}^* W_{-k,ms}^* W_{0,t0} W_{0,u0} + W_{k,ns}^* W_{-k,mr}^* W_{0,t0} W_{0,u0} \\
 &\quad + W_{0,0r} W_{0,0s} W_{k,tn}^* W_{-k,um}^* + W_{0,0r} W_{0,0s} W_{k,un}^* W_{-k,tm}^* \quad .
 \end{aligned} \tag{4.48}$$

If the interaction Hamiltonian is a sum of multiple terms, we apply this procedure to each of them individually and the Bogoliubov Hamiltonian is the sum of the individual Bogoliubov Hamiltonians. The resulting Bogoliubov Hamiltonian can then be diagonalized numerically again following the procedure from [202].

Hence we have developed a formalism that numerically obtains the Bogoliubov eigenenergies and -functions for an arbitrary multi-mode Hamiltonian. In particular, the formalism can also be applied to cases where the diagonalization of the noninteracting Hamiltonian is only numerically feasible. This is the approach we take for determining the symmetry and excitations of weakly interacting condensates in the s - p_x - p_y -lattice.

We make two final remarks: The first is that the form of the Bogoliubov Hamiltonian in Eq. 4.47 is redundant. In fact, we can reduce it to

$$H_{int} \approx \frac{Un_0}{2} \sum_k \begin{pmatrix} c_k^\dagger \\ c_{-k} \end{pmatrix}^T \begin{pmatrix} \alpha(k) & \gamma(k) \\ \gamma^\dagger(k) & \alpha^*(-k) \end{pmatrix} \begin{pmatrix} c_k \\ c_{-k}^\dagger \end{pmatrix} \quad .$$

For the Hamiltonian in Eq. 4.47 each of the eigenmodes we obtain will be four-fold degenerate, instead of two-fold.

Our second remark is that it is important to symmetrize the interaction terms that contribute to $\gamma_{nm}(k)$ in order to ensure that the Bogoliubov Hamiltonian is hermitian. Let us illustrate this using a simple example. Consider

$$\begin{aligned}
 H &= \sum_k (\epsilon_k - \mu) b_k^\dagger b_k + \sum_{kpq} U_{kpq} b_k^\dagger b_{q-k}^\dagger b_p b_{q-p} + \text{h.c.} \\
 &= \sum_k (\epsilon_k - \mu) b_k^\dagger b_k + \sum_{kpq} (U_{kpq} + U_{pkq}^*) b_k^\dagger b_{q-k}^\dagger b_p a_{q-p} \quad .
 \end{aligned}$$

Using the Bogoliubov approximation we obtain

$$\begin{aligned}
 H \approx \sum_k (\epsilon_k - \mu) b_k^\dagger b_k + \sum_k \left\{ 2\text{Re}(U_{kkk} + U_{k0k} + U_{0kk} + U_{00k}) b_k^\dagger b_k + \right. \\
 \left. (U_{k00} + U_{0k0}^*) b_k^\dagger b_{-k}^\dagger + (U_{0k0} + U_{k00}^*) b_k b_{-k} \right\} \quad .
 \end{aligned}$$

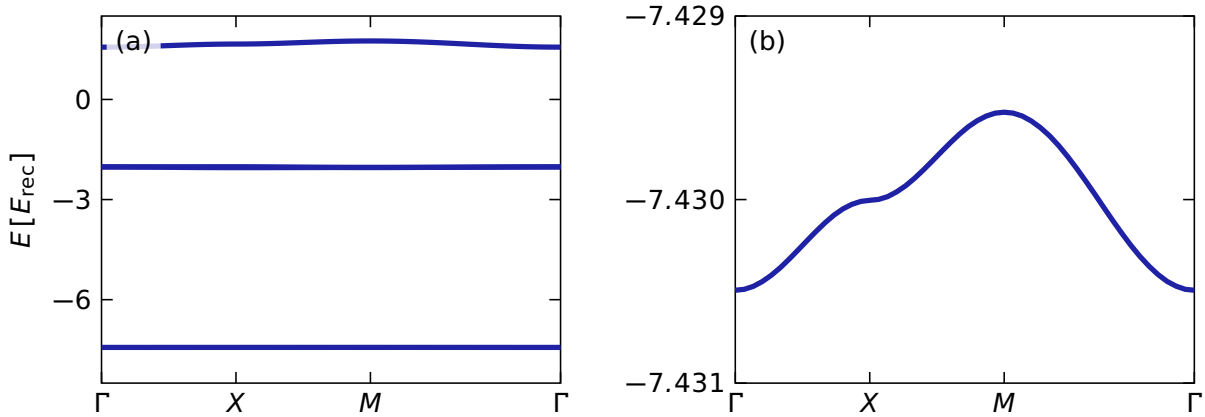


Figure 4.37 – Noninteracting band structure for the s - p_x - p_y -lattice for $\Delta V = -1.8 V_0$. Panel (a) shows the lowest four bands, while panel (b) shows only the lowest band. We use the tight-binding parameters computed in Sec. 4.1.2.

We note, however, that we could also rewrite

$$\sum_k (U_{k00} + U_{0k0}^*) b_k^\dagger b_{-k}^\dagger = \sum_k (U_{-k,0,0} + U_{0,-k,0}^*) b_k^\dagger b_{-k}^\dagger$$

and, when then writing the Hamiltonian in matrix form, the individual k -sections would not be hermitian any more. The safest way to proceed is therefore to symmetrize these parts of the Hamiltonian in the form

$$\sum_k \frac{1}{2} (U_{k00} + U_{0k0}^* + U_{-k,0,0} + U_{0,-k,0}^*) b_k^\dagger b_{-k}^\dagger \quad .$$

This is the approach we took for writing Eq. 4.48⁹.

4.3.2. Numerical results

Here we present the results for the calculation of the excitation spectra of atoms in the s - p_x - p_y -lattice. We follow the procedure presented in the previous section on the calculation of Bogoliubov spectra in order to obtain the effective excitation spectra for weak interactions. For comparison we also show the band structures of the corresponding noninteracting systems.

Band structure and excitation spectra for $\Delta V = -1.8 V_0$

First we consider the band structure for $\Delta V = -1.8 V_0$, see Fig. 4.37(a). This is the value where we load the atoms in the first band. This band is predominantly occupying

⁹Note that the extra factor of $1/2$ has been included in Eq. 4.47 already.

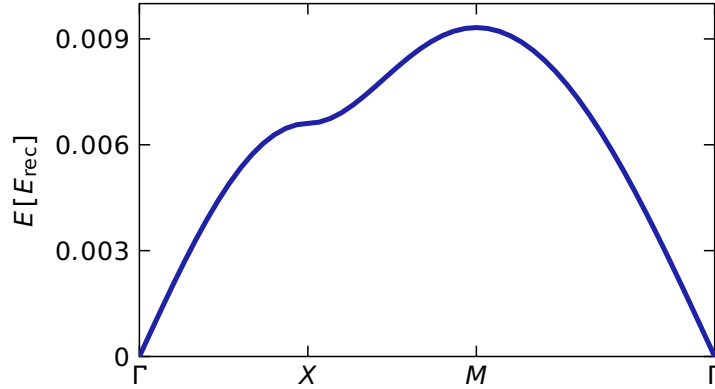


Figure 4.38 – Bogoliubov spectrum for the lowest band of the s - p_x - p_y -lattice for $\Delta V = -1.8 V_0$. We assume condensation at the Γ -point of the lowest band and use the tight-binding parameters computed in Sec. 4.1.2. All interaction parameters are scaled by the factor 0.1.

the s -orbitals of A -sublattice sites and has its minimum at the Γ -point, see Fig. 4.37(b). The second band is mainly occupying the s -orbitals of B -sublattice sites, while the third and fourth band are nearly degenerate and have p -orbital character. Here we assume condensation at the Γ -point of the lowest band and compute the corresponding Bogoliubov spectrum, see Fig. 4.38. In order to remain in the weakly interacting regime we reduce all interaction parameters and use only 10% of the values computed in Sec. 4.1.2. The spectrum obtains the characteristic linear onset that indicates the superfluidity of the condensate. From the slope of the linear onset we can estimate the sound velocity to be $3 \cdot 10^{-5} \text{ m s}^{-1}$. Furthermore we find that the bandwidth of the lowest band is significantly increased by interactions to $9 \cdot 10^{-3} E_{\text{rec}}$, as compared to the noninteracting value of $10^{-3} E_{\text{rec}}$.

Band structure and excitation spectra for $\Delta V = 0.6 V_0$

Next we consider the condensate after the atoms have been transferred to the second band. Here we exemplarily consider the point $\Delta V = 0.6 V_0$. At this point atoms in the first band mainly occupy s -orbitals on B -sites, atoms in the second band mainly occupy s -orbitals on A -sites and atoms in the third and fourth band mainly occupy p -orbitals on B -sites. The noninteracting band structure for the lowest four bands is shown in Fig. 4.39. We see that while the first band still has the minimum at the Γ -point the second band has the minimum at the X -points and the third and fourth band have a degenerate minimum at the M -points.

From Sec. 4.2.6 we know that the many-body ground state mixes the Bloch functions $|\psi_{\pm}\rangle$ at the X_+ and X_- points. Our setup for Bogoliubov theory can only mix eigenstates at the same momentum. We therefore apply a trick in order to circumvent this restriction:

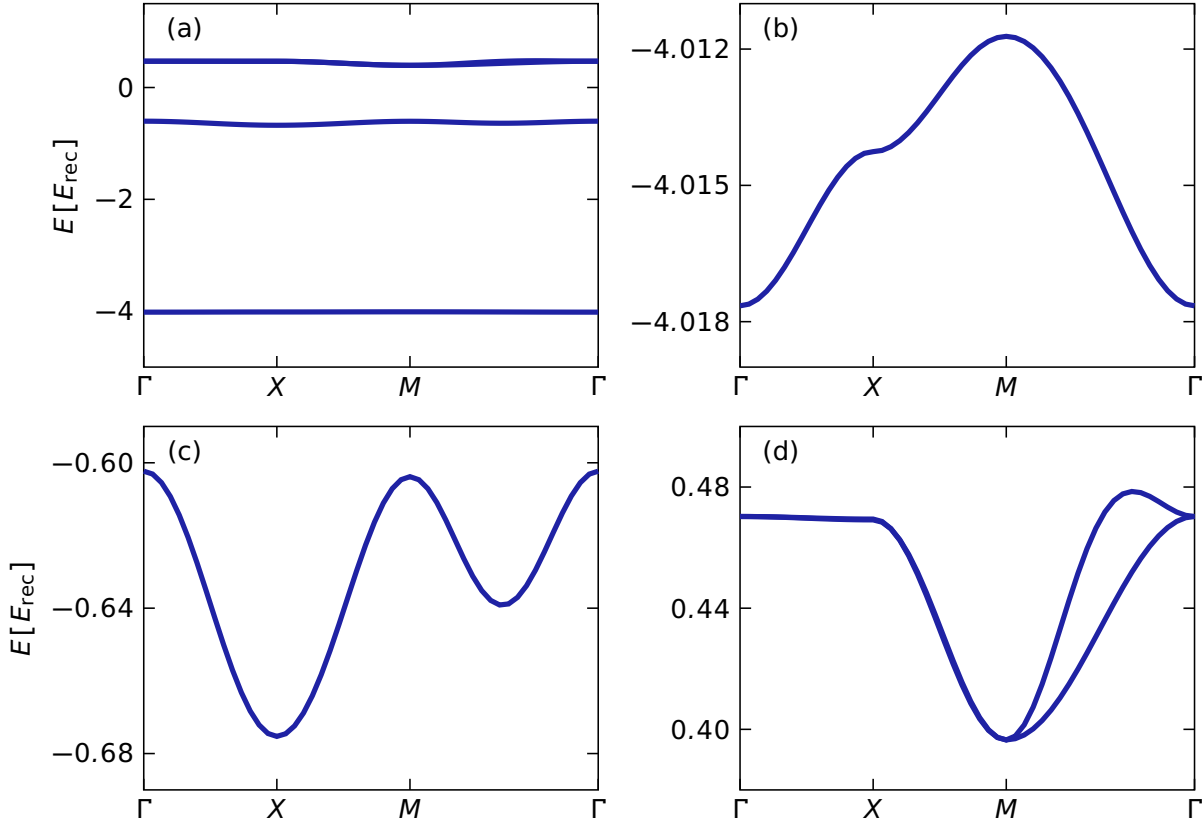


Figure 4.39 – Noninteracting band structure for the s - p_x - p_y -lattice for $\Delta V = 0.6 V_0$. Panel (a) shows the lowest four bands, while panel (b) shows only the first, panel (c) only the second and panel (d) the third and fourth band. We use the tight-binding parameters computed in Sec. 4.1.2.

we increase the size of the unit cell artificially, choosing the unit vectors $2\mathbf{e}_x$ and $2\mathbf{e}_y$. This backfolds the band structure, such that we obtain a total of 16 instead of 4 bands and both the M - and the X -points are mapped to $\mathbf{k} = 0$. We show the noninteracting band structure of the four bands that arise due to backfolding of the previous second band in Fig. 4.40(a). We assume condensation at $\mathbf{k} = 0$ of the lower two of these bands. As presented in Sec. 4.3.1 we now assume a general unitary transformation of the type

$$V = \begin{pmatrix} \sin(\theta) & -\cos(\theta)e^{i\phi} \\ \cos(\theta) & \sin(\theta)e^{i\phi} \end{pmatrix}$$

with arbitrary parameters θ and ϕ . The many-body ground state then mixes the wave functions at the X_+ - and X_- -points as

$$|\psi(\theta, \phi)\rangle = \cos(\theta) |\psi_+\rangle + \sin(\theta) e^{i\phi} |\psi_-\rangle \quad .$$

We find that the values $\theta = \pi/4$ and $\phi = \pm\pi/2$ minimize the Gross-Pitaevskii energy

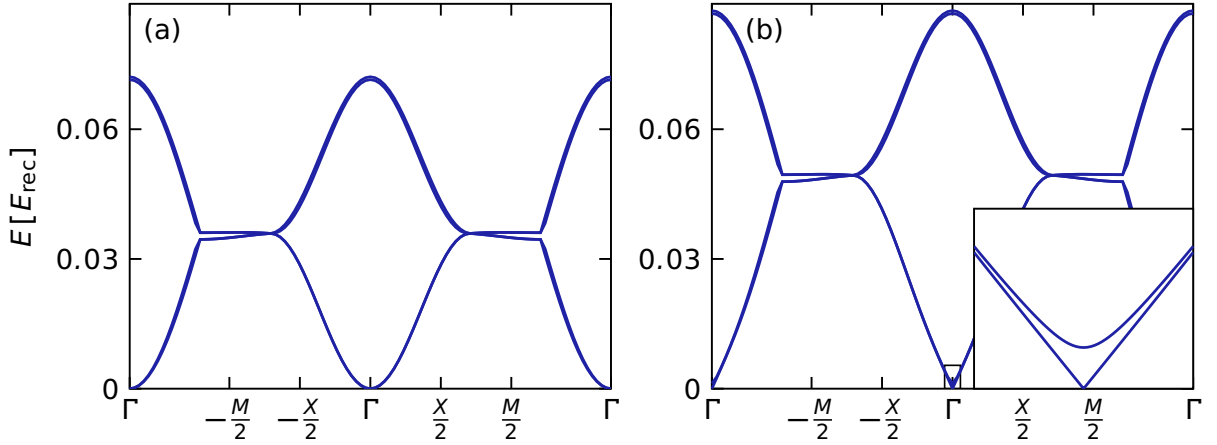


Figure 4.40 – (a) Backfolded noninteracting band structure for the s - p_x - p_y -lattice for $\Delta V = 0.6 V_0$. We use the unit vectors $2\mathbf{e}_x$ and $2\mathbf{e}_y$, such that both the X - and the M -points are backfolded to the Γ -point. We show the four bands that correspond to the second band from Fig. 4.39 and shift the energy, such that the minimum is at $E = 0$. (b) Corresponding Bogoliubov spectrum. We assume condensation in the mode $|\psi_+\rangle = |\psi_X\rangle + i|\psi_{X'}\rangle$. For both panels we use the tight-binding parameters computed in Sec. 4.1.2. All interaction parameters are scaled by the factor 0.2.

and hence confirm the many-body ground state $|\Xi_\pm\rangle = 1/\sqrt{2}(|\psi_+\rangle \pm i|\psi_-\rangle)$. We show the resulting Bogoliubov spectrum for $|\Xi_+\rangle$ in Fig. 4.40(b). The degeneracy of the bands is lifted by the interactions. The lower band has a linear dispersion relation and the corresponding sound velocity is $2 \cdot 10^{-4} \text{ m s}^{-1}$.

Finally, we lift the degeneracy of the X_+ - and X_- -points by introducing an imbalance between J_\perp in the k_x - and k_y -direction. In fact, we choose a finite value of the parameter s_\perp , that has been introduced in Eq. 4.9. We show the condensation mode as a function of imbalance in Fig. 4.41. For finite imbalance the minimum of the Gross-Pitaevskii energy is obtained for a state with unequal weight on the X_+ - and X_- -points, hence $\theta \neq \pi/4$. In fact, θ increases monotonically from $\theta = 0$ at $s_\perp = 0.978$ to $\theta = \pi/2$ at $s_\perp = 1.022$. Throughout this entire regime $\phi = \pm\pi/2$. For $s_\perp \leq 0.978$ only the X_+ -point is occupied and $\theta = 0$, while for $s_\perp \geq 1.022$ only the X_- -point is occupied and $\theta = \pi/2$. In both of the latter cases the angle ϕ is undetermined.

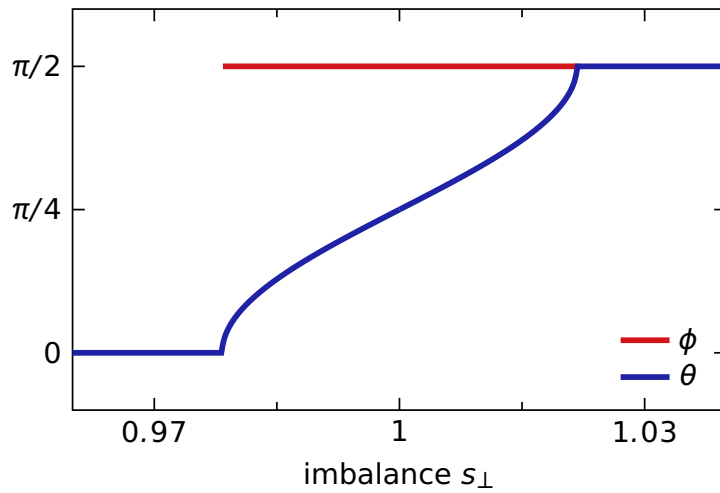


Figure 4.41 – We introduce an imbalance in the s - p -hopping parameters and plot the parameters minimizing the Gross-Pitaevskii energy as a function of imbalance parameter s_{\perp} . We only show ϕ for $0 < \theta < \pi/2$, since ϕ is undetermined for $\theta = 0$ and $\theta = \pi/2$.

5. Summary and Outlook

In this thesis we have studied three different examples of unconventional order in quantum systems. We have first studied dissipative solid-state graphene driven by circularly polarized light. In contrast to the high-frequency non-dissipative limit we have found that the Hall conductivity has opposite sign for low-frequency driving and its magnitude depends on the interplay of dissipation and driving. Nevertheless a major contribution to the Hall conductivity is obtained by weighting the Berry curvature of Floquet bands with their respective occupations. Hence our theoretical formalism represents a new approach to the application of periodic driving to solids and presents an interpretation of the experiments presented in Ref. [86]. We have considered the limit of increasing the driving frequency by orders of magnitude while keeping the gap at the Dirac point fixed and find that the resulting steady state is a high-temperature state with almost equal occupation in the lower and upper Floquet band. Only for low dissipation or short times the contribution of the Dirac point recovers the result expected in the high-frequency limit.

Our formalism is particularly well suited to the case of small dephasing-type dissipation (large decoherence time scale T_2). We do observe deviations of about 20% for larger dephasing-type dissipation. For future work it will therefore be interesting to extend the concepts of geometry and topology, such as Berry curvature, to dissipative systems. We expect such a formalism to yield even better predictions for stronger dissipation.

Another interesting extension of our work would be to consider the edge states of the periodically driven dissipative system. For undriven topological insulators there is the bulk-edge correspondence that relates the Chern number of the bulk to the number of edge states. It is an open discussion whether a similar relation holds for dissipative driven systems. Within our work we have found that the resonant drive leads to significant excitation in the bulk. Even for high-frequency off-resonant driving the interplay of dissipation and driving leads to a high-temperature steady state and vanishing Hall conductivity. Still it is an interesting direction for future work to investigate whether it is possible to probe the transport of edge states. A similar scenario has been proposed in Ref. [204].

In the second project we presented a method that allows an efficient detection of topological defects in the hexagonal lattice, which is also the underlying lattice structure for

graphene. The method is based on a periodic lattice modulation before performing a time-of-flight image. The resulting interference pattern gives direct access to the relative phase of the two sublattices of the hexagonal lattice and the emerging phase winding identifies topological defects. This has been used in Ref. [N1] to experimentally measure the merging transition of Dirac points in the hexagonal lattice. Our method can be straightforwardly extended to almost any lattice with two lattice sites per unit cell. In principle it could also be interesting to consider lattices with more than two lattice sites per unit cell. While we still expect our method to be applicable, the resulting equations will likely get rather complicated. An even more interesting direction for future work would be the extension to angle-resolved photoemission spectroscopy (ARPES) in solids. In fact, time-of-flight images in ultracold atoms are closely related to ARPES in solids. Here the main challenge lies in identifying an appropriate alternative to the periodic lattice modulation.

In the third project of this thesis we have presented a new mechanism for metastability where destructive interference leads to the inhibition of relaxation. In our case the chiral order of a Bose-Einstein condensate in the second band of a staggered square lattice inhibits decay to the first band. The condensate itself shows perfect destructive interference and hence is a dark state with infinite lifetime. Only the thermal fraction of atoms leads to decay on longer time scales. We have studied the underlying decay mechanisms and, depending on the relative depth of the two sublattices, identified either hopping-induced or interaction-induced decay as the main relaxation mechanism. We have confirmed the destructive interference due to the chiral order of the condensate for both relaxation mechanisms. Our classical-field-theory simulations agree well with experimental results from the group of Prof. Andreas Hemmerich [N3].

Along a different route we have considered the coherent instanton-type oscillations that emerge when preparing the atoms at only one of the two degenerate X -points of the lattice. We find oscillation frequencies comparable to the ones obtained in experiments from the group of Prof. Andreas Hemmerich [N4].

For future work it will be interesting to combine the two approaches of this thesis and consider p -orbital order in the hexagonal lattice [205]. The threefold rotational symmetry of the hexagonal lattice combined with the orientation of the p -orbitals will lead to similar frustration phenomena as for spins on a triangular lattice [72]. Also it will be interesting to study the interplay of topological properties of the hexagonal lattice and orbital order.

6. Declaration of contributions

Five of the authors publications, [N1–N5], are related to the work presented in this thesis. The remaining publications, [N6–N8], have been obtained as part of the author’s Bachelor’s and Master’s thesis. My supervisor Ludwig Mathey has been involved deeply in all of the publications.

Observation of Topological Bloch-State Defects and Their Merging Transition

[N1] *M. Tarnowski, M. Nuske, N. Fläschner, B. Rem, D. Vogel, L. Freystatzky, K. Senstock, L. Mathey, C. Weitenberg*

This publication has been written in close collaboration with the group of Christof Weitenberg. All theoretical results have been obtained by the author of this thesis, while all experimental results have been obtained by the group of Christof Weitenberg. The author of this thesis has been involved in the writing process. The perturbative results for the time evolution of the second quantization operators have been obtained before by Lukas Freystatzky and have been published as part of a Bachelor’s thesis [186].

Floquet dynamics in light-driven solids [N2] *M. Nuske, L. Broers, B. Schulte, G. Jotzu, S. A. Sato, A. Cavalleri, A. Rubio, J. W. McIver, L. Mathey*

All results presented in this publication, except for the ones mentioned below, have been obtained by the author of this thesis. As a comparison to the theoretical simulations the publication shows experimental results obtained in the group of James McIver. The results on the single-particle correlation function have been obtained by Lukas Broers. The author of this thesis has been involved deeply in the writing process. The formalism used for this publication is similar in nature to the formalism used in the group of Angel Rubio and we have extensively discussed the details of the formalism.

Metastable order via destructive many-body interference [N3] *M. Nuske, J. Vargas, M. Hachmann, R. Eichberger, L. Mathey, A. Hemmerich*

This publication has been written in close collaboration with the group of Andreas Hemmerich. All theoretical results have been obtained by the author of this thesis, while

all experimental results have been obtained by the group of Andreas Hemmerich. The author of this thesis has been involved deeply in the writing process.

Orbital many-body dynamics of bosons in the second Bloch band of an optical lattice [N4] *J. Vargas, M. Nuske, R. Eichberger, C. Hippler, L. Mathey, A. Hemmerich*

This publication has been written in close collaboration with the group of Andreas Hemmerich. All theoretical results have been obtained by the author of this thesis, while all experimental results have been obtained by the group of Andreas Hemmerich. The author of this thesis has contributed significantly to the writing of this publication.

Microscopic theory for the light-induced anomalous Hall effect in graphene [N5] *S. A. Sato, J. W. McIver, M. Nuske, P. Tang, G. Jotzu, B. Schulte, H. Hübener, U. De Giovannini, L. Mathey, M. A. Sentef, A. Cavalleri, A. Rubio*

The author of this thesis had only minor influence on the results presented in this publication. The formalism used in this publication is similar to the one presented in this thesis and we have extensively discussed the details of the formalism. Hence, the author of this thesis had an influence on the development of the formalism, but has not been involved in the actual calculations presented in this publication.

A. Appendix

A.1. Variational Monte-Carlo minimization

Here we describe the variational Monte-Carlo minimization procedure that we use in order to initialize the system for our (S)PGPE simulations, see Sec. 4.2.1, as well as for adjusting the tight-binding parameters of the s - p_x - p_y -lattice that are not fixed by symmetry considerations, see Sec. 4.1.2.

The goal of variational Monte-Carlo is to optimize a set of parameters p with respect to a given minimization function $\mathcal{F}_{\text{MC}}(p)$. This is achieved by iteratively improving the parameter set by performing a number N_{MC} of Monte-Carlo steps. In each step a new set of parameters p_n is obtained by applying a random variation to the previous set p_{n-1} . The new set is then accepted and used for the next iterative step if $\mathcal{F}_{\text{MC}}(p_n) < \mathcal{F}_{\text{MC}}(p_{n-1})$. If this is not the case the new set may still be accepted with a certain probability. This last aspect of Variational Monte-Carlo ensures that it is possible to leave local minima.

The initial set of parameters p_0 is usually chosen by an educated guess. In each Monte-Carlo step we first determine the new set of tight-binding parameters p_n by adding a normal-distributed random value to each parameter of the previous set of parameters p_{n-1} . The normal distribution we use has 0 mean and width σ_{MC} .

We evaluate the minimization Functional \mathcal{F}_{MC} for both the new and the previous set of parameters and compute the difference

$$\Delta\mathcal{F}_{\text{MC}}(n) = \mathcal{F}_{\text{MC}}(p_n) - \mathcal{F}_{\text{MC}}(p_{n-1}) \quad .$$

If it is positive we always accept the change of parameters and hence use p_n as the starting point for the variation in the next Monte-Carlo step. If $\Delta\mathcal{F}_{\text{MC}}(n)$ is negative we still accept it with probability $e^{\beta_{\text{MC}}\Delta\mathcal{F}_{\text{MC}}(n)}$. If the parameter set is rejected we use the last accepted set of parameters as the starting point for the next Monte-Carlo step, i.e. we set $p_n = p_{n-1}$. Here $\beta_{\text{MC}} = 1/(k_B T_{\text{MC}})$ is the inverse Monte-Carlo temperature. It determines how wide of a regime in parameter space is explored 'uphill' (i.e. for increasing \mathcal{F}_{MC}) of the current parameter set.

During the whole procedure we save the set of tight-binding parameters that has the

overall lowest $\mathcal{F}_{\text{MC}}(p)$.

The Monte-Carlo minimization works most efficiently if the average acceptance rate of the changes of parameters is close to 50%. We ensure this by adjusting the variance σ_{MC} of the parameter changes accordingly. This is done by computing the acceptance rate every 50 Monte-Carlo steps. If the acceptance rate is below 35% we divide σ_{MC} by 2 and if it is above 65% we multiply σ_{MC} by 2.

The success of Variational Monte-Carlo depends crucially on the choice of the inverse Monte-Carlo temperature β_{MC} . If it is too large 'uphill' changes of the parameters are highly unlikely and hence we get stuck in a local minimum. If it is too small it is equally likely to go 'uphill' than 'downhill' and the method has no advantage compared to just randomly sampling all parameter set. In practice it is often helpful to perform an annealing procedure of increasing β_{MC} (or equivalently decreasing T_{MC}). This is also the approach we take here. The value of β_{MC} is increased from $\beta_{\text{MC}}^{\text{initial}}$ to $\beta_{\text{MC}}^{\text{final}}$. The first 20% of the Monte-Carlo steps are done with $\beta_{\text{MC}}^{\text{initial}}$, while the final 20% are done with $\beta_{\text{MC}}^{\text{final}}$. In between we choose

$$\beta_{\text{MC}}^n = \beta_{\text{MC}}^{\text{initial}} \cdot \left(\frac{\beta_{\text{MC}}^{\text{final}}}{\beta_{\text{MC}}^{\text{initial}}} \right)^{(n-0.2N_{\text{MC}})/(0.6N_{\text{MC}})} .$$

A.1.1. Initial state for (S)PGPE simulations

For all results shown in Sec. 4.2 we use Variational Monte-Carlo in order to fill the initial state. Here the set of Monte-Carlo parameters is the set of complex-valued fields on each lattice site $\beta_i = x_i + iy_i$ and the minimization function is the energy of the corresponding lattice state. We start from an empty lattice ($\beta_i = 0$ for all i) and perform $N_{\text{MC}} = 50000$ Monte-Carlo steps. In each step we vary the complex fields on all lattice sites before comparing the energy of the resulting state with the previous. Initially $\sigma_{\text{MC}} = 1$ and $\beta_{\text{MC}}^{\text{initial}} = 1$. The final Monte-Carlo temperature is fixed by the temperature of the desired initial state $T_{\text{MC}} = T$.

A.1.2. Determining tight-binding parameters

In Sec. 4.1.2 our goal is to obtain a consistent set of tight-binding parameters for each value of θ between 0.35π and 0.569π (corresponding to $-1.8V_0 < \Delta V < 0.86V_0$). We do this by minimizing the energy difference between the tight-binding and the Bloch bands at certain symmetry points. Hence the parameter set for the minimization are the

tight-binding parameters and our minimization function is

$$\mathcal{F}_{\text{MC}}(p) = \sum_{b,i} w_b \cdot |E_{b,i}^{(\text{tb})} - E_{b,i}^{(\text{Bloch})}| \quad ,$$

where $E_{b,i}^{(\text{tb})}$ is the energy of the tight-binding bands, $E_{b,i}^{(\text{Bloch})}$ is the energy of the Bloch bands, b is the band index and i runs over the set of symmetry points. For our case we consider the Γ -, M - and X -point, as well as the point halfway in between Γ and X . We only consider the difference for the lowest four bands $i = \{1, 2, 3, 4\}$. For the weights we choose $w_1 = w_2 = 2$ and $w_3 = w_4 = 1$ since in our simulation the atoms are mostly occupying the lower two bands.

We sample 100 values of θ evenly spaced in the interval $0.35\pi < \theta < 0.569\pi$. For $\theta = 0.35\pi$ we use the following set of initial tight-binding parameters

$$\begin{aligned} V'_s &= 1.66 E_{\text{rec}} \\ J_{sp} &= 3.20 \cdot 10^{-4} E_{\text{rec}} \\ J_{sp}^{(d)} &= -1.59 \cdot 10^{-02} E_{\text{rec}} \\ J_{\perp} &= -3.42 \cdot 10^{-03} E_{\text{rec}} \end{aligned}$$

and optimize the values according to the Monte-Carlo minimization described above. For each subsequent value of θ we use the optimal set of the previous θ -value as the initial parameters for the Monte-Carlo minimization. This ensures that the hopping parameters are smooth when varying θ , which is important for our simulation of experiments with dynamic changes of θ .

For the results shown in Fig. 4.9 we have used a total of $N_{\text{MC}} = 10^7$ Monte-Carlo steps. Our initial value of $\sigma_{\text{MC}} = 0.001$, and the initial and final values of β_{MC} are $\beta_{\text{MC}}^{\text{initial}} = 10/E_{\text{rec}}$ and $\beta_{\text{MC}}^{\text{final}} = 1000/E_{\text{rec}}$.

A.2. Equations of motion

A.2.1. PGP-equations

Here we give the full set of equations used for our PGPE calculations

$$\frac{db_{s,\mathbf{R}_i}}{dt} = iJ_{ss} \left(\sum_{\mathbf{R}_j=\pm\mathbf{e}_x,\pm\mathbf{e}_y} b_{s,\mathbf{R}_i+\mathbf{R}_j} \right) + iJ_{ss}^d \left(\sum_{\mathbf{R}_j=\pm\mathbf{e}'_x/2,\pm\mathbf{e}'_y/2} b_{s,\mathbf{R}_i+\mathbf{R}_j} \right)$$

$$\begin{aligned}
& + iJ_z \left(\sum_{\mathbf{R}_j = \pm e_z} b_{s, \mathbf{R}_i + \mathbf{R}_j} \right) \\
& + iJ_{sp_x} b_{x, \mathbf{R}_i - \mathbf{e}'_x/2} - iJ_{sp-x} b_{x, \mathbf{R}_i + \mathbf{e}'_x/2} + iJ_{sp_y} b_{y, \mathbf{R}_i - \mathbf{e}'_y/2} - iJ_{sp-y} b_{y, \mathbf{R}_i + \mathbf{e}'_y/2} \\
& - i(V_s - \mu) b_{s, \mathbf{R}_i} - iU_A b_{s, \mathbf{R}_i}^\dagger b_{s, \mathbf{R}_i} b_{s, \mathbf{R}_i} \quad \text{for } \mathbf{R}_i \in A \\
\frac{db_{s, \mathbf{R}_i}}{dt} = & iJ'_{ss} \left(\sum_{\mathbf{R}_j = \pm e_x, \pm e_y} b_{s, \mathbf{R}_i + \mathbf{R}_j} \right) + iJ_{ss}^d \left(\sum_{\mathbf{R}_j = \pm \mathbf{e}'_x/2, \pm \mathbf{e}'_y/2} b_{s, \mathbf{R}_i + \mathbf{R}_j} \right) \\
& + iJ_z \left(\sum_{\mathbf{R}_j = \pm e_z} b_{s, \mathbf{R}_i + \mathbf{R}_j} \right) \\
& + iJ_{sp_x}^d (b_{x, \mathbf{R}_i - \mathbf{e}_x} + b_{x, \mathbf{R}_i - \mathbf{e}_y} - b_{x, \mathbf{R}_i + \mathbf{e}_x} - b_{x, \mathbf{R}_i + \mathbf{e}_y}) \\
& + iJ_{sp_y}^d (b_{y, \mathbf{R}_i + \mathbf{e}_x} + b_{y, \mathbf{R}_i - \mathbf{e}_y} - b_{y, \mathbf{R}_i - \mathbf{e}_x} - b_{y, \mathbf{R}_i + \mathbf{e}_y}) \\
& - i(V'_s - \mu) b_{s, \mathbf{R}_i} - iU_B \left[b_{s, \mathbf{R}_i}^\dagger b_{s, \mathbf{R}_i} b_{s, \mathbf{R}_i} + \frac{1}{2} b_{s, \mathbf{R}_i}^\dagger (b_{x, \mathbf{R}_i} b_{x, \mathbf{R}_i} + b_{y, \mathbf{R}_i} b_{y, \mathbf{R}_i}) \right. \\
& \left. + (b_{x, \mathbf{R}_i}^\dagger b_{x, \mathbf{R}_i} + b_{y, \mathbf{R}_i}^\dagger b_{y, \mathbf{R}_i}) b_{s, \mathbf{R}_i} \right] \quad \text{for } \mathbf{R}_i \in B \\
\frac{db_{x, \mathbf{R}_i}}{dt} = & iJ_{sp_x} b_{s, \mathbf{R}_i + \mathbf{e}'_x/2} - iJ_{sp-x} b_{s, \mathbf{R}_i - \mathbf{e}'_x/2} \\
& + iJ_{\parallel, x} \left(\sum_{\mathbf{R}_i = \pm e_x, \pm e_y} b_{x, \mathbf{R}_i + \mathbf{R}_j} \right) + iJ_{\perp} \left(\sum_{\mathbf{R}_j = \pm e_x, \pm e_y} b_{y, \mathbf{R}_i + \mathbf{R}_j} \right) \\
& + iJ_z \left(\sum_{\mathbf{R}_j = \pm e_z} b_{x, \mathbf{R}_i + \mathbf{R}_j} \right) \\
& + iJ_{sp_x}^d (b_{s, \mathbf{R}_i + \mathbf{e}_x} + b_{s, \mathbf{R}_i + \mathbf{e}_y} - b_{s, \mathbf{R}_i - \mathbf{e}_x} - b_{s, \mathbf{R}_i - \mathbf{e}_y}) \\
& - i(V_x - \mu) b_{x, \mathbf{R}_i} - iU_B \left[\left(\frac{3}{4} b_{x, \mathbf{R}_i}^\dagger b_{x, \mathbf{R}_i} + \frac{1}{2} b_{y, \mathbf{R}_i}^\dagger b_{y, \mathbf{R}_i} + b_{s, \mathbf{R}_i}^\dagger b_{s, \mathbf{R}_i} \right) b_{x, \mathbf{R}_i} \right. \\
& \left. + b_{x, \mathbf{R}_i}^\dagger \left(\frac{1}{4} b_{y, \mathbf{R}_i} b_{y, \mathbf{R}_i} + \frac{1}{2} b_{s, \mathbf{R}_i} b_{s, \mathbf{R}_i} \right) \right] \quad \text{for } \mathbf{R}_i \in B \\
\frac{db_{y, \mathbf{R}_i}}{dt} = & iJ_{sp_y} b_{s, \mathbf{R}_i + \mathbf{e}'_y/2} - iJ_{sp-y} b_{s, \mathbf{R}_i - \mathbf{e}'_y/2} \\
& + iJ_{\parallel, y} \left(\sum_{\mathbf{R}_i = \pm e_x, \pm e_y} b_{y, \mathbf{R}_i + \mathbf{R}_j} \right) + iJ_{\perp} \left(\sum_{\mathbf{R}_j = \pm e_x, \pm e_y} b_{x, \mathbf{R}_i + \mathbf{R}_j} \right) \\
& + iJ_z \left(\sum_{\mathbf{R}_j = \pm e_z} b_{y, \mathbf{R}_i + \mathbf{R}_j} \right) \\
& + iJ_{sp_y}^d (b_{s, \mathbf{R}_i - \mathbf{e}_x} + b_{s, \mathbf{R}_i + \mathbf{e}_y} - b_{s, \mathbf{R}_i + \mathbf{e}_x} - b_{s, \mathbf{R}_i - \mathbf{e}_y}) \\
& - i(V_y - \mu) b_{y, \mathbf{R}_i} - iU_B \left[\left(\frac{3}{4} b_{y, \mathbf{R}_i}^\dagger b_{y, \mathbf{R}_i} + \frac{1}{2} b_{x, \mathbf{R}_i}^\dagger b_{x, \mathbf{R}_i} + b_{s, \mathbf{R}_i}^\dagger b_{s, \mathbf{R}_i} \right) b_{y, \mathbf{R}_i} \right. \\
& \left. + b_{y, \mathbf{R}_i}^\dagger \left(\frac{1}{4} b_{x, \mathbf{R}_i} b_{x, \mathbf{R}_i} + \frac{1}{2} b_{s, \mathbf{R}_i} b_{s, \mathbf{R}_i} \right) \right] \quad \text{for } \mathbf{R}_i \in B
\end{aligned}$$

$$+ b_{y,\mathbf{R}_i}^\dagger \left(\frac{1}{4} b_{x,\mathbf{R}_i} b_{x,\mathbf{R}_i} + \frac{1}{2} b_{s,\mathbf{R}_i} b_{s,\mathbf{R}_i} \right) \Big] \quad \text{for } \mathbf{R}_i \in B \quad ,$$

where μ is the chemical potential.

A.2.2. SPGP-equations

Here we give the full set of equations used for our SPGPE calculations

$$\begin{aligned} \frac{dx_{s,\mathbf{R}_i}}{dt} &= -J_{ss} \left(\sum_{\mathbf{R}_j=\pm\mathbf{e}_x,\pm\mathbf{e}_y} y_{s,\mathbf{R}_i+\mathbf{R}_j} \right) - J_{ss}^d \left(\sum_{\mathbf{R}_j=\pm\mathbf{e}'_x/2,\pm\mathbf{e}'_y/2} y_{s,\mathbf{R}_i+\mathbf{R}_j} \right) - J_z \left(\sum_{\mathbf{R}_j=\pm\mathbf{e}_z} y_{s,\mathbf{R}_i+\mathbf{R}_j} \right) \\ &\quad - J_{sp_x} y_{x,\mathbf{R}_i-\mathbf{e}'_x/2} + J_{sp_{-x}} y_{x,\mathbf{R}_i+\mathbf{e}'_x/2} - J_{sp_y} y_{y,\mathbf{R}_i-\mathbf{e}'_y/2} + J_{sp_{-y}} y_{y,\mathbf{R}_i+\mathbf{e}'_y/2} \\ &\quad + (V_s - \mu) y_{s,\mathbf{R}_i} + U_A (x_{s,\mathbf{R}_i}^2 y_{s,\mathbf{R}_i} + y_{s,\mathbf{R}_i}^3 - y_{s,\mathbf{R}_i}) \quad \text{for } \mathbf{R}_i \in A \\ \frac{dy_{s,\mathbf{R}_i}}{dt} &= J_{ss} \left(\sum_{\mathbf{R}_j=\pm\mathbf{e}_x,\pm\mathbf{e}_y} x_{s,\mathbf{R}_i+\mathbf{R}_j} \right) + J_{ss}^d \left(\sum_{\mathbf{R}_j=\pm\mathbf{e}'_x/2,\pm\mathbf{e}'_y/2} x_{s,\mathbf{R}_i+\mathbf{R}_j} \right) + J_z \left(\sum_{\mathbf{R}_j=\pm\mathbf{e}_z} x_{s,\mathbf{R}_i+\mathbf{R}_j} \right) \\ &\quad + J_{sp_x} x_{x,\mathbf{R}_i-\mathbf{e}'_x/2} - J_{sp_{-x}} x_{x,\mathbf{R}_i+\mathbf{e}'_x/2} + J_{sp_y} x_{y,\mathbf{R}_i-\mathbf{e}'_y/2} - J_{sp_{-y}} x_{y,\mathbf{R}_i+\mathbf{e}'_y/2} \\ &\quad - (V_s - \mu) x_{s,\mathbf{R}_i} + U_A (-x_{s,\mathbf{R}_i} y_{s,\mathbf{R}_i}^2 - x_{s,\mathbf{R}_i}^3 + x_{s,\mathbf{R}_i}) \quad \text{for } \mathbf{R}_i \in A \\ \frac{dx_{s,\mathbf{R}_i}}{dt} &= -J'_{ss} \left(\sum_{\mathbf{R}_j=\pm\mathbf{e}_x,\pm\mathbf{e}_y} y_{s,\mathbf{R}_i+\mathbf{R}_j} \right) - J_{ss}^d \left(\sum_{\mathbf{R}_j=\pm\mathbf{e}'_x/2,\pm\mathbf{e}'_y/2} y_{s,\mathbf{R}_i+\mathbf{R}_j} \right) - J_z \left(\sum_{\mathbf{R}_j=\pm\mathbf{e}_z} y_{s,\mathbf{R}_i+\mathbf{R}_j} \right) \\ &\quad + J_{sp_x}^d (y_{x,\mathbf{R}_i+\mathbf{e}_x} + y_{x,\mathbf{R}_i+\mathbf{e}_y} - y_{x,\mathbf{R}_i-\mathbf{e}_x} - y_{x,\mathbf{R}_i-\mathbf{e}_y}) \\ &\quad + J_{sp_y}^d (y_{y,\mathbf{R}_i-\mathbf{e}_x} + y_{y,\mathbf{R}_i+\mathbf{e}_y} - y_{y,\mathbf{R}_i+\mathbf{e}_x} - y_{y,\mathbf{R}_i-\mathbf{e}_y}) \\ &\quad + (V'_s - \mu) y_{s,\mathbf{R}_i} \\ &\quad + U_B \left[(x_{s,\mathbf{R}_i}^2 y_{s,\mathbf{R}_i} + y_{s,\mathbf{R}_i}^3 - y_{s,\mathbf{R}_i}) \right. \\ &\quad + \frac{1}{2} (y_{s,\mathbf{R}_i} y_{x,\mathbf{R}_i}^2 + 2x_{s,\mathbf{R}_i} x_{x,\mathbf{R}_i} y_{x,\mathbf{R}_i} - y_{s,\mathbf{R}_i} x_{x,\mathbf{R}_i}^2) \\ &\quad + \frac{1}{2} (y_{s,\mathbf{R}_i} y_{y,\mathbf{R}_i}^2 + 2x_{s,\mathbf{R}_i} x_{y,\mathbf{R}_i} y_{y,\mathbf{R}_i} - y_{s,\mathbf{R}_i} x_{y,\mathbf{R}_i}^2) \\ &\quad \left. + y_{s,\mathbf{R}_i} (x_{x,\mathbf{R}_i}^2 + y_{x,\mathbf{R}_i}^2 + x_{y,\mathbf{R}_i}^2 + y_{y,\mathbf{R}_i}^2 - 1) \right] \quad \text{for } \mathbf{R}_i \in B \\ \frac{dy_{s,\mathbf{R}_i}}{dt} &= J'_{ss} \left(\sum_{\mathbf{R}_j=\pm\mathbf{e}_x,\pm\mathbf{e}_y} x_{s,\mathbf{R}_i+\mathbf{R}_j} \right) + J_{ss}^d \left(\sum_{\mathbf{R}_j=\pm\mathbf{e}'_x/2,\pm\mathbf{e}'_y/2} x_{s,\mathbf{R}_i+\mathbf{R}_j} \right) + J_z \left(\sum_{\mathbf{R}_j=\pm\mathbf{e}_z} x_{s,\mathbf{R}_i+\mathbf{R}_j} \right) \\ &\quad - J_{sp_x}^d (x_{x,\mathbf{R}_i+\mathbf{e}_x} + x_{x,\mathbf{R}_i+\mathbf{e}_y} - x_{x,\mathbf{R}_i-\mathbf{e}_x} - x_{x,\mathbf{R}_i-\mathbf{e}_y}) \\ &\quad - J_{sp_y}^d (x_{y,\mathbf{R}_i-\mathbf{e}_x} + x_{y,\mathbf{R}_i+\mathbf{e}_y} - x_{y,\mathbf{R}_i+\mathbf{e}_x} - x_{y,\mathbf{R}_i-\mathbf{e}_y}) \\ &\quad - (V'_s - \mu) x_{s,\mathbf{R}_i} \end{aligned}$$

$$\begin{aligned}
& + U_B \left[\left(-x_{s,\mathbf{R}_i} y_{s,\mathbf{R}_i}^2 - x_{s,\mathbf{R}_i}^3 - x_{s,\mathbf{R}_i} \right) \right. \\
& + \frac{1}{2} \left(x_{s,\mathbf{R}_i} y_{x,\mathbf{R}_i}^2 - 2y_{s,\mathbf{R}_i} x_{x,\mathbf{R}_i} y_{x,\mathbf{R}_i} - x_{s,\mathbf{R}_i} x_{x,\mathbf{R}_i}^2 \right) \\
& + \frac{1}{2} \left(x_{s,\mathbf{R}_i} y_{y,\mathbf{R}_i}^2 - 2y_{s,\mathbf{R}_i} x_{y,\mathbf{R}_i} y_{y,\mathbf{R}_i} - x_{s,\mathbf{R}_i} x_{y,\mathbf{R}_i}^2 \right) \\
& \left. + x_{s,\mathbf{R}_i} \left(1 - x_{x,\mathbf{R}_i}^2 - y_{x,\mathbf{R}_i}^2 - x_{y,\mathbf{R}_i}^2 - y_{y,\mathbf{R}_i}^2 \right) \right] \text{ for } \mathbf{R}_i \in B \\
\frac{dx_{x,\mathbf{R}_i}}{dt} = & -J_{sp_x} y_{s,\mathbf{R}_i + \mathbf{e}'_x/2} + J_{sp_{-x}} y_{s,\mathbf{R}_i - \mathbf{e}'_x/2} - J_z \left(\sum_{\mathbf{R}_j = \pm \mathbf{e}_z} y_{x,\mathbf{R}_i + \mathbf{R}_j} \right) \\
& - J_{\parallel,x} \left(\sum_{\mathbf{R}_j = \pm \mathbf{e}_x, \pm \mathbf{e}_y} y_{x,\mathbf{R}_i + \mathbf{R}_j} \right) - J_{\perp} \left(\sum_{\mathbf{R}_j = \pm \mathbf{e}_x, \pm \mathbf{e}_y} y_{y,\mathbf{R}_i + \mathbf{R}_j} \right) \\
& + J_{sp_x}^d \left(y_{s,\mathbf{R}_i - \mathbf{e}_x} + y_{s,\mathbf{R}_i - \mathbf{e}_y} - y_{s,\mathbf{R}_i + \mathbf{e}_x} - y_{s,\mathbf{R}_i + \mathbf{e}_y} \right) + (V_x - \mu) y_{x,\mathbf{R}_i} \\
& + U_B \left[\frac{3}{4} \left(x_{x,\mathbf{R}_i}^2 y_{x,\mathbf{R}_i} + y_{x,\mathbf{R}_i}^3 - y_{x,\mathbf{R}_i} \right) \right. \\
& + \frac{1}{2} y_{x,\mathbf{R}_i} \left(x_{y,\mathbf{R}_i}^2 + y_{y,\mathbf{R}_i}^2 - \frac{1}{2} \right) \\
& + \frac{1}{4} \left(y_{x,\mathbf{R}_i} y_{y,\mathbf{R}_i}^2 + 2x_{x,\mathbf{R}_i} x_{y,\mathbf{R}_i} y_{y,\mathbf{R}_i} - x_{y,\mathbf{R}_i}^2 y_{x,\mathbf{R}_i} \right) \\
& + \frac{1}{2} \left(y_{x,\mathbf{R}_i} y_{s,\mathbf{R}_i}^2 + 2x_{x,\mathbf{R}_i} x_{s,\mathbf{R}_i} y_{s,\mathbf{R}_i} - x_{s,\mathbf{R}_i}^2 y_{x,\mathbf{R}_i} \right) \\
& \left. + y_{x,\mathbf{R}_i} \left(x_{s,\mathbf{R}_i}^2 + y_{s,\mathbf{R}_i}^2 - \frac{1}{2} \right) \right] \text{ for } \mathbf{R}_i \in B \\
\frac{dy_{x,\mathbf{R}_i}}{dt} = & J_{sp_x} x_{s,\mathbf{R}_i + \mathbf{e}'_x/2} - J_{sp_{-x}} x_{s,\mathbf{R}_i - \mathbf{e}'_x/2} + J_z \left(\sum_{\mathbf{R}_j = \pm \mathbf{e}_z} x_{x,\mathbf{R}_i + \mathbf{R}_j} \right) \\
& + J_{\parallel,x} \left(\sum_{\mathbf{R}_j = \pm \mathbf{e}_x, \pm \mathbf{e}_y} x_{x,\mathbf{R}_i + \mathbf{R}_j} \right) + J_{\perp} \left(\sum_{\mathbf{R}_j = \pm \mathbf{e}_x, \pm \mathbf{e}_y} x_{y,\mathbf{R}_i + \mathbf{R}_j} \right) \\
& - J_{sp_x}^d \left(x_{s,\mathbf{R}_i - \mathbf{e}_x} + x_{s,\mathbf{R}_i - \mathbf{e}_y} - x_{s,\mathbf{R}_i + \mathbf{e}_x} - x_{s,\mathbf{R}_i + \mathbf{e}_y} \right) - (V_x - \mu) x_{x,\mathbf{R}_i} \\
& + U_B \left[\frac{3}{4} \left(-x_{x,\mathbf{R}_i} y_{x,\mathbf{R}_i}^2 - x_{x,\mathbf{R}_i}^3 + x_{x,\mathbf{R}_i} \right) \right. \\
& + \frac{1}{2} x_{x,\mathbf{R}_i} \left(\frac{1}{2} - x_{y,\mathbf{R}_i}^2 - y_{y,\mathbf{R}_i}^2 \right) \\
& + \frac{1}{4} \left(x_{x,\mathbf{R}_i} y_{y,\mathbf{R}_i}^2 - 2x_{y,\mathbf{R}_i} y_{x,\mathbf{R}_i} y_{y,\mathbf{R}_i} - x_{x,\mathbf{R}_i} x_{y,\mathbf{R}_i}^2 \right) \\
& + \frac{1}{2} \left(x_{x,\mathbf{R}_i} y_{s,\mathbf{R}_i}^2 - 2y_{x,\mathbf{R}_i} x_{s,\mathbf{R}_i} y_{s,\mathbf{R}_i} - x_{s,\mathbf{R}_i}^2 x_{x,\mathbf{R}_i} \right) \\
& \left. + x_{x,\mathbf{R}_i} \left(\frac{1}{2} - x_{s,\mathbf{R}_i}^2 - y_{s,\mathbf{R}_i}^2 \right) \right] \text{ for } \mathbf{R}_i \in B
\end{aligned}$$

$$\begin{aligned}
\frac{dx_{y,\mathbf{R}_i}}{dt} = & -J_{sp_y}y_{s,\mathbf{R}_i+\mathbf{e}'_y/2} + J_{sp_{-y}}y_{s,\mathbf{R}_i-\mathbf{e}'_y/2} - J_z \left(\sum_{\mathbf{R}_j=\pm\mathbf{e}_z} y_{y,\mathbf{R}_i+\mathbf{R}_j} \right) \\
& - J_{\parallel,y} \left(\sum_{\mathbf{R}_j=\pm\mathbf{e}_x,\pm\mathbf{e}_y} y_{y,\mathbf{R}_i+\mathbf{R}_j} \right) - J_{\perp} \left(\sum_{\mathbf{R}_j=\pm\mathbf{e}_x,\pm\mathbf{e}_y} y_{x,\mathbf{R}_i+\mathbf{R}_j} \right) \\
& + J_{sp_y}^d (y_{s,\mathbf{R}_i+\mathbf{e}_x} + y_{s,\mathbf{R}_i-\mathbf{e}_y} - y_{s,\mathbf{R}_i-\mathbf{e}_x} - y_{s,\mathbf{R}_i+\mathbf{e}_y}) + (V_y - \mu)y_{y,\mathbf{R}_i} \\
& + U_B \left[\frac{3}{4} (x_{y,\mathbf{R}_i}^2 y_{y,\mathbf{R}_i} + y_{y,\mathbf{R}_i}^3 - y_{y,\mathbf{R}_i}) \right. \\
& + \frac{1}{2} y_{y,\mathbf{R}_i} \left(x_{x,\mathbf{R}_i}^2 + y_{x,\mathbf{R}_i}^2 - \frac{1}{2} \right) \\
& + \frac{1}{4} (y_{y,\mathbf{R}_i} y_{x,\mathbf{R}_i}^2 + 2x_{y,\mathbf{R}_i} x_{x,\mathbf{R}_i} y_{x,\mathbf{R}_i} - x_{x,\mathbf{R}_i}^2 y_{y,\mathbf{R}_i}) \\
& + \frac{1}{2} (y_{y,\mathbf{R}_i} y_{s,\mathbf{R}_i}^2 + 2x_{y,\mathbf{R}_i} x_{s,\mathbf{R}_i} y_{s,\mathbf{R}_i} - x_{s,\mathbf{R}_i}^2 y_{y,\mathbf{R}_i}) \\
& \left. + y_{y,\mathbf{R}_i} \left(x_{s,\mathbf{R}_i}^2 + y_{s,\mathbf{R}_i}^2 - \frac{1}{2} \right) \right] \quad \text{for } \mathbf{R}_i \in B
\end{aligned}$$

$$\begin{aligned}
\frac{dy_{y,\mathbf{R}_i}}{dt} = & J_{sp_y}x_{s,\mathbf{R}_i+\mathbf{e}'_y/2} - J_{sp_{-y}}x_{s,\mathbf{R}_i-\mathbf{e}'_y/2} + J_z \left(\sum_{\mathbf{R}_j=\pm\mathbf{e}_z} x_{y,\mathbf{R}_i+\mathbf{R}_j} \right) \\
& + J_{\parallel,y} \left(\sum_{\mathbf{R}_j=\pm\mathbf{e}_x,\pm\mathbf{e}_y} x_{y,\mathbf{R}_i+\mathbf{R}_j} \right) + J_{\perp} \left(\sum_{\mathbf{R}_j=\pm\mathbf{e}_x,\pm\mathbf{e}_y} x_{x,\mathbf{R}_i+\mathbf{R}_j} \right) \\
& - J_{sp_y}^d (x_{s,\mathbf{R}_i+\mathbf{e}_x} + x_{s,\mathbf{R}_i-\mathbf{e}_y} - x_{s,\mathbf{R}_i-\mathbf{e}_x} - x_{s,\mathbf{R}_i+\mathbf{e}_y}) - (V_y - \mu)x_{y,\mathbf{R}_i} \\
& + U_B \left[\frac{3}{4} (-x_{y,\mathbf{R}_i} y_{y,\mathbf{R}_i}^2 - x_{y,\mathbf{R}_i}^3 + x_{y,\mathbf{R}_i}) \right. \\
& + \frac{1}{2} x_{y,\mathbf{R}_i} \left(\frac{1}{2} - x_{x,\mathbf{R}_i}^2 - y_{x,\mathbf{R}_i}^2 \right) \\
& + \frac{1}{4} (x_{y,\mathbf{R}_i} y_{x,\mathbf{R}_i}^2 - 2x_{x,\mathbf{R}_i} y_{y,\mathbf{R}_i} y_{x,\mathbf{R}_i} - x_{y,\mathbf{R}_i} x_{x,\mathbf{R}_i}^2) \\
& + \frac{1}{2} (x_{y,\mathbf{R}_i} y_{s,\mathbf{R}_i}^2 - 2y_{y,\mathbf{R}_i} x_{s,\mathbf{R}_i} y_{s,\mathbf{R}_i} - x_{s,\mathbf{R}_i}^2 x_{y,\mathbf{R}_i}) \\
& \left. + x_{y,\mathbf{R}_i} \left(\frac{1}{2} - x_{s,\mathbf{R}_i}^2 - y_{s,\mathbf{R}_i}^2 \right) \right] \quad \text{for } \mathbf{R}_i \in B \quad .
\end{aligned}$$

Author's publications

- [N1] Matthias Tarnowski, **Marlon Nuske**, Nick Fläschner, Benno Rem, Dominik Vogel, Lukas Freystatzky, Klaus Sengstock, Ludwig Mathey, and Christof Weitenberg. Observation of Topological Bloch-State Defects and Their Merging Transition. *Physical Review Letters*, 118(24):240403, June 2017.
- [N2] **M. Nuske**, L. Broers, B. Schulte, G. Jotzu, S. A. Sato, A. Cavalleri, A. Rubio, J. W. McIver, and L. Mathey. Floquet dynamics in light-driven solids. *arXiv:2005.10824 [cond-mat]*, May 2020.
- [N3] **M. Nuske**, J. Vargas, M. Hachmann, R. Eichberger, L. Mathey, and A. Hemmerich. Metastable order via destructive many-body interference. *arXiv:2004.00620*, April 2020.
- [N4] J. Vargas, **M. Nuske**, R. Eichberger, C. Hippler, L. Mathey, and A. Hemmerich. Orbital many-body dynamics of bosons in the second Bloch band of an optical lattice. *arXiv:2008.05471 [cond-mat]*, August 2020.
- [N5] S. A. Sato, J. W. McIver, **M. Nuske**, P. Tang, G. Jotzu, B. Schulte, H. Hübener, U. De Giovannini, L. Mathey, M. A. Sentef, A. Cavalleri, and A. Rubio. Microscopic theory for the light-induced anomalous Hall effect in graphene. *Physical Review B*, 99(21):214302, June 2019.
- [N6] **Marlon Nuske**, Eite Tiesinga, and L. Mathey. Optimization of collisional Feshbach cooling of an ultracold nondegenerate gas. *Physical Review A*, 91(4):043626, April 2015.
- [N7] **Marlon Nuske**, L. Mathey, and Eite Tiesinga. Sudden-quench dynamics of Bardeen-Cooper-Schrieffer states in deep optical lattices. *Physical Review A*, 94(2):023607, August 2016.
- [N8] **Marlon Nuske**. Master's thesis: Simulating graphene with ultra-cold atoms in optical lattices, 2015.

Bibliography

- [1] Siegfried Hunklinger. *Festkörperphysik*. De Gruyter Oldenbourg, Berlin ; Boston, 5th edition, December 2017.
- [2] David N. Mermin Neil W. Ashcroft. *Festkörperphysik*. Oldenbourg Wissensch. Vlg., München, 3rd edition, June 2007.
- [3] Robert Karplus and J. M. Luttinger. Hall Effect in Ferromagnetics. *Physical Review*, 95(5):1154–1160, September 1954.
- [4] W. Kohn and J. M. Luttinger. Quantum Theory of Electrical Transport Phenomena. *Physical Review*, 108(3):590–611, November 1957.
- [5] J. M. Luttinger and W. Kohn. Quantum Theory of Electrical Transport Phenomena. II. *Physical Review*, 109(6):1892–1909, March 1958.
- [6] E. N. Adams and E. I. Blount. Energy bands in the presence of an external force field—II: Anomalous velocities. *Journal of Physics and Chemistry of Solids*, 10(4):286–303, August 1959.
- [7] K. v. Klitzing, G. Dorda, and M. Pepper. New Method for High-Accuracy Determination of the Fine-Structure Constant Based on Quantized Hall Resistance. *Physical Review Letters*, 45(6):494–497, August 1980.
- [8] M. V. Berry. Quantal Phase Factors Accompanying Adiabatic Changes. *Proceedings of the Royal Society of London A: Mathematical, Physical and Engineering Sciences*, 392(1802):45–57, March 1984.
- [9] Frank Wilczek and Alfred Shapere. *Geometric Phases in Physics*. World Scientific, 1989.
- [10] Arno Bohm. *The geometric phase in quantum systems: foundations, mathematical concepts, and applications in molecular and condensed matter physics*. Texts and monographs in Physics and astronomy online library. Springer, Berlin, 2003.

- [11] D. J. Thouless, M. Kohmoto, M. P. Nightingale, and M. den Nijs. Quantized Hall Conductance in a Two-Dimensional Periodic Potential. *Physical Review Letters*, 49(6):405–408, August 1982.
- [12] C. L. Kane and E. J. Mele. Quantum Spin Hall Effect in Graphene. *Physical Review Letters*, 95(22):226801, November 2005.
- [13] C. L. Kane and E. J. Mele. Z_2 Topological Order and the Quantum Spin Hall Effect. *Physical Review Letters*, 95(14):146802, September 2005.
- [14] B. Andrei Bernevig and Shou-Cheng Zhang. Quantum Spin Hall Effect. *Physical Review Letters*, 96(10):106802, March 2006.
- [15] B. Andrei Bernevig, Taylor L. Hughes, and Shou-Cheng Zhang. Quantum Spin Hall Effect and Topological Phase Transition in HgTe Quantum Wells. *Science*, 314(5806):1757–1761, December 2006.
- [16] Markus König, Steffen Wiedmann, Christoph Brüne, Andreas Roth, Hartmut Buhmann, Laurens W. Molenkamp, Xiao-Liang Qi, and Shou-Cheng Zhang. Quantum Spin Hall Insulator State in HgTe Quantum Wells. *Science*, 318(5851):766–770, November 2007.
- [17] D. C. Tsui, H. L. Stormer, and A. C. Gossard. Two-Dimensional Magnetotransport in the Extreme Quantum Limit. *Physical Review Letters*, 48(22):1559–1562, May 1982.
- [18] Xiao-Gang Wen. Topological orders and Edge excitations in FQH states. *Advances in Physics*, 44(5):405–473, October 1995.
- [19] Horst L. Stormer, Daniel C. Tsui, and Arthur C. Gossard. The fractional quantum Hall effect. *Reviews of Modern Physics*, 71(2):S298–S305, March 1999.
- [20] M. Z. Hasan and C. L. Kane. *Colloquium* : Topological insulators. *Reviews of Modern Physics*, 82(4):3045–3067, November 2010.
- [21] Xiao-Liang Qi and Shou-Cheng Zhang. Topological insulators and superconductors. *Reviews of Modern Physics*, 83(4):1057–1110, October 2011.
- [22] B. Andrei Bernevig and Taylor L. Hughes. *Topological Insulators and Topological Superconductors*. Princeton University Press, Princeton, April 2013.
- [23] C. Dutreix, H. González-Herrero, I. Brihuega, M. I. Katsnelson, C. Chapelier, and V. T. Renard. Measuring the Berry phase of graphene from wavefront dislocations in Friedel oscillations. *Nature*, September 2019.

-
- [24] W. Ketterle, D. S. Durfee, and D. M. Stamper-Kurn. Making, probing and understanding Bose-Einstein condensates. *arXiv:cond-mat/9904034*, April 1999.
- [25] Alessio Celi, Anna Sanpera, Veronica Ahufinger, and Maciej Lewenstein. Quantum optics and frontiers of physics: the third quantum revolution. *Physica Scripta*, 92(1):013003, December 2016.
- [26] Oliver Morsch and Markus Oberthaler. Dynamics of Bose-Einstein condensates in optical lattices. *Reviews of Modern Physics*, 78(1):179–215, February 2006.
- [27] Maciej Lewenstein, Anna Sanpera, Veronica Ahufinger, Bogdan Damski, Aditi Sen De, and Ujjwal Sen. Ultracold atomic gases in optical lattices: mimicking condensed matter physics and beyond. *Advances in Physics*, 56(2):243–379, March 2007.
- [28] Immanuel Bloch, Jean Dalibard, and Sylvain Nascimbène. Quantum simulations with ultracold quantum gases. *Nature Physics*, 8(4):267–276, April 2012.
- [29] M. H. Anderson, J. R. Ensher, M. R. Matthews, C. E. Wieman, and E. A. Cornell. Observation of Bose-Einstein Condensation in a Dilute Atomic Vapor. *Science*, 269(5221):198–201, July 1995.
- [30] Kendall B. Davis, Marc-Oliver Mewes, Michael A. Joffe, Michael R. Andrews, and Wolfgang Ketterle. Evaporative Cooling of Sodium Atoms. *Physical Review Letters*, 74(26):5202–5205, June 1995.
- [31] C. C. Bradley, C. A. Sackett, and R. G. Hulet. Bose-Einstein Condensation of Lithium: Observation of Limited Condensate Number. *Physical Review Letters*, 78(6):985–989, February 1997.
- [32] Markus Greiner, Olaf Mandel, Tilman Esslinger, Theodor W. Hänsch, and Immanuel Bloch. Quantum phase transition from a superfluid to a Mott insulator in a gas of ultracold atoms. *Nature*, 415(6867):39–44, January 2002.
- [33] Tobias Salger. Klein Tunneling of a Quasirelativistic Bose-Einstein Condensate in an Optical Lattice. *Physical Review Letters*, 107(24), 2011.
- [34] Zachary A. Geiger, Kurt M. Fujiwara, Kevin Singh, Ruwan Senaratne, Shankari V. Rajagopal, Mikhail Lipatov, Toshihiko Shimasaki, Rodislav Driben, Vladimir V. Konotop, Torsten Meier, and David M. Weld. Observation and Uses of Position-Space Bloch Oscillations in an Ultracold Gas. *Physical Review Letters*, 120(21):213201, May 2018.

- [35] Nathan Goldman, Jean Dalibard, Alexandre Dauphin, Fabrice Gerbier, Maciej Lewenstein, Peter Zoller, and Ian B. Spielman. Direct imaging of topological edge states in cold-atom systems. *Proceedings of the National Academy of Sciences*, 110(17):6736–6741, April 2013.
- [36] B. K. Stuhl, H.-I. Lu, L. M. Ayccock, D. Genkina, and I. B. Spielman. Visualizing edge states with an atomic Bose gas in the quantum Hall regime. *Science*, 349(6255):1514–1518, September 2015.
- [37] M. Mancini, G. Pagano, G. Cappellini, L. Livi, M. Rider, J. Catani, C. Sias, P. Zoller, M. Inguscio, M. Dalmonte, and L. Fallani. Observation of chiral edge states with neutral fermions in synthetic Hall ribbons. *Science*, 349(6255):1510–1513, September 2015.
- [38] N. Goldman, J. C. Budich, and P. Zoller. Topological Quantum Matter with Ultracold Gases in Optical Lattices. *Nature Physics*, 12(7):639–645, June 2016.
- [39] Tomoki Ozawa and Hannah M. Price. Topological quantum matter in synthetic dimensions. *Nature Reviews Physics*, 1(5):349–357, May 2019.
- [40] Dan-Wei Zhang, Yan-Qing Zhu, Y. X. Zhao, Hui Yan, and Shi-Liang Zhu. Topological quantum matter with cold atoms. *Advances in Physics*, 67(4):253–402, October 2018.
- [41] A. Castro Neto, F. Guinea, N. Peres, K. Novoselov, and A. Geim. The electronic properties of graphene. *Reviews of Modern Physics*, 81(1):109–162, January 2009.
- [42] K. S. Novoselov, A. K. Geim, S. V. Morozov, D. Jiang, Y. Zhang, S. V. Dubonos, I. V. Grigorieva, and A. A. Firsov. Electric Field Effect in Atomically Thin Carbon Films. *Science*, 306(5696):666–669, October 2004.
- [43] A. K. Geim and K. S. Novoselov. The rise of graphene. *Nature Materials*, 6(3):183–191, March 2007.
- [44] K. S. Novoselov, A. K. Geim, S. V. Morozov, D. Jiang, M. I. Katsnelson, I. V. Grigorieva, S. V. Dubonos, and A. A. Firsov. Two-dimensional gas of massless Dirac fermions in graphene. *Nature*, 438(7065):197–200, November 2005.
- [45] Yuanbo Zhang, Yan-Wen Tan, Horst L. Stormer, and Philip Kim. Experimental observation of the quantum Hall effect and Berry’s phase in graphene. *Nature*, 438(7065):201–204, November 2005.
- [46] V. P. Gusynin and S. G. Sharapov. Unconventional Integer Quantum Hall Effect in Graphene. *Physical Review Letters*, 95(14):146801, September 2005.

-
- [47] M. I. Katsnelson, K. S. Novoselov, and A. K. Geim. Chiral tunnelling and the Klein paradox in graphene. *Nature Physics*, 2(9):620–625, September 2006.
- [48] S. Das Sarma, Shaffique Adam, E. H. Hwang, and Enrico Rossi. Electronic transport in two-dimensional graphene. *Reviews of Modern Physics*, 83(2):407–470, May 2011.
- [49] T. Reiss, K. Hjelt, and A. C. Ferrari. Graphene is on track to deliver on its promises. *Nature Nanotechnology*, 14(10):907–910, October 2019.
- [50] Di Xiao, Ming-Che Chang, and Qian Niu. Berry phase effects on electronic properties. *Reviews of Modern Physics*, 82(3):1959–2007, July 2010.
- [51] D. Fausti, R. I. Tobey, N. Dean, S. Kaiser, A. Dienst, M. C. Hoffmann, S. Pyon, T. Takayama, H. Takagi, and A. Cavalleri. Light-Induced Superconductivity in a Stripe-Ordered Cuprate. *Science*, 331(6014):189–191, January 2011.
- [52] W. Hu, S. Kaiser, D. Nicoletti, C. R. Hunt, I. Gierz, M. C. Hoffmann, M. Le Tacon, T. Loew, B. Keimer, and A. Cavalleri. Optically enhanced coherent transport in $\text{YBa}_2\text{Cu}_3\text{O}_{6.5}$ by ultrafast redistribution of interlayer coupling. *Nature Materials*, 13(7):705–711, July 2014.
- [53] M. Mitrano, A. Cantaluppi, D. Nicoletti, S. Kaiser, A. Perucchi, S. Lupi, P. Di Pietro, D. Pontiroli, M. Riccò, S. R. Clark, D. Jaksch, and A. Cavalleri. Possible light-induced superconductivity in $\text{K}_3\text{C}_6\text{O}$ at high temperature. *Nature*, 530(7591):461–464, February 2016.
- [54] Jun-ichi Okamoto, Andrea Cavalleri, and Ludwig Mathey. Theory of Enhanced Interlayer Tunneling in Optically Driven High- T_c Superconductors. *Physical Review Letters*, 117(22):227001, November 2016.
- [55] Jun-ichi Okamoto, Wanzheng Hu, Andrea Cavalleri, and Ludwig Mathey. Transiently enhanced interlayer tunneling in optically driven high- T_c superconductors. *Physical Review B*, 96(14):144505, October 2017.
- [56] Jon H. Shirley. Solution of the Schrödinger Equation with a Hamiltonian Periodic in Time. *Physical Review*, 138(4B):B979–B987, May 1965.
- [57] Hideo Sambe. Steady States and Quasienergies of a Quantum-Mechanical System in an Oscillating Field. *Physical Review A*, 7(6):2203–2213, June 1973.
- [58] Marin Bukov, Luca D’Alessio, and Anatoli Polkovnikov. Universal high-frequency behavior of periodically driven systems: from dynamical stabilization to Floquet engineering. *Advances in Physics*, 64(2):139–226, March 2015.

- [59] Gloria Platero and Ramón Aguado. Photon-assisted transport in semiconductor nanostructures. *Physics Reports*, 395(1):1–157, May 2004.
- [60] Sigmund Kohler, Jörg Lehmann, and Peter Hänggi. Driven quantum transport on the nanoscale. *Physics Reports*, 406(6):379–443, February 2005.
- [61] Toshimasa Fujisawa and Seigo Tarucha. Photon assisted tunnelling in single and coupled quantum dot systems. *Superlattices and Microstructures*, 21(2):247–254, March 1997.
- [62] T. H. Oosterkamp, T. Fujisawa, W. G. van der Wiel, K. Ishibashi, R. V. Hijman, S. Tarucha, and L. P. Kouwenhoven. Microwave spectroscopy of a quantum-dot molecule. *Nature*, 395(6705):873–876, October 1998.
- [63] W. G. van der Wiel, S. De Franceschi, J. M. Elzerman, T. Fujisawa, S. Tarucha, and L. P. Kouwenhoven. Electron transport through double quantum dots. *Reviews of Modern Physics*, 75(1):1–22, December 2002.
- [64] Jun-Won Rhim, Jens H. Bardarson, and Robert-Jan Slager. Unified bulk-boundary correspondence for band insulators. *Physical Review B*, 97(11):115143, March 2018.
- [65] J. K. Asbóth. Symmetries, topological phases, and bound states in the one-dimensional quantum walk. *Physical Review B*, 86(19):195414, November 2012.
- [66] Mark S. Rudner, Netanel H. Lindner, Erez Berg, and Michael Levin. Anomalous Edge States and the Bulk-Edge Correspondence for Periodically Driven Two-Dimensional Systems. *Physical Review X*, 3(3):031005, July 2013.
- [67] Seababrata Mukherjee, Alexander Spracklen, Manuel Valiente, Erika Andersson, Patrik Öhberg, Nathan Goldman, and Robert R. Thomson. Experimental observation of anomalous topological edge modes in a slowly driven photonic lattice. *Nature Communications*, 8:13918, January 2017.
- [68] André Eckardt. Colloquium: Atomic quantum gases in periodically driven optical lattices. *Reviews of Modern Physics*, 89(1):011004, March 2017.
- [69] André Eckardt, Christoph Weiss, and Martin Holthaus. Superfluid-Insulator Transition in a Periodically Driven Optical Lattice. *Physical Review Letters*, 95(26):260404, December 2005.
- [70] Alessandro Zenesini, Hans Lignier, Donatella Ciampini, Oliver Morsch, and Ennio Arimondo. Coherent Control of Dressed Matter Waves. *Physical Review Letters*, 102(10):100403, March 2009.

-
- [71] M. Aidelsburger, M. Atala, S. Nascimbène, S. Trotzky, Y.-A. Chen, and I. Bloch. Experimental Realization of Strong Effective Magnetic Fields in an Optical Lattice. *Physical Review Letters*, 107(25):255301, December 2011.
- [72] J. Struck, M. Weinberg, C. Ölschläger, P. Windpassinger, J. Simonet, K. Sengstock, R. Höppner, P. Hauke, A. Eckardt, M. Lewenstein, and L. Mathey. Engineering Ising-XY spin-models in a triangular lattice using tunable artificial gauge fields. *Nature Physics*, 9(11):738–743, November 2013.
- [73] M. Lohse, C. Schweizer, O. Zilberberg, M. Aidelsburger, and I. Bloch. A Thouless quantum pump with ultracold bosonic atoms in an optical superlattice. *Nature Physics*, 12(4):350–354, April 2016.
- [74] Christopher Grossert, Martin Leder, Sergey Denisov, Peter Hänggi, and Martin Weitz. Experimental control of transport resonances in a coherent quantum rocking ratchet. *Nature Communications*, 7(1):1–6, February 2016.
- [75] Shuta Nakajima, Takafumi Tomita, Shintaro Taie, Tomohiro Ichinose, Hideki Ozawa, Lei Wang, Matthias Troyer, and Yoshiro Takahashi. Topological Thouless pumping of ultracold fermions. *Nature Physics*, 12(4):296–300, April 2016.
- [76] Takashi Oka and Hideo Aoki. Photovoltaic Hall effect in graphene. *Physical Review B*, 79(8):081406, February 2009.
- [77] Takuya Kitagawa, Erez Berg, Mark Rudner, and Eugene Demler. Topological characterization of periodically driven quantum systems. *Physical Review B*, 82(23):235114, December 2010.
- [78] Takuya Kitagawa, Takashi Oka, Arne Brataas, Liang Fu, and Eugene Demler. Transport properties of non-equilibrium systems under the application of light: Photo-induced quantum Hall insulators without Landau levels. *Physical Review B*, 84(23), December 2011.
- [79] Hossein Dehghani, Takashi Oka, and Aditi Mitra. Out-of-equilibrium electrons and the Hall conductance of a Floquet topological insulator. *Physical Review B*, 91(15):155422, April 2015.
- [80] Takahiro Mikami, Sota Kitamura, Kenji Yasuda, Naoto Tsuji, Takashi Oka, and Hideo Aoki. Brillouin-Wigner theory for high-frequency expansion in periodically driven systems: Application to Floquet topological insulators. *Physical Review B*, 93(14), April 2016.

- [81] F. D. M. Haldane. Model for a Quantum Hall Effect without Landau Levels: Condensed-Matter Realization of the "Parity Anomaly". *Physical Review Letters*, 61(18):2015–2018, October 1988.
- [82] Leticia Tarruell, Daniel Greif, Thomas Uehlinger, Gregor Jotzu, and Tilman Esslinger. Creating, moving and merging Dirac points with a Fermi gas in a tunable honeycomb lattice. *Nature*, 483(7389):302–305, March 2012.
- [83] Thomas Uehlinger, Daniel Greif, Gregor Jotzu, Leticia Tarruell, Tilman Esslinger, Lei Wang, and Matthias Troyer. Double transfer through Dirac points in a tunable honeycomb optical lattice. *The European Physical Journal Special Topics*, 217(1):121–133, March 2013.
- [84] Gregor Jotzu, Michael Messer, Rémi Desbuquois, Martin Lebrat, Thomas Uehlinger, Daniel Greif, and Tilman Esslinger. Experimental realization of the topological Haldane model with ultracold fermions. *Nature*, 515(7526):237–240, November 2014.
- [85] M. Aidelsburger, M. Lohse, C. Schweizer, M. Atala, J. T. Barreiro, S. Nascimbène, N. R. Cooper, I. Bloch, and N. Goldman. Measuring the Chern number of Hofstadter bands with ultracold bosonic atoms. *Nature Physics*, 11(2):162–166, February 2015.
- [86] J. W. McIver, B. Schulte, F.-U. Stein, T. Matsuyama, G. Jotzu, G. Meier, and A. Cavalleri. Light-induced anomalous Hall effect in graphene. *Nature Physics*, 16(1):38–41, January 2020.
- [87] Hernán L. Calvo, Horacio M. Pastawski, Stephan Roche, and Luis E. F. Foa Torres. Tuning laser-induced band gaps in graphene. *Applied Physics Letters*, 98(23):232103, June 2011.
- [88] Gonzalo Usaj, P. M. Perez-Piskunow, L. E. F. Foa Torres, and C. A. Balseiro. Irradiated graphene as a tunable Floquet topological insulator. *Physical Review B*, 90(11):115423, September 2014.
- [89] P. M. Perez-Piskunow, Gonzalo Usaj, C. A. Balseiro, and L. E. F. Foa Torres. Floquet chiral edge states in graphene. *Physical Review B*, 89(12):121401, March 2014.
- [90] K. Kristinsson, O. V. Kibis, S. Morina, and I. A. Shelykh. Control of electronic transport in graphene by electromagnetic dressing. *Scientific Reports*, 6:srep20082, February 2016.
- [91] Netanel H. Lindner, Gil Refael, and Victor Galitski. Floquet topological insulator in semiconductor quantum wells. *Nature Physics*, 7(6):490–495, June 2011.

-
- [92] Arijit Kundu, H. A. Fertig, and Babak Seradjeh. Effective Theory of Floquet Topological Transitions. *Physical Review Letters*, 113(23):236803, December 2014.
- [93] M.A. Sentef, M. Claassen, A.F. Kemper, B. Moritz, T. Oka, J.K. Freericks, and T.P. Devereaux. Theory of Floquet band formation and local pseudospin textures in pump-probe photoemission of graphene. *Nature Communications*, 6:7047, May 2015.
- [94] T. Timberlake and L. E. Reichl. Changes in Floquet-state structure at avoided crossings: Delocalization and harmonic generation. *Physical Review A*, 59(4):2886–2893, April 1999.
- [95] Hossein Dehghani, Takashi Oka, and Aditi Mitra. Dissipative Floquet topological systems. *Physical Review B*, 90(19):195429, November 2014.
- [96] Alexander Schnell, André Eckardt, and Sergey Denisov. Is there a Floquet Lindbladian? *Physical Review B*, 101(10):100301, March 2020.
- [97] Milena Grifoni, Maura Sasseti, Jürgen Stockburger, and Ulrich Weiss. Nonlinear response of a periodically driven damped two-state system. *Physical Review E*, 48(5):3497–3509, November 1993.
- [98] T. Dittrich, B. Oelschlägel, and P. Hänggi. Driven Tunnelling with Dissipation. *Europhysics Letters (EPL)*, 22(1):5–10, April 1993.
- [99] R. Graham and R. Hubner. Generalized Quasi-Energies and Floquet States for a Dissipative System. *Annals of Physics*, 234(2):300–315, September 1994.
- [100] Milena Grifoni, Maura Sasseti, Peter Hänggi, and Ulrich Weiss. Cooperative effects in the nonlinearly driven spin-boson system. *Physical Review E*, 52(4):3596–3607, October 1995.
- [101] Christine Zerbe and Peter Hänggi. Brownian parametric quantum oscillator with dissipation. *Physical Review E*, 52(2):1533–1543, August 1995.
- [102] Sigmund Kohler, Thomas Dittrich, and Peter Hänggi. Floquet-Markovian description of the parametrically driven, dissipative harmonic quantum oscillator. *Physical Review E*, 55(1):300–313, January 1997.
- [103] Thomas Iadecola, Claudio Chamon, Roman Jackiw, and So-Young Pi. Generalized energy and time-translation invariance in a driven dissipative system. *Physical Review B*, 88(10):104302, September 2013.

- [104] Matthias Langemeyer and Martin Holthaus. Energy flow in periodic thermodynamics. *Physical Review E*, 89(1):012101, January 2014.
- [105] Tatsuhiko Shirai, Takashi Mori, and Seiji Miyashita. Condition for emergence of the Floquet-Gibbs state in periodically driven open systems. *Physical Review E*, 91(3):030101, March 2015.
- [106] Tatsuhiko Shirai, Juzar Thingna, Takashi Mori, Sergey Denisov, Peter Hänggi, and Seiji Miyashita. Effective Floquet-Gibbs states for dissipative quantum systems. *New Journal of Physics*, 18(5):053008, May 2016.
- [107] Tatsuhiko Shirai, Takashi Mori, and Seiji Miyashita. Floquet-Gibbs state in open quantum systems. *The European Physical Journal Special Topics*, 227(3-4):323-333, September 2018.
- [108] Walter Kohn. Periodic Thermodynamics. *Journal of Statistical Physics*, 103(3):417-423, May 2001.
- [109] Karthik I. Seetharam, Charles-Edouard Bardyn, Netanel H. Lindner, Mark S. Rudner, and Gil Refael. Controlled Population of Floquet-Bloch States via Coupling to Bose and Fermi Baths. *Physical Review X*, 5(4):041050, December 2015.
- [110] Jan Carl Budich, Peter Zoller, and Sebastian Diehl. Dissipative preparation of Chern insulators. *Physical Review A*, 91(4):042117, April 2015.
- [111] Sebastian Diehl, Enrique Rico, Mikhail A. Baranov, and Peter Zoller. Topology by dissipation in atomic quantum wires. *Nature Physics*, 7(12):971-977, December 2011.
- [112] Y. H. Wang, H. Steinberg, P. Jarillo-Herrero, and N. Gedik. Observation of Floquet-Bloch States on the Surface of a Topological Insulator. *Science*, 342(6157):453-457, October 2013.
- [113] Mikael C. Rechtsman, Julia M. Zeuner, Yonatan Plotnik, Yaakov Lumer, Daniel Podolsky, Felix Dreisow, Stefan Nolte, Mordechai Segev, and Alexander Szameit. Photonic Floquet topological insulators. *Nature*, 496(7444):196-200, April 2013.
- [114] Lukas J. Maczewsky, Julia M. Zeuner, Stefan Nolte, and Alexander Szameit. Observation of photonic anomalous Floquet topological insulators. *Nature Communications*, 8(1):1-7, January 2017.

-
- [115] Tomoki Ozawa, Hannah M. Price, Alberto Amo, Nathan Goldman, Mohammad Hafezi, Ling Lu, Mikael C. Rechtsman, David Schuster, Jonathan Simon, Oded Zeitlinger, and Iacopo Carusotto. Topological photonics. *Reviews of Modern Physics*, 91(1):015006, March 2019.
- [116] M. Weinberg, C. Staarmann, C. Ölschläger, J. Simonet, and K. Sengstock. Breaking inversion symmetry in a state-dependent honeycomb lattice: artificial graphene with tunable band gap. *2D Materials*, 3(2):024005, 2016.
- [117] H. M. Price and N. R. Cooper. Mapping the Berry curvature from semiclassical dynamics in optical lattices. *Physical Review A*, 85(3):033620, 2012.
- [118] Marcos Atala, Monika Aidelsburger, Julio T. Barreiro, Dmitry Abanin, Takuya Kitagawa, Eugene Demler, and Immanuel Bloch. Direct measurement of the Zak phase in topological Bloch bands. *Nature Physics*, 9(12):795–800, 2013.
- [119] L. Duca, T. Li, M. Reitter, I. Bloch, M. Schleier-Smith, and U. Schneider. An Aharonov-Bohm interferometer for determining Bloch band topology. *Science*, 347(6219):288–292, January 2015.
- [120] Philipp Hauke, Maciej Lewenstein, and André Eckardt. Tomography of Band Insulators from Quench Dynamics. *Physical Review Letters*, 113(4):045303, July 2014.
- [121] N. Fläschner, B. S. Rem, M. Tarnowski, D. Vogel, D.-S. Lühmann, K. Sengstock, and C. Weitenberg. Experimental reconstruction of the Berry curvature in a Floquet Bloch band. *Science*, 352(6289):1091–1094, May 2016.
- [122] N. Fläschner, D. Vogel, M. Tarnowski, B. S. Rem, D.-S. Lühmann, M. Heyl, J. C. Budich, L. Mathey, K. Sengstock, and C. Weitenberg. Observation of dynamical vortices after quenches in a system with topology. *Nature Physics*, 14(3):265–268, March 2018.
- [123] Alvaro Rubio-García, Chris N. Self, Juan Jose García-Ripoll, and Jiannis K. Pachos. Seeing topological edge and bulk currents in time-of-flight images. *arXiv:1910.06446 [cond-mat, physics:quant-ph]*, October 2019.
- [124] Congjun Wu. Unconventional bose–einstein condensations beyond the "no-node" theorem. *Modern Physics Letters B*, 23(01):1–24, January 2009.
- [125] Masatoshi Imada, Atsushi Fujimori, and Yoshinori Tokura. Metal-insulator transitions. *Reviews of Modern Physics*, 70(4):1039–1263, October 1998.

- [126] Y. Tokura and N. Nagaosa. Orbital Physics in Transition-Metal Oxides. *Science*, 288(5465):462–468, April 2000.
- [127] Yoshiteru Maeno, T. Maurice Rice, and Manfred Sigrist. The Intriguing Superconductivity of Strontium Ruthenate. *Physics Today*, 54(1):42–47, January 2001.
- [128] Andrew Peter Mackenzie and Yoshiteru Maeno. The superconductivity of Sr_2RuO_4 and the physics of spin-triplet pairing. *Reviews of Modern Physics*, 75(2):657–712, May 2003.
- [129] Patrick A. Lee, Naoto Nagaosa, and Xiao-Gang Wen. Doping a Mott insulator: Physics of high-temperature superconductivity. *Reviews of Modern Physics*, 78(1):17–85, January 2006.
- [130] Sadamichi Maekawa, Takami Tohyama, Stewart Edward Barnes, Sumio Ishihara, Wataru Koshibae, and Giniyat Khaliullin. *Physics of Transition Metal Oxides*. Springer, 2004 edition, March 2013.
- [131] Georg Wirth, Matthias Ölschläger, and Andreas Hemmerich. Evidence for orbital superfluidity in the P-band of a bipartite optical square lattice. *Nature Physics*, 7(2):147–153, February 2011.
- [132] Matthias Ölschläger, Georg Wirth, and Andreas Hemmerich. Unconventional Superfluid Order in the F Band of a Bipartite Optical Square Lattice. *Physical Review Letters*, 106(1):015302, January 2011.
- [133] Matthias Ölschläger, Georg Wirth, Thorge Kock, and Andreas Hemmerich. Topologically Induced Avoided Band Crossing in an Optical Checkerboard Lattice. *Physical Review Letters*, 108(7):075302, February 2012.
- [134] M. Ölschläger, T. Kock, G. Wirth, A. Ewerbeck, C. Morais Smith, and A. Hemmerich. Interaction-induced chiral $p_x \pm ip_y$ - superfluid order of bosons in an optical lattice. *New Journal of Physics*, 15(8):083041, 2013.
- [135] M. Di Liberto, T. Comparin, T. Kock, M. Ölschläger, A. Hemmerich, and C. Morais Smith. Controlling coherence via tuning of the population imbalance in a bipartite optical lattice. *Nature Communications*, 5:5735, 2014.
- [136] T. Kock, M. Ölschläger, A. Ewerbeck, W.-M. Huang, L. Mathey, and A. Hemmerich. Observing Chiral Superfluid Order by Matter-Wave Interference. *Physical Review Letters*, 114(11):115301, 2015.

-
- [137] T. Kock, C. Hippler, A. Ewerbeck, and A. Hemmerich. Orbital optical lattices with bosons. *Journal of Physics B: Atomic, Molecular and Optical Physics*, 49(4):042001, January 2016.
- [138] Kai Sun, W. Vincent Liu, Andreas Hemmerich, and S. Das Sarma. Topological semimetal in a fermionic optical lattice. *Nature Physics*, 8(1):67–70, January 2012.
- [139] M. Di Liberto, A. Hemmerich, and C. Morais Smith. Topological Varma Superfluid in Optical Lattices. *Physical Review Letters*, 117(16):163001, 2016.
- [140] Zhi-Fang Xu, Li You, Andreas Hemmerich, and W. Vincent Liu. π -Flux Dirac Bosons and Topological Edge Excitations in a Bosonic Chiral p -Wave Superfluid. *Physical Review Letters*, 117(8):085301, August 2016.
- [141] A. Isacsson and S. M. Girvin. Multiflavor bosonic Hubbard models in the first excited Bloch band of an optical lattice. *Physical Review A*, 72(5):053604, November 2005.
- [142] V. W. Scarola and S. Das Sarma. Quantum Phases of the Extended Bose-Hubbard Hamiltonian: Possibility of a Supersolid State of Cold Atoms in Optical Lattices. *Physical Review Letters*, 95(3):033003, July 2005.
- [143] W. Vincent Liu and Congjun Wu. Atomic matter of nonzero-momentum Bose-Einstein condensation and orbital current order. *Physical Review A*, 74(1):013607, July 2006.
- [144] Vladimir M. Stojanović, Congjun Wu, W. Vincent Liu, and S. Das Sarma. Incommensurate Superfluidity of Bosons in a Double-Well Optical Lattice. *Physical Review Letters*, 101(12):125301, September 2008.
- [145] Zi Cai and Congjun Wu. Complex and real unconventional Bose-Einstein condensations in high orbital bands. *Physical Review A*, 84(3):033635, September 2011.
- [146] Torben Müller, Simon Fölling, Artur Widera, and Immanuel Bloch. State Preparation and Dynamics of Ultracold Atoms in Higher Lattice Orbitals. *Physical Review Letters*, 99(20):200405, November 2007.
- [147] P. w Anderson, B. I. Halperin, and c M. Varma. Anomalous low-temperature thermal properties of glasses and spin glasses. *The Philosophical Magazine: A Journal of Theoretical Experimental and Applied Physics*, 25(1):1–9, January 1972.
- [148] V. V. Brazhkin. Metastable phases and ‘metastable’ phase diagrams. *Journal of Physics: Condensed Matter*, 18(42):9643–9650, October 2006.

- [149] Yuri Korniyushin. Studying Thermodynamics of Metastable States. *Facta Universitatis, Series: Physics, Chemistry and Technology*, 3(2):115–128, February 2005. arXiv:cond-mat/0702076.
- [150] A. Smerzi, S. Fantoni, S. Giovanazzi, and S. R. Shenoy. Quantum Coherent Atomic Tunneling between Two Trapped Bose-Einstein Condensates. *Physical Review Letters*, 79(25):4950–4953, December 1997.
- [151] Le-Man Kuang and Zhong-Wen Ouyang. Macroscopic quantum self-trapping and atomic tunneling in two-species Bose-Einstein condensates. *Physical Review A*, 61(2):023604, January 2000.
- [152] Kenichi Kasamatsu, Yukinori Yasui, and Makoto Tsubota. Macroscopic quantum tunneling of two-component Bose-Einstein condensates. *Physical Review A*, 64(5):053605, October 2001.
- [153] H.-J. Miesner, D. M. Stamper-Kurn, J. Stenger, S. Inouye, A. P. Chikkatur, and W. Ketterle. Observation of Metastable States in Spinor Bose-Einstein Condensates. *Physical Review Letters*, 82(11):2228–2231, March 1999.
- [154] Hannes Bernien, Sylvain Schwartz, Alexander Keesling, Harry Levine, Ahmed Omran, Hannes Pichler, Soonwon Choi, Alexander S. Zibrov, Manuel Endres, Markus Greiner, Vladan Vuletić, and Mikhail D. Lukin. Probing many-body dynamics on a 51-atom quantum simulator. *Nature*, 551(7682):579–584, November 2017.
- [155] C. J. Turner, A. A. Michailidis, D. A. Abanin, M. Serbyn, and Z. Papić. Weak ergodicity breaking from quantum many-body scars. *Nature Physics*, 14(7):745–749, July 2018.
- [156] Wen Wei Ho, Soonwon Choi, Hannes Pichler, and Mikhail D. Lukin. Periodic Orbits, Entanglement, and Quantum Many-Body Scars in Constrained Models: Matrix Product State Approach. *Physical Review Letters*, 122(4):040603, January 2019.
- [157] Leon Droenner, Regina Finsterhölzl, Markus Heyl, and Alexander Carmele. Stabilizing a discrete time crystal against dissipation. *arXiv:1902.04986*, February 2019.
- [158] Philip Pearle. Simple Derivation of the Lindblad Equation. *European Journal of Physics*, 33(4):805–822, July 2012.
- [159] Wilhelm Magnus. On the exponential solution of differential equations for a linear operator. *Communications on Pure and Applied Mathematics*, 7(4):649–673, 1954.

-
- [160] Philip Pechukas and John C. Light. On the Exponential Form of Time-Displacement Operators in Quantum Mechanics. *The Journal of Chemical Physics*, 44(10):3897–3912, May 1966.
- [161] S. Blanes, F. Casas, J. A. Oteo, and J. Ros. The Magnus expansion and some of its applications. *Physics Reports*, 470(5):151–238, January 2009.
- [162] W. R. Salzman. An alternative to the magnus expansion in time-dependent perturbation theory. *The Journal of Chemical Physics*, 82(2):822–826, January 1985.
- [163] Beilei Zhu, Tobias Rexin, and Ludwig Mathey. Magnus Expansion Approach to Parametric Oscillator Systems in a Thermal Bath. *Zeitschrift für Naturforschung A*, 71(10):921–932, 2016.
- [164] Wolfgang P. Schleich. *Quantum Optics in Phase Space*. Wiley-VCH, Berlin ; New York, 1st edition, February 2001.
- [165] N. Goldman and J. Dalibard. Periodically Driven Quantum Systems: Effective Hamiltonians and Engineered Gauge Fields. *Physical Review X*, 4(3):031027, August 2014.
- [166] André Eckardt and Egidijus Anisimovas. High-frequency approximation for periodically driven quantum systems from a Floquet-space perspective. *New Journal of Physics*, 17(9):093039, September 2015.
- [167] Takahiro Fukui, Yasuhiro Hatsugai, and Hiroshi Suzuki. Chern Numbers in Discretized Brillouin Zone: Efficient Method of Computing (Spin) Hall Conductances. *Journal of the Physical Society of Japan*, 74(6):1674–1677, June 2005.
- [168] P. M. Perez-Piskunow, L. E. F. Foa Torres, and Gonzalo Usaj. Hierarchy of Floquet gaps and edge states for driven honeycomb lattices. *Physical Review A*, 91(4):043625, April 2015.
- [169] J. K. Freericks, H. R. Krishnamurthy, and Th. Pruschke. Theoretical Description of Time-Resolved Photoemission Spectroscopy: Application to Pump-Probe Experiments. *Physical Review Letters*, 102(13):136401, 2009.
- [170] Eric L. Shirley, L. J. Terminello, A. Santoni, and F. J. Himpsel. Brillouin-zone-selection effects in graphite photoelectron angular distributions. *Physical Review B*, 51(19):13614–13622, May 1995.

- [171] Ferdinand Kuemmeth and Emmanuel I. Rashba. Giant spin rotation under quasiparticle-photoelectron conversion: Joint effect of sublattice interference and spin-orbit coupling. *Physical Review B*, 80(24):241409, December 2009.
- [172] Isabella Gierz, Jürgen Henk, Hartmut Höchst, Christian R. Ast, and Klaus Kern. Illuminating the dark corridor in graphene: Polarization dependence of angle-resolved photoemission spectroscopy on graphene. *Physical Review B*, 83(12):121408, March 2011.
- [173] Isabella Gierz, Jesse C. Petersen, Matteo Mitrano, Cephise Cacho, Edmond Turcu, Emma Springate, Alexander Stöhr, Axel Köhler, Ulrich Starke, and Andrea Cavalleri. Snapshots of non-equilibrium Dirac carrier distributions in graphene. *Nature Materials*, 12(12):1119–1124, October 2013.
- [174] Paul A. George, Jared Strait, Jahan Dawlaty, Shriram Shivaraman, Mvs Chandrashekar, Farhan Rana, and Michael G. Spencer. Ultrafast Optical-Pump Terahertz-Probe Spectroscopy of the Carrier Relaxation and Recombination Dynamics in Epitaxial Graphene. *Nano Letters*, 8(12):4248–4251, December 2008.
- [175] Markus Breusing, Claus Ropers, and Thomas Elsaesser. Ultrafast Carrier Dynamics in Graphite. *Physical Review Letters*, 102(8):086809, February 2009.
- [176] M. Breusing, S. Kuehn, T. Winzer, E. Malić, F. Milde, N. Severin, J. P. Rabe, C. Ropers, A. Knorr, and T. Elsaesser. Ultrafast nonequilibrium carrier dynamics in a single graphene layer. *Physical Review B*, 83(15):153410, April 2011.
- [177] T. Li, L. Luo, M. Hupalo, J. Zhang, M. C. Tringides, J. Schmalian, and J. Wang. Femtosecond Population Inversion and Stimulated Emission of Dense Dirac Fermions in Graphene. *Physical Review Letters*, 108(16):167401, April 2012.
- [178] Kuan-Chun Lin, Ming-Yang Li, L. J. Li, D. C. Ling, C. C. Chi, and Jeng-Chung Chen. Ultrafast dynamics of hot electrons and phonons in chemical vapor deposited graphene. *Journal of Applied Physics*, 113(13):133511, April 2013.
- [179] I. I. Rabi. Space Quantization in a Gyating Magnetic Field. *Physical Review*, 51(8):652–654, April 1937.
- [180] L. Allen and J. H. Eberly. *Optical Resonance and Two-Level Atoms*. Dover Publications, New York, December 1987.
- [181] A. Kastberg, W. D. Phillips, S. L. Rolston, R. J. C. Spreeuw, and P. S. Jessen. Adiabatic Cooling of Cesium to 700 nK in an Optical Lattice. *Physical Review Letters*, 74(9):1542–1545, February 1995.

-
- [182] T. Müller-Seydlitz, M. Hartl, B. Brezger, H. Hänsel, C. Keller, A. Schnez, R. J. C. Spreeuw, T. Pfau, and J. Mlynek. Atoms in the Lowest Motional Band of a Three-Dimensional Optical Lattice. *Physical Review Letters*, 78(6):1038–1041, February 1997.
- [183] Markus Greiner, Immanuel Bloch, Olaf Mandel, Theodor W. Hänsch, and Tilman Esslinger. Exploring Phase Coherence in a 2d Lattice of Bose-Einstein Condensates. *Physical Review Letters*, 87(16):160405, October 2001.
- [184] Michael Köhl, Henning Moritz, Thilo Stöferle, Kenneth Günter, and Tilman Esslinger. Fermionic Atoms in a Three Dimensional Optical Lattice: Observing Fermi Surfaces, Dynamics, and Interactions. *Physical Review Letters*, 94(8):080403, March 2005.
- [185] D. McKay, M. White, and B. DeMarco. Lattice thermodynamics for ultracold atoms. *Physical Review A*, 79(6):063605, June 2009.
- [186] Lukas Freystatzky. Bachelor’s thesis: Atomic dynamics in driven honeycomb lattices, 2016.
- [187] C. J. Pethick and H. Smith. *Bose–Einstein Condensation in Dilute Gases*. Cambridge University Press, Cambridge, 2nd edition, September 2008.
- [188] P. B. Blakie, A. S. Bradley, M. J. Davis, R. J. Ballagh, and C. W. Gardiner. Dynamics and statistical mechanics of ultra-cold Bose gases using c-field techniques. *Advances in Physics*, 57(5):363–455, September 2008.
- [189] C. W. Gardiner J. R. Anglin and T. I. A. Fudge. The stochastic Gross-Pitaevskii equation. *arXiv:cond-mat/0112129*, December 2001.
- [190] C. W. Gardiner and M. J. Davis. The stochastic Gross-Pitaevskii equation II. *Journal of Physics B: Atomic, Molecular and Optical Physics*, 36(23):4731–4753, December 2003.
- [191] S. P. Cockburn and N. P. Proukakis. The Stochastic Gross-Pitaevskii Equation and some Applications. *Laser Physics*, 19(4):558–570, April 2009.
- [192] Anatoli Polkovnikov. Phase space representation of quantum dynamics. *Annals of Physics*, 325(8):1790–1852, August 2010.
- [193] Matthew J. Davis, Tod M. Wright, P. Blair Blakie, Ashton S. Bradley, Rob J. Ballagh, and Crispin W. Gardiner. C-Field Methods for Non-Equilibrium Bose Gases. *arXiv:1206.5470 [cond-mat]*, 1:163–175, April 2013.

- [194] G. Kordas, S. Wimberger, and D. Witthaut. Decay and fragmentation in an open Bose-Hubbard chain. *Physical Review A*, 87(4):043618, April 2013.
- [195] Saurabh Paul and Eite Tiesinga. Formation and decay of Bose-Einstein condensates in an excited band of a double-well optical lattice. *Physical Review A*, 88(3):033615, September 2013.
- [196] Andreas Hemmerich. Bosons condensed in two modes with flavor-changing interaction. *Physical Review A*, 99(1):013623, January 2019.
- [197] Barry J. Harrington and Harvey K. Shepard. Thermodynamics of the Yang-Mills gas. *Physical Review D*, 18(8):2990–2994, October 1978.
- [198] David J. Gross, Robert D. Pisarski, and Laurence G. Yaffe. QCD and instantons at finite temperature. *Reviews of Modern Physics*, 53(1):43–80, January 1981.
- [199] Henk T. C. Stoof, Dennis B. M. Dickerscheid, and Koos Gubbels. *Ultracold Quantum Fields*. Theoretical and Mathematical Physics. Springer, 2009.
- [200] L. Pitaevskii and S. Stringari. *Bose-Einstein Condensation*. Clarendon Press, Oxford ; New York, 1st edition, June 2003.
- [201] Franz Schwabl. *Quantenmechanik für Fortgeschrittene*. Springer, Berlin, 5th edition, September 2008.
- [202] Jean-Paul Blaizot and Georges Ripka. *Quantum Theory of Finite Systems*. The MIT Press, Cambridge, MA, December 1985.
- [203] Ming-wen Xiao. Theory of transformation for the diagonalization of quadratic Hamiltonians. *arXiv:0908.0787 [math-ph]*, August 2009.
- [204] Iliya Esin, Mark S. Rudner, Gil Refael, and Netanel H. Lindner. Quantized transport and steady states of Floquet topological insulators. *Physical Review B*, 97(24):245401, June 2018.
- [205] Congjun Wu and S. Das Sarma. $p_{x,y}$ -orbital counterpart of graphene: Cold atoms in the honeycomb optical lattice. *Physical Review B*, 77(23):235107, June 2008.

Eidesstattliche Versicherung

Hiermit versichere ich an Eides statt, die vorliegende Dissertationsschrift selbst verfasst und keine anderen als die angegebenen Hilfsmittel und Quellen benutzt zu haben.

Die eingereichte schriftliche Fassung entspricht der auf dem elektronischen Speichermedium.

Die Dissertation wurde in der vorgelegten oder einer ähnlichen Form nicht schon einmal in einem früheren Promotionsverfahren angenommen oder als ungenügend beurteilt.

Hamburg, den 31.08.2020

Marlon Nuske